https://journals.vsu.ru/kcmf/about

ISSN 1606-867X
eISSN 2687-0711

Конденсированные среды и межфазные границы

РЕЦЕНЗИРУЕМЫЙ НАУЧНЫЙ ЖУРНАЛ

Condensed Matter and Interphases

PEER-REVIEWED SCIENTIFIC JOURNAL

Том / Vol. 25, № / No. 3
2023

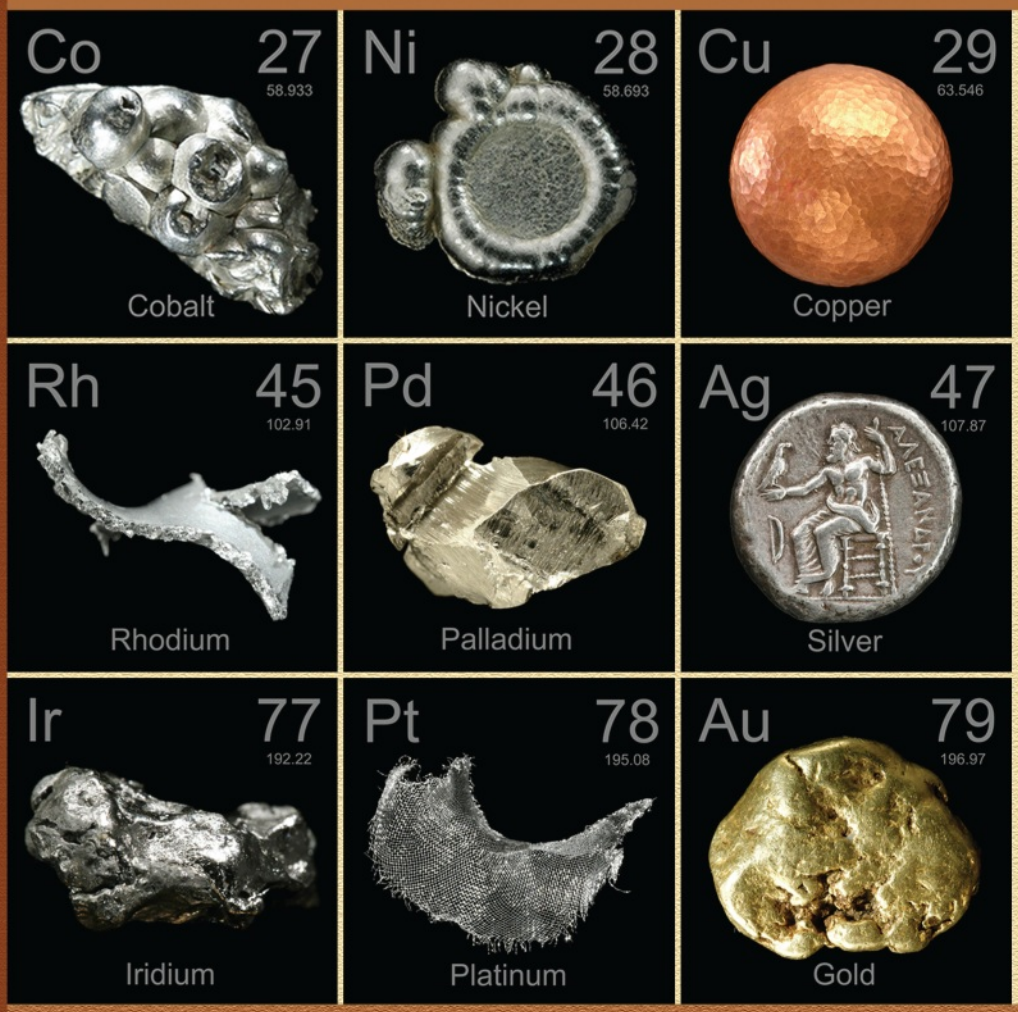

Condensed Matter and Interphases
Kondensirovannye sredy i mezhfaznye granitsy

Peer-reviewed scientific journal
Published since January 1999
Periodicity: Quarterly
Volume 25, No. 3, 2023

Full-text version is available in the Russian language on the website: https://journals.vsu.ru/kcmf

Condensed Matter and Interphases (Kondensirovannye Sredy i Mezhfaznye Granitsy) publishes articles in Russian and English dedicated to key issues of condensed matter and physicochemical processes at interfaces and in volumes.

The mission of the journal is to provide open access to the results of original research (theoretical and experimental) at the intersection of contemporary condensed matter physics and chemistry, material science and nanoindustry, solid state chemistry, inorganic chemistry, and physical chemistry, and to share scientific data in the **following sections**: atomic, electron, and cluster structure of solids, liquids, and interphase boundaries; phase equilibria and defect formation processes; structure and physical and chemical properties of interphases; laser thermochemistry and photostimulated processes on solid surfaces; physics and chemistry of surface, thin films and heterostructures; kinetics and mechanism of formation of film structures; electrophysical processes in interphase boundaries; chemistry of surface phenomena in sorbents; devices and new research methods.

The journal accepts for publication: reviews, original articles, short communications by leading Russian scientists, foreign researchers, lecturers, postgraduate and undergraduate students.

FOUNDER AND PUBLISHER:
Voronezh State University

The journal is registered by the Russian Federal Service for Supervision of Communications, Information Technology and Mass Media, Certificate of Registration ПИ № ФС77-78771 date 20.07.2020

The journal is included in the List of peer reviewed scientific journals published by the Higher Attestation Commission in which major research results from the dissertations of Candidates of Sciences (PhD) and Doctor of Science (DSc) degrees are to be published. Scientific specialties of dissertations and their respective branches of science are as follows: 1.4.1. – Inorganic Chemistry (Chemical sciences); 1.4.4. – Physical Chemistry (Chemical sciences); 1.4.6. – Electrochemistry (Chemical sciences); 1.4.15. – Solid State Chemistry (Chemical sciences); 1.3.8. – Condensed Matter Physics (Physical sciences).

The journal is indexed and archived in: Russian Scientific Index Citations, Scopus, Chemical Abstract, EBSCO, DOAJ, CrossRef

Editorial Board and Publisher Office:
1 Universitetskaya pl., Voronezh 394018
Phone: +7 (432) 2208445
https://journals.vsu.ru/kcmf
E-mail: kcmf@main.vsu.ru

Price – not fixed

Subscription index in the Catalogue «Russian Post» is ПН134

CONTENTS

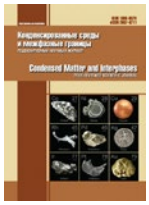

ISSN 1606-867X (Print)
ISSN 2687-0711 (Online)
Condensed Matter and Interphases
Kondensirovannye Sredy i Mezhfaznye Granitsy
https://journals.vsu.ru/kcmf/

Review

Review article
https://doi.org/10.17308/kcmf.2023.25/11256

Preparation, luminescence, and application of $LiMeBO_3$ borates, Me = Mg, Ca, Sr, Ba, Zn, Cd. Review

T. N. Khamaganova✉

Baikal Institute of Nature Management Siberian Branch of the Russian Academy of sciences
6 Sakhyanovoy st., Ulan-Ude, Buryatia, Russian Federation

Abstract

The review summarises and analyses data on the preparation, structure, and spectral-luminescent properties of $LiMeBO_3$-based borates, Me = bivalent metal.

These polycrystalline borates are prepared traditionally by solid-phase reactions and self-propagating high-temperature synthesis and its modifications based on a combustion reaction.

Frameworks of lithium borates with alkaline earth metals, zinc, and cadmium are formed from large metal polyhedra between which there are boron-oxygen triangles isolated from each other. Doping with rare-earth and heavy metal ions leads to the formation of solid solutions which normally have defective structures. Doped activator ions often become the main part of the luminescence centre in the phosphor. The luminescent properties of ions of rare-earth elements arise from the possibility of electronic transitions between states within the 4*f*-configuration. The paper discusses the most likely mechanisms of charge compensation during heterovalent substitution in $LiMeBO_3$ borates (co-doping and formation of cation vacancies). It is shown that charge compensation during the combined introduction of ions of REEs and alkali metals into the structure has a positive effect on the emission yield. The review considers the results of thermoluminescent, upconversion, and photoluminescent properties and processes and phenomena that cause them. It also explains the mechanism of resonance energy transfer from the sensitiser to the activator using the example of $Yb^{3+} \rightarrow Er^{3+}$.

It discusses the possibility of using the considered borates as phosphors that emit green, blue, and red light in white LEDs and as effective materials for personnel neutron dosimetry and the dosimetry of weak ionising radiation.

Keywords: Polycrystalline borates, Solid-phase synthesis, Combustion method, LEDs, Thermoluminescence, Green phosphor, Sensitisation

Funding: The study was supported by the Ministry of Science and Higher Education of the Russian Federation (the government order to the Baikal Institute of Nature Management, Siberian Branch of the Russian Academy of Sciences, project No. 0273–2021-0008).

For citation: Khamaganova T. N. Preparation, luminescence, and application of $LiMeBO_3$ borates, Me= Mg, Ca, Sr, Ba, Zn, Cd. Review. *Condensed Matter and Interphases.* 2023;25(3): 311–332. https://doi.org/10.17308/kcmf.2023.25/11256

Для цитирования: Хамаганова Т. Н. Получение, люминесценция и применение боратов $LiMeBO_3$, Me = Mg, Ca, Sr, Ba, Zn, Cd. Обзор. Конденсированные среды и межфазные границы. 2023;25(3): 311–332. https://doi.org/10.17308/kcmf.2023.25/11256

✉ Khamaganova T. N., e-mail: khama@binm.ru

1. Introduction

Lighting technology (residential and industrial, plasma and electroluminescent panels, mobile phones, displays, etc.) has been recently using white LEDs (w-LED) because of a number of advantages, i.e. reliability, high light efficiency, low energy consumption, environmental friendliness, and a long service life [1–3].

Developments in solid-state lighting have encouraged researchers to search for new efficient phosphors which can be used as sources of white light in LEDs. Ions of rare earth elements (REEs) and transition metals are used as activators in many inorganic phosphors (aluminates, vanadates, phosphates, etc.) due to the possibility to adjust their colour emission over a wide range of the visible spectrum [4-10].

Simple and complex borates are promising materials that meet the necessary requirements [3, 6, 8, 11–14]. Compounds of this class can be used as structural matrices of phosphors due to their high thermal and chemical stability, quantum efficiency, and crystallisation at relatively low temperatures [3, 6, 7]. They are characterised by high transparency in the visible region of the spectrum, a wide band gap, a high coefficient of thermal expansion, and strong absorption in the near ultraviolet region, which makes them excellent materials for optoelectronic devices, solid-state lighting, and data display devices [12–16].

In particular, due to ions of alkali and alkaline-earth metals, oxygen can be coordinated in borates in various ways, which results in various crystalline structures and allows finding new materials with excellent luminescent characteristics [3, 7, 12–20].

Recently, the problem of detecting and measuring radiation has become relevant. Methods based on the effects arising from the interaction of radiation with matter are used to record ionising radiation. Control of radiation doses is conducted with the help of sensors, whose action is based on the effect of thermally stimulated luminescence (TSL). TLD-600 (^{6}LiF:Mg,Ti) and TLD-700 (^{7}LiF:Mg,Ti) dosimeters have been successfully used for personnel neutron monitoring [21, 22]. However, they have many drawbacks, such as a complex structure of the glow curve, a complex annealing procedure, a loss of sensitivity when reused, and remaining residual signals [22, 23]. Therefore, it is necessary to search for and create new effective materials for these applications. Lithium borates are characterised by chemical resistance and stability, their synthesis is simple and relatively cheap and requires low temperatures [10, 13, 17]. These luminescent materials based on alkali and alkaline earth metal borates are promising for medical dosimetry due to the similarity of their effective atomic numbers to soft biological tissue (Z_{eff} = 7.4). Such materials are similar to it in terms of transmission and absorption of ionising radiation, which allows using them in individual, clinical, and radiobiological dosimetry of weak ionising radiation [24].

This paper systematises information on the synthesis, structures, and luminescent properties of lithium borates with bivalent metals of the following composition: $LiMeBO_3$, Me = Mg, Ca, Sr, Ba, Zn, Cd.

2. Methods for the preparation of LiMeBO3 lithium borates

Traditionally, the main method for the preparation of lithium borates of bivalent elements is solid-phase synthesis. It involves high-temperature sintering of lithium carbonate with metal carbonates (more rarely nitrates and fluorides) and boric acid [25–43]. $ZnLiBO_3$ borate is obtained by heating ZnO oxide with an excess of $LiBO_2$ at 800 ºC and extracting unreacted $LiBO_2$ in methanol [35].

Chang [44] prepared a single-phase polycrystalline sample of α-$LiZnBO_3$ by heating an equimolar mixture of $LiBO_2{\cdot}8H_2O$ and ZnO first at 620 ºC for 1 hour and then at 1,000 ºC for 12 hours. The authors [45] prepared α-$LiZnBO_3$ single-phase borate by annealing the same stoichiometric mixture of $LiBO_2{\cdot}8H_2O$ and ZnO at 600 °C for 1 month.

In [46], to prepare $LiZnBO_3$, a stoichiometric mixture of Li_2CO_3, ZnO, and H_3BO_3 was dissolved in diluted nitric acid. The solution was evaporated to remove water and nitric acid, heated at 600 °C and held for up to 3 weeks with intermediate homogenisation of the products. It was noted that the synthesised sample had a small amount of ZnO, which was associated with the volatilisation

of Li_2O during calcination. The authors of the work used a similar method to prepare $LiCdBO_3$ borate by keeping the mixture at 700 ºC, which was followed by quenching. In [47], $LiOH{\cdot}H_2O$ was used instead of Li_2CO_3 as the starting material and the heating temperature was 1,000 °C.

As a rule, solid-phase synthesis involves several stages and intermediate homogenisation of the products [48], for example, $LiMeBO_3$ (Me = Sr, Ba) was obtained by three-stage annealing [30]. The starting reagents for the $LiSrBO_3$ synthesis were Li_2CO_3, $SrCO_3$, and H_3BO_3, while $LiBaBO_3$ was synthesised from Li_2CO_3, BaF_2, and H_3BO_3. Annealing is sometimes conducted in a reducing atmosphere to prevent oxidation processes. For example, in [28], $LiSrBO_3$ phases: Eu^{3+}, Sm^{3+}, Tb^{3+}, and Dy^{3+} were prepared in air, while $LiSrBO_3$:Ce^{3+} was prepared in a reducing medium with a ratio of H_2:N_2 (5:95).

There is a growing number of publications dedicated to the synthesis of phosphors conducted by methods which result in the production of materials with nanoscale particles. For example, preparation of α-$LiZnBO_3$ by sol–gel technology [49]. It is known that this method is used to produce nanoscale particles and the process involves converting a liquid solution (hydrolysis and polycondensation) into a gel. The authors of the work dissolved the stoichiometric ratios of lithium nitrate, zinc (II) nitrate hexahydrate, and boric acid (1:1:1) in propionic acid. The resulting solution was stirred and heated at 100 °C to form a yellow gel. The gel was dried and the dried powder was heat treated at 700 ºC in an inert atmosphere. This resulted in the production of $LiZnBO_3$ borate particles of spherical shape.

In [50–56], the combustion method was proposed to be used to produce fine powders. In literature, depending on the reaction conditions this method is known as the method of self-propagating high-temperature synthesis (SHS) [54]. SHS is an autowave process that spontaneously propagates in a chemically active environment when the chemical reaction is localised in the combustion zone. It is used mainly for the production of inorganic materials: powders, pastes, ceramics, intermetallides, and refractory coatings. The SHS method differs from other methods involving high temperatures and short synthesis time since it allows controlling the process, has lower energy costs, and requires simple equipment [54, 55]. Among the varieties of self-propagating high-temperature synthesis are pyrohydrolytic synthesis, modified solid-phase diffusion method, and the Pechini process. These methods are universal and simple, the processes within them proceed quickly and allow obtaining various types of dispersed materials (including nanoscale) from simple binary compounds to complex doped phases. The process involves a self-sustaining reaction in a homogeneous solution of various oxidising agents (e.g., metal nitrates) and organic reducing agents (e.g., urea, glycine, hydrazine, citric acid, etc.). It is important that oxidation occurs in the absence of oxygen from the environment, but due to the fuel in the solution [56–58].

The Pechini process has been used to synthesise fine $LiMgBO_3$ powder [51]. For this, nitrate solutions of the corresponding metals and boric acid were separately prepared in deionised water. After they were mixed and sonicated, citric acid and ethylene glycol were slowly added to the resulting homogeneous solution at a molar ratio of 1:1 and 1:2, respectively. The solution was treated with nitric acid and evaporated to obtain a viscous yellow polymer resin. The resin was first dried at 200 °C and then annealed for 2–3 minutes at 550 °C. Remaining impurity traces were removed by sintering at 700 °C. Annealing of the resulting solid foamy black mass at 750 °C produced $LiMgBO_3$ nanoparticles. In this process, citric acid ($C_6H_8O_7$) and ethylene glycol ($CH_2(OH)CH_2OH$) were used as chelating and stabilising agents and fuels. The combustible agent and foaming agent was nitric acid (HNO_3). Similar conditions for the $LiMgBO_3$:Dy^{3+} synthesis were used in works [51, 52]. $CO(NH_2)_2$ urea can be used as a combustible material [59]. A study of the morphology of the surface of the $LiMgBO_3$:Dy^{3+} material synthesised by combustion showed that the shape of particles was irregular and their dimensions were within 5–10 μm [50]. The authors attributed a large number of cracks, voids, and pores on the surface to varying consumption of the mass during combustion.

A modified combustion method has also been used to obtain the considered borates [53, 58–65]. In [53], a simple and time-saving technology was used to produce $LiCaBO_3$:Tb^{3+}, which involved

preparing a mixture of lithium, calcium, and terbium nitrates and boric acid. Ammonium nitrate and urea were used as combustible materials. Fig. 1 presents a scanning electron microscope (SEM) image showing the morphology of the surface of the $LiCaBO_3:Tb^{3+}$ phosphor.

Due to the incongruent melting of $LiMeBO_3$ (Me = Zn, Cd), the solution-melt technology for growing crystals has become the most commonly used. Simple borates, such as $Li_2B_4O_7$, Bi_2O_3 bismuth oxide, and low-melting chlorides, for example, LiCl, BaF, were used as solvents.

The hydrothermal method allows obtaining $LiMeBO_3$ crystals, Me = Zn, Cd, at low temperatures from 250 to 450 °C [66-68].

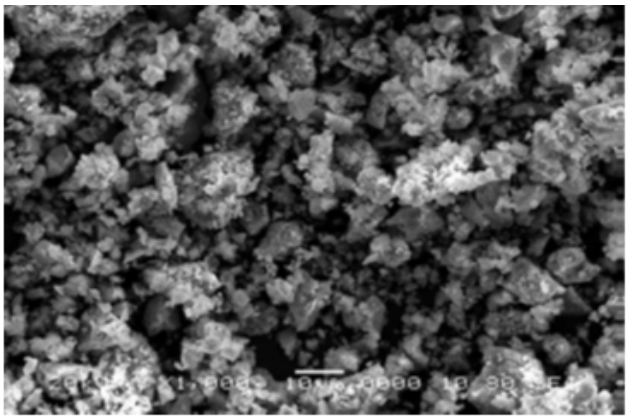

Fig. 1. SEM image of the $LiCaBO_3$:Tb3+ phosphor [53]

3. Crystalline structures of $LiMeBO_3$, Me = Mg, Ca, Sr, Ba, Zn, Cd

Crystallographic characteristics of $LiMBO_3$ obtained by X-ray diffraction analysis of single crystals are given in Table 1. It should be noted that this paper does not discuss in detail the structures of $LiMeBO_3$ with Zn, Cd since they will be considered in another article.

According to Norrestam, the structure of $LiMgBO_3$ determined by a single crystal is isotypical to the structure of monoclinic β-$LiZnBO_3$ [69]. The compound crystallises in the C2/c sp. gr. According to [69], Mg atoms are located in five-vertex polyhedra with Mg-O distances from 1.97 to 2.12 Å, and Li atoms are coordinated by four oxygen atoms with bond lengths from 1.88 to 2.33 Å and have trigonal-bipyramidal coordination. They are disordered and shifted from the central position by 0.3 Å above and below the trigonal plane.

Double borates $LiMBO_3$, M = Sr, Ba crystallise in the monoclinic crystal system and have one structural type [30]. In $LiSrBO_3$ and $LiBaBO_3$ structures, M atoms differ in their environment: CN(Sr) = 7 and CN(Ba) = 9. Li atoms are coordinated by five oxygen atoms and are inside distorted trigonal bipyramids. Boron atoms have

Table 1. Crystallographic characteristics of $LiMeBO_3$

M	Crystal system	Пр. гр	Lattice parameters, Å			α, β, γ, °	Z	Ref.
			a	b	s			
Mg	monocl.	C2/c	5.161(1)	8.880(2)	9.911(2)	β = 91.29(2)	8	[69]
Ca	rhomb.	Pbca	13.227(13)	6.167(16)	6.0620(6)		8	[31]
Sr	monocl.	$P2_1/n$	6.4800(13)	6.680(15)	6.8400(14)	β = 109.41(3)	4	[30]
Ba	monocl.	$P2_1/n$	6.372 (1)	7.022(3)	7.058 (1)	β = 113.89(1)	4	[30]
α-Zn	monocl.	C2/c	8.746(2)	5.091(1)	6.129(1)	β = 118.75(13)	4	[45]
α-Zn	tricl.	P-1	5.0915(9)	5.059(1)	6.156(1)	α = 65.81(1) β = 65.56(1) γ = 59.77(1)	8	[44]
β-Zn	monocl.	C2/c	5.094(1)	8.806(3)	10.374(4)	β = 91.09(3)	8	[68]
Zn	tricl.	P-1	5.0559(15)	6.097(2)	8.0359(18)	α = 75.75(2) β = 89.86(2) γ = 89.79(3)	4	[46]
I – Cd	hex.	P-6	6.324(2)		3.2638(7)		3	[66]
II – Cd	tricl.	P-1	6.118 (4)	8.486(3)	5.257(2)	α = 91.46(3) β = 89.64(4) γ = 104.85(4)	4	[67]
Cd	monocl.	$P\ 2_1/c$	10.4159 (14)	9.005(2)	10.756(2)	β = 92.521(13)	16	[46]

CN = 3 and an average distance B-O of 1.377 Å and O-B-O angles between 118.3(7) and 122.6(7) Å, which is typical for flat $(BO_3)^{3-}$ groups. The structures of the compounds are constructed from multiple [LiO]- and [MO]- layers isolated in the direction of [10-1], boron atoms are localised between the layers in the form of bridges. In [LiO]-layers, adjacent LiO_5 polyhedra form dimers connected by edges, wherein each dimer is linked with four adjacent dimers and forms two-dimensional sheets parallel to the diagonal *ac* plane.

The SrO_7 polyhedra in the $LiSrBO_3$ crystal were described as distorted single-capped trigonal prisms. In layers, SrO_7 polyhedra are linked by vertices and form chains that extend along the *b* axis. In turn, the adjacent chains are linked through oxygen atoms in the form of close-packed sheets parallel to the *ac* plane. Strontium-oxygen sheets, [LiO]-layers, are linked through oxygen atoms of BO_3 triangles along the [101] direction and form a three-dimensional framework. In the $LiBaBO_3$ double borate crystal, the BaO_9 polyhedra were described as distorted single-capped square antiprisms. In the [BaO] layers, the polyhedra form chains linked through common oxygen vertices. Similar to the $LiSrBO_3$ structure, the neighbouring chains of the Ba-polyhedra are linked through oxygen atoms and form close-packed sheets in the direction of the *b* axis. The sheets of Ba-polyhedra, [LiO]-layers, extend in the [10$\bar{1}$] direction and form a three-dimensional framework by means of bridging boron-oxygen atoms.

$LiCaBO_3$ borate crystallises in the orthorhombic crystal system (sp. gr. Pbca) [31]. Its crystalline structure consists of alternating [LiBO] and [CaO] layers elongated in the [100] direction. In the [LiBO]-layers, isolated $[BO_3]^{3-}$ groups are distributed along two directions: [011] and [01-1]. In the layers, the LiO_5 five-vertex polyhedra linked through common vertices are localised in the [011] and [0-11] directions and the BO_3 groups act as bridges. The projection of the $LiCaBO_3$ crystalline structure in the [001] and [100] directions is shown in Fig. 2. The average distances of 1.379 Å and the values of O–B–O angles between 119.19 (11) and 120.62 (8) are quite normal for flat BO_3 triangles. CaO_7 polyhedra form distorted single-capped trigonal prisms that are linked through edges and form layers parallel to the *bc* plane. Adjacent [CaO] layers are connected by flat boron-oxygen triangles. The crystalline structure of $LiCaBO_3$ differs from the structures of the other three compounds of alkaline earth metals $LiMBO_3$, M = Mg, Sr, Ba, which are monoclinic. In $LiMgBO_3$, flat BO_3 triangles are parallel to each other, while in structures with larger alkali metals they are neither parallel, nor perpendicular to each other [31]. The four studied structures have the same environment for the lithium atom, whose polyhedron was described as a distorted trigonal bipyramid.

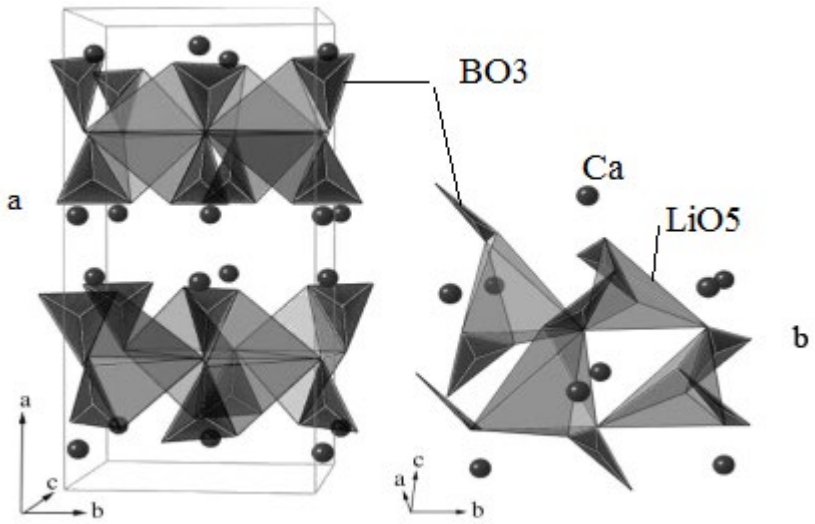

Fig. 2. $LiCaBO_3$ structure along [001] (a) and [100] (b) [31]

The structure of the monoclinic β-$LiZnBO_3$ crystal grown hydrothermally was established for the first time by Bondareva et al [68]. Chen et al. [45] named the structure of this modification as α-$LiZnBO_3$. It crystallises in the *C2/c* sp.gr., however, the parameters of its crystal lattice are different. The parameters of the unit cells of the $LiZnBO_3$ triclinic modification found in [44, 46] also differ. In the α-$LiZnBO_3$ structure, there are ZnO_4 tetrahedra, LiO_5 five-vertex polyhedra, and BO_3 triangles [45]. The two ZnO_4 tetrahedra connected by common edges form Zn_2O_6 dimers. Each Zn_2O_6 dimer connected by common O vertices with six other dimers forms a three-dimensional ZnO framework. The framework has hexagonal channels occupied by Li atoms and triangular voids occupied by boron atoms.

$LiMBO_3$ double borates, M = Cd, Zn, crystallise in 3 polymorphic modifications, their crystallographic characteristics are given in Table 1. The structural characteristics have been determined for two $LiCdBO_3$ modifications, low-temperature (triclinic, hexagonal [α-form]) and high-temperature (β-form). The $LiZnBO_3$ crystalline structures have been determined for triclinic and monoclinic modifications. Since the production of single crystals is challenging, the structure of the hexagonal low-temperature form has not been determined yet.

Therefore, crystals of isoformular $LiMBO_3$ lithium borates of alkaline earth metals belong to the lowest category and are characterised by triclinic, monoclinic, and rhombic crystal systems. Their framework structures include polyhedra of large metals and the available voids are occupied by boron-oxygen triangles isolated from each other.

3.1. Crystalline structures and luminescent properties of $LiMeBO_3$

Doping with metals

Mn^{2+} ions are important for creation of new luminescent materials since they are used to produce all known green phosphors [70]. Narrow-band red phosphors with an emission range of 620-650 nm for warm white LEDs are also being actively developed. Since the position of the lower excited state of Mn^{2+} strongly depends on the strength of the crystalline field, this will allow shifting the radiation of the Mn^{2+} substituted centres from green to red. A tetrahedral-coordinated Mn^{2+} ion with a weak crystalline field typically produces green radiation, while the octahedral coordinated Mn^{2+} (a strong crystalline field) produces orange-red radiation [70].

Inorganic materials doped with REE ions exhibit intense photoluminescence (PL) in the visible and infrared regions of the spectrum. Most lanthanide ions have luminescent properties, which is associated with the presence of *f–f* transitions [4–10, 62–63, 65, 71]. The intensity of PL lanthanide ions is determined by the efficiency of the occupation of excited states of Ln^{3+} and a decreasing probability of non-radiative processes. It depends significantly on a number of factors. For inorganic salts, the symmetry of the ions' environment and the absence of phonon quenching of photoluminescence are important factors for the intensity of PL. The peculiarities of the crystalline environment of the doped ion of REE affect the spectral-luminescent characteristics of the Ln^{3+} ion in the crystal (the position of its energy levels, the intensity of lines in the absorption and luminescence spectra) [9, 10, 20, 62, 70–76].

As the analysis of literature has shown, isovalent substitutions of cations of alkaline earth metals (Mg^{2+}, Ca^{2+}, Sr^{2+}, Ba^{2+}) for Mn^{2+}, Pb^{2+}, Eu^{2+} do not lead to fundamental changes in the structures of $LiMeBO_3$ borates. It is obvious that the introduction of a trivalent metal ion into the borate composition affects the valence balance. Ionic phases, which the considered borates can be attributed to, require the conditions of electroneutrality, i.e. the equality of the total positive and negative charges. There are various charge compensation mechanisms for crystalline phases with ionic bonds. Let us consider the most likely mechanisms of heterovalent substitutions applicable to $LiMeBO_3$ borates. In the case when the activator is a trivalent ion of REE, it is possible to substitute two identical atoms at equivalent positions with two different atoms of the same total valence. For example, codoping with a monovalent cation according to the scheme: $2Me^{2+} = R^{3+} + M^{+}$.

For instance, ions of alkali metals (Li^{+}, Na^{+}, K^{+}) have been used as charge compensators of lanthanide ions in a number of works [13, 14, 28, 32]. In all cases, the authors succeeded in

achieving electroneutrality and maintaining the crystalline structure. In the absence of charge compensators in the structure of the ionic crystal, vacancies in the cationic sublattice were formed. Many authors mention functional properties that are sensitive to the slightest changes in structure. However, this issue is hardly ever discussed and a detailed interpretation of the structure is hardly ever given. Very few works used the Rietveld method to determine the structure and occupied metal positions and to find correlations between the structure and photoluminescence [32, 74]. The results of interpretation of the $LiMgBO_3$:$x$$Tb^{3+}$ structure [74] in accordance with the data [69] showed the presence of two independent Li positions occupied by ~ 50% and one Mg position. In this structure, heavy metal atoms had CN=5 and were described as trigonal bipyramids (Fig. 3). Coordination of Li, B, and Mg atoms was confirmed by the IR spectra of the phases. The Li^+, Mg^{2+}, and Tb^{3+} ionic radii for CN = 6 were 0.76, 0.72, and 0.92 Å, respectively. The ionic radii and the charge difference between the dopant and the metal ions allowed assuming that Tb^{3+} could occupy both Mg^{2+} and Li^+ positions in the structure. However, clarification of the occupied positions indicated mixing of cations and a preference of Mg^{2+} positions over Li^+ positions in the $LiMgBO_3$ lattice. Since the difference in the Mg^{2+} and Tb^{3+} radii exceeded the difference in the Tb^{3+} and Li^+ radii, there was a high probability of a transition of Tb^{3+} at the Li^+ position. Then, the difference in their charges was +2 and new cationic vacancies of negative charge necessary for the balance of charges appeared. To study the local environment of $Tb3^+$, the photoluminescence lifetime was measured. The authors obtained two different lifetime values indicating two local environments of $Tb3^+$. It was assumed that $Tb3^+$ could be present in the lattice in two possible ways: either in two different points or in the same point, but with different surroundings defects. Since *f–f* transitions of Tb^{3+} are spin and parity forbidden, they can become permitted in an asymmetric position, i.e. a short lifetime may be due to the fact that Tb^{3+} occupies distorted positions of Li^+. The percentage of the short-lived component is only 8%, which indicates a low probability of this option. In contrast, the long-lived component, which is 92%, should be due to the high Tb^{3+}

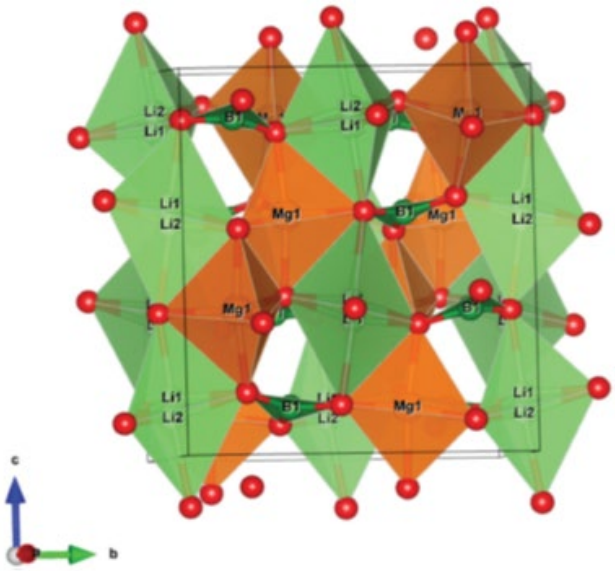

Fig. 3. $LiMgBO_3$ structure [74]

content in the symmetrical position of Mg^{2+}. The maximum peak intensity of the magnetic dipole transition at 545 nm in the emission spectra of all $LiMgBO_3$:$x$$Tb^{3+}$ phases confirms the fact that Tb^{3+} occupies the symmetric position of Mg^{2+} since the electric dipole transition line is permitted only in the case of its asymmetric position. Therefore, two different PL lifetime values may be due to two Tb^{3+} ions located at crystallographically identical positions of Mg^{2+} but with different surrounding defective centres. According to [75], some defective centres can act as electron-trapping centres and increase the lifetime, while others can provide non-radiative pathways to an excited state and reduce the lifetime value. The distances between such defective centres and lattice points affect the excited states [76]. For example, the short-lived component of PL can be located near defective centres, while the long-lived component can be far from them. The authors [74] noted that the values of short-lived and long-lived components of photoluminescence depend on the concentration of dopant, which determines the amount of charge imbalance in the initial matrix.

The formation of cationic vacancies for charge compensation was reported in [32] during the study of the luminescence of solid solutions of $LiSrBO_3$:Dy^{3+}, Tm^{3+}, Eu^{3+}. The authors emphasised that their work was focused on the behaviour of phases during energy transfer and colour adjustment, but it ignored the effect of the dopant concentration on LSBO. However, they identified

4 structures of $LiSrBO_3$ powders doped with each of these REE cations and with all three at the same time, they provided the coordinates of the atoms and their isotropic thermal parameters. It is interesting that the crystalline structures were specified in the $P2_1/c$ sp. gr. [32] and have acceptable divergence factors. However, according to the structural interpretation of the single crystal of a pure undoped compound, $LiSrBO_3$ borate crystallises in the $P2_1/n$ sp.gr. [30]. The authors referred to this work, but did not discuss this issue in any way. It was indicated that dopant cations occupied the positions of Sr^{2+}. Obviously, doping with REE ions leads to a noticeable distortion of the structure of the initial matrix and its reconstruction caused by the compensation of charges that occurs during the formation of new phases. The reconstruction of the structure is expressed in the changing symmetry of the crystals, which leads to the $P2_1/n \rightarrow P2_1/c$ sp.gr. transition. Emission spectra of the phases indirectly confirm the results of the determination of the structure. For example, in the radiation spectrum excited at 350 nm, there were bands at 490 nm (corresponding to the $^4F_{9/2} \rightarrow {}^6H_{15/2}$ transition of Dy^{3+}ions) and the most intense one at 576 nm (the $^4F_{9/2} \rightarrow {}^6H_{13/2}$ electric dipole transition permitted when Dy^{3+} is in a local position outside the inversion centre). This indicated that $Dy3^+$ ions occupied positions distant from the inversion centre in the $P2_1/c$ sp.gr. The same results were obtained for other REE ions.

The data [32, 74] further confirm that luminescence is a structurally sensitive method that is effective for characterising the features of the crystalline structure of the studied phases.

It is known that Eu^{3+} or Eu^{2+} ions when introduced into the lattices of various matrices emit perfectly fine in the blue and red regions of visible light and are actively used to develop various light-emitting devices [8, 63, 70]. Photoluminescence spectra of $LiMgBO_3$:Eu^{3+} was investigated by Liang et al. [25]. When excited by near ultraviolet (UV) (395 nm) and visible light (466 nm), the studied sample exhibited intense red glow with λ = 615 nm, which corresponds to the $^5D_0 \rightarrow {}^7F_2$ forced electric-dipole transition of Eu^{3+} ions. When the $LiMgBO_3$:Eu^{3+} sample was doped together with a sensitiser (Bi^{3+} ions), the absorbance of the $^7F_0 \rightarrow L_6$ and $^7F_0 \rightarrow {}^5D_2$ transitions increased. The authors attributed the increase in the luminescence intensity of the $LiMg_{0.75-y}BO_3$:$Eu_{0.25}{}^{3+}$, $Bi_y{}^{3+}$ sample to the $Bi^{3+} \rightarrow Eu^{3+}$ energy transfer. They believed that main energy transfer mechanism in the sample was the quadrupole-quadrupole interaction. The authors considered both new phosphors as pumping materials in the near UV range of the spectrum.

Dy^{3+} ions provided emission bands in the blue (480 nm) and yellow (570 nm) regions of the spectrum corresponding to the transitions: $^4F_{9/2} \rightarrow {}^6H_{15/2}$ magnetic dipole and $^4F_{9//2} \rightarrow {}^6H_{13/2}$ hypersensitive electric dipole transitions. Moreover, the intensity of the yellow glow was strongly influenced by the oxygen environment of the ion, which created a crystalline field of the host lattice and a radial integral of 4*f*- and 5*d*-electrons [60].

White light can be obtained by changing the intensity ratio of yellow and blue (Y/B) glow [1–5,70]. When excited in the near UV range, the phosphor emitted intense blue and yellow glow and a weak red band at 484, 573, and 669 nm, respectively, attributed to the $^4F_{9/2} \rightarrow {}^6H_{15/2}$, $^6H_{13/2}$, $^6H_{11/2}$ transitions of Dy^{3+} ions. The band gap width and average size of the material crystals were approximately 5.4 eV and 35 nm, respectively. The CIE chromaticity coordinates for $LiMgBO_3$:$0.02Dy^{3+}$ phosphor were in the white region, although they were far from the ideal values of the white light (0.333, 0.333) (see Table 2).

3.2. Thermoluminescence

All phosphors show a different thermoluminescent (TL) response to different types of exposure (X-, gamma-, ultraviolet rays, heavy ions) due to the unequal distribution of doses at different exposures [77]. The efficiency of luminescence and afterglow also depends on the method of material preparation, the chemical composition, and the particle size [71, 77, 78].

Work [79] describes dosimetric studies of $LiMgBO_3$:Dy^{3+} exposed to X-rays [50], gamma rays, and C^{+5} heavy carbon ions [52], gamma radiation, and Ag^{9+} heavy silver ions with an energy of 120 MeV.

Work [50] studied the relationship between the TL response and the amount of absorbed

Table 2. Chromaticity coordinates and excitation wavelength in $LiMeBO_3$ borates

Material	Chromaticity coordinates (*x*, *y*)	λ_{ex} (nm)	Colour	Reference
$LiMgBO_3$:0.02Er^{3+},0.08Yb^{3+}	(0.6080, 0.3914)	980	orange	[65]
$LiMgBO_3$: 0.02Dy^{3+}	(0.45, 0.46)	348	white	[60]
$LiMgBO_3$: 0.01Tb^{3+} $LiMgBO_3$: 0.04Tb^3 $LiMgBO_3$: 0.06Tb^3	(0.32, 0.50) (0.29, 0.53) (0.39, 0.52)	235	green	[74]
$LiCaBO_3$: 0.02Dy^{3+} $LiCaBO_3$: 0.03Dy^{3+}	(0.35, 0.39) (0.35, 0.39)	351 351	white	[98]
$LiCaBO_3$: 0.005Tb^{3+}	(0.28, 0.71)	240	green	[53]
$LiSr_{0.995}BO_3$:0.005Ce^{3+} $LiSr_{0.955}BO_3$:0.005Ce^{3+},0.04 Tb^{3+} $LiSr_{0.915}BO_3$:0.005Ce^{3+},0.08 Tb^{3+} $LiSr_{0.875}BO_3$:0.005Ce^{3+},0.12 Tb^{3+}	(0.196, 0.242) (0.217, 0.282) (0.301, 0.412) (0.326, 0.423)	337	blue yellowish-green	[95]
$LiBaBO_3$:0.05 Ce^{3+}/0.02Mn^{2+}	(0.358, 0.251)	345	white	[34]
$LiBaBO_3$:0,02Er^{3+}, 0,08Yb^{3+}	(0.6060, 0.3914)	980	orange	[92]
$LiBa_{0.98}$ BO_3: 0.02Eu^{3+} $LiBa_{0.975}$ BO_3: 0.025Eu^{3+}	(0.368, 0.378) (0.376, 0.366)	354	white	[7]

dose for several samples. The authors compared thermoluminescence curves for $LiMgBO_3$:Dy^{3+} and commercial TLD–100 irradiated with 5 Gy. It was established that the glow curve of the material had a simple symmetrical shape of ~ 154 °C and, according to the peak shape method [80, 81], it obeyed first-order kinetics. The glow intensity was approximately half of the TL of the commercial TLD-100. The obtained linear dependence in a wide range of doses of 0.5–25 Gy indicated the good quality of the thermoluminescent material. Its disadvantage is a decrease in the luminescence intensity over time.

Fig. 4 shows thermoluminescence curves for different concentrations of Dy^{3+} in the $LiMgBO_3$:Dy^{3+} phosphor [52]. Kinetic parameters are given in Table 3. The samples' fading was studied by appropriate irradiation and exposure in the dark for 27 days (Fig. 5). After the samples were exposed to γ-rays and carbon rays, the fading

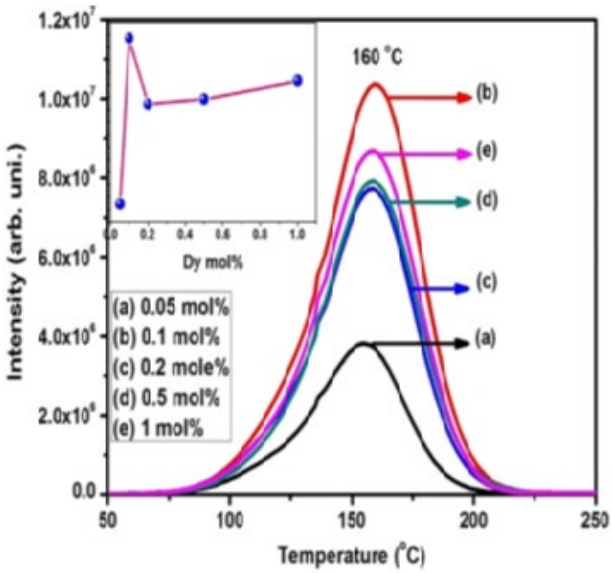

Fig. 4. Thermoluminescence curves for different concentrations of Dy^{3+} in the $LiMgBO_3$:Dy^{3+} phosphor according to [52]

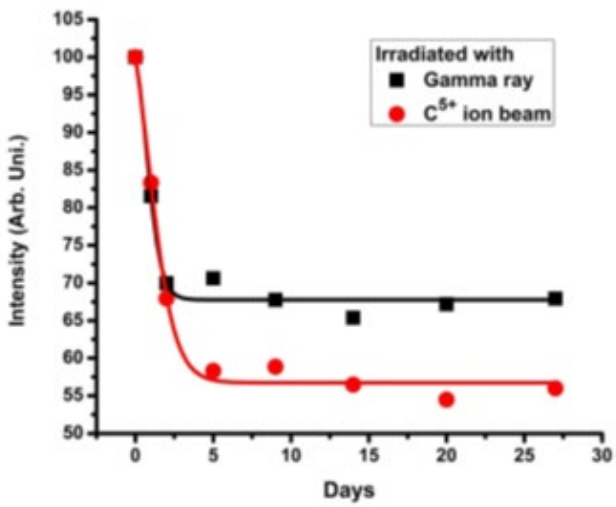

Fig. 5. Fading of synthesised $LiMgBO_3$:Dy^{3+} under exposure to γ-radiation and a C^{5+} beam according to [52]

Table 3. Kinetic parameters for $LiMeBO_3$ borates irradiated with γ-radiation

Material	Method of calculation	Peak No.	Order of kinetics	Activation energy, *E* (eV)	*S* (C^{-1})	Ref.
$LiMgBO_3:Dy^{3+}$	Форма пика	1	1.38	0.997	$1.31\cdot10^{11}$	[52]
	Вариации скоростей нагрева		1.35	1.003		
$LiMgBO_3:0.04Tb^{3+}$	Форма пика		1.1	0.92±0.01	$(1.4\pm0.2)\cdot10^{9}$	[74]
	Вариации скоростей нагрева			1.01	$1.02\cdot10^{10}$	
$LiMgBO_3:Dy^{3+}$	Форма пика	1	2	1.26	$3.09\cdot10^{16}$	[79]
		2			$3.88\cdot10^{11}$	
$LiCaBO_3:Dy^{3+}$	Форма пика	1	1.9	1.075	$2.71\cdot10^{12}$	[62]
		2	1.8	0.536	$3.173\cdot10^{5}$	
$LiCaBO_3:0.01Ce^{3+}$	Форма пика	1	2	0.655	$1.00\cdot10^{7}$	[33]
		2	1.76	1.448	$1.215\cdot10^{15}$	
		3		1.515	$7.506\cdot10^{11}$	
$LiSrBO_3$: $0.01Tm^{3+}$	Форма пика	1	1.26	0.63	$2.62\cdot10^{7}$	[101]
		2	2	0.96	$5.85\cdot10^{9}$	

for the first 3 days was approximately 30%. On the fifth day, the fading of the sample exposed to C^{+5} rays reached 42%. The $LiMgBO_3:Dy^{3+}$ sample irradiated with γ-rays showed a linear dependence of TL on the absorbed dose in the range from 10 Gy to 1 kGy. Samples irradiated with C^{+5} also showed a linear dependence of thermoluminescence on the current density in the range of $2\times^{10}-1\times10^{11}$ ions/cm^2.

In [79], $LiMgBO_3:Dy^{3+}$ samples were exposed to γ-radiation of 0.01–5 kGy and fast Ag^{9+} with ion content in the range of $1\cdot10^{11}-1\cdot10^{13}$ cm^{-2}. The glow curves were taken at different heating rates and were analysed by the Chen method [80]. It was found that the glow of samples exposed to ions began with a lower temperature (390 K) as compared to the glow of samples irradiated with γ-rays (396 K). The authors concluded that $LiMgBO_3:Dy^{3+}$ is suitable for γ-radiodosimetry. On the contrary, the material irradiated with heavy silver ions is not suitable for dosimetric applications, since the absorbed dose shifted even at room temperature, which leads inevitably to fading.

The thermoluminescent properties of $LiCaBO_3$ polycrystalline phosphors doped with REEs were studied in [6, 61, 82]. The $LiCaBO_3:Tm^{3+}$ samples exhibited the maximum TL sensitivity with a favourable shape of the glow curve [61]. The thermoluminescence curve of the $LiCaBO_3:Tm^{3+}$ sample irradiated with γ-rays contained 2 peaks at 230 and 430 °C, and the intensity of the second peak by almost three times exceeded the intensity of the first peak. Both peaks showed an almost linear dependence of intensity on the absorbed dose up to a value of 103 Gy. It was noted that the sensitivity of phosphor thermoluminescence to gamma radiation was about eight times higher than that ofTLD-100.

The thermoluminescence of $LiCaBO_3$ activated by dysprosium and cerium ions, when exposed to γ-quanta and a beam of C^{5+} carbon ions was studied in [62]. Both phosphors showed good TL sensitivity to the dose of γ-quanta irradiation in the range of 0.4–3.1 rad. with a ^{137}Cs source. The TL intensity increased with an increase in the content of Dy^{3+}ions in the $LiCaBO_3$ matrix and was maximum at a concentration of 0.5 mol. % Dy^{3+}. The maximum TL intensity of the second sample corresponded to the content of Ce^{3+}ions of 1 mol. %. After 20 days of exposure, the average fading for both materials was between 3 and 14%. Samples treated with a beam of C^{5+} ions showed a decrease in intensity and an increase in energy density.

In [83], thermoluminescence curves of the $LiCaBO_3:Tb^{3+}$ material contained one maximum at 240 °C and showed stability and insignificant fading.

The study of TL phosphors exposed to different types of irradiation is necessary to determine the areas of their possible use. In particular, dosimetry of heavy charged particle or heavy ion radiation is in the focus of research due to importance of its application in medicine (cancer and tumour treatment).

Searching for materials for neutron dosimetry is of paramount importance as it exhibits the highest relative biological efficiency (RBE) as compared to other types of radiation.

In [74], the method of electron paramagnetic resonance (EPR) was used to identify various defective centres caused by neutrons and gamma radiation. The lifetime of neutron-irradiated PL of materials correlated well with PL peaks and their relative contribution. To understand the kinetics of the processes, the parameters of the traps were calculated by different methods. Unlike the LiF:Mg,Ti reference, the $LiMgBO_3$:Tb^{3+} beam thermoluminescence showed a simple glow curve. The TL sensitivity to neutrons and the ability of $LiMgBO_3$:Tb^{3+} to separate the dose were 2.2 and 4.5 times higher than that of the standard material (Fig. 6). In addition, the TL response demonstrated excellent linearity up to a neutron dose of 105 mSv. It is noteworthy that the decay of the TL signal was < 10% when stored for 90 days. According to the diffuse reflection spectra, the green phosphor has a wide band gap (6.3 eV), is highly effective, and close to the tissue equivalent. The CIE chromaticity coordinates for $LiMgBO_3$:$x$$Tb^{3+}$ phosphors are given in Table 2. According to the authors [74], the obtained characteristics meet the criteria for the practical application of the material, which can be a worthy alternative to the existing LiF:Mg,Ti dosimeter for personnel neutron dosimetry.

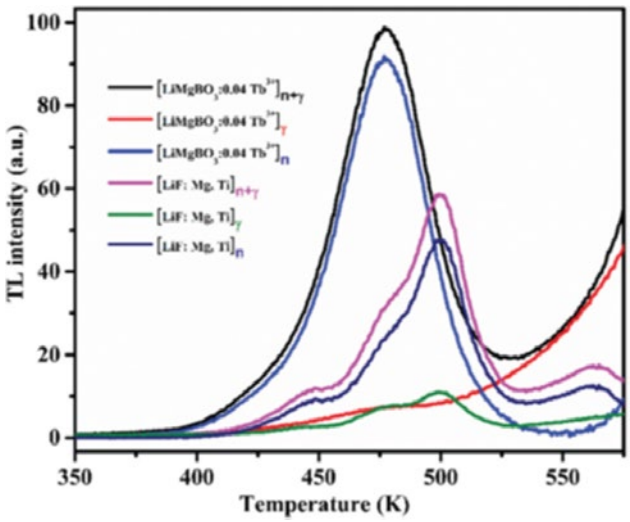

Fig. 6. Comparison of glow curves for TL $LiMgBO_3$:0.04Tb^{3+} and LiF:Mg,Ti [74]

3.3. Upconversion (ASL, anti-stokes luminescence)

According to Stokes' rule, the photoluminescence wavelength should be greater than the excitation wavelength due to the transfer of part of the absorbed energy of the exciting light [20]. Therefore, luminescence that occurs in the visible spectrum under the influence of infrared excitation radiation is known as 'anti-stokes" luminescence. Information about anti-stokes luminescence (ASL) appeared after the study of barium fluorides doped with Er^{3+}, Ho^{3+}, Tm^{3+}, and Yb^{3+} ions [84]. In literature, it is known as upconversion, which literally means "up frequency conversion". Upconversion involves excitation and luminescence processes in systems with several energy levels. It can be observed in REE ions due to an unfilled inner *4-f* shell which is screened from the outer shells and has a unique energy structure of the levels [20, 72, 73, 85, 86]. There are three main ASL mechanisms: 1) absorption in the ground state; 2) subsequent absorption in the excited state; 3) absorption in the ground state and energy transfer to another ion. In this case, a sensitiser is the ion that gives off energy, and the ion that receives energy is known as an activator. The phenomenon of upconversion is most evident when the best initial matrix with low photon energy is chosen [20, 72, 73]. ASL formation is accompanied by the absorption of the exciting light, radiative and non-radiative processes, and the process of energy transfer.

Let us consider the processes of resonance non-radiative energy transfer and non-radiative photon transfer. Energy can be transferred from the sensitiser (S) to the activator (A) if the distance between them is quite small and the excitation energies are almost equal. In this case, A transits from the ground state to the excited state before S emits photons (Fig. 7) [86]. There is energy difference during the S → A non-radiative photon transfer so photon transfer requires the process of energy transfer to cover it. The condition for

resonance energy transfer is the overlapping of the sensitiser's radiation spectrum and the activator's absorption spectrum. Fig. 8 shows a diagram of the energy levels of Yb^{3+} and Er^{3+} ions, which explains the mechanism of luminescence sensitisation and the occurrence of glow upon excitation by IR radiation. The Yb^{3+} ion absorbs the quantum of infrared radiation in the region of 980 nm and transits to the $^2F_{5/2}$ excited state. During the resonance energy transfer to the Er^{3+} ion, it also transits to the $^2I_{11/2}$ excited state and the sensitiser returns to the $^2F_{7/2}$ ground state. After transferring the energy of the second quantum to the activator, it moves to a higher level of $^4F_{7/2}$. The $^4I_{11/2} \rightarrow {}^4F_{7/2}$ transition in the Eg^{3+} ion to the more excited state also resonates with the transition in the Yb^{3+} ion (980 nm). Having lost some of the energy in the form of photons, the excited Eg^{3+} ion first transits to the $^4S_{3/2}$ radiative level and then to the ground state emitting a quantum with an energy almost twice as much as the energy of the excitation quanta. Co-doping with Yb^{3+}- Er^{3+} ions allows obtaining blue ($^2H_{9/2}\rightarrow{}^4I_{15/2}$), green ($^2H_{11/2}\rightarrow{}^4I_{15/2}$ and $^4S_{3/2}\rightarrow{}^4I_{15/2}$), and red radiation ($^4F_{9/2}\rightarrow{}^2I_{15/2}$) [20, 87, 88], which can be explained by the considered mechanism.

There are data about the introduction of Yb^{3+} ions as an additional doping material (sensitiser) into matrices activated by Er^{3+} ions [89]. It has been reported that the luminescent properties of such materials can be improved by the resonance energy transfer from Yb^{3+} to Er^{3+} during the absorption of a photon with a wavelength of λ = 980 nm [90].

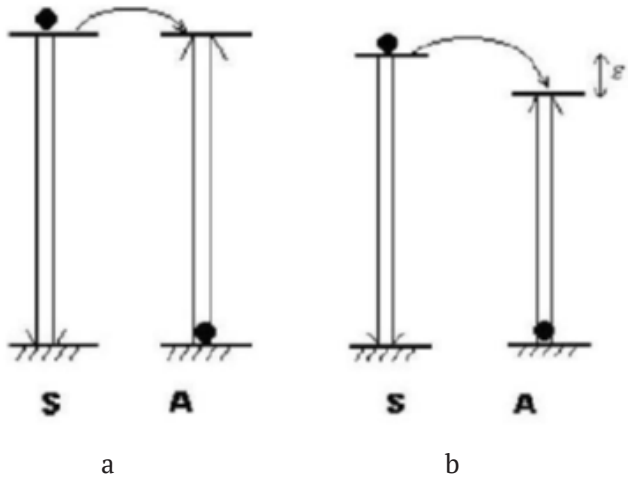

Fig. 7. Energy transfer processes between sensitiser (S) and activator (A) ions: (a) resonance non-radiative energy transfer; (b) non-radiative photon transfer [85]

Upconversion materials activated by rare earth ions are widely used in different areas starting with medicine and ending with solar energy. These are materials for solid-state lasers, biological sensors, laser beam visualisers, solar batteries, etc [86–91].

The phenomenon of upconversion in the $LiMgBO_3$ samples with a fixed concentration of Er^{3+} and Yb^{3+} ions has been studied [65]. The absorption spectrum of the $LiMgBO_3$:0.02 Er^{3+}, 0.08 Yb^{3+} phase showed a wide band with a maximum intensity in the region of 820–1,080 nm at λ = 980 nm ($^4I_{15/2}\rightarrow{}^4I_{11/2}$ resonance transitions in Er^{3+} and $^2F_{7/2}\rightarrow{}^2F_{11/2}$ resonance transitions in Yb^{3+}). There were also two peaks with wavelengths of 545 and 656 nm, which corresponded to the $^4I_{15/2}\rightarrow{}^4S_{3/2}$ and $^4I_{15/2}\rightarrow{}^4F_{9/2}$ transitions in Er^{3+} ions. The upconversion spectra of the phosphor showed Er^{3+} emission in the range (590 and 596 nm) due to mixed transitions from $^4F_{9/2}$ and $^4S_{3/2}$ to $^4I_{15/2}$. Works [92, 93] studied the upconversion emission properties of $LiBaBO_3$ and

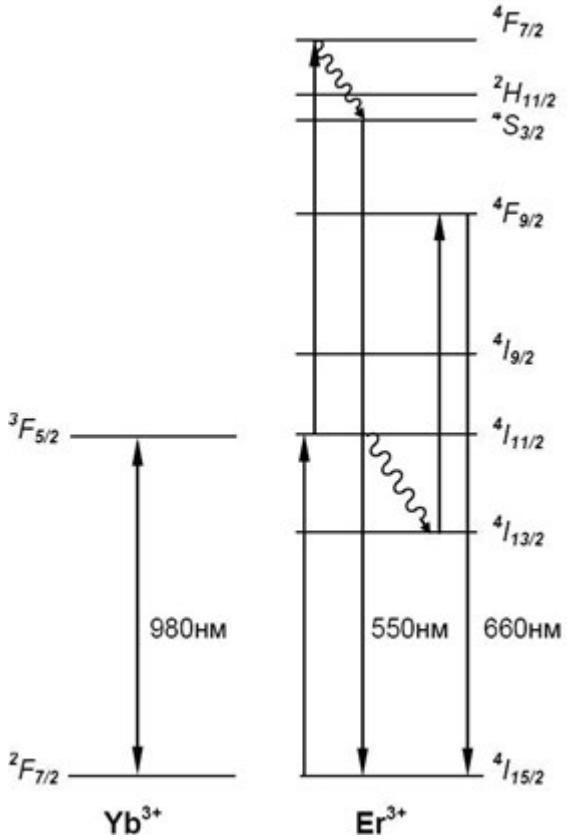

Fig. 8. Diagram of the energy levels of Yb^{3+} and Er^{3+} ions [20]

$LiSrBO_3$ borates doped with Er^{3+} and Yb^{3+} ions with fixed concentrations. The synthesised materials emitted light in the visible region after excitation in the infrared region. $LiBaBO_3$:0.02Er^{3+}, 0.08Yb^{3+} and $LiSrBO_3$:0.02Er^{3+}, 0.08Yb^{3+} phosphors showed absorption lines in the infrared region, 820-1,080 nm and at 545 nm, 656 nm, respectively. The upconversion spectra of phosphors showed persistent emission in Er^{3+} ions (590 and 596 nm) due to mixed transitions from $^4F_{9/2}$ and $^4S_{3/2}$ to $^4I_{15/2}$. Intense radiation with increasing frequency in these crystal phosphors can be useful in various areas of modern lighting technology.

To adjust the colours or increase the radiation intensity, heavy metal ions, for example, Mn^{2+}, Bi^{3+}, can be doped together with REE ions [25, 94]. Bi^{3+} ions as a co-activator can act as a primary energy excitation centre and non-radiatively transfer their energy to enhance the radiation intensity of another dopant ion, i.e. play the role of a sensitiser [63].

The tunable luminescence of a number of $LiBaBO_3$:Ce^{3+}/Mn^{2+} samples was studied by Li et al. [34]. The authors expected the $Ce^{3+}\rightarrow Mn^{2+}$ energy transfer due to the overlapping $LiBaBO_3$:Ce^{3+} emission spectrum and the $LiBaBO_3$:Mn^{2+} absorption spectrum. It was confirmed that the process of the $Ce^{3+}\rightarrow Ce^{3+}$ non-radiative energy transfer can be described by exchange interaction, radiation reabsorption, and multipolar interaction. When the content of Ce^{3+} ions was 5 mol.%, the glow intensity of borates gradually decreased with an increase in the concentration of Mn^{2+} ions, which can be explained by an increase in the efficiency of the $Ce^{3+}\rightarrow Mn^{2+}$ energy transfer. The glow colour of the $LiBaBO_3$:5 mol. % Ce^{3+}/y mol. % Mn^{2+} phosphors (y = 0, 1, 2, 3, 4, and 5) changed from blue to orange. It was noted that the material with the composition of $LiBaBO_3$:5 mol. % Ce^{3+}/2 mol. % Mn^{2+} had a glow close to white light. Previously, double blue and orange radiation, which is the result of 5*d*–4*f* transitions in Ce^{3+} ions and a forbidden transition in Mn^{2+} ions, was detected in $LiCaBO_3$:Ce^{3+}, Mn^{2+} [94]. The process of the $Ce^{3+}\rightarrow Mn^{2+}$ energy transfer was classified as resonance transfer. It has a dipole-dipole (*d*-*d*) mechanism with a critical distance of about 4.1 Å. Due to strong excitation bands in the range of 325–375 nm, the studied phosphors with double radiation can be used in near UV radiation light-emitting diodes (LEDs). The same energy transfer mechanism has been found in $LiSrBO_3$:Ce^{3+}, Tb^3 polycrystals [95].

The photoluminescent, structural, and optical properties of $LiBaBO_3$ phosphors doped with Eu^{3+} ions and codoped with Bi^{3+} ions were studied by Lephoto and colleagues [7]. They studied the mechanism of the $Bi^{3+}\rightarrow Eu^{3+}$ energy transfer. The materials showed tunable radiation based on simultaneous broadband radiation at a wavelength of 593 nm and narrowband radiation associated with the *f*–*d* and *f*–*f* Eu^{2+} and Eu^{3+} transitions, respectively. According to the results of the study, part of Eu^{3+} ions reduced to Eu^{2+}. The samples had greenish-blue (493 nm) and red (613 nm) glows, which were attributed to the emission of Eu^{2+} and Eu^{3+} ions. Co-alloying with Bi^{3+} ions significantly increased the intensity of the Eu^{3+}narrowband radiation, whose maximum was located at a wavelength of 613 nm. Narrowband radiation at 613 nm depended on the concentration of the co-activator, which indicated a non-radiative transfer of energy from Bi^{3+} ions to Eu^{3+} ions. Chromatic coordinates according to (CIE) are given in Table 2.

3.4. Photoluminescent properties

$LiCaBO_3$

Excitation and emission spectra of $LiCaBO_3$:Tb^{3+} materials were studied in [6, 14, 53, 83]. A study of the effect of embedded ions (Li^+, Na^+, K^+) on the emission intensity of $LiCaBO_3$:Tb^{3+} showed that it is maximum for Li^+ ions (4 mol. %) [14]. The results [14] are consistent with the data presented in work [83], in which the maximum green emission of $LiCaBO_3$:Tb^{3+} was observed at a wavelength of 545 nm. At UV excitation with λ_{em} = 254 nm, 4 distinct bands at wavelengths of 486, 545, 590, and 622 nm were detected in the emission spectrum corresponding to typical radiative transitions of Tb^{3+} ions: $^5D_4\rightarrow{}^7F_6$, $^5D_4\rightarrow{}^7F_5$, $^5D_4\rightarrow{}^7F_4$, $^5D_4\rightarrow{}^7F_3$. Among the emission lines, the dominant emission was observed at 547 nm, which corresponded to the $^5D_4\rightarrow{}^7F_5$ transition. The $^5D_4\rightarrow{}^7F_5$ emission line is the strongest line in almost all crystalline matrices when the Tb^{3+} content is a few mole percent or higher [53]. Photoluminescence radiation and excitation spectra were studied in detail for

$LiCa_{1-x}BO_3$:$x$$Tb^{3+}$ with x = 0.005. The excitation spectrum at λ_{em} = 547 nm had a wide band in the range of 250–300 nm, which corresponded to the $f^8 \rightarrow 4f^7 5d$ permitted transitions of Tb^{3+} ions. In [14], the emission intensity increased with increasing concentration of active ions and reached a maximum at 3 mol. % Tb^{3+}. The authors [6] associated this with the greatest probability of attributing these transitions to both electric dipole and magnetic dipole induced transitions.

According to the authors [53], the peak at ~240 nm in the excitation spectra can be easily classified as $4f^8$–$4f^7 5d$ spin permitted transitions of Tb^{3+}, whose exact position depends on the crystalline field of the lattice. For λ_{ex} = 240 nm, the radiation intensity first increased with increasing activator concentration and reached a maximum at x = 0.005. After that, there was a concentration quenching mainly associated with the quadrupole-quadrupole interaction. The CIE chromaticity coordinates for the synthesised green $LiCaBO_3$:Tb^{3+} phosphor are given in Table 2.

According to the excitation and emission spectra data, $LiCaBO_3$:Eu^{3+} phosphors were excited effectively by near UV (400 nm) and blue light (470 nm) and emitted red light [13]. The radiation intensity increased with increasing concentration of Eu^{3+} and reached a maximum at 3 mol. % Eu^{3+}. Then, the intensity decreased due to concentration quenching. According to Dexter's theory [96], the mechanism of concentration quenching of Eu^{3+} ions in $LiCaBO_3$ is caused by a dipole-dipole interaction. In [97], $LiCaBO_3$:Dy^{3+}/Eu^{3+} phosphors were characterised by photoluminescence spectra. $LiCaBO_3$:Dy^{3+} emission spectra showed two peaks (484 and 577 nm). The maximum radiation intensity was shown by the $LiCaBO_3$: 0.01Dy^{3+} sample. A further increase in the activator content led to concentration quenching and the calculated critical distance between the Dy^{3+} ions was about 22.76 Å. Similar to [13], the red radiating $LiCaBO_3$:Eu^{3+} phosphor can be excited effectively by near UV radiation (392 nm). The emission spectra showed the $^5D_0 \rightarrow {}^7F_J$ (J = 0–2) transition with the main glow at a wavelength of 614 nm due to the electric-dipole transition caused by an acentric point group. The $LiCaBO_3$:Eu^{3+} sample had concentration quenching at 0.2 mol. % and the critical distance was about 38.93 Å. The critical distance was defined as the average distance between the closest Eu^{3+} ions involved in the energy transfer. According to Dexter's theory, the concentration quenching of inorganic materials is determined by electric multipolar interaction or magnetic dipole interaction between activator ions. The authors associated concentration quenching of the $LiCaBO_3$:Eu^{3+} phosphor with non-radiative transitions between Eu^{3+} ions.

$LiCaBO_3$:Dy^{3+} photoluminescence temperature dependence was studied by Beck et al. [98] The time of luminescence emission and decay were recorded in the temperature range of 100–480 K. It was found that the maximum intensity of PL radiation was observed when the content of active Dy^{3+} ions was 2–3 mol. %. The emission intensity ratios (Y/B) were selected depending on the concentration of Dy^{3+} ions. The $LiCaBO_3$:Dy^{3+} material had excellent heat resistance, its colour was in the near white region, the values of the correlated first and total temperature were in the range of 4,955–5,955 K. It was found that the phosphor's quantum yield was 0.25 and the width of the band gap was 4.85 eV. The photoluminescent properties of $LiCaBO_3$ borates doped with different concentrations of Pb^{2+} and Bi^{3+} ions were studied at room temperature [99]. $LiCaBO_3$:Pb^{2+} and $LiCaBO_3$:Bi^{3+} radiation emission bands were observed at wavelengths of 296 nm and 378 nm, respectively. The calculated Stokes shifts of the samples was 3,952 nm^{-1} for $LiCaBO_3$:Pb^{2+} and 6,440 nm for $LiCaBO_3$:Bi^{3+}.

$LiCaBO_3$:Gd^{3+} phosphors have been characterised by photoluminescence spectroscopy and electron paramagnetic resonance (EPR) [100]. The introduction of the Gd^{3+} ion into the $LiCaBO_3$ matrix lattice contributed to the appearance of a narrow band of UV radiation at a wavelength of 315 nm when excited with λ = 274 nm. The mechanism of concentration quenching was studied and described.

$LiSrBO_3$

The luminescent characteristics of $LiSrBO_3$ activated by REE ions was studied in works [28, 29, 32, 101]. Excitation and emission spectra for $LiSrBO_3$:M, M = Ce^{3+}, Eu^{2+}, Eu^{3+}, Sm^{3+}, Tb^{3+}, Dy^{3+} showed effective excitation with UV LEDs and satisfactory red, green, and blue characteristics [28].

The authors [29] compared their results with the data [102] and discovered a difference in the location of the photoluminescence excitation bands (PLE) and photoluminescence, as well as the difference in the energies of the higher and lower energy levels. They attributed the differences to the different crystallinities of the samples, greater bond covalence, and the high crystal field splitting. The results of the prefabricated LED are shown in Fig. 9. The experimental sample of the material was produced by combining a 460 nm LED chip with $LiSrBO_3:Eu^{2+}$ borate. The quantum efficiency of the $LiSrBO_3:Eu^{2+}$ material was significantly inferior to the quantum efficiency of the commercial red phosphor (18% of the industrial phosphor). The authors concluded that it is necessary to optimise the content of Eu^{2+}, its crystallinity and to increase its quantum efficiency to use the new $LiSrBO_3:Eu^{2+}$ material.

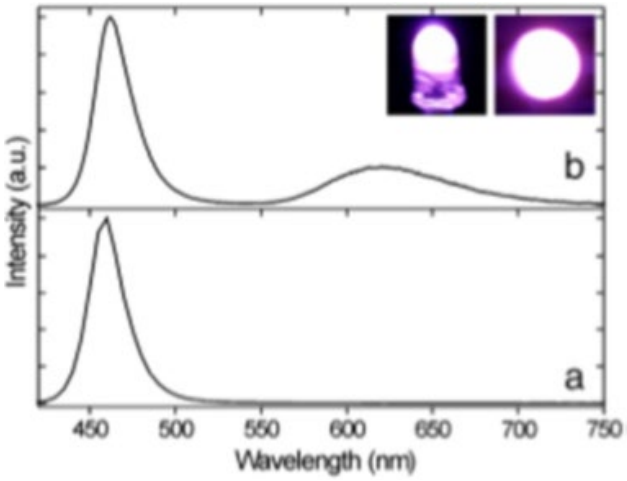

Fig. 9. Emission spectra of (a) a 460 nm bare chip LED and (b) a 460 nm LED chip combined with sample B [29]

The emission band of trivalent thulium ions with a centre at about 450 nm coincided with one of the absorption bands of dysprosium ions [103, 104]. Therefore, energy transfer is possible between Dy^{3+} and Tm^{3+} ions in the same matrix. Tm^{3+} ions can be added as a sensitiser to increase the luminescence intensity of powders doped with Dy^{3+}. $LiSrBO_3$ borates were co-doped with Dy^{3+}, Tm^{3+}, and Eu^{3+} in [32]. According to powder X-ray data, active REE ions completely dissolved in the host lattice and occupied positions that did not coincide with the inversion centre. According to the excitation spectra data, phosphors were effectively excited by UV at 350–400 nm. At a doping concentration of $x = 0.03$, there was concentration quenching of $LiSrBO_3:Na^+$, Tm^{3+}. The lifetime of $LiSrBO_3:0.05Dy^{3+}$, $0.005Tm^{3+}$; $LiSrBO_3:0.01Dy^{3+}$, $0.005Tm^{3+}$, and $LiSrBO_3:0.015Dy^{3+}$, $0.005Tm^{3+}$ phosphors calculated from the decay curves was 0.99 ms, 0.986 ms, and 0.96 ms, respectively. Compositional dependence of the luminescence properties were studied for the $LiSrBO_3:x(Tm^{3+}$,

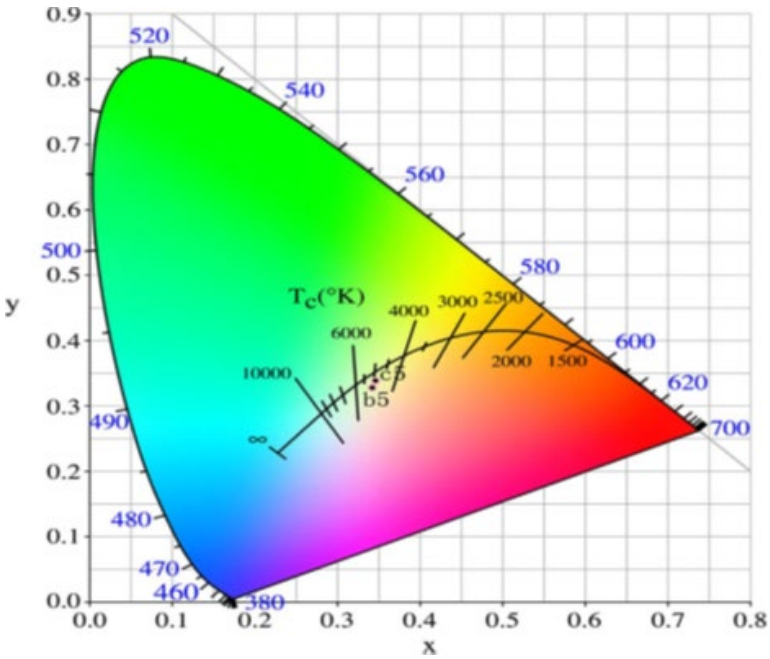

Fig. 10. Correlated colour temperature chart for LSBO:$0.01Dy^{3+}$, $0.005Tm^{3+}$, $0.03Eu^{3+}$, and LSBO:$0.015Dy^{3+}$, $0.005Tm^{3+}$, $0.03Eu^{3+}$ exited at 380 nm [32]

Na^+) samples. According to the chromaticity diagrams, phosphors can emit white light: from cold to warm (see Fig. 10).

In [8], when $LiSrBO_3:Sm^{3+}$ borate was exposed to UV radiation (221 nm) and a low-voltage electron beam (2 keV, 12 mA/cm^2), there was a strong emission at a wavelength of 601 nm corresponding to the $^4G_{5/2}\rightarrow H_{7/2}$ transitions of Sm^{3+} ions. Prolonged bombardment with low-energy electrons resulted in stable emission of cathodoluminescence (CL), which appeared after a dose of electrons of 100 CL/cm^2. Before and after a dose of electrons of 300 Kl/cm^2, the shape of the emission spectra of Auger electrons changed and their energy shifted for boron and strontium atoms in the structure of the $LiSrBO_3:Sm^{3+}$ material. It was assumed that during bombardment with an electron beam new surface chemicals formed which were responsible for the cathodoluminescence stability in the new orange-red phosphor.

$LiBaBO_3$

The analysis of the $LiBaBO_3:Sm^{3+}$ excitation and emission spectra showed that the material is excited effectively by ultraviolet (UV) light and demonstrates satisfactory red light characteristics (597 nm), which makes it fit easily into the UV LED chip [105]. The radiation intensity of the $LiBaBO_3:Sm^{3+}$ phosphor increases with an increase in the content of Sm^{3+} ions up to 3 mol. % followed by concentration quenching. The quenching mechanism is associated with the *d–d* interaction according to Dexter's theory. The glow intensity of the materials increases due to compensation of the charge of the doping alkaline Li^+, Na^+, K^+ ions. What is more, it is higher when doped with Li^+ ions as compared to Na^+ and K^+ ions [105, 13, 14, 28].

Meng et al [106] investigated optical properties of $LiBaBO_3$ borate doped with Eu^{2+} at a temperature between 10 and 525 K. The excitation spectra contained wide bands at wavelengths from 220 to 450 nm. The wide emission band with a maximum of about 485 nm observed at room temperature was attributed to the $4f^65d^1\rightarrow 4f^7$ transition of Eu^{2+} ions. The radiation intensity decreased insignificantly at temperatures below room temperature, however, it dropped sharply at higher temperatures. The calculated Stokes shift was 0.52 eV.

$LiZnBO_3$

Wang and collaborators [48] investigated α-$LiZnBO_3:Mn^{2+}$ borate. They expected substitution of Zn^{2+} ions with Mn^{2+} ions in the tetrahedron. The presence of Mn^{2+} ions in the α-$LiZnBO_3$ matrix was confirmed by EPR spectra. Strong narrow absorption bands in the range of 400–450 nm were found in the light reflection spectra of all doped samples. During excitation with a wavelength of 431 nm, there was an abnormal red emission band in the range of 550–800 nm due to a strong crystalline field caused by a distorted tetrahedron. The emission spectra contained a wide band of red radiation with a maximum at 647 nm for all doped samples regardless of the excitation wavelength and Mn^{2+} concentration. Red radiation is anomalous for the tetrahedral-coordinated Mn^{2+} in α-$LiZnBO_3$. The authors associated it with further splitting of the *d*-level of Mn^{2+} during the $^4T_1$ (^4G)→$^6A_1$ (^6S) transition from the excited state to the ground state. At a concentration of x = 7 mol. % Mn^{2+} luminescence quenching was observed. The calculated phosphor chromaticity coordinate (0.66, 0.34) was very close to the standard red colour (0.66, 0.33).

The optical properties of the orange-red $LiZnBO_3:Sm^{3+}$ phosphor obtained by solution combustion were investigated by photoluminescence and ultraviolet-visible spectroscopy [107]. In the radiation spectrum at λ_{ex} = 401 nm, there were peaks at 565, 602, and 648 nm, which were attributed to electric dipole transitions. The width of the material's band gap calculated from the diffuse reflection spectrum was 5.8 eV. It was concluded that it is possible to use this phosphor in near UV LEDs.

4. Conclusions

The analysis of the literature dedicated to the production of $LiMeBO_3$ borates (Me = Mg, Ca, Sr, Ba, Zn, Cd) revealed a variety of possible methods of their synthesis. Polycrystalline borates are traditionally obtained by high-temperature solid-phase reactions. The starting materials are the corresponding nitrates or carbonates. Sometimes a reducing atmosphere is used to dope samples with REE ions to avoid possible oxidation of ions with variable valence at high temperatures. Along with the traditional solid-phase method, such methods as SHS and its modifications

have become widespread. These relatively new methods based on the combustion reaction, require reagents that promote the self-sustaining exothermic reaction. Normally, these are such accessible materials as urea and ammonium nitrate used as fuel and oxidiser. They allow obtaining nanoscale powders. $LiMeBO_3$ lithium and alkaline earth metal borates are successfully doped with rare earth ions (Ce^{3+}, Sm^{3+}, Gd^{3+}, Eu^{2+}, Eu^{3+}, Tb^{3+}, Dy^{3+}, Tm^{3+}, Er^{3+}, Yb^{3+}) and Mn^{2+}, Pb^{2+}, Bi^{3+} heavy metal ions. Co-doping is also used, for example, REE ions –REE: Dy^{3+} with Eu^{3+}; Dy^{3+} with Tm^{3+}; Ce^{3+} with Tb^{3+} and Er^{3+} with Yb^{3+} or REE ions – Me^{2+} or REE-M $^{3+}$, for example, Ce^{3+}/Mn^{2+}; Eu^{3+}/Bi^{3+}. Some works provide information about the size, morphology, microstructure of particles and attempt to analyse the effect of codoping on the morphology of particles. For example, in [25] it was noted that doping with Bi^{3+} ions affects the morphology of $LiMgBO_3$:Eu^{3+}. According to SEM of the $LiMg_{0.945}BO_3$:$Eu^{3+}{}_{0.05}$,$Bi^{3+}{}_{0.005}$ borate, the size of phosphor particles increases with the addition of Bi^{3+} ions. Table 4 presents data on synthesis methods and possible areas of application of some representatives of the studied borates.

Literature indicates the possibility to use $LiMeBO_3$ borate compounds to develop luminescent matrices. These are framework crystalline structures. They are based on polyhedra of large metals linked by common edges and vertices of boron-oxygen triangles that are not connected to each other. Numerous spectral luminescence studies which have been carried out in recent decades have shown their ability to emit light after the absorption of external energy (UV, X-rays, γ-radiation, etc.). The spectral data considered in this paper were obtained by methods of photoluminescence analysis, thermoluminescence, upconversion, etc. It is known that external influences affect the structure of the material and leads to its defectiveness. The introduction of dopants into the crystalline structure also causes its distortion. For example, the introduction of rare earth elements creates a new energy of state near the conduction band that alters this phenomenon. The excellent luminescent properties of ions of rare-earth elements arise from the possibility of electronic transitions between states within the 4*f*-configuration. This becomes possible because the ground state configurations are always half full, the 4*f* shell is screened by the 5*s* and 5*p* outer electron shells. Doped activator ions often become the main part of the phosphor luminescence centre. Sometimes the activator ion exhibits low absorption and another ion (sensitiser) is added to start the luminescence process [25, 32, 34, 62, 94, 95]. The absorbed energy is transferred from the sensitiser to the activator. After that, the activator emits a photon of a certain wavelength. Small

Table 4. Methods of synthesis and possibilities of $LiMeBO_3$ application

Matrix	Doping ions	Method of synthesis	Area of possible	Reference
$LiMgBO_3$	Eu^{3+}, Bi^{3+}	Solid-phase	White LEDs	[25]
$LiMgBO_3$	Dy^{3+}	Solution combustion	Dosimetry	[50]
$LiMgBO_3$	Er^{3+}/ Yb^{3+}	Solution combustion	Phosphor	[65]
$LiCaBO_3$	Eu^{3+}	Solid-phase	Red phosphor for white LEDs	[13]
$LiCaBO_3$	Tb^{3+}	Solid-phase	Green phosphor for white LEDs	[14]
$LiCaBO_3$	Dy^{3+}	Solid-phase	White LEDs	[98]
$LiSrBO_3$	Eu^{3+}, Sm^{3+},Tb^{3+} Ce^{3+}, Dy^{3+}	Solid-phase	Red phosphor for white LEDs	[28]
$LiSrBO_3$	Eu^{2+}	Solid-phase	Yellow phosphor for white LEDs	[29]
$LiSrBO_3$	Dy^{3+}, Tb^{3+}, Tm^{3+}, Ce^{3+}	Solid-phase	Dosimetry	[101]
$LiBaBO_3$	Ce^{3+}/ Mn^{2+}	Solid-phase	White LEDs	[34]
α-$LiZnBO_3$	Mn^{2+}	Solid-phase	Red phosphor	[48]
$LiZnBO_3$	Sm^{3+}	Solution combustion	White LEDs	[107]
α-$LiCdBO_3$		Solid-phase	Pink phosphor	[36]
β-$LiCdBO_3$		Solid-phase	Red phosphor	[36]

amounts of dopants cause minor defects in the $LiMeBO_3$ structure leading to blue, green, and red light emissions of great commercial interest. The introduction of a suitable dopant may improve the luminescent properties of these borates. When bivalent Me^{2+} ions are substituted in $LiMeBO_3$ with trivalent ions, such as Tb^{3+}, Eu^{3+}, the balance of charges is disturbed. Compensation is possible by introducing into the ions' structure Li^+, Na +, K^+ alkali metals affecting the emission yield. In all considered cases, the radiation intensity increased. It was shown experimentally that the most suitable charge compensator is Li^+ ions.

Some crystals are capable of self-producing luminescence under certain conditions. For example, in UV light $LiCdBO_3$ crystals of the triclinic modification produce red luminescence and in IR light they produce yellow luminescence [36]. Co-doping of REE ions (Ce^{3+}, Eu^{3+}) with heavy metal ions, such as Mn^{2+}, Bi^{3+}, in $LiMeBO_3$ contributes to an increase in the radiation intensity in the materials and allows tuning colours from blue to orange.

Numerous studies dedicated to the conditions for obtaining $LiMeBO_3$ borates, methods of their synthesis, and their spectral-luminescent properties allow considering them as promising materials. They can be considered as phosphors that emit green, blue, and red light, which can be used in white LEDs and as effective materials for personnel neutron dosimetry and the dosimetry of weak ionising radiation.

Conflict of interests

The author declares that they has no known competing financial interests or personal relationships that could have influenced the work reported in this paper.

References

1. Nakamura S., Fasol G. *The Blue Laser Diode*. Berlin: Springer, 1997. p. 343. https://doi.org/10.1007/978-3-662-03462-0

2. Cho J., Park J. H., Kim J. K., Schubert E. F. White light-emitting diodes: History, progress, and future. *Laser & Photonics Reviews*. 2017;11(2): 1600147. https://doi.org/10.1002/lpor.201600147

3. Zheng J., Cheng Q., Wu J., Cui X., Chen R., Chen W., Chen C. A novel single-phase white phosphor: Dy^{3+}, K^+ for near-UV white light-emitting diodes. *Materials Research Bulletin*. 2016;73: 38–47. https://doi.org/10.1016/j.materresbull.2015.08.007

4. Zhu G., Wang Y., Wang Q., Ding X., Geng W., Shi Y. A novel white emitting phosphor of Dy^{3+} doped $Ca_{19}Mg_2(PO_4)_{14}$ for light-emitting diodes. *Journal of Luminescence*. 2014;154: 246–250. https://doi.org/10.1016/j.jlumin.2014.04.041

5. Ji Y., Cao J., Zhu Z., Li J., Wang Y., Tu C. Synthesis and white light emission of Dy^{3+} ions doped hexagonal structure $YAlO_3$ nanocrystalline. *Journal of Luminescence*. 2012;132: 702–706. https://doi.org/10.1016/j.jlumin.2011.10.019

6. Bajaj N. S., Omanwar S. K. Combustion synthesis and thermo luminescence in γ-irradiated borate phosphors activated with terbium (III). *Asian Journal of Chemistry*. 2012;24: 5945–5946.

7. Lephoto M. A., Tshabalala K. G., Motloung S. J., Shaat S. K. K., Ntwaeaborwa O. M. Tunable emission from $LiBaBO_3$: Eu^{3+}; Bi^{3+} phosphor for solid-state lighting. *Journal of Luminescence*. 2017;32(6): 1084–1091. https://doi.org/10.1002/bio.3295

8. Pitale S. S., Nagpure I. M., Kumar V., Ntwaeaborwa O. M., Terblans J. J., Swart H. C. Investigations on the low voltage cathodoluminescence stability and surfacechemical behaviour using Auger and X-ray photoelectron spectroscopy on $LiSrBO_3$:Sm^{3+}phosphor. *Materials Research Bulletin*. 2011;46: 987–994. https://doi.org/10.1016/j.materresbull.2011.03.022

9. Raghuvanshi G. S., Bist H. D., Kandpal H. C. Luminescence characteristics of Dy^{3+} in different host matrices. *Journal of Physics and Chemistry of Solids*. 1982;43(8): 781–783. https://doi.org/10.1016/0022-3697(82)90246-3

10. Huy B. T., Quang V. X., Chau H. T. B. Effect of doping on the luminescence properties of $Li_2B_4O_7$. *Journal of Luminescence*. 2008;128: 1601–1605. https://doi.org/10.1016/j.jlumin.2008.03.007

11. Bubnova R., Volkov S., Albert B., Filatov S. Borates-crystal structures of prospective nonlinear optical materials: high anisotropy of the thermal expansion caused by anharmonic atomic vibrations. *Crystals*. 2017;7: 93. https://doi.org/10.3390/cryst7030093

12. Li P., Yang Z., Wang Z., Guo Q. Luminescent characteristics of $LiCaBO_3$:Eu^{3+} phosphor for white light emitting diode. *Journal of Rare Earths*. 2009; 27(3): 390–393. https://doi.org/10.1016/S1002-0721(08)60257-4

13. Wang Z., Yang Z., Li P., Guo Q., Yang Y. Luminescence characteristic of $LiCaBO_3$: Tb^{3+} phosphor for white LEDs. *Journal of Rare Earths*. 2010;28(1): 30–33. https://doi.org/10.1016/S1002-0721(09)60044-2

14. Un A. Investigation of dopant effect on some TL dosimeters containing boron. *Radiation Physics and Chemistry*. 2013;85: 23–35. https://doi.org/10.1016/j.radphyschem.2012.10.016

15. Omanwar S. K., Koparkar K. A., Virk H. S. Resent advances and opportunites in TLD materials: a review.

Defect and Diffusion Forum. 2014;347: 75–110. https://doi.org/10.4028/www.scientific.net/DDF.347.75

16. Chikte D., Omanwar S. K. Moharil S. V. Luminescence properties of red emitting phosphor $NaSrBO_3:Eu^{3+}$ prepared with novel combustion synthesis method. *Journal of Luminescence*. 2013;142: 180–183. https://doi.org/10.1016/j.jlumin.2013.03.045

17. Doull B. A., Oliveira L. C., Wang D. Y, Milliken E. D., Yukiharan E. G. Thermoluminescent properties of lithium borate, magnesium borate and calcium sulfate eveloped for temperature sensing. *Journal of Luminescence*. 2014;146: 408–417. https://doi.org/10.1016/j.jlumin.2013.10.02218

18. Verma S., Verma K., ... Swart H. C. Recent advances in rare earth doped alkali-alkaline earth borates for state lighting applications. *Physica B: Condensed Matter*. 2018;535: 106–113. https://doi.org/10.1016/j.physb.2017.06.07319

19. Lakshmanan A. R. A review on the role of thermoluminescent dosimeters in fast-neutron personnel dosimetry. *Nuclear Tracks and Radiation Measurements*. 1982;6(2–3): 59–78. https://doi.org/10.1016/0735-245X(82)90030-8

20. Petrik V. I. *Anti-Stokes compounds and materials based on them**. Irkutsk: Oblastnaya tipografiya No 1 Publ., 2012. 400 p. (In Russ.)

21. Budzanowski M., Bilski P., Olko P., Niewiadomski T., Burgkhardt B., Piesch E. New TL detectors for personal neutron dosimetry. *Radiation Protection Dosimetry*. 1993;47(1-4): 419–423. https://doi.org/10.1093/rpd/47.1-4.419

22. Horowitz Y. S. LiF:Mg,Ti versus LiF:Mg,Cu,P: the competition heats up. *Radiation Protection Dosimetry*. 1993;47(1-4): 135–141. https://doi.org/10.1093/oxfordjournals.rpd.a081718

23. Lee J. I., Yang J. S., Kim J. L., Pradhan A. S., Lee J. D., Chung K. S., Choe H. S. Dosimetric characteristics of LiF:Mg,Cu,Si thermoluminescent materials. *Applied Physics Letters*. 2006; 89: 094110. https://doi.org/10.1063/1.234528024

24. Subanakov A. K., Bazarov B. G., Perevalov A. V., Bazarova Zh. G. Thermoluminescent phosphor synthesis on the basis of MgB_4O_7:Dy. *Advances in Current Natural Sciences*. 2016;12(2): 36–41. (In Russ.). Available at: https://natural-sciences.ru/ru/article/view?id=36257

25. Liang Z., Mo F., Zhang X., Zhoun L. Luminescence of the $LiMgBO_3:Eu^{3+}$, Bi^{3+} phosphor. *Journal of Luminescence*. 2014; 151:47–51. http://dx.doi.org/10.1016/j.jlumin.2014.02.001

26. Wu L., Chen X. L., Tu Q. Y., He M., Zhang Y., Xu Y. P. Phase relations in the system Li_2O-MgO-B_2O_3. *Journal of Alloys and Compounds*. 2002;33391-2): 154-158. https://doi.org/10.1016/S0925-8388(01)01702-9

27. Bazarova Zh. G., Nepomnyashchikh A. I., Kozlov A. A., ... Kurbatov R. V. Phase equilibria in the Li_2O–MgO–B_2O_3 system. *Russian Journal of Inorganic Chemistry*. 2007;52: 1971–1973. https://doi.org/10.1134/S003602360712025X

28. Li P., Wang Z., Yang Z., Guo Q., Fu G. Luminescent characteristics of $LiSrBO_3$:M (M= Eu^{3+}, Sm^{3+}, Tb^{3+}, Ce^{3+}, Dy^{3+}) phosphor for white light-emitting diode. *Materials Research Bulletin*. 2009;44: 2068–2071. https://doi.org/10.1016/j.materresbull.2009.07.008

29. Zhang J., Zhang X., Gong M., Shi J., Yu L., Rong C., Lian S. $LiSrBO_3:Eu^{2+}$: A novel broad-band red phosphor under the excitation of a blue light. *Materials Letters*. 2012;79: 100–102. https://doi.org/10.1016/j.matlet.2012.04.011

30. Cheng W.-D., Zhang H., Lin Q.-S., Zheng F.-K. Syntheses, crystal and elektronic structures and linear optics of $LiMBO_3$ (M = Sr, Ba) orthoborates. *Chemistry of Materials*. 2001;13: 1841–1847. https://doi.org/10.1021/cm000808i

31. Wu L., Chen X. L., Li H., He M., Dai L., Li X. Z., Xu Y. P. Structure determination of a new $LiCaBO_3$. *Journal of Solid State Chemistry*. 2004;177: 1111–1116. https://doi.org/10.1016/j.jssc.2003.10.018

32. Cai G. M., Yang M., Liu H. X., Si J. Y., Zhang Y. Q. Single-phased and color tunable $LiSrBO_3:Dy^{3+}$, Tm^{3+}, Eu^{3+} phosphors for white-light-emitting application. *Journal of Luminescence*. 2017;187: 211–220. https://doi.org/10.1016/j.jlumin.2017.03.017

33. Jiang L. H., Zhang Y. L., Li C. Y., Pang R., Hao J. Q., Su Q. Thermoluminescence characteristics of rare-earth-doped $LiCaBO_3$ phosphor. *Journal of Luminescence*. 2008;128: 1904–1908. https://doi.org/10.1016/j.jlumin.2008.05.017

34. Li J., Li X., Xing H.-W., Zhang Y.-Z., Yang A.-M., Pan Y.-H., Liu W.-X. Solid state synthesis of $LiBaBO_3:Ce^{3+}/Mn^{2+}$ Phosphors and tunable luminescence induced by energy transfer from Ce^{3+} to Mn^{2+}. *Journal of Materials Science – Materials in Electronics*. 2017;28: 4738–4743. https://doi.org/10.1007/s10854-016-6117-6

35. Lehmann H.-A., Schadov H. Bildung und darstellung von gemischten monoboraten des typs $MeLiBO_3$, (Me = Co, Zn, Mn). *Zeitschrift für Anorganische und Allgemeine Chemie*. 1966;348: 42-48. https://doi.org/10.1002/zaac.19663480106

36. Buludov N. T., Karaev Z. Sh., Abdullaev G. K. $LiBO_2$–CdO system. *Russian Journal of Inorganic Chemistry*. 1985;30(6): 1523–1526. (In Russ.).

37. Wei L., Huang Q., Zhou Z., Yin X., Dai G., Liang J. Phase diagram of the $LiBO_2$–CdO system, phase transition, and structure of $LiCdBO_3$. *Journal of Solid State Chemistry*. 1990; 89(1): 16–22. https://doi.org/10.1016/0022-4596(90)90289-A

38. Yin X. D., Huang Q. Z., Ye S. S., Lei S. R., Chen C. T. Search for the borate nonlinear optical materials: synthesis of lithium cadmium borate α-$LiCdBO_3$. *Acta Chimica Sinica*. 1985;43(9): 822–826. Available at:

http://sioc-journal.cn/Jwk_hxxb/EN/Y1985/V43/I9/822

39. Khamaganova T. N., Khumaeva T. G. Phase Equilibria in the $Li_2O–CdO–B_2O_3$ system. *Russian Journal of Inorganic Chemistry*. 2013;58(12): 1571–1575. https://doi.org/10.1134/s0036023614010057

40. Khamaganova T. N., Khumaeva T. G. $Li_2O–ZnO–B_2O_3$ system. *BSU Bulletin. Chemistry. Physics*. 2014;(3): 6–8. (In Russ.). Available at: https://elibrary.ru/item.asp?id=21403564

41. Khamaganova T. N., Humaeva T. G. *Method for producing lithium and zinc borate**. Patent RF No. 2550206. Publ. 2015; Bull. No 13. (In Russ.).

42. Khamaganova T. N. Synthesis of high-temperature modifications of orthoborates $LiMeBO_3$, Me = Cd, Zn*. In: *XVIII Intern. Sci. Pract. Conf. "Kulagin Readings: Technique and Technology of Processes". Pt 1*. Chita: Izdatel'stvo Zabaikal'skogo gosudarstvennogo universiteta Publ.; 2018. p. 145–149. (In Russ.).

43. Khamaganova T. N. *Method for obtaining borate α-$LiCdBO_3$**. Patent RF No. 2729805. Publ. 12.08.2020; Bull. No. 23. (In Russ.).

44. Chang K.-S. $LiZnBO_3$: crystal structure. *Journal of the Korean Chemical Society*. 2001;45(3): 251–255.

45. Chen X., Yang C., Chang X., Zang H., Xiao W. Synthesis and characterization of two alkali – metal zinc borates, α-$LiZnBO_3$ and $Li_{0.48}Na_{0.52}ZnBO_3$. *Solid State Sciences*. 2009;11: 2086–2092. https://doi.org/10.1016/j.solidstatesciences.2009.08.024

46. Chen X., Wang K., Chang X., Xiao W. Syntheses and characterization of two alkaline and transition metal orthoborates, $LiMBO_3$ (M = Zn, Cd). *Solid State Sciences*. 2016;52: 132–140. http://dx.doi.org/10.1016/j.solidstatesciences.2015.12.014

47. Tsuyumoto I., Kihara A. Synthesis, characterization and charge- discharge properties of layer-structure lithium zinc borate, $LiZnBO_3$. *Materials Sciences and Applications*. 2013;4: 246–249. https://doi.org/10.4236/msa.2013.44030

48. Wang H., Wu L., Yi H., Wang B., Wu L., Gua Y., Zhang Y. Abnormal luminescent property of Mn^{2+} in α-$LiZnBO_3$:Mn^{2+}. *Dalton Transactions*. 2015; 44: 1427–1434. https://doi.org/10.1039/c4dt02626h

49. Ragupathi V., Krishnaswamy S., Panigrahi P., Subramaniam G., Nagarajan S. Spherical $LiZnBO_3$: structural, optical and electrochemical properties. *Materials Science for Energy Technologies*. 2019;2: 267–271. https://doi.org/10.1016/j.mset.2018.12.003

50. Bajoj N. S., Omarwanr S. K. Advances in synthesis and characterization of $LiMgBO_3$: Dy^{3+}. *Optik*. 2014;125: 4077–4080. https://doi.org/10.1016/j.ijleo.2014.01.110

51. Prasad K. H., Subramanian S., Sairam T. N., Amarendra G., Srinadhu E. S., Satyanarayana N. Structural, electrical and dielectric properties of nanocrystalline $LiMgBO_3$ particles synthesized by Pechini process. *Journal of Alloys and Compounds*. 2017;718: 459–470. https://doi.org/10.1016/j.jallcom.2017.05.157

52. Yerpude M. M., Chopra V., Dhoble N. S., Kadam R. M., Krupski Aleksander R., Dhople S. Y. Luminescence study of $LiMgBO_3$:Dy for γ-ray and carbon ion beam exposure. *Journal of Luminescence*. 2019;34: 933–944. https://doi.org/10.1002/bio.3694

53. Bajaja N. S., Omanwar S. K. Studies on optical properties of $LiCaBO_3$: Tb^{3+} phosphor. *Indian Journal of Pure & Applied Physics*. 2016;54: 458–462.

54. Merzhanov A. G. *Self-propagating high-temperature synthesis. Physical chemistry. Modern problems**. Yearbook. Moscow: Khimiya Publ.; 1983. p. 6–44. (In Russ.)

55. Itin V.I., Nayborodenko Yu. S. *High temperature synthesis of intermetallic connections**. Tomsk: Tomsk University Press Publ., 1989. 214 p. (In Russ.)

56. Ketsko V. A., Beresnev E. N., Chmyrev V. I., Alikhanyan A. S., Kop'eva M. A., Kuznetsov N. T. *Oxide nanopowders and oxidation-reduction reactions in gels**. Moscow: Sputnik+ Publ.; 2011. 92 p. (In Russ.)

57. Patil K. C. Advanced ceramics: Combustion synthesis and properties. *Bulletin of Materials Science*. 1993;16(6): 533–541. https://doi.org/10.1007/BF02757654

58. Thakare D. S., Omanwar S. K., Moharil S. V., Dhopt S. M., MuthalR. M. P. L., Kondawar V. K. Combustion synthesis of borate phosphors. *Optical Materials*. 2007;29: 1731–1735. https://doi.org/10.1016/j.optmat.2006.09.016

59. Aruna S. T., Mukasyan A. S. Combustion synthesis and nanomaterials. *Current Opinion in Solid State and Materials Science*. 2008;12(3-4): 44–50. https://doi.org/10.1016/j.cossms.2008.12.002

60. Bedyal A. K., Kumar V., Prakash R., Ntwaeaborwa O. M., Swart H. C. A near-UV-converted $LiMgBO_3$:Dy^{3+} nanophosphor: Surface andspectral investigations. *Applied Surface Science*. 2015;329: 40–46. https://doi.org/10.1016/j.apsusc.2014.12.056

61. Anishia S. R., Jose M. T., Annalakshmi O., Ponnusamy V., Ramasamy V. Dosimetric properties of rare earth doped $LiCaBO_3$ thermoluminescence phosphors. *Journal of Luminescence*. 2010;130: 1834–1840. https://doi.org/10.1016/j.jlumin.2010.04.019

62. Oza A. H., Dhoble N. S., Lochab S. P., Dhoble S. J. Luminescence study of Dy or Ce activated $LiCaBO_3$ phosphor for γ-ray and C^{5+} ion beam irradiation. *Journal of Luminescence*. 2015;30(7): 967-977. https://doi.org/10.1002/bio.2846

63. Gorelik V. S., Ivicheva S. N., Kargin Yu. F., Kozulin R. K., Europium superluminescence in optically transparent photonic crystals. *Inorganic Materials*. 2014;50: 150–157. https://doi.org/10.1134/S0020168514020058

64. Wu L., Bai Y., ... Xu J. Analysis of the structure and abnormal photoluminescence of a red-emitting $LiMgBO_3$:Mn^{2+} phosphor. *Dalton Transactions*. 2018;47: 13094–13105. https://doi.org/10.1039/c8dt02450b

65. Hargunani R. P., Sonekar R. P., Omanwar S. K. Synthesis and photoluminiscence properties of Er^{3+}–Yb^{3+} co-doped $LiMgBO_3$ Phosphor. *International Journal of Current Engineering and Scientific Researgch (IJCESR)*. 2018;5(1): 218–221.

66. Kazanskaya E. V., Sandomirsky P. A., Simonov M. A., Belov N.V. Crystal structure of $LiCdBO_3$*. *Report Academy of Sciences of the USSR*. 1978;238(6): 1340–1343. (In Russ.).

67. Sokolova E. V., Boronikhin V. A., Simonov M. A. Belov N. V. Crystal structure of the triclinic modification of $LiCdBO_3$*. *Report Academy of Sciences of the USSR*. 1979;246(5): 1126–1129. (In Russ.).

68. Bondareva O. S., Simonov M. A., Egorov-Tismenko Yu. K., Belov N. V. Crystal structures of $LiZn[BO_3]$ and $LiMn[BO_3]$. *Soviet Physics. Crystallography*. 1978;23(3): 487–491. (In Russ.).

69. Norrestam R. The crystal structure of monoclinic $LiMgBO_3$. *Zeitschrift für Kristallographie*. 1989; 187(1-2): 103–110. https://doi.org/10.1524/zkri.1989.187.1-2.103

70. Blasse G., Grabmaier B. C. A general introduction to luminescent materials. In: *Luminescent Materials*. Berlin. Heidelberg. Springer-Verlag; 1994. p. 233. https://doi.org/10.1007/978-3-642-79017-1_1

71. Du F., Nakai Y., Tsuboi T., Huang Y., Seo H. J. Luminescence properties and site occupations of Eu^{3+} ions doped in double phosphates $Ca_9R(PO_4)_7$ (R = Al, Lu). *Journal of Materials Chemistry*. 2011; 21: 4669–4678. https://doi.org/10.1039/c0jm03324c

72. Troup G. J., *Advances in Quantum Electronics*. J. R. Singer (ed.). New York—London: 1961. p. 85.

73. Kaminsky A. A. *Physics and spectroscopy of crystals**. Moscow: Nauka Publ., 1986. 272 p. (In Russ.).

74. Sen M., Shukla R., Pathak N., ... Tyagi A. K. Development of $LiMgBO_3$:Tb^{3+} as a new generation material for thermoluminescence based personnel neutron dosimetry. *Materials Advances*. 2021;2: 3405-3419. https://doi.org/10.1039/d0ma00737d

75. Das P., Pathak N., Sanyal B., Dash S., Kadam R. M. Exploring $Na_{0.1}Sr_{9.8}Eu_{0.1}(PO_4)_6F_2$ both as a potential phosphor material and host for radioactive waste immobilization. *Journal of Alloys and Compounds*. 2019;810: 151906. https://doi.org/10.1016/j.jallcom.2019.151906

76. Gupta S. K., Pathak N., Kadam R. M. An efficient gel-combustion synthesis of visible light emitting barium zirconate perovskite nanoceramics: probing the photoluminescence of Sm^{3+} and Eu^{3+} doped $BaZrO_3$. *Journal of Luminescence*. 2016;169: 106–114. https://doi.org/10.1016/j.jlumin.2015.08.032

77. Yukihara E. G., Gaza R., McKeever S. W. S., Soares C. G. Optically stimulated luminescence and thermoluminescence efficiencies forhigh-energy heavy charged particle irradiation in Al_2O_3:C. *Radiation Measurements*. 2004;38(1): 59–70. https://doi.org/10.1016/s1350-4487(03)00251-8

78. Huang D., Zhou Y., Xu W., ... Yu J. Photoluminescence properties of M^{3+} (M^{3+} = Bi^{3+}, Sm^{3+}) activated $Na_5Eu(WO_4)_4$ red-emitting phosphors for white LEDs. *Journal of Alloys and Compounds*. 2013;554: 312–318. https://doi.org/10.1016/j.jallcom.2012.11.172

79. Bedyal A. K., Kumar V., Ntwaeaborwa O. M., Swart H. C. Thermoluminescence response of 120 MeVAg^{9+} and γ-ray exposed $LiMgBO_3$:Dy^{3+} nanophosphors for dosimetry. *Ceramics International*. 2016;42: 18529–18535. https://doi.org/10.1016/j.ceramint.2016.08.191

80. Chen R. Glow curves with general order kinetics. *Journal of the Electrochemical Society*. 1969;116(9): 1254-1257. https://doi.org/10.1149/1.2412291

82. Jose M. T., Anishia S. R., Annalakshmi O., Ramasamy V. Determination of thermoluminescence kinetic parameters of thulium doped lithium calcium borate. *Radiation Measurements*. 2011;46: 1026–1032. https://doi.org/10.1016/j.radmeas.2011.08.001

83. Sonekar R. P., Gawande A. B., Ingle J. T., Omanwar S. K. Photoluminescence of a Green emitting phosphor $LiCaBO_3$:Tb^{3+}. *International Journal of Knowledge Engineering*. 2012;3(1): 53-54.

84. Ovsyankin V. V., Feofilov P. P. Cooperative sensitization of luminescence in crystals activated by rare earth ions. *JETP Letters*. 1966;4(11): 471. Available at: http://jetpletters.ru/ps/1642/article_25070.pdf

85. Chen J., Zhao J. X. Upconversion nanomaterials: synthesis, mechanism, and applications in sensing. *Sensors*. 2012;12(3): 2414-2435. https://doi.org/10.3390/s120302414

86. Auzel F. Upconversion and anti-stokes processes with *f* and *d* ions in solids. *Chemical Reviews*. 2004;104(1): 139–174. https://doi.org/10.1021/cr020357g

87. Lyapin A. A.,Gushchin S. V., Kuznetsov S. V., ... Ivanov V. K. Infrared-to visible upconversion luminescence in SrF_2:Er powders upon excitation of the $^4I_{13/2}$ level. *Optical Materials Express*. 2018;8(7): 1863–1869. https://doi.org/10.1364/ome.8.001863

88. Radzhabov E. A., Shendrik R. Y. Upconversion of infrared radiation in Er^{3+}-doped alkaline-earth fluorides. *Opt. Spectrosc*. 2020;128: 1752–1757. https://doi.org/10.1134/S0030400X20110211

89. Krut'ko V. A., Ryabova A. V., Komova M. G., ... Loschenov V. B. Synthesis and luminescence of ultrafine Er^{3+}- and Yb^{3+}-doped $Gd_{11}SiP_3O_{26}$ and

$Gd_{14}B_6Ge_2O_{34}$ particles for cancer diagnostics. *Inorganic Materials*. 2013;49: 76–81. https://doi.org/10.1134/s0020168513010044

90. Park S., Cho S.-H. Spectral-converting behaviors of Er^{3+}–Yb^{3+}doped YOCl phosphors. *Journal of Alloys and Compounds*. 2014;584: 524-529. https://doi.org/10.1016/j.jallcom.2013.09.118

91. Milliez J., Rapaport A., Bass M., Cassanho A., Jenssen H. P. High-brightness white-light source based on up-conversion phosphors. *Journal of Display Technology*. 2006;2(3): 307–311. https://doi.org/10.1109/jdt.2006.879183

92. Hargunani S. P. Synthesis and upconversion properties of Er^{3+}–Yb^{3+} co-doped $LiBaBO_3$ phosphor. *International Advanced Research Journal in Science, Engineering and Technology*. 2016;3(11): 216–218. https://doi.org/10.17148/IARJSET.2016.31142

93. Hargunani S. P., Sonekar R. P., Omanwar S. K. Synthesis and upconversion properties of Er^{3+}–Yb^{3+} co-doped $LiSrBO_3$ phosphor. *International Journal of Luminescence and Applications*. 2017;7(2): 382-385.

94. Guo C., Yu J., Ding X., Lai M., Ren Z., Bai J. A dual-emission phosphor LiCaBO3: Ce3+, Mn2+ with energy transfer for near-UV LEDs. *Journal of the Electrochemical Society*. 2011;158(2): J42–J46. https://doi.org/10.1149/1.3526319

95. Zhang Z.-W., Lv R.-J., Zhu X.-Y., ... Wang D.-J. Investigation of luminescence properties and the energy transfer mechanism of $LiSrBO_3$:Ce^{3+}, Tb^{3+} phosphors. *Journal of Materials Science: Materials in Electronics*. 2016;27: 6925–6931. https://doi.org/10.1007/s10854-016-4646-7

96. Dexter D. L. Concentration and excitation effects in multiphonon non-radiative transitions of rare-earth ions. *Journal of Chemistry and Physics*. 1954;22(6): 1063.

97. Kharabe V. R., Oza A. H., Dhoble S. J. Synthesis, PL characterization and concentration quenching effect in $Dy^{3+}$and Eu^{3+} activated $LiCaBO_3$ phosphor. *Journal of Luminescence*. 2015;30 (4): 432–438. https://doi.org/10.1002/bio.2756

98. Beck A. R., Das S., Manam J. Temperature dependent photoluminescence of Dy^{3+} doped $LiCaBO_3$ phosphor. *Journal of Materials Science: Materials in Electronics*. 2017;28(22): 17168–17176. https://doi.org/10.1007/s10854-017-7645-4

99. Pekgozl I., Erdogmus E., Cubuk S., Basak A. S. Synthesis and photoluminescence of $LiCaBO_3$: M (M: Pb^{2+} and Bi^{3+}) phosphor. *Journal of Luminescence*. 2012;132: 1394–1399. https://doi.org/10.1016/j.jlumin.2012.01.001

100. Tamboli S., Rajeswari B., Dhoble S. J. Investigation of UV-emitting Gd^{3+}-doped $LiCaBO_3$ phosphor. *Luminescence: the Journal of Biological and Chemical Luminescence*. 2015;31(2): 551–556. https://doi.org/10.1002/bio.2994

101. Jiang L. H., Zhang Y. L., Li C. Y., Hao J. Q., Su Q. Thermoluminescence studies of $LiSrBO_3$: RE $^{3+}$ (RE = Dy, Tb, Tm and Ce). *Applied Radiation and Isotopes*. 2010;68(1): 196–200. https://doi.org/10.1016/j.apradiso.2009.10.001

102. Wang Z.-J., Li P.-L., Yang Z.-P., Guo Q.-L., Li X. A novel yellow phosphor for white light emitting diodes. *Chinese Physics B*. 2010;19(1): 017801. https://doi.org/10.1088/1674-1056/19/1/017801

103. Li Y. C., Chang Y. H., Lin Y. F., Lin Y. J., Chang Y. S. High color purity phosphors of $LaAlGe_2O_7$ doped with Tm^{3+} and Er^{3+}. *Applied Physics Letters*. 2006;89: 081110–081113. https://doi.org/10.1063/1.2337275

104. Li L., Liu Y., Li R., Leng Z., Gan S. Tunable luminescence properties of the novel Tm^{3+}- and Dy^{3+}-codoped $LiLa(MoO_4)_x(WO_4)_{2-x}$ phosphors for white light-emitting diodes. *RSC Advances*. 2015;5: 7049–7057. https://doi.org/10.1039/C4RA15643A

105. Li P., Wang Z., Yang Z., Guo Q., Li X. Emission features of $LiBaBO_3$:Sm^{3+} red phosphor for white LED. *Materials Letters*. 2009;63: 751–753. https://doi.org/10.1016/j.matlet.2008.12.041

106. Meng F., Zhang J., Yuan G., Seo H. J. Effect of temperature on the luminescence and decay behavior of divalent europium in lithium barium borate. *Physical Status Solidi. Applications and materials science*. 2015;212: 2922–2927. https://doi.org/10.1002/pssa.201532399

107. Mahajan R., Kumar S., Prakash R., Kumar V. Synthesis and luminescent properties of Sm^{3+} activated lithium zinc borate phosphor. *AIP Conference Proceedings*. 2018.;2006: 030045. https://doi.org/10.1063/1.5051301

108. Bhargavi G. N., Khare A. Luminescence studies of perovskite structured titanates: a Review. *Optika i Spektroskopiya*. 2015;118 (6): 933–948. 2015;118(6): 933–948. https://doi.org/10.7868/s003040341506015x

* *Translated by author of the article.*

Information about the author

Tatyana N. Khamaganova, Cand. Sci. (Chem.), Associate Professor, Senior Researcher Oxide Systems Laboratories, Baikal Institute of Nature Management Siberian Branch, Russian Academy of Sciences (Ulan-Ude, Russian Federation). Baikal Institute of Nature Management Siberian Branch of the Russian Academy of sciences (Ulan-Ude, Buryatia, Russian Federation).

https://orcid.org/0000-0002-8970-1481

khama@binm.ru

Received 24.11.2022; approved after reviewing 20.02.2023; accepted for publication 15.05.2023; published online 25.09.2023.

Translated by Irina Charychanskaya

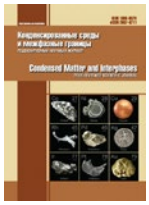

ISSN 1606-867X (Print)
ISSN 2687-0711 (Online)
Condensed Matter and Interphases
Kondensirovannye Sredy i Mezhfaznye Granitsy
https://journals.vsu.ru/kcmf/

Original articles

Research article
https://doi.org/10.17308/kcmf.2023.25/11311

Interdiffusion in the formation of thin niobium films on single-crystal silicon under vacuum annealing conditions

N. N. Afonin[1]✉, V. A. Logacheva[2]

[1]*Voronezh State Pedagogical University,*
86 ul. Lenina, Voronezh 394043, Russian Federation

[2]*Voronezh State University,*
1 Universitetskaya pl., Voronezh 394018, Russian Federation

Abstract

For the design of technological process for creating device structures based on niobium and single-crystal silicon with the desired properties, empirical and theoretical knowledge about the solid-phase interaction process in the system of a thin niobium film is required. The purpose of the research was a comprehensive study of the redistribution of components during the formation of thin niobium films on single-crystal silicon obtained by magnetron-assisted sputtering followed by vacuum annealing.

The structure and phase composition were studied by X-ray phase analysis, scanning electron microscopy, and atomic force microscopy. Distribution of components along the depth was determined using the Rutherford backscattering spectrometry.

The traditional experimental method for studying the process of interdiffusion of components in binary macroscopic systems is the placing of inert marks. However, the use of this method in systems containing thin films is hindered by the comparable thicknesses of the films and marks. This circumstance makes the mathematical modelling the most convenient method for the analysis of the interdiffusion process in thin-film systems.

The interdiffusion model during the formation of polycrystalline niobium film – single-crystal silicon systems, developing the Darken's theory for the limited solubility components was proposed. Grain boundary diffusion of silicon in the intergrain space of a polycrystalline niobium film was proposed. Numerical analysis of the experimental distribution of concentrations within the model established that silicon is the dominant diffusant in the studied system. The temperature dependence of the individual diffusion coefficient of silicon $D_{Si} = 3.0\ 10^{-12}\exp(-0.216\ \text{eV}/(kT))\ \text{cm}^2/\text{s}$ in the temperature range 423–773 K was determined.

The model is applicable to the description of the redistribution of components in the thin niobium film – single-crystal silicon system prior to synthesis conditions providing the chemical interaction of the metal with silicon and the formation of silicides. It illustrates the mechanism of the possible formation of silicide phases not by layer-by-layer growth at the Nb/Si grain boundary, but in its vicinity due to deep mutual diffusion of the components.

Keywords: Reactive interdiffusion, Limited solubility, Thin films, Niobium, Single-crystal silicon, Magnetron-assisted sputtering, Vacuum annealing, Rutherford backscattering spectrometry, Simulation method, Darken's theory

Acknowledgements: X-ray phase analysis and studied by atomic force microscopy were carried out using the equipment of the VSU Centre for Collective Use of Scientific Equipment https://ckp.vsu.ru/

For citation: Afonin N. N., Logacheva V. A. Interdiffusion in the formation of thin niobium films on single-crystal silicon under vacuum annealing conditions. *Condensed Matter and Interphases*. 2023;25(3): 333–342. https://doi.org/10.17308/kcmf.2023.25/11311

Для цитирования: Афонин Н. Н., Логачева В. А. Взаимодиффузия при формировании тонких плёнок ниобия на монокристаллическом кремнии в условиях вакуумного отжига. *Конденсированные среды и межфазные границы*. 2023;25(3): 333–342. https://doi.org/10.17308/kcmf.2023.25/11311

✉ Nikolay N. Afonin, e-mail: nafonin@vspu.ac

1. Introduction

Thin film niobium-silicon systems are widely used in superconductors [1–2]. The high radiation resistance of layered NbC-Si and Nb-Si systems in combination with their thermal stability make their application in X-ray optics promising [3, 4]. In the technology of integrated circuits, thin layers of niobium are used as a barrier between transition metals and single-crystal silicon or silicon dioxide [5].

A feature of the Nb-Si system is the slight solubility of silicon in niobium and niobium crystallites in single-crystal silicon. According to the Nb–Si binary phase diagram (Fig. 1), the maximum solubility of Si in bulk Nb samples is 3.5–4.36 at. %, and the solubility of niobium in silicon is negligible, Fig. 2 [6]

In two-layer systems Nb-Si and Si-Nb, obtained by vacuum sputtering on single-crystal Si (100), under conditions of insignificant solubility of Si and Nb in each other (the solubility limit of Si in the Nb solid solution phase from 0.6 to 1.7 at. % [8]), mutual diffusion between Nb and Si during annealing at 200°C leading to solid-phase amorphisation of the polycrystalline Nb layer and the formation of a mixed amorphous layer was demonstrated in [7]. Mutual diffusion of layers of materials during low-temperature annealing (100–250 °C) – is commonly observed phenomenon in metal – silicon systems [9, 10]. At these temperatures, grain boundary diffusion, usually, predominates in comparison with the diffusion of vacancies through the bulk. Mutual diffusion in the Nb-Si system during annealing T = 200 °C, the authors [7] explained by the diffusion of Si atoms into the Nb layer, which was due to the presence of grain boundaries in the polycrystalline Nb layer. Thermally activated interdiffusion in nanoscale thin film systems initiates several different temperature dependent

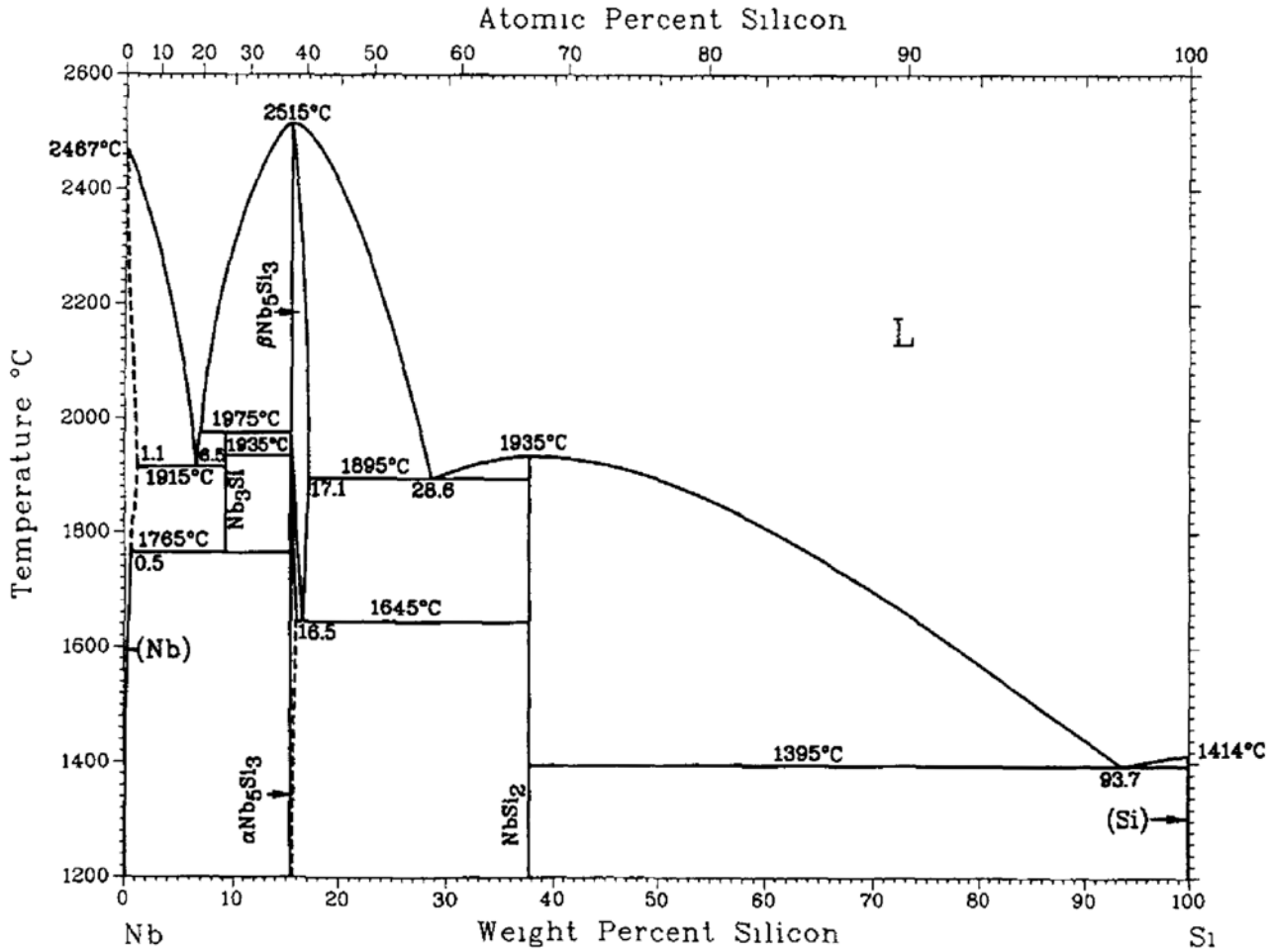

Fig. 1. Phase diagram of the niobium-silicon system [6]

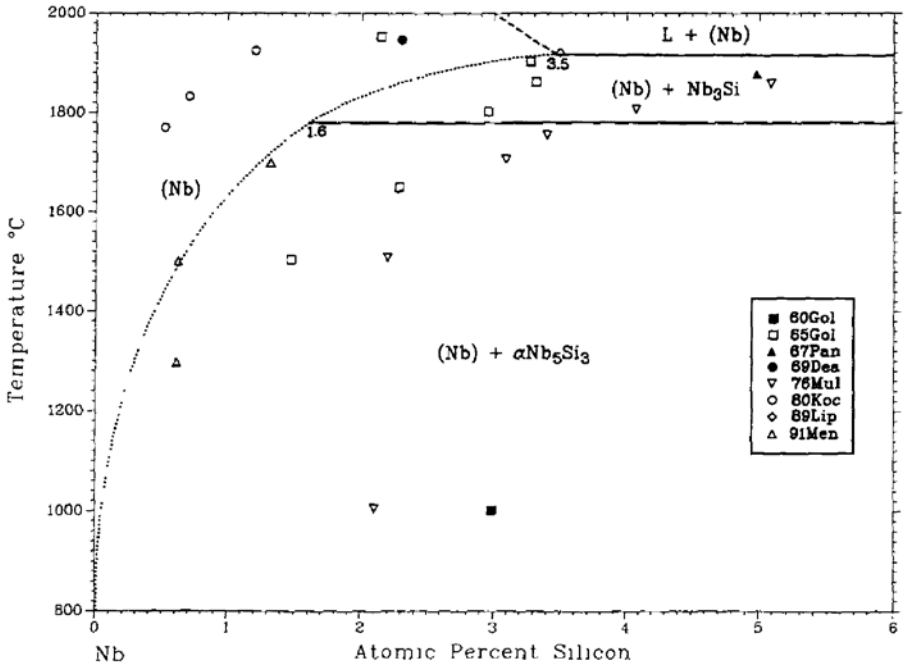

Fig. 2. The solubility of Si in Nb measured by different authors [6]

processes such as solid phase amorphisation, phase formation and crystallization.

Another feature of the Nb-Si system is that the metal film, both after deposition on single-crystal silicon and during subsequent annealing in an inert medium, has a polycrystalline character [7, 11].

According to modern concepts, the interaction of metal atoms with the silicon crystal lattice weakens the Si–Si covalent bonds and leads to the formation of free atoms in it [12]. Heat treatment can promote accelerated diffusion of mobile silicon along the grain boundaries of the metal under conditions of low solid solubility in its crystallites and the formation of solid solutions in a wide temperature range.

The process of mutual diffusion redistribution in the Nb-Si system suggests that the flow of silicon atoms into the niobium film is accompanied by an oppositely directed flow of niobium atoms into silicon. A significant difference in the intensity of these flows will lead to the displacement of the grain boundary in the diffusion pair (the Kirkendall effect) [13].

The question of the mechanisms of heterodiffusion of niobium in silicon and silicon in niobium, as well as of interdiffusion in the Nb–Si system, has not been sufficiently developed in the literature.

To design a technological process for creating device structures based on niobium and single-crystal silicon with the desired properties, empirical and theoretical knowledge about the solid-phase interaction process in the system of a thin niobium film is required. Insufficient discussion of these issues in the literature makes their comprehensive study an urgent and important task.

The purpose of this research was a comprehensive investigation into the redistribution of components during the formation of thin niobium films on single-crystal silicon under vacuum annealing conditions.

2. Experimental

Niobium films were deposited on single-crystal silicon wafers by magnetron-assisted sputtering. In the vacuum chamber, immediately before the sputtering process, a residual pressure level of $2.7 \cdot 10^{-3}$ Pa was reached using a diffusion pump. Then, an electric discharge was excited in high-purity argon at a pressure of $13.3 \cdot 10^{-2}$ Pa, discharge voltage of 430 V, and current strength of 0.7 A. The deposition rate of the niobium film was 0.67 nm/s, the sputtering time determined the thickness of the deposited films. A metal niobium target with an impurity content not higher than 0.01 at. % was used as the cathode material.

The synthesized samples were annealed using LG-220/1000 halogen lamps in a vacuum chamber at a residual pressure $R = 2.7 \cdot 10^{-3}$ Pa in the temperature range 423–773 K.

X-ray phase analysis of the thin Nb film – single-crystal Si system was carried out using an ARLX'TRA diffractometer (Switzerland). Studies were performed using radiation $K\alpha 1$ emission line of copper (1.54056 Å) in automatic mode with a step displacement of 0.05°. The exposure time at each point was 1 s. The diffraction patterns were interpreted using the JCPDC database [14].

The surface relief of the films was studied by atomic force microscopy (AFM) using a Solver P47PRO microscope (Russia) in the semi-contact (intermittent-contact) scanning mode.

The microstructure and thickness of the films were studied on the sample cleavage using a JSM-6380 LV scanning electron microscope.

The concentration distributions of the components over the depth of the system were determined by the Rutherford backscattering spectrometry (RBS) on proton beams and singly charged helium ions – 4 of electrostatic generator EG-5 in the laboratory of neutron physics of the Joint Institute for Nuclear Research.

The traditional experimental method for studying the process of interdiffusion of components in binary macroscopic systems is the placing of inert marks [13]. However, the use of this method in systems containing thin films is hindered by the comparable thicknesses of the films and the marks. This circumstance makes the mathematical modelling the most convenient method for the analysis of the interdiffusion process in thin-film systems.

3. Experimental section

Micrographs of the cleavage of a thin Nb film – single-crystal Si system after deposition (a) and vacuum annealing at $T = 773$ K for 30 min (b) are shown in Fig. 3. The metal film thickness was 189 nm.

As can be seen from Fig. 3, after deposition at the niobium-silicon grain boundary, a thin transition layer was observed, and the thickness of the layer increased during subsequent vacuum annealing. Interdiffusion in the niobium-silicon system was also observed in [7].

X-ray diffraction pattern of a niobium film on single-crystal Si was shown after annealing at $T = 773$ K for 30 min is shown in Fig. 4 (the diffraction lines from the silicon wafer at $2\theta = 32.906°$ were cut off). The only phase detected in the film was cubic Nb: $2\theta = 37.14°$, $d = 2.41901$ Å (ICDD card no. 00-003-0905).

According to the Debye-Scherrer formula [15], the coherent scattering region (CSR) was estimated, and the CSR was 52 nm.

AFM images of the surface of the Nb film after vacuum annealing at $T = 773$ K are shown in Fig. 5. The film has a smooth surface with an average roughness of 0.18 nm. The distribution of heights on the histogram (Fig. 4d) allows for estimating the grain size ~ 32 nm with a height (Z) of from 0.4 to 2 nm. The phase contrast confirmed the absence of phases other than niobium (Fig. 4b).

The calculated CSR size according to the Scherrer equation (~ 52 nm), and the grain

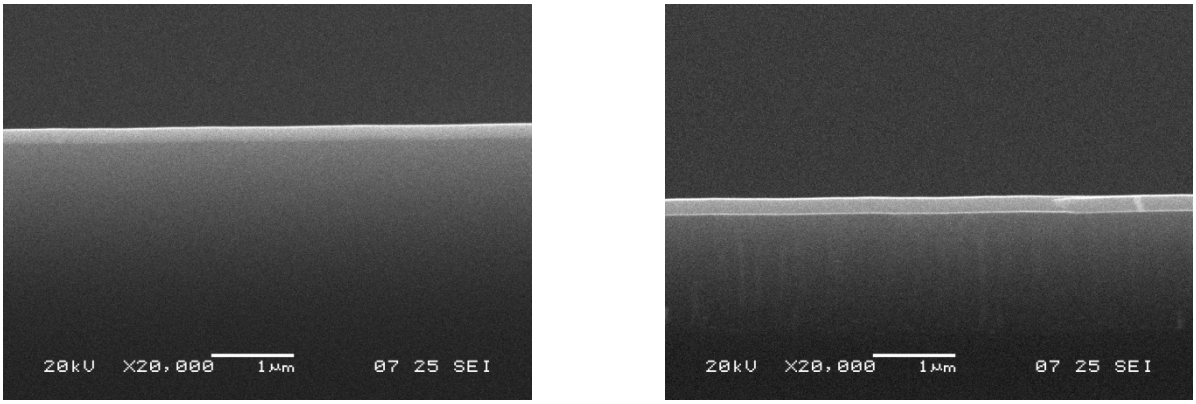

a b

Fig. 3. Microphotographs of a thin Nb film – single-crystal Si system cleavage after deposition (a) and annealing in vacuum at a temperature at $T = 773$ K for 30 minutes (b)

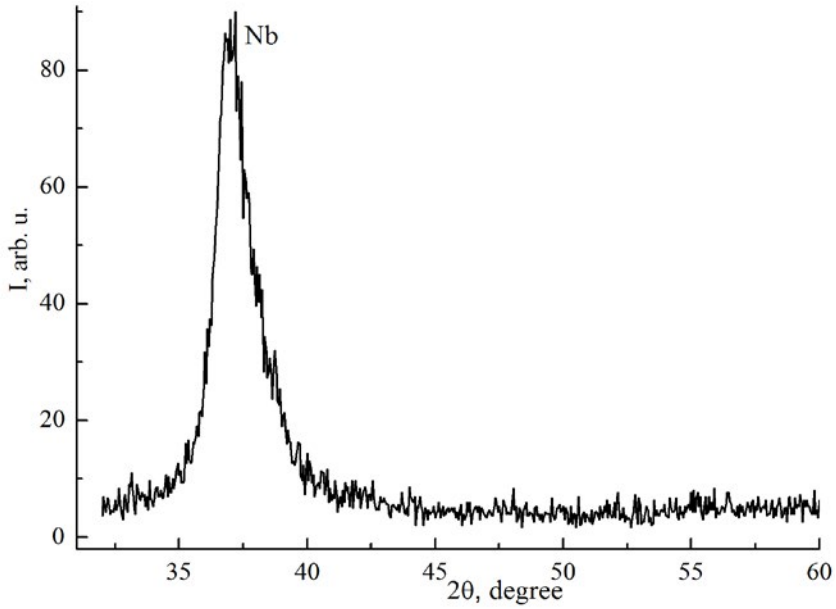

Fig. 4. X-ray diffraction pattern of thin Nb film – single-crystal Si system after annealing at T = 773 K for 30 min

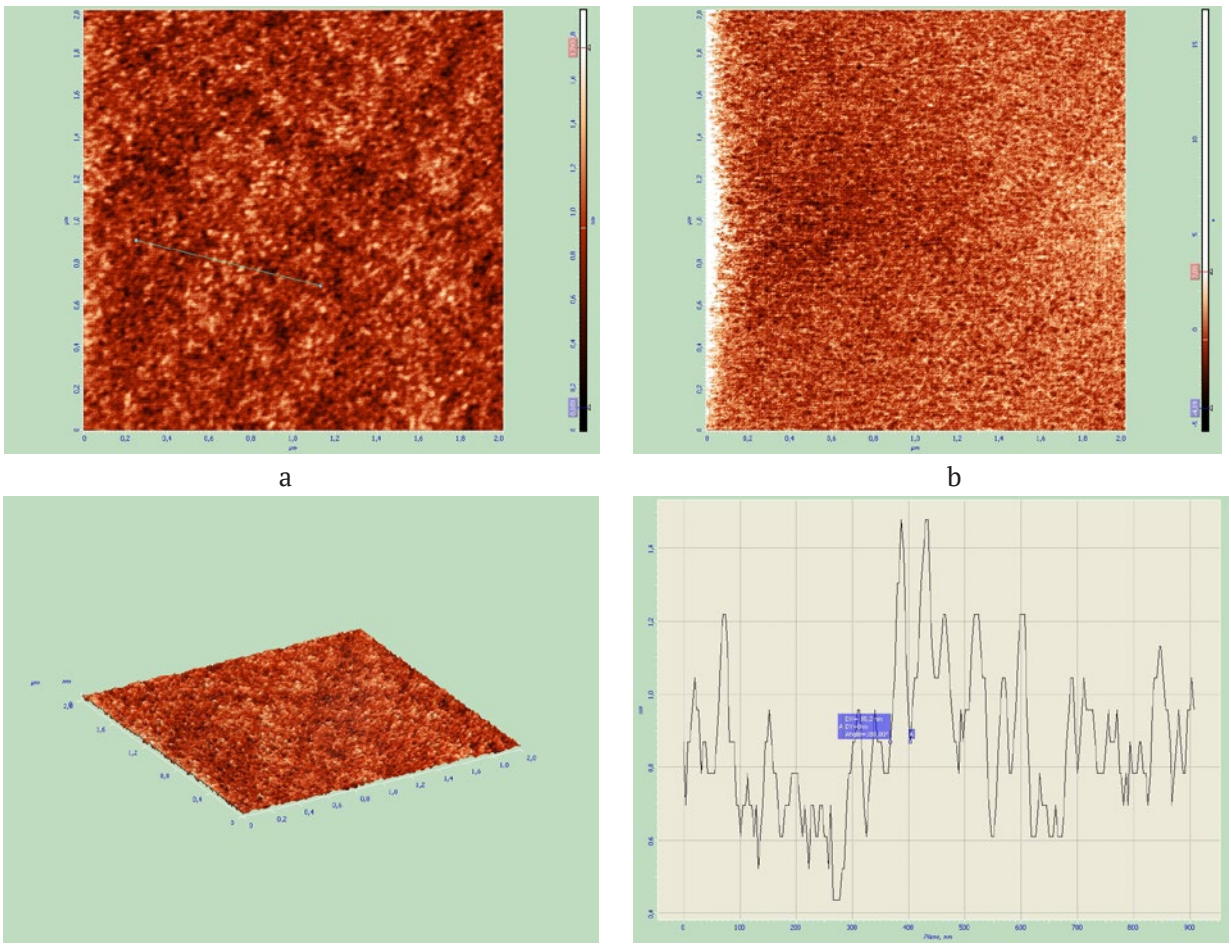

Fig. 5. AFM image of the surface of 2×2 μm films of thin Nb film – single-crystal Si system after annealing at T = 773 K for 30 min: film surface (a); phase contrast (b); 3-d image of the surface (c); surface relief section (d)

size obtained from AFM images of the surface (~ 35 nm) confirmed the nanoscale polycrystalline nature of the niobium metal film formed by magnetron-assisted sputtering followed by vacuum annealing.

The results of the analysis of samples by the RBS method are shown in Fig. 6. As can be seen from Fig. 6, in the obtained system, the Nb/Si MPB has the form of a boundary region transitional in concentration.

4. Description of the interdiffusion model in the Nb-single-crystal Si system

A qualitative nature of the process suggests that the interaction of niobium with the lattice of single-crystal silicon leads to its partial destruction. The mechanism of this destruction will be left outside the scope of the model. The consequence of this interaction is the appearance of free silicon atoms capable of migration. In the silicon lattice, they can migrate as interstitial atoms.

Silicon has low solubility in the bulk of niobium crystallites. This circumstance justifies ignoring the effect of diffusion penetration and dissolution of silicon in the bulk of niobium crystallites. However, the presence of developed grain boundaries makes the deep diffusion of silicon in a niobium film potentially possible and increases its solubility in the intergrain space.

The intergrain space of a polycrystalline niobium film contains coordinatively unsaturated bonds. Let us assume that they act as segregation trapping centres with respect to mobile silicon atoms, onto which silicon is captured with the release of free niobium. Thus, the dissolution of

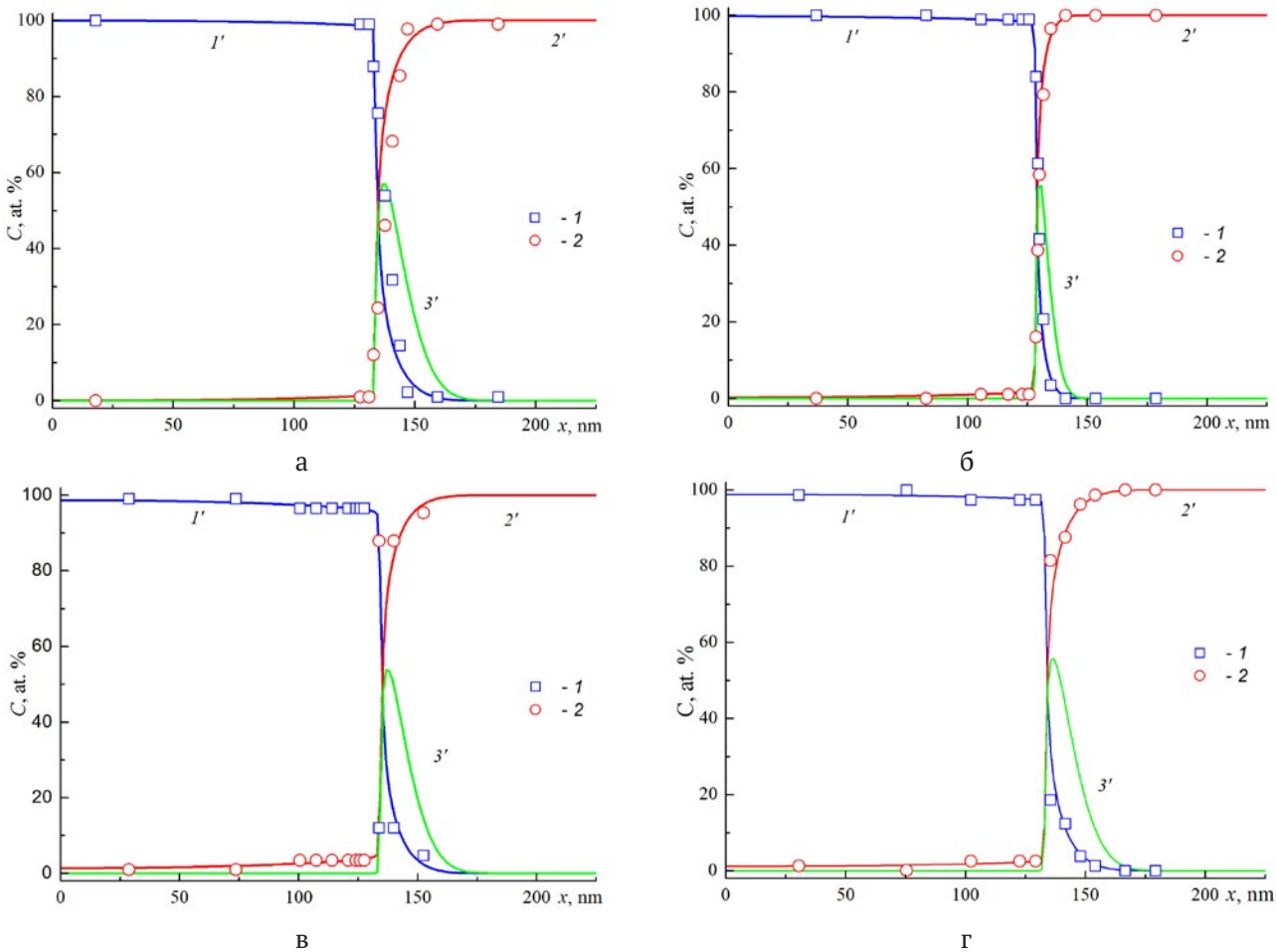

Fig. 6. Experimental (RBS method, symbols *1,2*) and calculated (curves *1', 2', 3'*) distribution over the depth of thin Nb film – single-crystal Si system of full concentration *C* of niobium (*1'*), silicon (*2'*) and its mobile part (*3'*). *1* — Nb, *2* — Si; curves: *1'*— Nb, *2'* — Si after magnetron-assisted sputtering and vacuum annealing in the T = 673 K, t = 30 min

silicon in a niobium film will be represented as the process of its reactive grain boundary diffusion in the intergrain space.

The stage of segregation capture of silicon on intergrain traps is initially carried out according to the physical sorption mechanism and is not accompanied by chemical interaction with the formation of silicides. It occurs in the volume of the metal film, has a topochemical character, and is localized in its intergrain space. The high defectiveness of the intergrain space of the film contains a sufficient free volume, which ensures the exchange sorption process with minimal energy loss for bond deformation.

The process of formation of a silicon solid solution in a niobium film will be limited by the concentration of traps, which is the fraction r from the total metal concentration.

With regard to niobium, we will assume that its diffusion and solubility as an impurity in single-crystal silicon is limited by the decomposition process of a solid niobium solution in silicon with the formation of immobile multiparticle complexes containing silicon point defects and metal atoms.

A mathematical model that describes the process of interdiffusion in a binary system with unlimited solubility of components was proposed in [16]. It assumes the invariance of the molar volume of the system and the absence of changes in its composition as a result of chemical transformations. The theory [16] suggests obtaining the distribution of concentrations of components as a solution to a boundary value problem containing two diffusion equations with one effective interdiffusion coefficient.

In [17], the model [16] was applied to the analysis of phase formation in the diffusion zone. In [18], the model [16] was developed for the description of bulk reactions of silicide formation in the Ni – SiC. In [19], the mathematical form [16] was used in a quantitative model that developed the model [16] for reactive interdiffusion in metal – second metal oxide two-layer systems with limited component solubility. In [20], it was developed for the case of reactive interdiffusion of components under vacuum annealing conditions for polycrystalline nonstoichiometric film oxide systems with limited solubility. In [21], the possibility of using the mathematical form of the model [16] for the description of the interdiffusion process in the thin polycrystalline metal film – single-crystal silicon system under conditions of limited solubility of components was demonstrated.

In our case, the qualitative nature of the solid-phase interaction in the thin Nb film – single-crystal Si system during vacuum annealing also assumes a constant molar volume. Therefore, we use the mathematical formalism of the theory [17] for the description of the reactionary interdiffusion process in it. Diffusion-reaction equations for the components of a thin Nb film – single-crystal Si system were as follows:

$$\frac{\partial C_A}{\partial t} = \frac{\partial}{\partial x}\left(D^* \frac{\partial C_A}{\partial x}\right) - k_1 \cdot C_C \cdot C_A, \quad (1)$$

$$\frac{\partial C_B}{\partial t} = \frac{\partial}{\partial x}\left(D^* \frac{\partial C_B}{\partial x}\right) + k_1 \cdot C_A \cdot C_C - k_2 \cdot C_{Ct} \cdot C_B - k_3 \cdot C_B \cdot C_C, \quad (2)$$

$$\frac{\partial C_{Bt}}{\partial t} = \frac{\partial}{\partial x}\left(D^* \frac{\partial C_{Bt}}{\partial x}\right) + k_2 \cdot C_{Ct} \cdot C_B, \quad (3)$$

$$\frac{\partial C_{Ct}}{\partial t} = \frac{\partial}{\partial x}\left(D^* \frac{\partial C_{Ct}}{\partial x}\right) - k_2 \cdot C_B \cdot C_{Ct}, \quad (4)$$

$$\frac{\partial C_{Cp}}{\partial t} = \frac{\partial}{\partial x}\left(D^* \frac{\partial C_{Cp}}{\partial x}\right) + k_3 \cdot C_B \cdot C_C, \quad (5)$$

$$\frac{\partial C_C}{\partial t} = \frac{\partial}{\partial x}\left(D^* \frac{\partial C_C}{\partial x}\right) + k_2 \cdot C_{Ct} \cdot C_B - k_3 \cdot C_B \cdot C_C, \quad (6)$$

where t is time, x is the depth measured from the outer surface of the niobium film; C_A, C_B, C_{bt}, C_{Ct}, C_{cp}, C_C is the concentration of silicon (A) at the sites of the crystal lattice of silicon, mobile silicon (B), formed as a result of the interaction of niobium with silicon; silicon (Bt) trapped in the intergrain space of the niobium film; free trap centres (C_t) for mobile silicon in the intergrain space of the niobium film; immobile complexes (C_p) in silicon containing niobium and silicon atom; and mobile niobium (C), respectively.

k_1, k_2 and k_3 – are the rate constants for the generation of free silicon B, its capture by intergrain traps in niobium, and the formation of niobium-silicon complexes C_p respectively.

For the effective interdiffusion coefficient, the ratio was used:

$$D^* = \frac{D_B \cdot C_C + D_C \cdot C_B}{C_{tot}}, \quad (7)$$

where D_B and D_C – individual diffusion coefficients of mobile components – of free silicon B and niobium C, respectively, $C_{tot} = C_A + C_B + C_C + C_{Cp} + C_{Bt} + C_{Ct}$ – total concentration of all components of the system.

In the case when the values of the individual diffusion coefficients of the mobile components of the system differ significantly from each other, the Nb/Si grain boundary in the selected reference system will move, while the stationary components of the system will serve as inert markers in the Smigelskas and Kirkendall experiment [22].

As a boundary condition for all components of the system, the reflection condition was assumed:

$$\frac{\partial C_A}{\partial x} = \frac{\partial C_B}{\partial x} = \frac{\partial C_C}{\partial x} = \frac{\partial C_{Cp}}{\partial x} = \frac{\partial C_{Bt}}{\partial x} = \frac{\partial C_{Ct}}{\partial x} = 0 \quad (8)$$

at $x = 0$ and $x = L$

where L is the thickness of the solution region in silicon.

The following conditions were used as initial conditions:

$$C_A(x,0) = 0,\ C_{Ct}(x,0) = r \cdot N_{SC},\ C_C(x,0) = (1 - r) \cdot N_{SC}, \quad (9)$$
at $0 \leqslant x \leqslant h$,

$$C_A(x,0) = N_{SA},\ C_{Ct}(x,0) = 0,\ C_C(x,0) = 0, \quad (10)$$
at $h < x \leqslant L$,

$$C_B(x,0) = 0,\ C_{Bt}(x,0) = 0,\ C_{Cp}(x,0) = 0 \quad (11)$$
for all $0 \leqslant x \leqslant L$,

where h is the thickness of the niobium film, $N_{SA} = 4.98 \cdot 10^{22}$ cm^{-3} is the intrinsic concentration of Si atoms, $N_{SC} = 5.55 \cdot 10^{22}$ cm^{-3} is the intrinsic concentration of niobium atoms, r is the fraction of traps for silicon atoms in the intergrain space of the niobium film.

For the numerical solution of the system of diffusion-reaction equations (1)–(6) with a concentration-dependent effective interdiffusion coefficient (7), implicit conservative difference schemes and the factorization method were used [23].

The model parameters were: individual diffusion coefficients of silicon and niobium, rate constants k_1, k_2, k_3, and r.

The results of numerical simulation (curves *1′, 2′*) in comparison with the experimental distribution of concentrations of Nb and Si obtained by the RBS method over the depth of thin Nb film – single-crystal Si system (points *1, 2*) after magnetron-assisted sputtering of Nb onto single-crystal silicon and vacuum annealing during isochronous annealing at t = 30 min in temperature range T = 423–673 K are shown in Fig. 6a–c.

The experimental and calculated distributions were in good agreement for identical values $k_1 = 1 \cdot 10^{-25}$ cm^3/s, $k_2 = 1 \cdot 10^{-20}$ cm^3/s, $k_3 = 1 \cdot 10^{-19}$ cm^3/s, r = 0.028. The individual diffusion coefficient of niobium in the studied system under experimental conditions was $D_{Nb} = 4.0 \cdot 10^{-16}$ cm^2/s, and for silicon, the temperature dependence was determined (Fig. 7):

$$D_{Si} = 3.0 \cdot 10^{-12} \cdot \exp(-0.216\ \text{эВ}/(kT))\ \text{cm}^2/\text{s}. \quad (12)$$

In [24], for the study of the interdiffusion of amorphous Si–Nb multilayers during annealing in the temperature range of 423–523 K obtained by ion-beam sputtering with a repeating film thickness of 3.2 nm, the interdiffusion coefficient was determined $D^* = 2.2 \cdot 10^{-18} \exp(-0.55\ \text{eV}/(kT))$ cm^2/s. The authors explain the low value of the pre-exponential factor by the high concentration of traps in amorphous silicon [24].

As can be seen from the obtained data, the dominant diffusant in the studied system is mobile silicon (curves *3′* in Fig. 6a–d). The maximum of its distribution is localized on the Nb/Si interface.

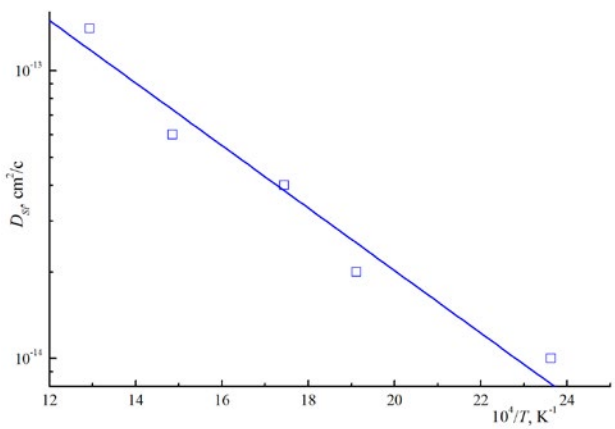

Fig. 7. Temperature dependence of the individual diffusion coefficient of silicon in thin Nb film – single-crystal Si system. Dots are the results of numerical analysis; curve was obtained by approximation using the Arrhenius equation (12)

4. Conclusions

Thin films of niobium obtained on single-crystal silicon by magnetron-assisted sputtering followed by vacuum annealing were polycrystalline with a grain size ~ of 32 nm. The Nb/Si grain boundary has the form of a transition region in terms of concentration, indicating the mutual diffusion of the components in the polycrystalline niobium film – single-crystal silicon system. This process was studied by the simulation method. A model that takes into account the limited solubility of the components was developed. The model describes the solubility of silicon in the intergrain space of niobium with its segregation on intergrain traps, as well as the solubility of the metal in silicon, limited by the complexation process. It is applicable to the description of the redistribution of components up to synthesis conditions, providing the chemical interaction of niobium with silicon and the formation of silicides.

Numerical analysis of the experimental distribution of concentrations of the components in Nb film – single-crystal Si system within the framework of the model established that silicon is the dominant diffusant in the studied diffusion pair. The values of the individual diffusion coefficients of niobium and silicon in the temperature range 423–773 K, as well as the fraction of traps for Si atoms in the intergrain space of Nb, were determined.

Contribution of the authors

The authors contributed equally to this article.

Conflict of interests

The authors declare that they have no known competing financial interests or personal relationships that could have influenced the work reported in this paper.

References

1. Bromley D., Wright A. J., Jones L. A. H., ... O'Brien L. Electron beam evaporation of superconductor-ferromagnet heterostructures. *Scientific Reports*. 2022;12(1): 7786. https://doi.org/10.1038/s41598-022-11828-y

2. Yusuf S.; Iii R. M. O.; Jiang J. S.; Sowers C. H.; Bader S. D.; Fullerton E. E.; Felcher G. P. Magnetic profile in Nb/S isuperconducting multilayers. *Journal of Magnetism and Magnetic Materials*. 1999; 198–199(1-3): 564–566. https://doi.org/10.1016/s0304-8853(98)01215-3

3. Modi M. H., Rai S. K., Idir M., Schaefers F., Lodha G. S. NbC/Si multilayer mirror for next generation EUV light sources. *OptExpress*. 2012;14: 15114-15120. https://doi.org/10.1364/OE.20.015114

4. Ichimaru, S.; Ishino, M.; Nishikino, ... Oku, S. Irradiation damage test of Mo/Si, Ru/Si and Nb/Si multilayers using the soft X-ray laser built at QST. In: Kawachi, T., Bulanov, S., Daido, H., Kato, Y. (eds) *X-Ray Lasers 2016. ICXRL 2016*. Springer Proceedings in Physics, vol. 202. Springer, Cham. https://doi.org/10.1007/978-3-319-73025-7_45

5. Jang S.-Y.; Lee S.-M.; Baik H.-K. Tantalum and niobium as a diffusion barrier between copper and silicon. *Journal of Materials Science: Materials in Electronics*. 1996;7(4): 1736–1738. https://doi.org/10.1007/BF00188954

6. Schlesinger M. E., Okamoto H., Gokhale A. B., Abbaschian, R. (1993). The Nb-Si (Niobium-Silicon) system. *Journal of Phase Equilibria*. 1993;14(4): 502–509. https://doi.org/10.1007/bf02671971

7. Chandrasekaran A., van de Kruijs R. W. E., Sturm J. M., Bijkerk F. Nb texture evolution and interdiffusion in Nb/Si-layered systems. *ACS Applied Materials & Interfaces*. 2021;13(26): 31260–31270. https://doi.org/10.1021/acsami.1c06210

8. Saito S., Takashima T., Horiuchi T., Miura S., Narita, T. Investigation of the cross-sectional structure and isothermal section at 1150°C of a Nb–Re–Si alloy fabricated using a tetra-arc furnace. *Materials Transactions*. 2019;60(4): 611–615. https://doi.org/10.2320/matertrans.m2018396

9. Bruijn S., Van De Kruijs R. W. E., Yakshin A. E., Bijkerk F. In-situ study of the diffusion-reaction mechanismin Mo/Si multilayered films. *Applied Surface Science*. 2011;257: 2707–2711. https://doi.org/10.1016/j.apsusc.2010.10.049

10. Huang Q., Zhang, J., ... Wang Z. Structure and stress studies of low temperatureannealed W/Si multilayers for the X-ray telescope. *Express*. 2016;24: 15620. https://doi.org/10.1364/oe.24.015620

11. Zaytseva I., Abal'oshev O., Dłużewski P., ... Cieplak M. Z. Negative Hall coefficient of ultrathin niobium in Si/Nb/Si trilayers. *Physical Review B*. 2014;90(6). https://doi.org/10.1103/physrevb.90.060505

12. *Thin Films: Interdiffusion and Reactions* (Eds: J. M. Poate, K. N. Tu and J. W. Mayer). New York: Wiley; 1978. 578 p.]

13. Smigelskas A. D., Kirkendall E. O. Zinc diffusion in alpha-brass. *Transactions of the American Institute of Mining and Metallurgical Engineers*. 1947;171: 130–142.

14. JCPDC PCPDFWIN: A Windows Retrieval/Display Program for Accessing the ICDD PDF-2 Data Base, International Centre for Diffraction Data, 1997.

15. Brandon D., Kaplan W. D. *Microstructural characterization of materials*. John Wiley & Sons Ltd. 2013. 560 p.

16. Darken L. S., Diffusion, mobility and their interrelation through free energy in binary metallic systems. *Transactions of the American Institute of Mining and Metallurgical Engineers*. 1948;175: 84–201. https://doi.org/10.1007/s11661-010-0177-7

17. Gurov K. P., Kartashkin B. A., Ugaste Yu. E. *Mutual diffusion in multiphase metallic systems*[*]. (Ed. K. P. Gurov. Moscow: Nauka Publ.; 1981. 352 p. (in Russ.)

18. Aleksandrov O. V., Kozlovski V. V. Simulation of interaction between nickel and silicon carbide during the formation of ohmic contacts. *Semiconductors*. 2009;43: 885–891. https://doi.org/10.1134/S1063782609070100

19. Afonin N. N., Logacheva V. A. Modeling of the reaction interdiffusion in the polycrystalline systems with limited component solubility. *Industrial Laboratory. Diagnostics of Materials*. 2019;85(9):35-41. (in Russ.) https://doi.org/10.26896/1028-6861-2019-85-9-35-41

20. Afonin N. N., Logachova V. A. Reactive interdiffusion of components in a non-stoichiometric two-layer system of polycrystalline titanium and cobalt oxides. *Condensed Matter and Interphases*. 2020;22(4): 430–437. https://doi.org/10.17308/kcmf.2020.22/3058

21. Afonin N. N., Logachova, V. A. A model of interdiffusion occurring during the formation of thin metal films on single-crystal silicon under conditions of limited solubility of the components. *Condensed Matter and Interphases*. 2022;24(1), 129–135. https://doi.org/10.17308/kcmf.2022.24/9063

22. Smigelskas A. D., Kirkendall E. O. Zinc diffusion in alpha-brass. Transactions of the *American Institute of Mining and Metallurgical Engineers*. 1947;171: 130–142.

23. Samarskii A. A. *Theory of difference schemes*[*]. Moscow: Nauka Publ.; 1977. 656 p. (in Russ.)

24. Zhang M., Yu W., Wang W. H., Wang, W. K. Interdiffusion in compositionally modulated amorphous Nb/Si multilayers. *Thin Solid Films*. 1996;287(1–2), 293–296. https://doi.org/10.1016/s0040-6090(96)08765-2

[*]*Translated by author of the article*.

Information about the authors

Nikolay N. Afonin, Dr. Sci. (Chem.), Research Fellow, Professor at the Department of Science and Technology Studies, Voronezh State Pedagogical University (Voronezh, Russian Federation).

https://orcid.org/0000-0002-9163-744X
nafonin@vspu.ac.ru

Vera A. Logachova, Cand. Sci. (Chem.), Research Fellow at the Department of General and Inorganic Chemistry, Voronezh State University (Voronezh, Russian Federation).

https://orcid.org/0000-0002-2296-8069
kcmf@main.vsu.ru

Received 22.12.2022; approved after reviewing 27.01.2023; accepted for publication 15.02.2023; published online 25.09.2023.

Translated by Valentina Mittova

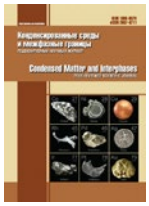

ISSN 1606-867X (Print)
ISSN 2687-0711 (Online)
Condensed Matter and Interphases
Kondensirovannye Sredy i Mezhfaznye Granitsy
https://journals.vsu.ru/kcmf/

Original articles

Research article
https://doi.org/10.17308/kcmf.2023.25/11257

Biocatalysts based on complexes of carbon nanomaterials with cysteine proteases

S. S. Goncharova[1], E. A. Shchegolevatykh[1], D. A. Zhukalin[1], M. G. Holyavka[1,2]✉, V. G. Artyukhov[1]

[1]*Voronezh State University,*
1 Universitetskaya pl., Voronezh 394018, Russian Federation

[2]*Sevastopol State University,*
33 Universitetskaya str., Sevastopol 299053, Russian Federation

Abstract

The purpose of the research is to develop and study biocatalysts based on complexes of cysteine proteases with fullerenes and carbon nanotubes.

During the formation of ficin complexes with fullerenes and carbon nanotubes, the activity of hybrid preparations was 70 and 45%, respectively. During the formation of papain complexes with fullerenes and carbon nanotubes, the proteolytic ability of the enzyme remained at the same level for the samples with fullerene and decreased by 27% for the preparations with carbon nanotubes. The formation of bromelain complexes with fullerenes and carbon nanotubes contributed to a decrease in the proteolytic activity of the biocatalyst by 18 and 48% as compared to the free enzyme. While determining the stability of complexes of nanomaterials and cysteine proteases during a 7-day incubation in 0.05 M tris-HCl buffer (pH 7.5) at 37 °C, we noticed a decrease in the proteolytic activity of the samples.

Complexation with carbon nanoparticles and fullerenes increased the stability of ficin and bromelain, while the stability of papain in the complexes remained unchanged.

Keywords: Cysteine proteases, Ficin, Papain, Bromelain, Fullerenes, Carbon nanotubes

Acknowledgements: The research was funded by the Ministry of Science and Higher Education of the Russian Federation in the framework of the government order to higher education institutions in the sphere of scientific research for years 2023-2025, project No. FZGU-2023-0009.

For citation: Goncharova S. S., Shchegolevatykh E. A., Zhukalin D. A., Holyavka M. G., Artyukhov V. G. Biocatalysts based on complexes of carbon nanomaterials with cysteine proteases. *Condensed Matter and Interphases*. 2023;25(3): 343–349. https://doi.org/10.17308/kcmf.2023.25/11257

Для цитирования: Гончарова С. С., Щеголеватых Е. А., Жукалин Д. А., Холявка М. Г., Артюхов В. Г. Биокатализаторы на основе комплексов углеродных наноматериалов с цистеиновыми протеазами. *Конденсированные среды и межфазные границы*. 2023;25(3): 343–349. https://doi.org/10.17308/kcmf.2023.25/11257

✉ Marina G. Holyavka, e-mail: holyavka@rambler.ru

1. Introduction

Carbon materials are of great interest to various areas of science. Currently, there is a growing amount of research aimed at expending the application of carbon nanomaterials, including fullerenes and nanotubes. These nanostructures are to some extent considered as possible synthons for biologically active substances [1].

Fullerenes are a new allotropic modification of carbon. The fullerene molecule is a spheroidal hollow framework molecule of an even number of covalently bonded carbon atoms located at the vertices of hexagons or pentagons [2]. Inside the molecule, there is a cavity into which atoms and molecules of other substances can be introduced [3]. It has been established that fullerenes have a stabilising effect on enzymes, which protects them from thermal inactivation and oxidation [4]. In biological systems, fullerenes can have both an antioxidant effect (they add reactive oxygen species) and oxidising effect due to their photosensitising properties. Fullerene molecules are lipophilic and exhibit a membranotropic effect. They interact with various biological structures and can alter their functions, which increases the lipophilicity of the active molecule. Fullerenes can enable the targeted delivery of some therapeutic agents [5], they can be used in X-ray imaging as inhibitors of the process of human immunodeficiency virus multiplication and chemotherapeutic agents. A distinctive feature of fullerenes is their ability to combine several functions, which allows using them in precision medicine. Precision medicine opens a new path to personalised nanomedicine, where the course of the treatment can be controlled and thus adapted for each individual patient [6-8].

Carbon nanotubes are extended cylindrical hollow structures with a diameter of one to several tens of nanometres, a length of tens of microns or, in some cases, of even a centimetre , which are formed by one or more graphene sheets rolled into a seamless tube. Their advantages include a large specific surface area, high stability, strength, thermal conductivity, and unusual electronic and emission properties [5]. The specific surface area of carbon nanotubes is from 150 to 1,500 $m^2 \cdot g^{-1}$, which is many times higher than that of fullerenes [9, 10]. Carbon nanotubes have the potential to be used as safe and effective alternatives to existing drug delivery methods: they can pass through the membranes together with treatment medications, vaccines, and nucleic acids and penetrate deep into the cell to reach substrate targets; they serve as ideal non-toxic carriers, which in some cases increase the solubility of the preparation and enhance its efficiency and safety [11]. Carbon nanotubes were used to develop estrogen and progesterone test strips, DNA and protein microarrays, and NO_2 and cardiac troponin sensors. Similar sensors have been used to detect gases and toxins [12-14].

A high specificity of enzyme catalysis provides for an impressive target product yield and an almost waste-free production. Proteolytic plant enzymes are often used in medicine. The most popular among them are ficin (EC 3.4.22.3), bromelain (EC 3.4.22.32), and papain (EC 3.4.22.2) [15,16].

Ficin (EC 3.4.22.3) is made from the *Ficus* plants. It is a cysteine proteolytic enzyme. The molecular weights of the enzyme is 25-26 kDa. Ficin has a wide range of pH values (6.5-9.5) in which it exhibits high activity [17]. The isoelectric point of the enzyme is 9.0. The ficin molecule consists of a single polypeptide chain with an N-terminal leucine residue [18-20]. Ficin exhibits antimicrobial activity against gram-positive and gram-negative bacteria. In addition, it is also known to have anti-inflammatory, anthelminthic, antithrombotic, fibrinolytic, and anti-cancer properties and an immunomodulatory effect [21, 22].

Papain (EC 3.4.22.2) is extracted from papaya (*Carica papaya*). Its molecular weight is 23 kDa. The enzyme consists of 212 amino acid residues with isoleucine at the N-terminus and asparagine at the C-terminus. Papain has a high activity in different media: at pH 5.0-7.5, it hydrolyses proteins, peptides, and amides. The most favourable temperature for the enzyme functioning is in the range of 50–60 °C. Its isoelectric point is 8.75 [23–25]. Papain can break down proteins with a greater speed and efficiency than many animal and bacterial enzymes, it can contribute to a faster healing of wounds, bedsores, and trophic ulcers, it has anti-inflammatory properties, and allows other drugs to penetrate the skin without violating its integrity [26–29].

Bromelain (EC 3.4.22.32) is a proteolytic plant enzyme which is made from pineapples. The molecular weight of bromelain is 33 kDa and the isoelectric point is 9.55. The most favourable temperature for the enzyme is 62 °C, and the pH is 7.0 [30, 31]. Bromelain is used to improve digestion, to mitigate the symptoms of inflammatory processes, to reduce edema, and to increase the rate of tissue regeneration. It is characterised by anti-cancer properties, it can prevent thrombus formation, accelerates tissue regeneration processes during depolymerisation of intercellular structures, changes the permeability of blood vessels, and has an immunomodulatory effect [32–35].

However, there are several reasons that prevent the large-scale use of the enzymes: the instability of the preparations under various conditions, high cost, and impossibility of their repeated use. These problems can be largely overcome by using associated enzymes, which are more stable and have a sustained action [36, 37].

Therefore, the aim of this research was to develop biocatalysts based on complexes of cysteine proteases with carbon nanotubes and fullerenes and to study their catalytic activity.

2. Experimental

Ficin, papain, and bromelain were in the focus of the study and azocasein (Sigma, USA) was used as a substrate for hydrolysis. For complexation, the following certified carbon nanomaterials were used: Nanocyl-7000 nanotubes (NANOCYL S.A.) with a length of 0.7–3.0 μm and a diameter of 5–35 nm; C_{60} NeoTechProduct fullerenes with a purity of 99.5%.

The enzyme complex with carbon nanotubes and fullerenes was prepared as follows: an enzyme solution (2 mg/ml in 50 mM of glycine buffer, pH 10.0 and 9.0 for ficin and papain and in 50 mM of tris-glycine buffer, pH 9.0 for bromelain) was mixed in equal volumes with a solution of carbon nanotubes and fullerenes and kept at room temperature for 2 h. The protease activity of the obtained compounds was measured as described in [38].

To determine the sizes and surface charges of the nanoparticles, we used a Nano Zetasizer ZS (Malvern Instruments, USA) equipped with a 4 mW He/Ne laser with $\lambda = 632.8$ nm, the scattering angle was 173°.

3. Results and discussion

In the first series of experiments, we determined the size and zeta potential of fullerenes and carbon nanotubes. The parameters of the nanoparticles are presented in Table 1. The average size of fullerenes was 113 nm and the average size of carbon nanotubes was 153 nm. The median zeta potential was –12 mV for fullerenes and –20 mV for carbon nanotubes.

During the formation of ficin complexes with fullerenes and carbon nanotubes, the activity of the associates was 70 and 45% of the values for the native enzyme, respectively. During the formation of papain complexes with fullerenes and carbon nanotubes, the proteolytic ability of the enzyme remained at the same level for the fullerene and decreased by 27% for the carbon nanotubes. The formation of bromelain complexes with fullerenes and carbon nanotubes contributed to an 18 and 48% decrease in proteolytic activity as compared to the free enzyme (Fig. 1).

We conducted experiments aimed to determine the residual activity of cysteine proteases at 37 °C and pH 7.5 in 0.05 M HCl buffer for free enzymes and their complexes with fullerenes and carbon nanotubes. All samples showed a decrease in their activity within 7 days.

A solution of native ficin after a 7 day incubation retained 8% of its original proteolytic activity, its complexes with fullerenes and carbon nanotubes showed 46 and 43% of their ability to hydrolyse azocasein, respectively. Native papain after its incubation for 7 days retained 15% of its activity, and papain samples with fullerenes

Table. 1. Parameters of nanoparticles

Nanoparticles	Average size, nm	Size range, nm	Median zeta-potential, mV	Zeta-potential range, mV
Fullerenes	113.8	91.2-141.8	–12.3	from –25.8 to 13.9
Carbon nanotubes	153.4	122.4-190.1	–20.1	from –35.7 to –5.99

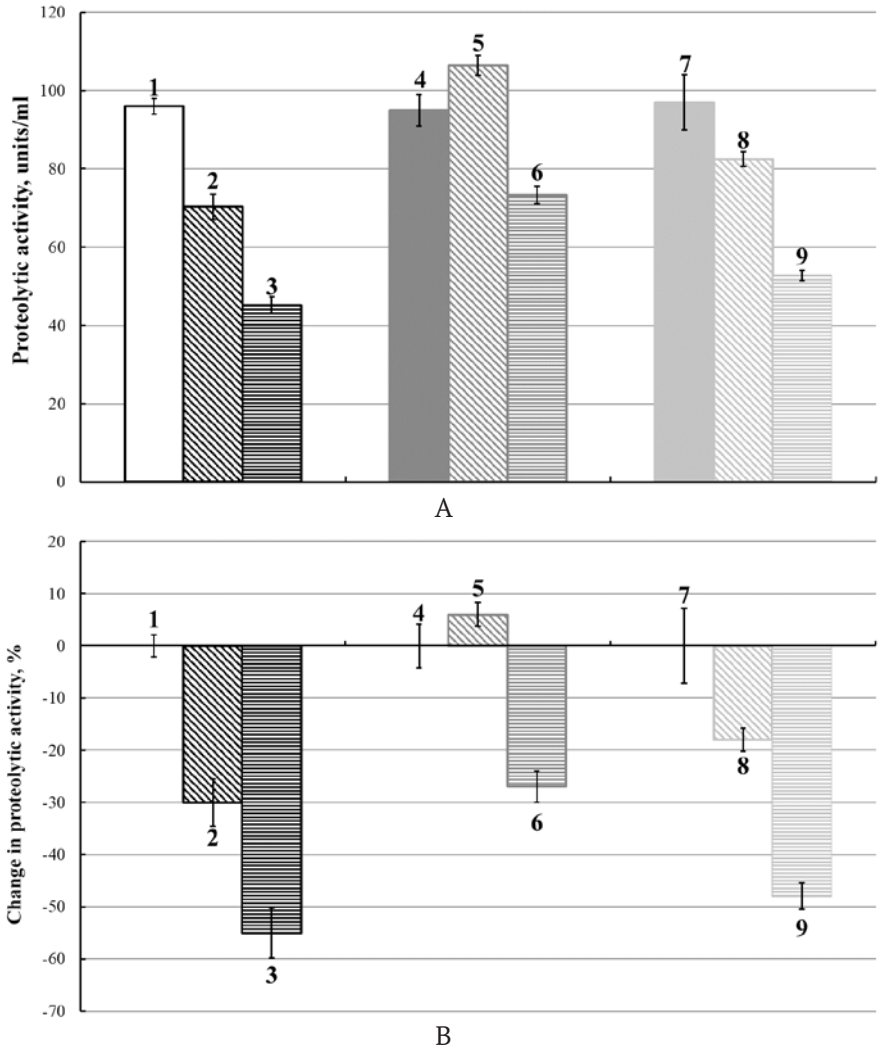

Fig. 1. Catalytic activity of ficin, papain, and bromelain, units/ml (A) and its change, % (B): soluble ficin (1); ficin complex with fullerene (2); ficin complex with carbon nanotubes (3); soluble papain (4); papain complex with fullerene (5); papain complex with carbon nanotubes (6); soluble bromelain (7); bromelain complex with fullerene (8); bromelain complex with carbon nanotubes (9). The activity of free enzymes under optimum hydrolysis conditions was taken as 100%

and carbon nanotubes showed 27 and 22%. The bromelain solution retained 13% of its proteolytic activity after 7 days of incubation, while its complexes with fullerenes and carbon nanotubes retained 26 and 29% (Fig. 2).

4. Conclusions

Therefore, as a result of research we obtained complexes of cysteine proteases with fullerenes and carbon nanotubes. Papain complexes with fullerenes showed higher values of proteolytic activity in relation to azocasein than the other studied biocatalysts.

While determining the stability of the complexes of nanoparticles and cysteine proteases, we noticed a decrease in the proteolytic activity of the samples within seven days. Both complexation with fullerenes and carbon nanotubes increased the stability of ficin and bromelain, while the stability of papain in the complexes remained at the level of the free enzyme.

Contribution of the authors

The authors contributed equally to this article.

Conflict of interests

The authors declare that they have no known competing financial interests or personal relationships that could have influenced the work reported in this paper.

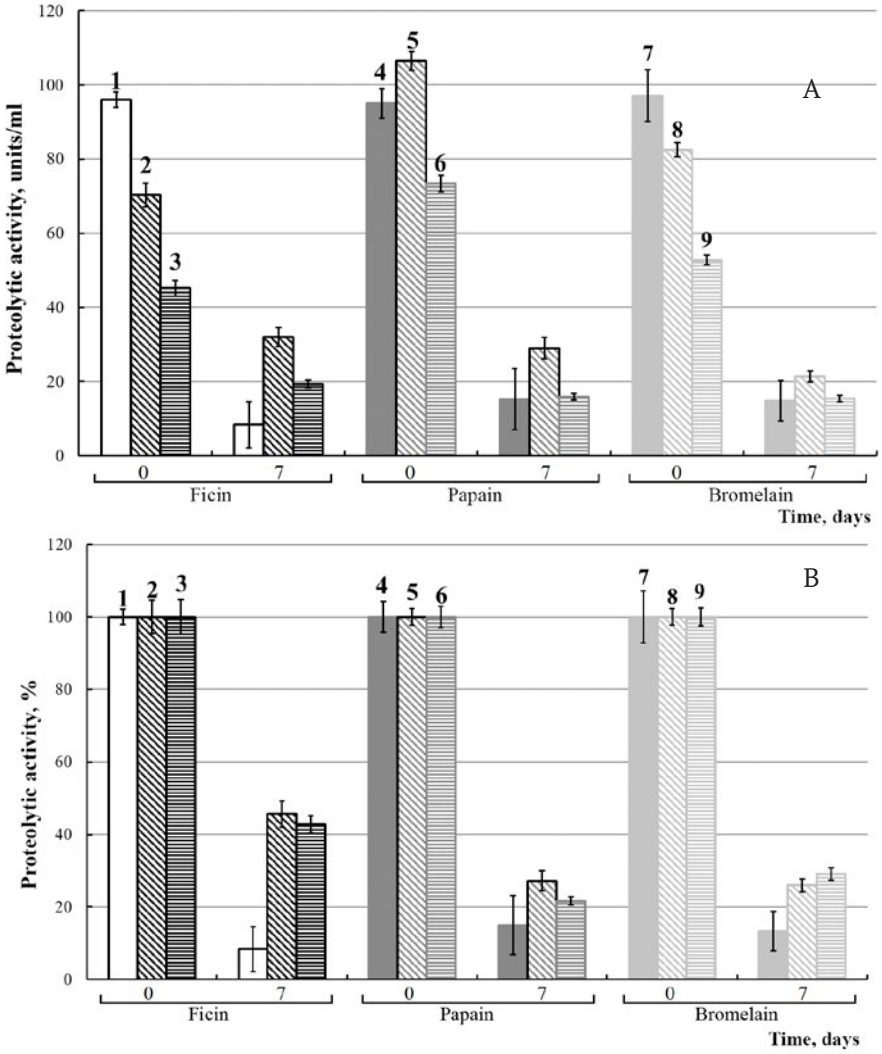

Fig. 2. Residual catalytic activity of ficin, papain, and bromelain after the incubation of samples at 37 °C ((A) in units/ml of solution or suspension, (B) in % of the initial level): soluble ficin (1); ficin complex with fullerene (2); ficin complex with carbon nanotubes (3); soluble papain (4); papain complex with fullerene (5); papain complex with carbon nanotubes (6); soluble bromelain (7); bromelain complex with fullerene (8); bromelain complex with carbon nanotubes (9). The proteolytic activity of the samples without pre-incubation and under optimum hydrolysis conditions was taken as 100%

References

1. Dumpis M. A., Nikolaev D. N., Litasova E. V., Ilyin V. V., Brusina M. A., Piotrovsky L. B. Biological activity of fullerenes - realities and prospects. *Reviews on Clinical Pharmacology and Drug Therapy*. 2018;16(1): 4–20. (In Russ., abstract in Eng.). https://doi.org/10.17816/RCF1614-20

2. Churilov G. N., Vnukova N. G., Dudnik A. I., … Samoylova N. A. A method and apparatus for high-throughput controlled synthesis of fullerenes and endohedral metal fullerenes. *Technical Physics Letters*. 2016;42(5): 475–477. https://doi.org/10.1134/S1063785016050072

3. Melker A. I., Krupina M. A., Matvienko A. N. Nucleation and growth of fullerenes and nanotubes having three-fold t-symmetry. *Frontier Materials & Technologies*. 2022;2: 37–53. https://doi.org/10.18323/2782-4039-2022-2-37-53

4. Zhukalin D. A., Tuchin A. V., Goloshchapov D. L., Bityutskaya L. A. Formation of nanostructures from colloidal solutions of silicon dioxide and carbon nanotubes. *Technical Physics Letters*. 2015;41(2): 157–159. https://doi.org/10.1134/S1063785015020297

5. Postnov V. N., Rodinkov O. V., Moskvin L. N., Novikov A. G., Bugaichenko A. S., Krokhina O. A. From carbon nanostructures to highly efficient sorbents for chromatographic separation and concentration. *Advances in Chemistry*. 2016;85(2): 115–138. https://doi.org/10.1070/RCR4551

6. Rašović I. Water-soluble fullerenes for medical applications. *Materials Science and Technology*. 2017;33(7): 777–794. https://doi.org/10.1080/02670836.2016.1198114

7. Krishna V., Singh A., Sharma P., ... Moudgil B. Polyhydroxy fullerenes for non-invasive cancer imaging and therapy. *Small*. 2010;6(20): 2236–2241. https://doi.org/10.1002/smll.201000847

8. Chen Z., Ma L., Liu Y., Chen C. Applications of functionalized fullerenes in tumor theranostics. *Theranostics*. 2012;2(3): 238–250. https://doi.org/10.7150/thno.3509

9. Bryantsev Ya. A., Arhipov V. E., Romanenko A. I., Berdinsky A. S., Okotrub A. V. Control conductance of single walled carbon nanotubes films during synthesis. *Journal of Siberian Federal Universit. Mathematics and Physics*. 2018;11(2): 222–226. https://doi.org/10.17516/1997-1397-2018-11-2-222-226

10. Dvuzhilova Y. V., Dvuzhilov I. S., Belonenko M. B. Three-dimensional light bullets in an optically anisotropic photonic crystal with carbon nanotubes. *Bulletin of the Russian Academy of Sciences: Physics*. 2022;86(1): 46–49. https://doi.org/10.3103/S1062873822010087

11. De Volder M. F. L., Tawfick S. H., Baughman R. H., Hart A. J. Carbon nanotubes: present and future commercial applications. *Science*. 2013;339(6119): 535–539. https://doi.org/10.1126/science.1222453

12. Zare Y., Rhee K. Y. Modeling of the interfacial stress transfer parameter for polymer/carbon nanotube nanocomposites. *Fizicheskaya Mezomekhanika*. 2020;23(2): 94–99. https://doi.org/10.24411/1683-805X-2020-12010

13. Ahmad A., Kholoud M. M., Abou E., Reda A. A., Abdulrahman A. W. Carbon nanotubes, science and technology part (I) structure, synthesis and characterization. *Arabian Journal of Chemistry*. 2012;5(1): 1–23. https://doi.org/10.1016/j.arabjc.2010.08.022

14. Ibrahim K. S. Carbon nanotubes-properties and applications: a review. *Carbon Letters*. 2013;14(3): 131–144. https://doi.org/10.5714/cl.2013.14.3.131

15. Holyavka M., Faizullin Dzh., Koroleva V., ... Artyukhov V. Novel biotechnological formulations of cysteine proteases, immobilized on chitosan. Structure, stability and activity. *International Journal of Biological Macromolecules*. 2021;180: 161–176. https://doi.org/10.1016/j.ijbiomac.2021.03.016

16. Ol'shannikova S. S., Holyavka M. G., Artyukhov V. G. Method development for ficin entrapment into gels based on food-grade chitosan and chitosan succinate. *Pharmaceutical Chemistry Journal*. 2021;54(10): 1067–1070. https://doi.org/10.1007/s11094-021-02321-3

17. Silva M. Z. R., Oliveira J. P. B., Ramos M. V., ... Freitas C. D. T. Biotechnological potential of a cysteine protease (CpCP3) from Calotropis procera latex for cheesemaking. *Food Chemistry*. 2020;307: 125574. https://doi.org/10.1016/j.foodchem.2019.125574

18. Sun Y., Pan Y, Jiang W., ... Zhou L. The inhibitory effects of ficin on streptococcus mutans biofilm formation. *Biomed Research International*. 2021;2021: 11. https://doi.org/10.1155/2021/6692328

19. Hamed M. B., El-Badry M. O., Fahmy A. S., Kandil E. I., Borai I. H. A contradictory action of procoagulant ficin by a fibrinolytic serine protease from Egyptian Ficus carica latex. *Biotechnology Reports*. 2020;27: e00492. https://doi.org/10.1016/j.btre.2020.e00492

20. Uba G., Manogaran M., Shukor M. Y. A., Gunasekaran B., Halmi M. I. E. Improvement of ficin-based inhibitive enzyme assay for toxic metals using response surface methodology and its application for near real-time monitoring of mercury in marine waters. *International Journal of Environmental Research and Public Health*. 2020;17(22): 1–15. https://doi.org/10.3390/ijerph17228585

21. Olshannikova S., Koroleva V., Holyavka M., Pashkov A., Artyukhov V. Covalent Immobilization of Thiol Proteinases on Chitosan. *The 1st International Electronic Conference on Catalysis Sciences*. 2020;2(1): 7. https://doi.org/10.3390/ECCS2020-07527

22. Silva-López R. E., Gonçalves R. N. Therapeutic proteases from plants: biopharmaceuticals with multiple applications. *Journal of Applied Biotechnology & Bioengineering*. 2019;6(2): 101–109. https://doi.org/10.15406/jabb.2019.06.00180

23. McKerrow J. H. The diverse roles of cysteine proteases in parasites and their suitability as drug targets. *PLOS Neglected Tropical Diseases*. 2018;12(8): e0005639. https://doi.org/10.1371/journal.pntd.0005639

24. Rieder A. S., Deniz B. F., Netto C. A., Wyse A. T. S. A review of in silico research, SARS-CoV-2, and neurodegeneration: focus on papain-like protease. *Neurotoxicity Research*. 2022;40(5): 1553–1569. https://doi.org/10.1007/s12640-022-00542-2

25. Sokolova R. S. Papain medication of hemophthalmos. *The Russian Annals of Ophthalmology*. 1976;92(4): 54–56. (In Russ.)

26. Semashko T. A., Lysogorskaya E. N., Oksenoit E. S., Bacheva A. V., Filippova I. Yu. Chemoenzymatic synthesis of new fluorogenous substrates for cysteine proteases of the papain family. *Russian Journal of Bioorganic Chemistry*. 2008;34(3): 339–343. https://doi.org/10.1134/S1068162008030151

27. Rinaldi F., Tengattini S., ... Peters B. Monolithic papain-immobilized enzyme reactors for automated structural characterization of monoclonal antibodies. *Frontiers in Molecular Biosciences*. 2021;8: 765683. https://doi.org/10.3389/fmolb.2021.765683

28. Pankova S. M., Sakibaev F. A., Holyavka M. G., Artyukhov V. G. A possible role of charged amino-acid

clusters on the surface of cysteine proteases for preserving activity when binding with polymers *Biophysics*. 2022;67(1): 8–14. https://doi.org/10.1134/S0006350922010146

29. Hu R., Chen G., Li Y. Production and characterization of antioxidative hydrolysates and peptides from corn gluten meal using papain, ficin, and bromelain. *Molecules*. 2020;25(18): 4091. https://doi.org/10.3390/molecules25184091

30. Koroleva V. A., Olshannikova S. S., Holyavka M. G., Artyukhov V. G. Thermal inactivation of cysteine proteases: the key stages. *Biophysics*. 2021;66(3): 364–372. https://doi.org/10.1134/S0006350921030088

31. Ribeiro J. S., Barboza A. da S., Cuevas-Suárez C. E., da Silva A. F., Piva E., Lund R. G. Novel in-office peroxide-free tooth-whitening gels: bleaching effectiveness, enamel surface alterations, and cell viability. *Scientific Reports*. 2020;10: 8. https://doi.org/10.1038/s41598-020-66733-z

32. Aider M. Potential applications of ficin in the production of traditional cheeses and protein hydrolysates. *JDS Communications*. 2021;2(5): 233–237. https://doi.org/10.3168/jdsc.2020-

33. Ebrahimian M., Hashemi M., Mahvelati F., Malaekeh-Nikouei B., Hashemi E., Oroojalian F. Bromelain loaded lipid-polymer hybrid nanoparticles for oral delivery: formulation and characterization. *Applied Biochemistry and Biotechnology*. 2022;194: 3733–3748. https://doi.org/10.1007/s12010-022-03812-z

34. Kumar R., Sharma N., Khurana N., Singh S. K., Satija S., Mehta M., Vyas M. Pharmacological evaluation of bromelain in mouse model of Alzheimer's disease. *NeuroToxicology*. 2022;90: 19–34. https://doi.org/10.1016/j.neuro.2022.02.009

35. Ma X., Chen Z., Li C., ... Lin F. Fabrication of immobilized bromelain using cobalt phosphate material prepared in deep eutectic solvent as carrier. *Colloids and Surfaces B: Biointerfaces*. 2022;210: 112251. https://doi.org/10.1016/j.colsurfb.2021.112251

36. Smirnova N. N., Pokryshkina A. S., Smirnov K. V. Immobilization of reactive dyes on the surface of ultrafiltration membranes based on poly-m-phenylenisophthalamide. *ChemChemTech*. 2022;65(1): 30–37. https://doi.org/10.6060/ivkkt.20226501.6378

37. Ol'shannikova S. S., Red'ko Y. A., Lavlinskaya M. S. Sorokin A. V., Holyvka M. G., Artyukhov V. G. Preparation of papain complexes with chitosan microparticles and evaluation of their stability using the enzyme activity level. *Pharmaceutical Chemistry Journal*. 2022;55: 1240–1244. https://doi.org/10.1007/s11094-022-02564-8

38. Sabirova A. R., Rudakova N. L., Balaban N. P., ... Sharipova M. R. A novel secreted metzincin metalloproteinase from Bacillus intermedius. *FEBS Letters*. 2010;584(21): 4419–4425. https://doi.org/10.1016/j.febslet.2010.09.049

Information about the authors

Svetlana S. Goncharova, Junior Researcher of the Department of Biophysics and Biotechnology, Voronezh State University (Voronezh, Russian Federation).

https://orcid.org/0000-0003-3381-2008
Olshannikovas@gmail.com

Ekaterina A. Shchegolevatykh, student of the Department of Biophysics and Biotechnology, Voronezh State University (Voronezh, Russian Federation).

https://orcid.org/0000-0002-6861-4776

Dmitry A. Zhukalin, Cand. Sci. (Phys.–Math.), Associate Professor of the Department of Physics of Semiconductors and Microelectronics, Voronezh State University (Voronezh, Russian Federation).

https://orcid.org/0000-0002-0754-4989
d.zhukalin@mail.ru

Marina G. Holyavka, Dr. Sci. (Biology), Professor, Department of Biophysics and Biotechnology, Voronezh State University (Voronezh, Russian Federation), Professor of Physics Department, Sevastopol State University (Sevastopol, Russian Federation).

https://orcid.org/0000-0002-1390-4119
holyavka@rambler.ru

Valery G. Artyukhov, Dr. Sci. (Biology), Professor, Head of the Biophysics and Biotechnology Department, Voronezh State University (Voronezh, Russian Federation)

artyukhov@bio.vsu.ru

Received 27.12.2023; approved after reviewing 07.03.2023; accepted for publication 15.04.2023; published online 25.09.2023.

Translated by Irina Charychanskaya

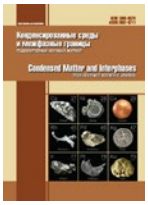

ISSN 1606-867X (Print)
ISSN 2687-0711 (Online)
Condensed Matter and Interphases
Kondensirovannye Sredy i Mezhfaznye Granitsy
https://journals.vsu.ru/kcmf/

Original articles

Research article
https://doi.org/10.17308/kcmf.2023.25/11258

Formation of plasmon-exciton nanostructures based on quantum dots and metal nanoparticles with a nonlinear optical response

A. I. Zvyagin✉, T. A. Chevychelova, A. S. Perepelitsa, M. S. Smirnov, O. V. Ovchinnikov

Voronezh State University,
1 Universitetskaya pl., Voronezh 394018, Russian Federation

Abstract

The establishment of the conditions for the formation of nanostructures with plasmon-exciton interaction based on quantum dots and plasmonic nanoparticles that provide unique nonlinear optical properties is an urgent task. The study demonstrates the formation of plasmon-exciton nanostructures based on hydrophilic colloidal $Zn_{0.5}Cd_{0.5}S$, Ag_2S quantum dots and metal nanoparticles.

Transmission electron microscopy and optical absorption and luminescence spectroscopy were used to substantiate the formation of plasmon-exciton hybrid nanostructures. The phase composition of the studied samples was determined by X-ray diffraction. The results obtained using ARLX'TRA diffractometer (Switzerland) indicated a cubic crystal structure ($F\bar{4}3m$) of synthesised $Zn_{0.5}Cd_{0.5}S$ quantum dots and monoclinic ($P2_1/C$) crystal lattice of Ag_2S. Transmission electron microscopy revealed that plasmonic nanoparticles are adsorption centres for quantum dots. The average sizes of the studied samples were determined: colloidal Ag_2S quantum dots (2.6 nm), $Zn_{0.5}Cd_{0.5}S$(2.0 nm) and metal nanoparticles: silver nanospheres (10 nm) and gold nanorods (4x25 nm). The transformation of the extinction spectra of the light and the luminescence quenching of quantum dots have been established in mixtures of quantum dots and plasmonic nanoparticles. The nonlinear optical parameters of the studied samples were determined using the Z-scanning method at wavelengths of 355 and 532 nm in the field of nanosecond laser pulses. The conditions for the formation of hybrid nanostructures that provide an increase of the coefficient of nonlinear absorption of laser pulses (355 and 532 nm) up to 9 times with a duration of 10 ns due to the reverse saturable absorption occurring due to cascade two-quantum transitions in the intrinsic and local states of colloidal quantum dots and the suppression of nonlinear refraction, were determined.

The observed changes were explained by the manifestation of the Purcell effect on the states of quantum dots in the presence of nanoresonators (gold nanorods and silver nanospheres). The results of these studies create new opportunities for the development of original systems for controlling the intensity of laser radiation, as well as quantum sensors of a new generation.

Keywords: Nonlinear refraction, Nonlinear absorption, Quantum dot, Ag_2S, $Zn_{0.5}Cd_{0.5}S$, Plasmonic nanoparticle, Z-scan

Funding: The study was supported by the grant of the President of the Russian Federation No. MK-4408.2022.1.2

Acknowledgments: the study of structural properties by transmission electron microscopy and X-ray diffraction were carried out using the equipment of the VSU Centre for Collective Use of Scientific Equipment.

For citation: Zvyagin A. I., Chevychelova T. A., Perepelitsa A. S., Ovchinnikov O. V., Smirnov M. S. Formation of plasmon-exciton nanostructures based on quantum dots and metal nanoparticles with a nonlinear optical response. *Condensed Matter and Interphases*. 2023;25(3): 350–358. https://doi.org/10.17308/kcmf.2023.25/11258

Для цитирования: Звягин А. И., Чевычелова Т. А., Перепелица А. С., Смирнов М. С., Овчинников О. В. Формирование плазмон-экситонных наноструктур на основе квантовых точек и наночастиц металлов с нелинейно-оптическим откликом. *Конденсированные среды и межфазные границы*. 2023;25(3): 350–358. https://doi.org/10.17308/kcmf.2023.25/11258

✉ Andrey I. Zvyagin, e-mail: andzv92@yandex.ru

1. Introduction

The creation of hybrid nanostructures with a "plasmon-exciton" interaction based on plasmonic nanoparticles (NPs) of noble metals, semiconductor quantum dots (QDs), and/or dye molecules recently became a promising and urgent task [1]. The properties of such nanostructures, which are not characteristic of individual components, primarily optical ones, and the problem of their prediction and control is especially topical are of interest. They are determined both by the composition and spectral resonances of the components and by the mechanisms of intermolecular interactions. The interaction between the components of such hybrid systems is manifested in the absorption and luminescence spectra of QDs and the extinction spectra of nanoparticles. In the case of luminescence, the manifestation of the interaction of components is often the signs of the exchange of electronic excitations between the components of the nanosystem [2–4], as well as the effects of plexiton coupling that occurs upon electronic excitation of the system [1, 5–7]. In the latter case, the tuning of the optical resonances of the structure components, e.g., the degree of their overlap, is of fundamental importance.

A separate problem in the physics of plasmon-exciton nanostructures is the establishment of the conditions for their formation, which provide a significant modification of the nonlinear optical properties of their components. Similar systems can be used for quantum sensorics. In a number of studies, the possibility of modifying/hybridising the nonlinear optical properties of dye molecules adsorbed on plasmonic nanoparticles was discovered [4, 8, 9]. In such hybrid nanostructures, the processes of transfer of electronic excitations provide changes in the nonlinear optical response. The interaction in mixtures of spherical gold nanoparticles and methylene blue dye enhances the reverse saturable absorption due to the Purcell effect, which manifests as an increase in the probability of triplet-triplet absorption of methylene blue [10]. The conditions for the formation of nanostructures with a plasmon-exciton interaction based on quantum dots and plasmonic nanoparticles, which provide unique nonlinear optical properties, still remain unclear. This study partially fills this gap and is devoted to establishing the laws governing the formation of plasmon-exciton nanostructures based on colloidal Ag_2S (2.6 nm), $Zn_{0.5}Cd_{0.5}S$ (2.0 nm) quantum dots, passivated with thioglycolic acid, and silver and gold nanoparticles, providing an 8–9-fold increase in nonlinear absorption in QDs.

2. Experimental

The studied samples were synthesised using the aqueous colloidal synthesis methods. In the synthesis of colloidal Ag_2S QDs, passivated with thioglycolic acid (TGA), the silver precursor was an aqueous solution of silver nitrate ($AgNO_3$). An aqueous solution of TGA was added to this solution with constant stirring, and the Ag-TGA complex was formed. As the pH of the solution increased to 11, the solution became clear. Next, an aqueous solution of Na_2S was added as a source of sulphur. Molar ratios of TGA/$AgNO_3$/Na_2S precursor were 2:1:0.5. $Zn_{0.5}Cd_{0.5}S$ QDs were synthesised in a similar way, except that the pH of the Zn(Cd)-TGA complex was increased to 7. For the removal of the reaction products after synthesis, QDs were precipitated by centrifugation with the addition of ethanol and redispersed in water.

Gold nanorods (Au NRs) were formed using multistage colloidal synthesis [11]. An aqueous solution of the surfactant cetyltrimethylammonium bromide (CTAB) was used for the growth of cylindrical NRs, being both a weak reducing agent and an anisotropic medium. Initially, a seed solution of gold nanospheres 3 nm in size was obtained by reducing aqueous chloroauric acid $HAuCl_4$ (7 µl, 0.36 mol) by $NaBH_4$ solution (1.0 ml, 5 mmol) in CTAB aqueous solution (20 ml, 0.02 mmol). The growth anisotropy of NPs was ensured by introducing a mixture of $HAuCl_4$ (28 µl, 0.36 mol), CTAB (50 ml, 0.1 mmol), $AgNO_3$ (0.1 ml, 0.02 mol) and $C_6H_8O_6$ (5 ml, 0.05 µmol). The addition of $AgNO_3$ contributes to the control of the length-to-diameter ratio of Au NRs.

The synthesis of silver nanoparticles of spherical geometry (Ag NP) is based on the successive reduction of silver nitrate $AgNO_3$ by sodium borohydride ($NaBH_4$) and stabilisation with sodium citrate ($Na_3C_6H_5O_7$) and hydrogen peroxide (H_2O_2). Potassium bromide (KBr) limits

the growth of silver nanoparticles, which leads to the production of nanospheres of a given size [12]. The prepared colloidal solutions of metal nanoparticles were purified from reaction products by washing with distilled water through several centrifugation-dispersion cycles. Mixtures of the studied samples were prepared by introducing a solution of metal nanoparticles into a QDs solution.

The size of the studied QDs and metal nanoparticles was determined using a Libra 120 transmission electron microscope (TEM) (Carl Zeiss, Germany) with an accelerating voltage of 120 kV. The phase composition of the studied samples was determined by X-ray diffraction; the results were obtained on an ARLX'TRA diffractometer (Switzerland) with the $K\alpha 1$ radiation of a copper line (1.54056 Å). Optical absorption and luminescence spectra were recorded using USB2000+ spectrometer (OceanOptics, USA) with a USB-DT radiation source (OceanOptics, USA). The luminescence decay kinetics of QDs was measured using a TimeHarp~260 module (PicoQuant, Germany) operating in the single photon counting mode. The detector was a PMT PMC-100-20 (Becker&Hickl Germany) with a time resolution of 0.2 ns. The luminescence decay curves were approximated by the theoretical curve using the deconvolution procedure with the experimentally measured instrument response function.

Analysis of the nonlinear optical response of the studied samples was performed using the Z-scan method [13]. This method is based on measuring the normalised transmission of the test sample as it moves relative to the focal plane of a converging lens along the optical z axis. The normalised transmittance was determined as the ratio of the sample transmittance T(z) at the point with coordinate z to the sample transmittance in the linear mode at low intensity, which is recorded far from the lens focus $T(z \to \infty)$. In this method, the transmission of the sample was measured under the condition of different transverse dimensions of the Gaussian beam (different intensities). In other words, when changing the z coordinate, the scanning according to the laser radiation intensity was actually carried out.

We used the radiation of the third and second harmonics of YAG:Nd^{3+} laser (LS-2132UTF, LOTIS TII) with a wavelength of 355 and 532 nm, respectively, a duration of 10 ns and a repetition rate of 1 Hz. The radiation was focused by a spherical lens with a focal length of 300 mm. Quartz cuvettes with the thickness of 5 mm containing the studied samples were moved along the optical z axis of the probing laser pulse through the focal plane of the collecting lens using a linear translator. The waist radius was ~30 μm. The measurements were carried out using pulse energies of 1.33 mJ (355 nm) and 0.16 mJ (532 nm).

3. Results and discussion

TEM images of the initial components and their mixtures are shown in Fig. 1. It can be seen

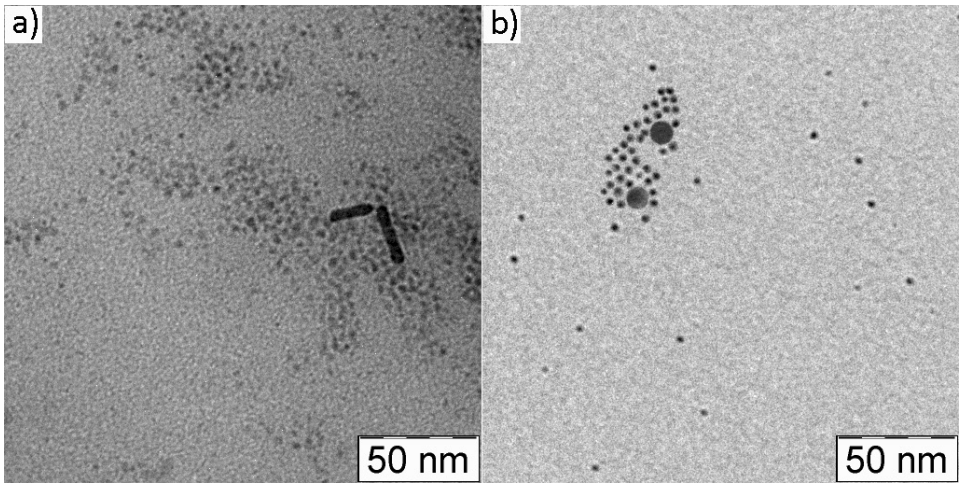

Fig. 1. TEM images of synthesised Ag_2S QDs conjugated with gold nanorods (a), $Zn_{0.5}Cd_{0.5}S$ QDs conjugated with silver nanospheres (b)

from Fig. 1a. individual QDs of Ag_2S with an average size of 2.6 nm with a size dispersion of 20–30% were formed within the framework of the used approaches to synthesis. The resulting gold nanoparticles were nanorods with an average size of 4×25 nm (Fig. 1a). According to TEM images, $Zn_{0.5}Cd_{0.5}S$ QDs had an average ensemble size of 2.0 nm at the same dispersion (Fig. 1b). Silver nanoparticles Ag NPs of spherical geometry had an average size of 10 nm. According to X-ray diffraction data, it was possible to establish a cubic crystal structure ($F\bar{4}3m$) for $Zn_{0.5}Cd_{0.5}S$ QDs (Fig. 2a). The diffraction pattern of Ag_2S QDs was a system of broadened reflections against the background of a noticeable halo, corresponding to the monoclinic ($P2_1/C$) Ag_2S crystal lattice (Fig. 2a). Figure 2b shows X-ray diffraction patterns of Ag and Au nanoparticles. The diffraction peaks at 38, 44, 64, and 77° corresponded to the (111), (200), (220), and (311) planes of the face-centred cubic crystal lattice. It has been found that plasmonic nanoparticles are adsorption centres for quantum dots. The TEM images showed the largest accumulation of QDs near Au NRs and Ag NPs (Fig. 1). Thus, it has been established that the approaches used for the synthesis of mixtures of QDs of metal nanoparticles ensure the compatibility of the components in the formation of hybrid structures.

Optical absorption spectra of colloidal solutions of Ag_2S QDs were broad bands with an exciton peak at 810 nm (1.53) eV (Fig. 3a, black curve), which was due to the quantum size effect, since the band gap of bulk Ag_2S crystals is 1.0 eV. Luminescence spectrum of Ag_2S QDs was a broad band with a peak at 881 nm (Fig. 3b, black curve).

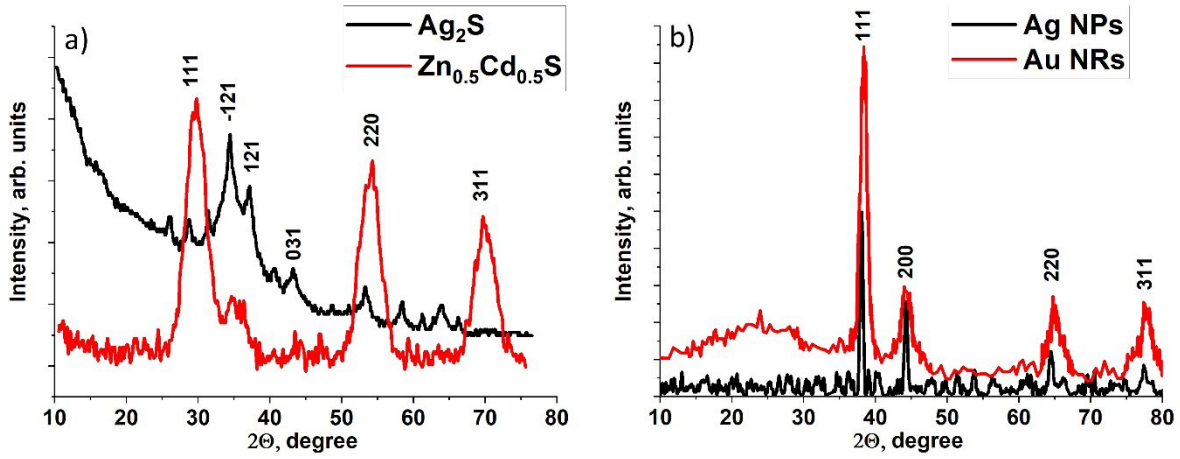

Fig. 2. X-ray diffraction obtained on Ag_2S and $Zn_{0.5}Cd_{0.5}S$ QDs (a) and silver and gold nanoparticles

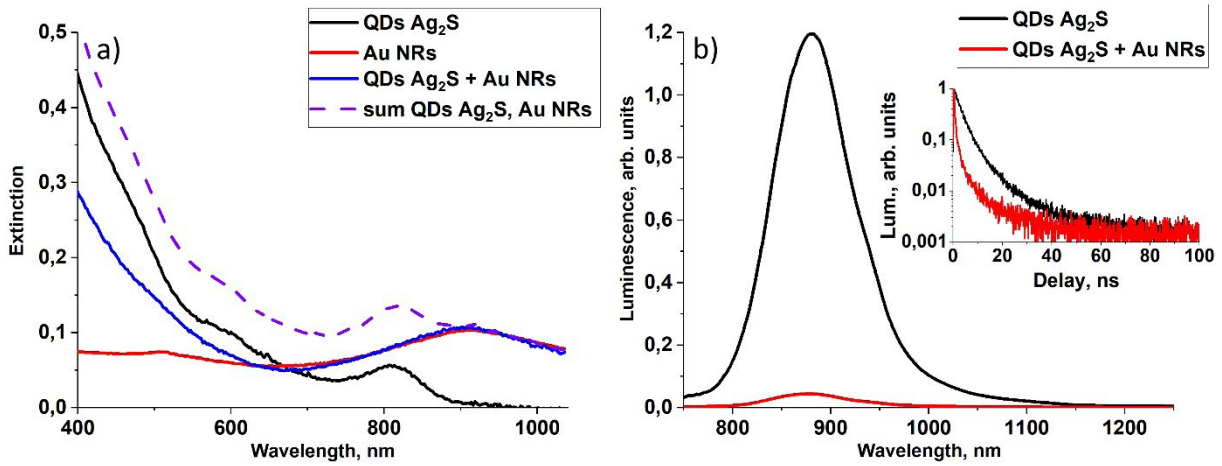

Fig. 3. Light extinction spectra of synthesised Ag_2S QDs, Au NRs and their mixtures (a) and luminescence spectra of Ag_2S QDs and their mixtures with Au NRs (b). The inset shows the luminescence decay kinetics of the studied samples

The light extinction spectrum of Au NRs consisted of two broad bands with peaks at 523 and 910 nm (Fig. 3a, red curve). The short-wavelength band is determined by the transverse plasmon resonance in Au NRs, while the long-wavelength band was determined by the longitudinal one [14]. Thus, the peak of the longitudinal plasmon resonance of Au NRs coincided with the luminescence band of Ag_2S QDs.

Such tuning of resonances in the extinction of light and luminescence of nanostructures suggests the possibility of the exchange of electronic excitations between the components of the nanosystem. In the extinction spectra of mixtures of Ag_2S QDs and Au NRs hybrid association was manifested as the disappearance of the feature associated with exciton absorption in Ag_2S QDs, and a decrease in the extinction of two components in the region of 400–600 nm (Fig. 3a, blue curve). The resulting extinction spectrum is not the sum of the extinction spectra of the components of the hybrid associate (Fig. 3a, purple curve), which indirectly indicated the manifestation of interaction in the resulting mixture [15–20]. Luminescence spectrum of Ag_2S QDs in the presence of gold nanorods demonstrates a decrease in the luminescence intensity by 27 times (Fig. 3b, red curve). It should be noted that this quenching cannot be explained by the filter effect alone. Approximation of the luminescence decay kinetics (Fig. 3b, inset) allowed to determine the luminescence decay time. Pure Ag_2S QDs showed an average luminescence decay time of 5.2 ns, while for a mixture with gold nanorods it was 1.5 ns, i.e., 3.5 times lower. Luminescence quenching, accompanied by a reduction in the luminescence decay time, indicated a resonant nonradiative transfer of excitation energy from radiative recombination centres to plasmonic nanoparticles as a result of plasmon–exciton interaction. In this case, there were no characteristic features of the manifestation of the Purcell effect in Ag_2S QDs in the presence of Au NRs.

In the absorption spectrum of $Zn_{0.5}Cd_{0.5}S$ QDs, a peculiarity in absorption associated with the most probable transition at a wavelength of 341 nm was observed. The extinction spectrum of Ag NPs had a plasmon resonance peak with a maximum at 400 nm (Fig. 4a). When pairing these nanostructures, an increase in the extinction of the mixture was observed in the wavelength range of 380–600 nm. Luminescence spectrum of $Zn_{0.5}Cd_{0.5}S$ QDs was a broad band peaking at 480 nm. A significant Stokes shift of 1 eV relative to the exciton absorption peak indicates the recombination nature of the luminescence. When the data for QDs were paired with Ag NPs, luminescence quenching by 2 times was observed (Fig. 4b) and the luminescence kinetics accelerated from 446 to 348 ns. Quenching of the luminescence, acceleration of the kinetics, and change in the extinction of the obtained nanostructure indicated a resonant nonradiative transfer of the excitation energy from the QDs to the plasmonic nanoparticle.

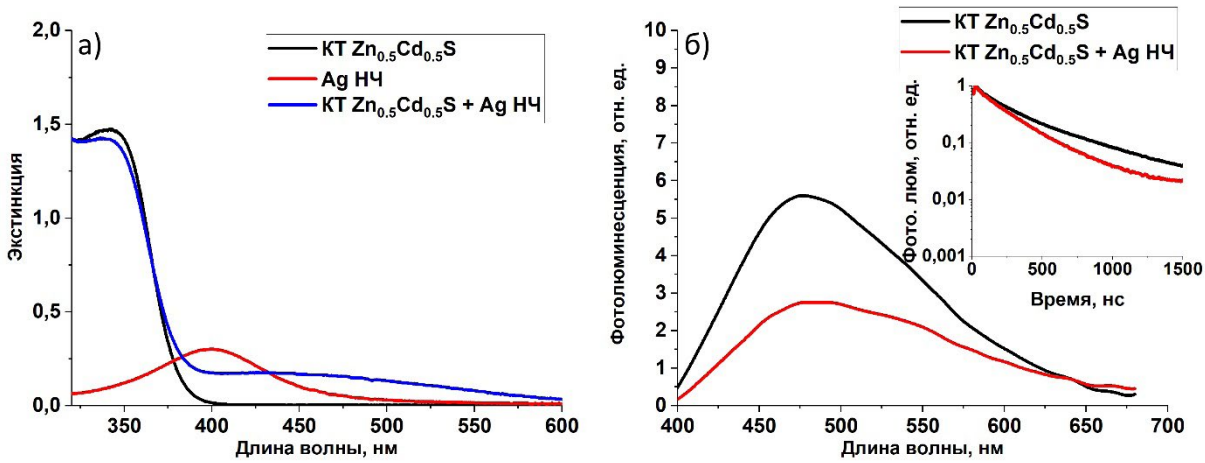

Fig. 4. Extinction spectra of synthesised $Zn_{0.5}Cd_{0.5}S$ QDs, Ag NPs, and their mixtures (a) and luminescence spectra of $Zn_{0.5}Cd_{0.5}S$ QDs, Ag NPs (b). The inset shows the luminescence decay kinetics of the studied samples

We will consider the nonlinear optical properties of the studied samples. The obtained Z-scans of the initial components and the hybrid nanostructure based on Ag_2S QDs, Au NRs are shown in Fig. 5a. There was a noticeable increase in the nonlinear absorption upon association of Ag_2S QDs, Au NRs compared to the original QDs (dip in the focal plane of the converging lens at z = 0). A colloidal solution of pure Au NRs did not show a nonlinear optical response under our experimental conditions (Fig. 5a, blue straight line). Z-scan of Ag_2S QDs obtained in closed-aperture geometry demonstrate defocusing of laser radiation, which is suppressed upon association with gold nanorods.

In the case of probing with laser pulses with a wavelength of 355 nm, $Zn_{0.5}Cd_{0.5}S$ QDs, Ag NPs, a picture similar to the previous result was observed. Significant increase in nonlinear absorption was observed, when $Zn_{0.5}Cd_{0.5}S$ QDs and Ag NPs were coupled. This pattern was not a manifestation of the sum of effects in the nonlinear optical response, since no useful signal was found in the study of metal nanoparticles, and quantum dots had a significantly lower nonlinear absorption (a dip in the focal plane in the Z-scan).

For further consideration of the above picture, it is worth referring to the nonlinearity mechanisms in the studied structures. For Ag_2S and $Zn_{0.5}Cd_{0.5}S$ quantum dots are characterised by the nonlinear refraction of laser radiation. The defocusing of laser radiation arises due to the band filling effect [21, 22]. The filling of localised states is redistributed under the action of laser pulses on colloidal QDs, which in turn will lead to a change in the refractive index of the colloidal solution in accordance with the Kramers–Kroning relations [13]. The mechanism of nonlinear absorption in this case is the reverse saturable absorption on real states, which are traps (broken bonds on the QDs surface and structural defects) and/or luminescence centres. This was confirmed by the results of our studies [23–25]. Noble metal nanoparticles are characterised by bleaching of plasmon resonances in the field of femtosecond pulses, dynamic scattering, and photodestruction in the field of picosecond and nanosecond pulses [26]. In our experiments, the contribution of the dynamic scattering into the nonlinear optical response is low, as was experimentally confirmed by recording the signal on an additional photodiode located at an angle to the optical axis of the converging lens during Z-scanning. The absence of dynamic scattering was determined by the weak extinction of Au NRs solutions at the probing wavelength and the low energy of laser pulses.

Thus, an increase in nonlinear absorption was observed upon conjugation of QDs and plasmonic nanoparticles. The experimentally obtained Z-scans were approximated by the expression

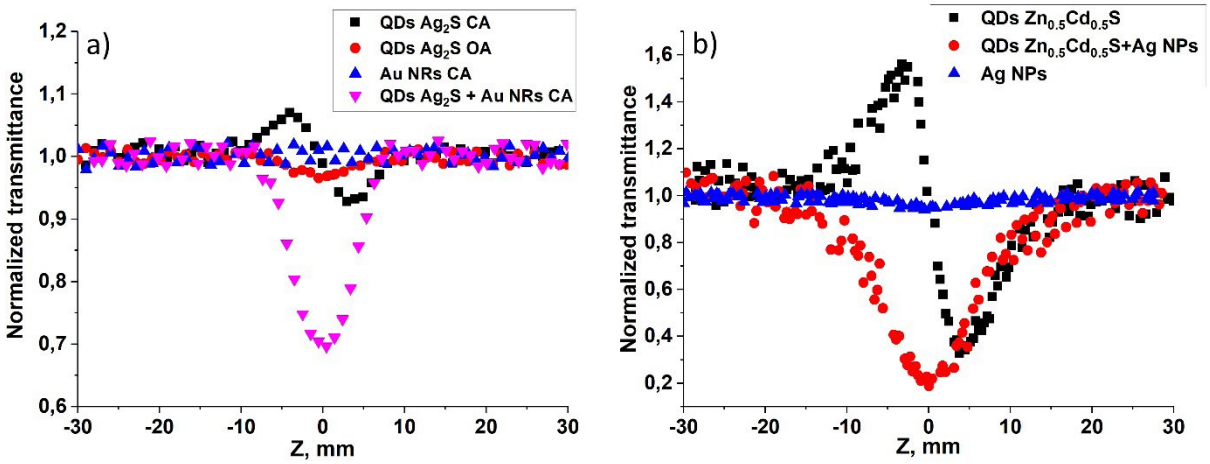

Fig. 5. Z-scan curves of the investigated Ag_2S QDs samples, Au NRs and their mixtures in the field of laser pulses with a wavelength of 532 nm, a duration of 10 ns and a pulse energy of 0.16 mJ, obtained in open (OA) and closed (CA) aperture geometry (a). Z-scan curves of the investigated $Zn_{0.5}Cd_{0.5}S$ QDs, Ag NPs samples and their mixtures in the field of laser pulses with a wavelength of 355 nm, a duration of 10 ns, and pulse energy of 1.33 mJ obtained in a geometry with a closed aperture

given in [27], which allowed to determine the coefficients of nonlinear absorption and nonlinear refraction. Nonlinear refraction coefficient of Ag_2S QDs was $-2.5\cdot10^{-15}$ $cm^2\cdot W^{-1}$, non-linear absorption coefficient – $8\cdot10^{-11}$ $cm\cdot W^{-1}$. Nonlinear absorption coefficient of Ag_2S QDs and Au NRs mixture and was $7\cdot10^{-10}$ $cm\cdot W^{-1}$, which was 8.5 times higher than that of pure Ag_2S QDs. In the case of $Zn_{0.5}Cd_{0.5}S$ QDs non-linear refraction coefficient was $-1\cdot10^{-15}$ $cm^2\cdot W^{-1}$, nonlinear absorption coefficient was $1.4\cdot10^{-11}$ $cm\cdot W^{-1}$. Conjugation with silver nanospheres led to an increase in the nonlinear absorption coefficient up to $1.3\cdot10^{-10}$ $cm\cdot W^{-1}$, i.e., by 9.3 times compared to pure $Zn_{0.5}Cd_{0.5}S$ QDs. This increase in nonlinear absorption can be explained by an increase in reverse saturable absorption occurring as a result of cascade two-quantum transitions in the intrinsic and local states of colloidal quantum dots in the presence of plasmonic metal nanoparticles due to resonant non-radiative energy transfer resulted from plasmon-exciton interaction.

4. Conclusion

Substantiation of the formation of nanostructures with plasmon-exciton interaction based on $Zn_{0.5}Cd_{0.5}S$, Ag_2S quantum dots and silver and gold nanoparticles of spherical and cylindrical shape, respectively was performed using transmission electron microscopy and absorption and luminescence spectroscopy. The studied samples were selected taking into account different settings of optical resonances in absorption, luminescence of QDs, and extinction of metal nanoparticles. Experimental confirmation of the formation of hybrid plasmon-exciton nanostructures was the analysis of TEM images showing the adsorption of QDs on metal nanoparticles, as well as the transformation of the light extinction spectra of the mixture of QDs and NPs. The quenching of the QDs luminescence and the acceleration of its kinetics also indicated an interaction sufficient for resonant non radiative transfer of the electronic excitation energy from the recombination luminescence centres of QDs to plasmonic nanoparticles. For Ag_2S QDs and cylindrical gold nanoparticles mixture and $Zn_{0.5}Cd_{0.5}S$ QDs with silver nanoparticles mixture in the pulsed laser field with a wavelength of 355 nm, an increase in the nonlinear absorption coefficient of QDs in the presence of plasmonic metal nanoparticles up to 9 times was established using Z-scan method in the field of nanosecond laser pulses with a wavelength of 532 nm. The results of these studies create new opportunities for the development of original systems for controlling the intensity of laser radiation, as well as quantum sensors of a new generation.

Author contributions

A. I. Zvyagin – conducting scientific research, writing of the article, scientific editing of the text. T. A. Chevychelova – conducting scientific research. A. S. Perepelitsa – conducting scientific research. M. S. Smirnov – scientific editing of the text, discussion of the results of the study. O. V. Ovchinnikov – scientific editing of the text, discussion of the results of the study.

Conflict of interests

The authors declare that they have no known competing financial interests or personal relationships that could have influenced the work reported in this paper.

References

1. Cao E., Lin W., Sun M., Liang W., Song Yi. Exciton-plasmon coupling interactions: from principle to applications. *Nanophotonics*. 2018;7(1): 145–167. https://doi.org/10.1515/nanoph-2017-0059

2. Ke L., Katsnelson M. I. Electron correlation effects on exchange interactions and spin excitations in 2D van der Waals materials. *npj Computational Materials*. 2021;7(4): 1–8. https://doi.org/10.1038/s41524-020-00469-2

3. De Vera P., Abril I., Garcia-Molina R. Excitation and ionisation cross-sections in condensed-phase biomaterials by electrons down to very low energy: application to liquid water and genetic building blocks. *Physical Chemistry Chemical Physics*. 2021;23: 5079–5095. https://doi.org/10.1039/d0cp04951d

4. Yadav R. K., Aneesh J., Sharma R., ... Adarsh K. V. Designing hybrids of graphene oxide and gold nanoparticles for nonlinear optical response. *Physical Revied Applied*. 2008;9(4): 044043(10). https://doi.org/10.1103/PhysRevApplied.9.044043

5. Davoodi F., Talebi N. Plasmon-exciton interactions in nanometer-thick gold-WSe_2 multilayer structures: implications for photodetectors, sensors, and light-emitting devices. *ACS Applied Nano Materials*. 2021;4(6): 6067–6074. https://doi.org/10.1021/acsanm.1c00889

6. Kholmicheva N., Royo Romero L., Cassidy J., Zamkov M. Prospects and applications of plasmon-

exciton interactions in the near-field regime. *Nanophotonics*. 2019;8(4): 613–628. https://doi.org/10.1515/nanoph-2018-0143

7. Hu S., Ren Y., Wang Y., ... Tang Y. Surface plasmon resonance enhancement of photoluminescence intensity and bioimaging application of gold nanorod@CdSe/ZnS quantum dots. *Beilstein Journal of Nanotechnology*, 2019;10: 22–31. https://doi.org/10.3762/bjnano.10.3

8. Danilov V. V., Panfutova A. S., Khrebtov A. I., Ambrosini S., Videnichev D. A. Optical limiting as result a of photoinduced electron transfer in hybrid systems with CdSe/ZnS quantum dots, C60, and Perylene. *Optics Letters*. 2012;37(19): 3948–3950. https://doi.org/10.1364/OL.37.003948

9. Zvyagin A. I., Perepelitsa A. S., Ovchinnikov O. V., Smirnov M. S., Ganeev R. A. Nonlinear optical properties of associates of erythrosine molecules and gold nanoparticles. *Materials Research Express*. 2019;6: 1150c8. https://doi.org/10.1088/2053-1591/ab4e2a

10. Ovchinnikov O. V., Smirnov M. S., Chevychelova T. A., Zvyagin A. I., Selyukov A. S. Nonlinear absorption enhancement of Methylene Blue in the presence of Au/SiO_2 core/shell nanoparticles. *Dyes and Pigments*. 2022;197: 109829. https://doi.org/10.1016/j.dyepig.2021.109829

11. Jana N. R., Gearheart L., Murphy C. J. Seed-mediated growtha for shape-controlled synthesis of spheroidal and rod-like gold nanoparticles using a surfactant template. *Advanced Materials*. 2001;13(18): 1389–1393. https://doi.org/10.1002/1521-4095(200109)13:18<1389::aid-adma1389>3.0.co;2-f

12. Frank A. J., Cathcart N., Maly K. E., Kitaev V. Synthesis of silver nanoprisms with variable size and investigation of their optical properties: a first-year undergraduate experiment exploring plasmonic nanoparticles. *Journal of Chemical Education*, 2010;87(10): 1098–1101. https://doi.org/10.1021/ed100166g

13. Sheik-Bahae M., Hutchings D. C., Hagan D. J., Van Stryland E. W. Dispersion of bound electron nonlinear refraction in solids. *IEEE Journal of Quantum Electronics*. 1991;27: 1296-1309, https://doi.org/10.1109/3.89946

14. Amendola V., Pilot R., Frasconi M., Marago O. M, Iati M. A. Surface plasmon resonance in gold nanoparticles: a review. *Journal of Physics: Condensed Matter*. 2017;29: 203002(48). https://doi.org/10.1088/1361-648X/aa60f3

15. Grevtseva I. G., Chevychelova T. A., Derepko V. N., Ovchinnikov O. V., Smirnov M. S., Perepelitsa A. S., Parshina A. S. Spectral manifestations of the exciton-plasmon interaction of Ag_2S quantum dots with silver and gold nanoparticles. *Condensed Matter and Interphases*. 2021;23(1): 25–31. https://doi.org/10.17308/kcmf.2021.23/3294

16. Daniel M. C., Astruc D. Gold nanoparticles: assembly, supramolecular chemistry, quantum-size-related properties, and applications toward biology, catalysis, and nanotechnology. *Chemical Reviews*. 2004;104(1): 293–346. https://doi.org/10.1021/cr030698+

17. Durach M., Rusina A., Stockman M. I., Nelson K. Toward full spatiotemporal control on the nanoscale. *Nano Letters*. 2007;7(10): 3145–3149. https://doi.org/10.1021/nl071718g

18. Komarala V. K., Rakovich Yu. P., Bradley A. L. Off-resonance surface plasmon enhanced spontaneous emission from CdTe quantum dots. *Applied Physics Letters*. 2006;89(25): 253118. https://doi.org/10.1063/1.2422906

19. Gong H. M., Wang X. H., Du Y. M., Wang Q. Q. Optical nonlinear absorption and refraction of CdS and CdS-Ag core-shell quantum dots. *The Journal of Chemical Physics*. 2006;125(2): 024707. https://doi.org/10.1063/1.2212400

20. Ovchinnikov O. V., Smirnov M. S., Grevtseva I. G., ... Kondratenko T. S. Luminescent properties of colloidal mixtures of $Zn_{0.5}Cd_{0.5}S$ quantum dots and gold nanoparticles. *Condensed Matter and Interphases*. 2021;23(1): 49–55. https://doi.org/10.17308/kcmf.2021.23/3302

21. Ganeev R. A., Ryasnyansky A. I., Tugushev R. I., Usmanov T. Investigation of nonlinear refraction and nonlinear absorption of semiconductor nanoparticle solutions prepared by laser ablation. *Journal of Optics A: Pure and Applied Optics* 2003;5(4): 409–417. https://doi.org/10.1088/1464-4258/5/4/317

22. Chang Q., Gao Y., Liu X., Chang C. Nonlinear properties of water-soluble Ag_2S and PbS quantum dots under picosecond laser pulses. *IOP Conference Series: Earth and Environmental Science*. 2018;186(4): 012076. https://doi.org/10.1088/1755-1315/186/4/012076

23. Kondratenko T. S., Zvyagin A. I., Smirnov M. S., Grevtseva I. G., Perepelitsa A. S., Ovchinnikov O. V. Luminescence and nonlinear optical properties of colloidal Ag_2S quantum dots. *Journal of Luminescence*. 2019;208: 193–200. https://doi.org/10.1016/j.jlumin.2018.12.042

24. Zvyagin A. I., Chevychelova T. A., Chirkov K. S., Smirnov M. S., Ovchinnikov O. V. Nonlinear optical properties of colloidal PbS and Ag_2S quantum dots passivated with 2-mercaptopropionic acid. *Bulletin of the Russian Academy of Sciences: Physics*. 2022;86: 1183–1187. https://doi.org/10.3103/S1062873822100264

25. Smirnov M. S., Ovchinnikov O. V., Zvyagin A. I., ... Pham H. M. Transient absorption dynamics and nonlinear optical response in colloidal Ag_2S quantum dots. *Optics and Spectroscopy*. 2022;130(3): 224–231. https://doi.org/10.1134/S0030400X22030146

26. Chevychelova T. A., Zvyagin A. I., Perepelitsa A. S., Ovchinnikov O. V., Smirnov M. S., Selyukov A. S. Role of photoinduced destruction of gold nanorods in the formation of nonlinear optical response. *Optik*. 2022;250(2): 168352, https://doi.org/10.1016/j.ijleo.2021.168352

27. Liu X., Guo S., Wang H., Hou L. Theoretical study on the closed-aperture Z-scan curves in the materials with nonlinear refraction and strong nonlinear absorption. *Optics Communications*. 2001;197(4-6): 431–437. https://doi.org/10.1016/s0030-4018(01)01406-7

Information about the authors

Andrey I. Zvyagin, Cand. Sci. (Phys.–Math.), Lecturer, Department of Optics and Spectroscopy, Voronezh State University (Voronezh, Russian Federation).

https://orcid.org/0000-0002-1914-9054
andzv92@yandex.ru

Tamara A. Chevychelova, postgraduate student, Department of Optics and Spectroscopy, Voronezh State University (Voronezh, Russian Federation).

https://orcid.org/0000-0001-8097-0688
tamarachevychelova@yandex.ru

Aleksey S. Perepelitsa, Cand. Sci. (Phys.–Math.), Associate Professor at the Department of Optics and Spectroscopy, Voronezh State University (Voronezh, Russian Federation).

https://orcid.org/0000-0002-1264-0107
a-perepelitsa@yandex.ru

Mikhail S. Smirnov, Dr. Sci. (Phys.–Math.), Associate Professor, Department of Optics and Spectroscopy, Voronezh State University (Voronezh, Russian Federation).

https://orcid.org/0000-0001-8765-0986
smirnov_m_s@mail.ru

Oleg V. Ovchinnikov, Dr. Sci. (Phys.–Math.), Full Professor, Dean of the Faculty of Physics, Head of the Department of Optics and Spectroscopy, Voronezh State University (Voronezh, Russian Federation).

https://orcid.org/0000-0001-6032-9295
ovchinnikov_o_v@rambler.ru

Received 07.12.2022; approved after reviewing 21.12.2022; accepted for publication 26.12.2022; published online 25.09.2023.

Translated by Valentina Mittova

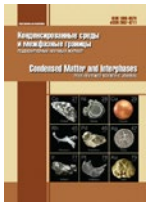

ISSN 1606-867X (Print)
ISSN 2687-0711 (Online)
Condensed Matter and Interphases
Kondensirovannye Sredy i Mezhfaznye Granitsy
https://journals.vsu.ru/kcmf/

Original articles

Research article
https://doi.org/10.17308/kcmf.2023.25/11259

Structure and composition of a composite of porous silicon with deposited copper

A. S. Lenshin[1,2]✉, K. B. Kim[2], B. L. Agapov[1], V. M. Kashkarov[1], A. N. Lukin[1], S. I. Niftaliyev[2]

[1]*Voronezh State University,*
1 Universitetskaya pl., Voronezh 394018, Russian Federation

[2]*Voronezh State University of Engineering Technologies,*
Revolution Avenue, 19, Voronezh 394036, Russian Federation

Abstract

Porous silicon is a promising nanomaterial for optoelectronics and sensorics, as it has a large specific surface area and is photoluminescent under visible light. The deposition of copper particles on the surface of porous silicon will greatly expand the range of applications of the resulting nanocomposites. Copper was chosen due to its low electrical resistivity and high resistance to electromigration compared to other metals. The purpose of this research was to study changes in the structure and composition of porous silicon after the chemical deposition of copper.

Porous silicon was obtained by the anodisation of monocrystalline silicon wafers KEF (100) (electronic-grade phosphorus-doped silicon) with an electrical resistivity of 0.2 Ohm·cm. An HF solution in isopropyl alcohol with the addition of H_2O_2 solution was used to etch the silicon wafers. The porosity of the samples was about 70 %. The porous silicon samples were immersed in copper sulphate solution ($CuSO_4 \cdot 5H_2O$) for 7 days. We used scanning electron microscopy, IR spectroscopy, and ultrasoft X-ray emission spectroscopy to obtain data on the morphology and composition of the initial sample and the sample with deposited copper. The chemical deposition of copper on porous silicon showed a significant distortion of the pore shape as well as the formation of large cavities inside the porous layer. However, in the lower part the pore morphology remained the same as in the original sample. It was found that the chemical deposition of copper on porous silicon leads to copper penetrating into the porous layer, the formation of a composite structure, and it prevents the oxidation of the porous layer during storage. Thus, it was demonstrated that the chemical deposition of copper on a porous silicon surface leads to visible changes in the surface morphology and composition. Therefore, it should have a significant impact on the catalytic, electrical, and optical properties of the material.

Keywords: Porous silicon, Composites, Copper, Ultrasoft X-ray emission Spectroscopy, Electronic structure

Funding: The study was supported by the Russian Foundation for Basic Research, project No. 22-73-0154.

For citation: Lenshin A. S., Kim K. B., Agapov B. L., Kashkarov V. M., Lukin A. N., Niftaliev S. I. Structure and composition of a composite of porous silicon with deposited copper. *Condensed Matter and Interphases*. 2023;25(3): 359–366. https://doi.org/10.17308/kcmf.2023.25/11259

Для цитирования: Леньшин А. С., Ким К. Б., Агапов Б. Л., Кашкаров В. М., Лукин А. Н., Нифталиев С. И. Строение и состав композита пористого кремния с осажденной медью. *Конденсированные среды и межфазные границы*. 2023;25(3): 359–366. https://doi.org/10.17308/kcmf.2023.25/11259

✉ Alexander S. Lenshin, e-mail: lenshinas@phys.vsu.ru

1. Introduction

Nowadays, the demand for nanostructured and nanoscale systems is increasing significantly [1–2], as they are widely used in microelectronics and optoelectronics [3–8], as well as in medicine and chemistry [9–11]. One of the most common nanomaterials used in modern industry and science is porous silicon (por-Si) [12–15]. Porous silicon is a material obtained by anodising monocrystalline silicon. Depending on the properties of the original silicon wafer and the anodisation process parameters, por-Si can have different morphology and different optical and electrophysical characteristics [16–18]. Various electrolytic cell configurations are used to produce por-Si [19–21]. In contrast to bulk silicon, porous silicon exhibits a number of properties such as a high specific surface area, photo- and electroluminescence, and biocompatibility. Due to these unique properties, por-Si can be successfully applied in optoelectronics, micromechanical systems, and biomedicine. Recently, the deposition of metals on porous silicon has been extensively studied, which will greatly expand the application of the resulting composite material [22–25].

It is known that copper has a lower electrical resistivity and has a higher electromigration immunity compared to aluminium [26], which may be of use in electroluminescence and gas sensors.

In study [27], porous silicon with electrochemically deposited copper particles was successfully applied as a photodetector. The authors of [28] obtained samples of porous silicon with Cu particles which exhibited infrared luminescence bands with peaks at 660.6 and 802.2 nm. Also, por-Si with deposited Cu particles is used as a sensor showing high catalytic activity, reproducibility, wide range of study, as well as stability of operation [29, 30]. When porous silicon doped with copper particles is used as a gas sensor for phosphine detection, the sensitivity is 5 times better than that of its counterparts [31].

There are various methods of copper deposition on porous silicon: vacuum evaporation, electrodeposition, chemical deposition, and immersion plating. The advantage of the chemical deposition of copper is the deep penetration of metal atoms into the pores [32]. In addition, this method is simple and inexpensive.

The choice of the method of film deposition on porous silicon is largely determined by the requirements for the resulting material. In turn, the mechanical, chemical, and physical properties of the films depend on the microstructural characteristics of por-Si: pore size and distribution, texture, etc.

Thus, the aim of this research was to study the change in the structure and composition of porous silicon after chemical deposition of copper.

2. Experimental

Porous silicon samples were produced from monocrystalline silicon wafers (electronic-grade phosphorus-doped silicon, orientation 100, and resistivity of 0.2 Ohm·cm) by electrochemical anodisation in an electrolyte based on hydrofluoric acid [33]. Then, the samples were immersed in a colloidal $CuSO_4 \cdot 5H_2O$ solution (C = 0.1 mol/dm^3) for 7 days (at room temperature, in low light) [34]. The pH of the solution, at which copper was deposited, was 3–3.5. Next, the samples were washed in isopropanol and stored under laboratory conditions in sealed polyethylene bags.

A comparative analysis of the pore size and the thickness of the porous layer of the original sample and the resulting sample was carried out by scanning electron microscopy (JSM-6380LV microscope with microanalysis unit).

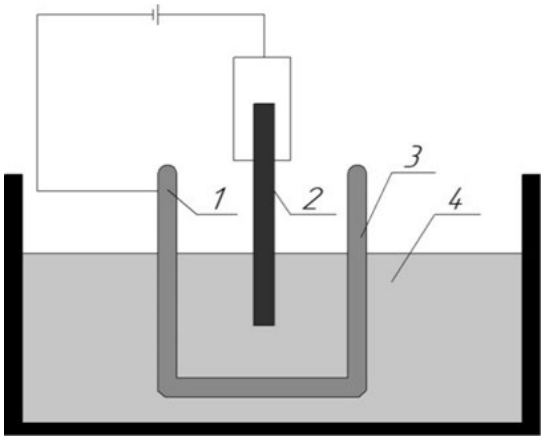

Fig. 1. Scheme of electrochemical etching of porous silicon samples: 1 - cathode, 2 - anode, 3 - stainless steel electrode, and 4 - electrolyte solution

The electronic structural features and phase composition of the initial sample of porous silicon and the resulting sample containing metal were determined by ultrasoft X-ray emission spectroscopy (USXES). The Si $L_{2,3}$ spectra of porous silicon samples were obtained using an RSM-500 X-ray spectrometer-monochromator, which allows the study of spectra in the wavelength range from 0.5 to 50 nm. The analysis depth was 20 nm, at an electron energy of 1.5 keV exciting the X-rays. The USXES spectra were modelled by weighting coefficients using custom-made software. When modelling the Si $L_{2,3}$ spectra of por-Si samples, we used reference spectra of monocrystalline silicon c-Si, amorphous hydrogenated silicon a-Si:H, low-coordinated silicon Si_{lc}, silicon suboxide SiO_x (x ~ 1.3), and silicon dioxide SiO_2 [35–36]. The modelling error was defined as the difference between the areas under the experimental and modelled Si $L_{2,3}$ spectrum that did not exceed 10%. The tests were carried out two weeks after the samples were prepared.

In order to obtain data on the chemical bonds and their possible deformations on the surface of the por-Si samples, IR spectroscopy was carried out. IR transmission spectra of porous silicon samples were obtained using a Vertex 70 FTIR spectrometer (Bruker) with an ATR unit. All tests were performed one month after the samples were prepared.

3. Results and discussion

Fig. 2 shows the SEM images of the cleavages of the original porous silicon and the samples with chemically deposited copper. The average pore diameter in porous silicon is ~100–150 nm, which is typical for por-Si obtained by the previously described method. Image analysis shows that the pore shape was distorted by the chemical deposition of copper on porous silicon. Inside porous silicon, cavities up to 4–5 μm high were formed, which is approximately half the height of the original sample (~10 μm). There is no apparent change in the lower part, and the predominant orientation (100) perpendicular to the surface is retained.

To confirm the presence of copper in the porous layer, an energy dispersive microanalysis of the sample cleavages was carried out (Fig. 2). It showed the presence of ~10 at. % of copper (light inclusions). Similar results were obtained earlier during tin deposition [37]. The nucleation and growth of copper inclusions can be explained mainly by physical adsorption onto a substrate with a sufficiently high specific surface area.

The USXES Si $L_{2,3}$ surface spectra of the samples are shown in Fig. 3. Modelling results using the reference sample spectra showed that the porous silicon samples with deposited copper differ significantly in their phase composition from the original porous silicon. The surface layer of the original porous silicon contains crystalline and

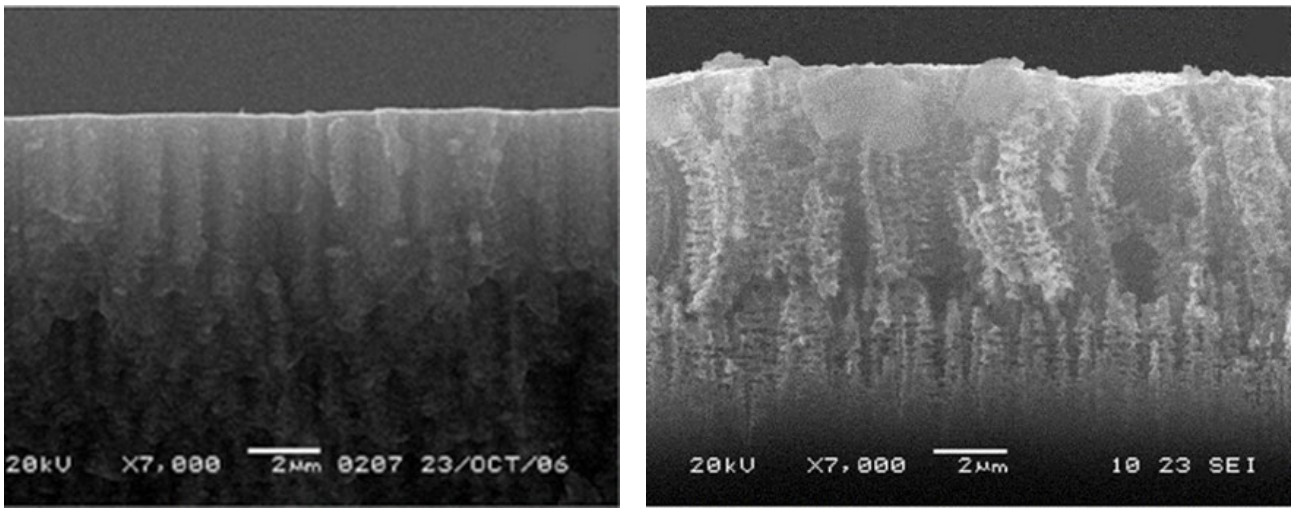

a b

Fig. 2. SEM images of the porous silicon cleavage with nanoparticle inclusions: a: original porous silicon, b: porous silicon with deposited Cu (light inclusions)

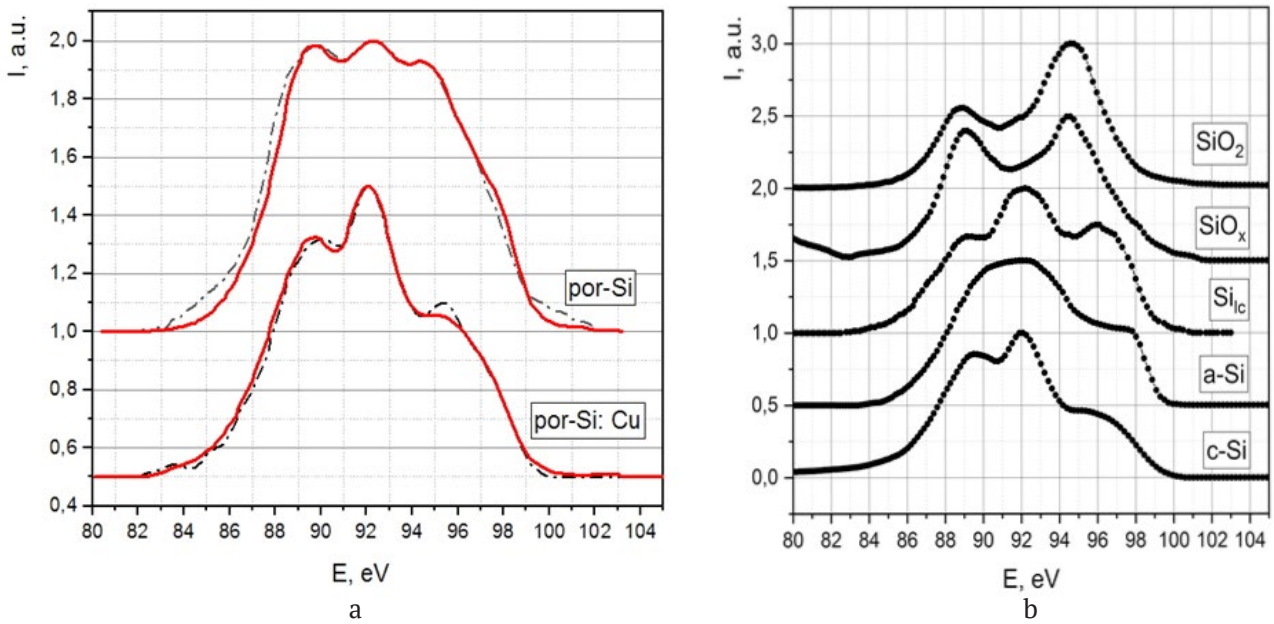

Fig. 3. USXES Si $L_{2,3}$ spectra of the porous layer of the original sample and samples with deposited copper

partially disordered silicon, amorphous silicon, silicon suboxide, and silicon dioxide (Table 1).

The composite sample obtained by chemical deposition of copper has significantly higher percentage of unoxidised crystalline c-Si and partially disordered silicon Si_{lc} phases (~95 % vs. 60 %) with a significantly lower percentage of oxide phases of SiO_x+SiO_2 (Table 1). Most likely, it is due to the fact that the introduction of a sufficiently large (up to 10 at. %) amount of copper particles into the porous layer leads to the formation of a continuous thin layer on the pore surface. In turn, this largely prevents further oxidation of the porous layer during storage.

The transmission spectra of the samples of porous silicon and porous silicon with deposited copper, obtained by IR spectroscopy using the ATR unit, are shown in Fig. 4. Despite the fact that the analysis depth of this method is ~1–2 μm, while the depth of the USXES method is 20 nm, the obtained data correlate with each other well enough.

The IR transmission spectra of porous silicon samples after 30-day storage in air under laboratory conditions show the typical features of this material (Table 2) [38, 39]. Analysis of the por-Si spectrum suggests the presence of the main transmission band corresponding to Si-Si vibrations (616 cm^{-1}) and different configurations of Si-H_x bonds (625, 2084, and 2200 cm^{-1}), as well as bonds of the O_x-SiH_y (865 cm^{-1}) and O_3-SiH (900 cm^{-1}) types. In the range of wavelength numbers between 2500 and 4500 cm^{-1}, almost no peculiarities were observed in the spectra of the samples. The absorption bands in the region of 2360 cm^{-1} correspond to adsorbed CO_2.

The IR spectrum of the sample with deposited copper is generally similar to the spectrum of the original crystalline silicon substrate (Fig. 4). It shows much less pronounced features in the same areas as in the original porous silicon. The absorption band corresponding to Si-O-Si bonds and the bands characteristic of Si-H_x and O_y-Si-H_y bonds are practically absent. It should

Table 1. Phase composition of samples of original porous silicon and samples with chemically deposited copper

	"Phases", %					
20 nm	nc-Si	Si_{lc}	a-Si:H	SiO_x	SiO_2	Error, %
por-Si, 20 nm	19	5	35	28	13	5
por-Si: Cu, 20 nm	80	13	–	–	7	5

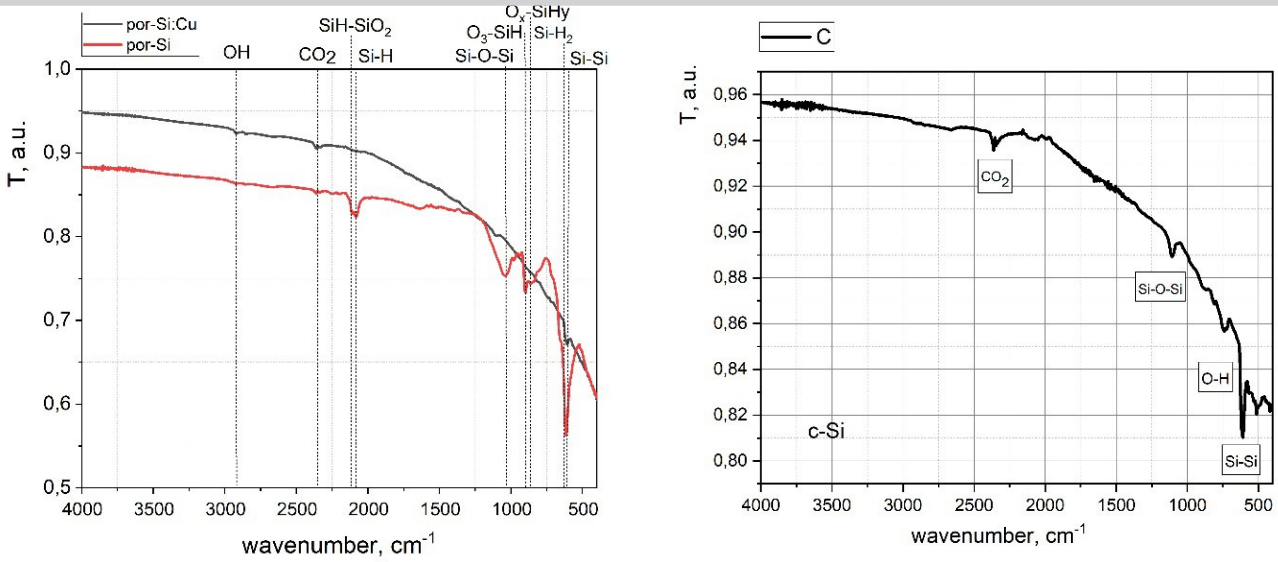

a b

Fig. 4. IR spectra of porous silicon and por-Si with deposited copper (a), as well as reference spectra (b)

be noted that Si-H_x and Oy-Si-H_y bonds in porous silicon actively participate in oxidation processes during storage of samples. They are replaced by Si-O-Si bonds and cause changes and degradation of various functional characteristics of the structures [40].

When studying the kinetics of sorption of porous silicon in air, its oxidation was observed after 30 days [41]. In the case of porous silicon with precipitated copper no such changes occur. Therefore, the absence of oxidation after 30 days of exposure of the samples to air may indicate significant stabilisation of the composition and surface properties of the composite, as we assumed further changes in the functional characteristics of the original porous silicon in the process of natural ageing. The assumed mechanism of slowing down the oxidation of porous silicon is that copper prevents oxygen from penetrating into the porous layer when interacting with the atmosphere. It is oxidised in the first place.

4. Conclusions

In this study, a method for the chemical deposition of copper into porous silicon from an aqueous solution of copper sulphate was developed. The results showed that copper penetrates the pores reasonably well when using chemical deposition and slows the oxidation of the porous layer during long-term storage in air. Thus, the methodology developed in the study can be successfully applied to create composite materials with improved properties.

Table 2. IR absorption bands in porous silicon and the composite with chemically deposited copper

Wave number, cm^{-1}	Por-Si
615	Si-Si val. sym.
625	Si-H_2 pend.
865	O_x-SiH_y deform., SiF
900	O_3-SiH deform.
1057	Si-O-Si val. TO
2084	Si-H val. long.
2200	SiH-SiO_2 struc.
2360	CO_2

Contribution of the authors

The authors contributed equally to this article.

Conflict of interests

The authors declare that they have no known competing financial interests or personal relationships that could have influenced the work reported in this paper.

References

1. Willander M., Nur O., Lozovik Yu E., … Klason P. Solid and soft nanostructured materials: Fundamentals and applications. *Microelectronics Journal*. 2005;36(11): 940–949. https://doi.org/10.1016/j.mejo.2005.04.020

2. Ilyas N., Wang J., Li C., ... Li W. Nanostructured materials and architectures for advanced optoelectronic synaptic devices. *Advanced Functional Materials*. 2022;3(2110976): 1–29. https://doi.org/10.1002/adfm.202110976

3. Ammar A. H., Farag A. A. M., Gouda M. A., Roushdy N. Performance of novel nanostructured thin films of 2-cyano-N-(9,10-dioxo-9,10-dihydro-anthracene-2-yl)-2-(2-phenylhydrazono)acetamide: Synthesis and optoelectronic characteristics. *Optik*. 2021;226(2): 165967–166009. https://doi.org/10.1016/j.ijleo.2020.165967

4. Sicchieri N. B., Chiquito A. J., Gouveia R. C. Electronic and optoelectronic properties of intrinsic and cooper-doped germanium nanowire network devices. *Materials Today: Proceedings*. 2022;51(5):1872–1877. https://doi.org/10.1016/j.matpr.2021.10.081

5. Zhang S., Wei S., Liu Z., ... Zhang H. The rise of AI optoelectronic sensors: From nanomaterial synthesis, device design to practical application. *Materials Today Physics*. 2022;27 (100812): 1–26. https://doi.org/10.1016/j.mtphys.2022.100812

6. Zhao J.-H., Li X.-B., Chen Q.-D., Chen Z.-G., Sun H.-B. Ultrafast laser-induced black silicon, from micro-nanostructuring, infrared absorption mechanism, to high performance detecting devices. *Materials Today Nano*. 2020;11: 100078–100098. https://doi.org/10.1016/j.mtnano.2020.100078

7. Ni Z., Zhou Sh., Zhao Sh., Peng W., Yang D., Pi X. Silicon nanocrystals: unfading silicon materials for optoelectronics. *Materials Science and Engineering R*. 2019;138: 85–117. https://doi.org/10.1016/j.mser.2019.06.001

8. Xu C., Ravi Anusuyadevi P., Aymonier C., Luque R., Marre S. Nanostructured materials for photocatalysis. *Chemical Society Reviews*. 2019;48: 3868–3902. https://doi.org/10.1039/C9CS00102F

9. Jesionowski T., Kuznowicz M., Jędrzak A., Rębiś T. Sensing materials: biopolymeric nanostructures. *Encyclopedia of Sensors and Biosensors*. 2023;2: 286–304. https://doi.org/10.1016/B978-0-12-822548-6.00015-7

10. Kumar V., Minocha N., Garg V., Dureja H. Nanostructured materials used in drug delivery. *Materials Today: Proceedings*. 2022;69(2): 174–180. https://doi.org/10.1016/j.matpr.2022.08.306

11. Truong V. K., Kobaisi M. A., Vasilev K., Cozzolino D., Chapman J. Current perspectives for engineering antimicrobial nanostructured materials. *Current Opinion in Biomedical Engineering*. 2022;23: 100399. https://doi.org/10.1016/j.cobme.2022.100399

12. Khinevich N., Bandarenka H., Zavatski S., Girel K., Tamulevičienė A., Tamulevičius T., Tamulevičius S. Porous silicon - a versatile platform for mass-production of ultrasensitive SERS-active substrates. *Microporous and Mesoporous Materials*. 2021;323: 111204. https://doi.org/10.1016/j.micromeso.2021.111204

13. Alhmoud H., Brodoceanu D., Elnathan R., Kraus T., Voelcker N. H. Reprint of: A MACEing silicon: towards single-step etching of defined porous nanostructures for biomedicine. *Progress in Materials Science*. 2021;120: 100817, https://doi.org/10.1016/j.pmatsci.2021.100817

14. Alhmoud H., Brodoceanu D., Elnathan R., Kraus T., Voelcker N. H. A MACEing silicon: towards single-step etching of defined porous nanostructures for biomedicine. *Progress in Materials Science*. 2021;116: 100636. https://doi.org/10.1016/j.pmatsci.2019.100636

15. Pan M., Yang J., Liu K., ... Wang S. Noble metal nanostructured materials for chemical and biosensing systems. *Nanomaterials*. 2020;10(2): 209. https://doi.org/10.3390/nano10020209

16. Saini A., Abdelhameed M., Rani D., ... Dutta M. Fabrication of periodic, flexible and porous silicon microwire arrays with controlled diameter and spacing: Effects on optical properties. *Optical Materials*. 2022;134 (A): 113181. https://doi.org/10.1016/j.optmat.2022.113181

17. Sun X., Sharma P., Parish G., Keating A. Enabling high-porosity porous silicon as an electronic material. *Microporous and Mesoporous Materials*. 2021;312: 110808. https://doi.org/10.1016/j.micromeso.2020.110808

18. Aksimentyeva O. I., Tsizh B. R., Monastyrskii L. S., Olenych I. B., Pavlyk M. R. Luminescence in porous silicon – poly(para–phenylene) hybrid nanostructures. *Physics Procedia*. 2015;76: 31–36. https://doi.org/10.1016/j.phpro.2015.10.006

19. Goryachev D. N., Belyakov L. V., Yeltsina O. S., Vainshtein J., Sreseli O. M. On the metal-assisted chemical etching of nanoporous silicon. *ECS Meeting Abstracts*. 2012;MA2012-02(26): 2372–2372. https://doi.org/10.1149/MA2012-02/26/2372

20. Taurbayev Y. T., Gonchar K. A., Zoteev A. V., Timoshenko V., Zhanabayev Z. Zh., Nikulin V. E., Taurbayev T. I. Electrochemical nanostructuring of semiconductors by capillary-cell method. *Key Engineering Materials*. 2010;442: 1–6. https://doi.org/10.4028/www.scientific.net/KEM.442.1

21. Spivak Yu. M., Belorus A. O., Somov P. A., Tulenin S. S., Bespalova K. A., Moshnikov V. A. Porous silicon nanoparticles for target drag delivery: structure and morphology. *Journal of Physics: Conference Series*. 2015;643: 012022. https://doi.org/10.1088/1742-6596/643/1/012022

22. Belkacem W., Belhi R., Mliki N. Magneto-optical properties of cobalt nanoparticles in porous silicon. *Journal of Magnetism and Magnetic Materials*. 2022;563: 169882. https://doi.org/10.1016/j.jmmm.2022.169882

23. Grevtsov N., Chubenko E., Bondarenko V., Gavrilin I., Dronov A., Gavrilov S. Electrochemical deposition of indium into oxidized and unoxidized porous silicon. *Thin Solid Films*. 2021;734: 138860. https://doi.org/10.1016/j.tsf.2021.138860

24. Ensafi A. A., Abarghoui M. M., Rezaei B. Electrochemical determination of hydrogen peroxide usingcopper/porous silicon based non-enzymatic sensor. *Sensors and Actuators B*. 2014;196: 398–405. https://dx.doi.org/10.1016/j.snb.2014.02.028

25. Moshnikov V. A., Gracheva I., Lenshin A. S., Spivak Y. M., Anchkov M. G., Kuznetsov V. V., Olchowik J. M. Porous silicon with embedded metal oxides for gas sensing applications. *Journal of Non-Crystalline Solids*. 2012;358: 590–595. http://dx.doi.org/10.1016/j.jnoncrysol.2011.10.017

26. Save D., Braud F., Torres J., Binder F., Müller C., Weidner J. O., Hasse W. Electromigration resistance of copper interconnects. *Microelectronic Engineering*. 1997;33 (1-4): 75–84. https://doi.org/10.1016/S0167-9317(96)00033-0

27. Al-Jumaili B. E. B., Talib Z. A., Ramizy A., ... Lee H. K. Formation and photoluminescence properties of porous silicon/copper oxide nanocomposites fabricated via electrochemical deposition technique for photodetector application. *Digest Journal of Nanomaterials and Biostructures*. 2021,16: 297–310. https://doi.org/10.15251/DJNB.2021.161.297

28. Huang Y. M. Photoluminescence of copper-doped porous silicon. *Applied Physics Letters*. 1996;69(19): 2855. https://doi.org/10.1063/1.117341

29. Ensafi A. A., Mokhtari Abarghoui M., Rezaei B. A new non-enzymatic glucose sensor based on copper/porous silicon nanocomposite. *Electrochimica Acta*. 2014,123: 219–226. https://doi.org/10.1016/j.electacta.2014.01.031

30. Ensafi A. A., Abarghoui M. M., Rezaei B. Electrochemical determination of hydrogen peroxide using copper/porous silicon based non-enzymatic sensor. *Sensors and Actuators B: Chemical*. 2014,196: 398–405. https://doi.org/10.1016/j.snb.2014.02.028

31. Ozdemir S., Gole J. L. A phosphine detection matrix using nanostructure modified porous silicon gas sensors. *Sensors and Actuators B: Chemical*. 2010;151(1): 274-280. https://doi.org/10.1016/j.snb.2010.08.016

32. Darwich W., Garron A., Bockowski P., Santini C., Gaillard F., Haumesser P.-H. Impact of surface chemistry on copper deposition in mesoporous silicon. *Langmuir*. 2016;32(30): 7452–7458. https://doi.org/10.1021/acs.langmuir.6b00650

33. Kashkarov V. M., Len'shin A. S., Popov A. E., Agapov B. L., Turishchev S. Yu. Composition and structure of nanoporous silicon layers with galvanically deposited Fe and Co. *Bulletin of the Russian Academy of Sciences: Physics*. 2008;72(4): 453–458. https://doi.org/10.3103/s1062873808040084

34. Canham L. *Handbook of porous silicon*. Springer Cham; 2018., 1613 p. https://doi.org/10.1007/978-3-319-71381-6

35. Manukovsky E. Yu. *Electronic structure, composition and photoluminescence of porous silicon*[*]. Cand. phys.-math sci. diss. Voronezh, VSU; 1999. (In Russ.). Available at: https://www.dissercat.com/content/elektronnaya-struktura-sostav-i-fotolyuminestsentsiya-poristogo-kremniya

36. Kashkarov V., Nazarikov I., Lenshin A., Terekhov ... Domashevskaya E. Electron structure of porous silicon obtained without the use of HF acid. *Physica Status Solidi (C) Current Topics in Solid State Physics*. 2009;6 (7): 1557–1560. https://doi.org/10.1002/pssc.200881019

37. Len'shin A. S., Kashkarov V. M., Domashevskaya E. P., Seredin P. V., Bel'tyukov A. N., Gil'mutdinov F. Z. Composition of nanocomposites of thin tin layers on porous silicon, formed by magnetron sputtering. *Physics of the Solid State*. 2017;59(4): 791–800. https://doi.org/10.1134/S1063783417040138

38. Terekhov V. A., Kashkarov V. M., Manukovskii E. Yu., Schukarev A. V., Domashevskaya E. P. Determination of the phase composition of surface layers ofporous silicon by ultrasoft X-ray spectroscopy and X-ray photoelectronspectroscopy techniques. *Journal of Electron Spectroscopy and Related Phenomena.* 2001; 114–116: 895–900. https://doi.org/10.1016/S0368-2048(00)00393-5

39. Len'shin A. S., Kashkarov V. M., Tsipenyuk V. N., Seredin P. V., Agapov B. L., Minakov D. A., Domashevskaya E. P. Optical properties of porous silicon processed in tetraethyl orthosilicate. *Technical Physics*. 2013;58(2): 284–288. https://doi.org/10.1134/S1063784213020151

40. Lenshin A. S., Seredin P. V., Kashkarov V. M., Minakov D. A. Origins of photoluminescence degradation in porous silicon under irradiation and the way of its elimination. *Materials Science in Semiconductor Processing*. 2017;64: 71–76. https://doi.org/10.1016/j.mssp.2017.03.020

41. Turishchev S. Yu., Lenshin A. S., Domashevskaya E. P., Kashkarov V. M., Terekhov V. A., Pankov K. N., Khoviv D. A. Evolution of nanoporous silicon phase composition and electron energy structure under natural ageing. *Physica Status Solidi C*. 2009;6(7): 1651–1655. https://doi.org/10.1002/pssc.200881015

Information about the authors

Alexander S. Lenshin, Dr. Sci. (Phys.–Math.), Leading Researcher, Department of Solid State Physics and Nanostructures, Voronezh State University (Voronezh, Russian Federation).
https://orcid.org/0000-0002-1939-253X
lenshinas@mail.ru

Kseniya B. Kim, Cand. Sci. (Chem.), Associate Professor, Department of Inorganic Chemistry and Chemical Technology, Voronezh State University of Engineering Technologies (Voronezh, Russian Federation).
https://orcid.org/0000-0001-5564-8267
kmkseniya@yandex.ru

Boris L. Agapov, Cand. Sci. (Tech.), Centre for Collective Use of Scientific Equipment, Voronezh State University (Voronezh, Russian Federation).
b.agapov2010@yandex.ru

Vladimir Kashkarov, Cand. Sci. (Phys.–Math.), Associate Professor, Department of Solid State Physics and Nanostructures, Voronezh State University (Voronezh, Russian Federation).
https://orcid.org/0000-0001-9460-9244
kash@phys.vsu.ru

Anatoly N. Lukin, Cand. Sci. (Phys.–Math.), Associate Professor, Department of Solid State Physics and Nanostructures, Voronezh State University (Voronezh, Russian Federation).
https://orcid.org/0000-0001-6521-8009
ckp_49@mail.ru

Sabukhi I. Niftaliyev, Dr. Sci. (Chem.), Professor, Head of the Department of Inorganic Chemistry and Chemical Technology, Voronezh State University of Engineering Technologies (Voronezh, Russian Federation).
https://orcid.org/0000-0001-7887-3061
sabukhi@gmail.com

Received 28.11.2022; approved after reviewing 25.12.2022; accepted for publication 26.12.2023; published online 25.09.2023.

Translated by Anastasiia Ananeva

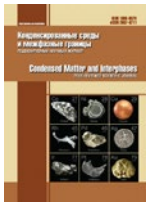

ISSN 1606-867X (Print)
ISSN 2687-0711 (Online)
Condensed Matter and Interphases
Kondensirovannye Sredy i Mezhfaznye Granitsy
https://journals.vsu.ru/kcmf/

Original articles

Research article
https://doi.org/10.17308/kcmf.2023.25/11260

A study of the local atomic structure the environment of zinc ions of different concentrations during their interaction with the arachidic acid Langmuir monolayer

V. Yu. Lysenko[1], M. A. Kremennaya[1], S. N. Yakunin[2], A. V. Rogachev[2], G. E. Yalovega[1]✉

[1]*Southern Federal University*
105/42 Bolshaya Sadovaya st., Rostov-on-Don 344006, Russian Federation

[2]*National Research Centre "Kurchatov Institute"*
1 Academician Kurchatova pl., Moscow 123182, Russian Federation

Abstract

Vital cellular processes depend on the controlled transport of metal ions across biological membranes. A biological membrane is a complex system consisting of lipids and proteins, that is why simplified systems, in particular monomolecular layers, are used to model it.

This work presents the results of a study of the interaction of zinc ions from the aqueous subphase with the Langmuir monolayer of arachidic acid. The study was carried out for the first time and used total external reflection X-ray absorption spectroscopy. It considers the influence of the concentration of a $ZnCl_2$ aqueous subphase solution on the local environment of zinc ions when interacting with the lipid monolayer immediately after its formation.

The theoretical analysis of experimental XANES spectra showed that one of the interaction ways of arachidic acid molecules with zinc ions immediately after the monolayer formation is an intramolecular interaction with the formation of spodium bonds between the zinc cation and the OH carboxyl group of arachidic acid.

Keywords: arachidic acid, X-ray absorption spectroscopy, total external reflection, lipid layer, Langmuir bath, subphase, thin films

Funding: The study was supported by the grant of the President of the Russian Federation (grant No. MK-2767.2021).

For citation: Lysenko V. Yu., Kremennaya M. A., Yakunin S. N., Rogachev A. V., Yalovega G. E. A study of the local atomic structure the environment of zinc ions of different concentrations during their interaction with the arachidic acid Langmuir monolayer. *Condensed Matter and Interphases*. 2023;25(3): 367–372. https://doi.org/10.17308/kcmf.2023.25/11260

Для цитирования: Лысенко В. Ю., Кременная М. А., Якунин С. Н., Рогачев А. В., Яловега Г. Э. Исследование локальной атомной структуры окружения ионов цинка различной концентрации при их взаимодействии с ленгмюровским монослоем арахиновой кислоты. *Конденсированные среды и межфазные границы*. 2023;25(3): 367–372. https://doi.org/10.17308/kcmf.2023.25/11260

✉ Galina E. Yalovega, e-mail: yalovega@sfedu.ru

1. Introduction

The structure and functioning of biological membranes is still one of the most important issues in biology and medicine. Biological membranes are molecular "shells" that separate the content of cells from the external environment. They provide barrier, transport, receptor, energy, and other functions of cells. They regulate the interaction of the cell with the external environment and are the medium for many biochemical processes [1]. Such diverse functions are impossible without a complex structure, which is provided by the diversity of the main components of the membrane and their interactions. Biological membranes consist of two main components: lipids and proteins. The structural backbone of the membrane is its lipid bilayer, in which various proteins are embedded [2].

Simplified artificial models of biological membranes are used to better understand the interactions between lipids and the cellular medium at the molecular level. There are two groups of models of biological membranes: vesicular and planar. The planar model uses lipid monolayers as a model biological membrane. Despite the fact that biomembranes have a double layer, the molecular monolayer method allows modelling some processes occurring in lipid bilayers and in the lipid monolayer on the water surface [3].

The lipid monolayer model is also suitable for studying membrane binding by introducing the tested substance into an aqueous subphase under the monolayer. In particular, vital cellular processes depend on the controlled transport of metal ions across the membrane. In these cases, Langmuir monolayers at the air-water interface are the best model for studying the interaction of lipids with metal ions.

Layers of arachidic acid can be used as a model of a cell membrane. Arachidic acid is a saturated long-chain fatty acid with twenty carbon chains containing an aliphatic tail. Zinc is an essential microelement for almost all existing living forms and at high concentrations can act as a toxic agent [4]. Its high biological accumulation in organisms and plants is due, among other things, to the good solubility of zinc chlorides in water [5]. In our work, we considered the interaction of arachidic acid with zinc ions from a $ZnCl_2$ aqueous solution as a model for the interaction of zinc ions from a body fluid with the lipid layer of the biomembrane.

Inorganic ions present in the subphase alter the arrangement of the monolayer molecules in arachidic acid at the air-water interface. Inorganic ions of different species differently affect the structural organisation of the monolayer and the separation of the surface and volume of stearic acid monolayers [6].

Currently, there is a big variety of physico-chemical methods for studying biochemical processes in cells. However, the study of the effect of microelements on the course of various cellular processes is still a challenging task due to their presence in the body in trace amounts. Unlike other methods, X-ray absorption spectroscopy in the near-edge region (XANES – X-ray Absorption Near Edge Structure) can be applied to almost any kind of atom and any concentration of the studied element. X-ray absorption spectroscopy is sensitive to the local chemical environment of a particular element, the nature of the chemical bond, the number and type of ligands, metal-ligand distances, and the degree of metal oxidation [7, 8].

XANES measurements in fluorescence mode under total external reflection (TER) conditions on the surface of the liquid subphase is an evolving method that opens up new opportunities for *in situ* monitoring of the structure formation processes in two-dimensional monolayers and the study of objects with extremely low concentrations of the absorbing atom, such as metalloproteins monolayers and lipids [9, 10].

This work is devoted to the study of the interaction of zinc ions from the aqueous subphase with the Langmuir layer of arachidic acid by X-ray absorption spectroscopy XANES. It analyses the changes in the local environment of zinc ions depending on the concentrations of a $ZnCl_2$ solution. It presents the results of the theoretical analysis of experimental spectra, which were used to study one of the ways of interaction of the monolayer with zinc ions.

2. Experimental and theoretical methods

Sample preparation. Arachidic acid was purchased from Sigma-Aldrich Co. A $ZnCl_2$ aqueous solution was used as a subphase in the

Langmuir bath. Measurements were made for three concentrations of $ZnCl_2$ in the solution: $6{\cdot}10^{-4}$, $6{\cdot}10^{-5}$, $3{\cdot}10^{-6}$ M. A solution of arachidic acid was applied to the subphase surface. The layers were compressed to a surface pressure of π = 20 mN/m, the pressure was constant during X-ray measurements.

The XANES measurements on the arachidic acid monolayer at the air/liquid interface were performed in the Kurchatov Center for Synchrotron Radiation on the LANGMUIR bending magnet line. The zinc K-edge XANES spectra were recorded in fluorescence mode under total external reflection conditions using a Si(111) monochromator with a spectral width of ~2 eV. The X-ray beam was directed to the surface of the liquid using two flat mirrors. XANES spectra were measured at a fixed incident angle of 0.8 critical angle θ_C. The X-ray penetration depth, which determines the sensitivity of the measurements, was approximately 85 Å.

Theoretical analysis of the zinc K-edge X-ray absorption spectra was carried out by the finite-difference method at full potential using the FDMNES code [11]. The size of the clusters for the calculation was selected so that all atoms of the studied model were included. Lorentzian convolution was performed for the obtained spectra to determine spreading effects.

3. Results and discussion

Arachidic acid ($C_{20}H_{40}O_2$) has a hydrophilic carboxyl group and hydrophobic hydrocarbon chains in its composition. The structure of arachidic acid determines the location of these molecules in the composition of the monolayer on the surface of the aqueous subphase of the $ZnCl_2$ solution in the Langmuir bath. Polar carboxyl groups are immersed in the liquid phase, while non-polar hydrocarbon chains face the air medium (Fig. 1).

The surface pressure of the lipid monolayer is an important parameter for the analysis of the dynamic and structural properties of monolayers [12]. To investigate lipid binding, the studied bioactive substance is introduced into the aqueous subphase under the lipid monolayer. Its penetration into the lipid layer can be controlled by recording changes in the surface pressure or changes in the monolayer area at certain pressure values [13]. During our experiment, changes in the monolayer area were used to control the dynamics of the ongoing processes.

The measurements of the zinc K-edge XANES spectra in the system of a monolayer of arachidic acid on the surface of a $ZnCl_2$ solution (indicated in the figure as AA+$ZnCl_2$) began almost immediately (about 7 minutes) after the surface pressure reached the value of 20 mN/m. The measurements were taken for 3 concentrations of $ZnCl_2$ in the solution: $6{\cdot}10^{-4}$, $6{\cdot}10^{-5}$, $3{\cdot}10^{-6}$ M. For all concentrations, the pressure in the monolayer was constant during the measurements.

The general trend for changing spectra for the system (AA+$ZnCl_2$) with an increase in the concentration of $ZnCl_2$ in the solution was the shift of the absorption edge by ~ 1.1 eV, a decrease in the intensities of peak A and C with a simultaneous increase in the energy distances between them, as well as an increase in the intensity of peak B (Fig. 2, the direction of changes is shown by arrows). The observed differences in spectra reflect changes in the local environment of zinc ions in the presence of arachidic acid depending on the concentration of the $ZnCl_2$ solution. As can be seen from Fig. 2, the spectra for the AA+$ZnCl_2$ system coincided in shape (the same set of maxima and redistribution of intensities between peaks) with the spectrum of the $ZnCl_2$ solution (in the absence of arachidic acid) [10], however, they differed in intensity and energy distances between the peaks. This indicates differences in the local environment of zinc ions in the pure solution and in the presence of arachidic acid. The spectrum of the

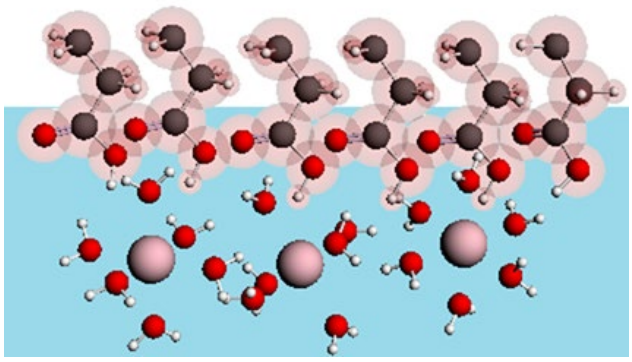

Fig. 1. Schematic representation of the arrangement of the molecules of arachidic acid on the surface of a $ZnCl_2$ solution (blue plane)

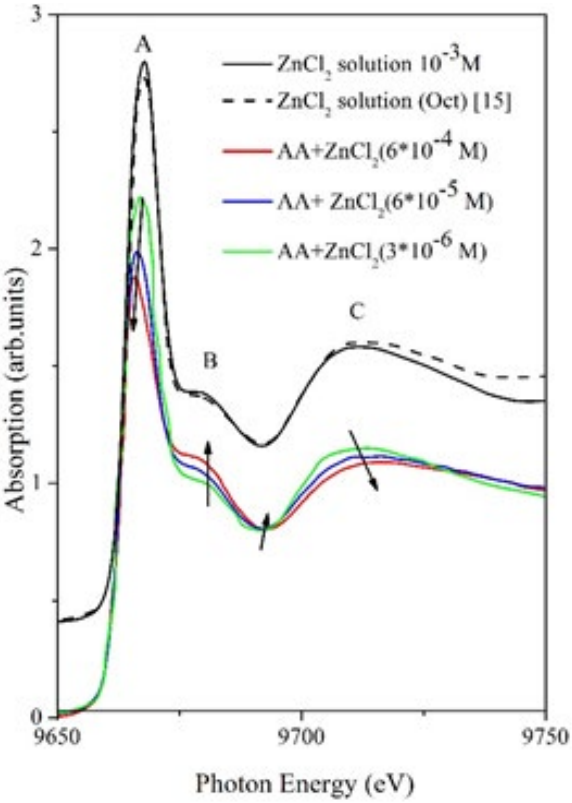

Fig. 2. Experimental zinc K-edge XANES spectra: (a) of a $ZnCl_2$ solution with a concentration of 10^{-3} M as compared with the spectrum from work [15]; (b) monolayer of arachidic acid (AA) on the surface of $ZnCl_2$ solutions with concentrations of $6{\cdot}10^{-4}$, $6{\cdot}10^{-5}$, $3{\cdot}10^{-6}$ M

solution with a concentration of 10^{-3} M almost completely coincided with the spectrum from the work [14] (Fig. 2, dotted line), where Zn^{2+} was in the octahedral environment. It should be noted that the spectra of the solution were obtained by the same registering method as in the AA+$ZnCl_2$ system, however, from the subphase volume, i.e. at the X-ray beam incidence angle greater than critical angle θ_C.

Theoretical modelling of XANES experimental spectra was used to study the changes in the local structure of Zn^{2+} when zinc ions came into contact with the monolayer. Zinc chlorides in an aqueous solution can form complexes of different types with the different number of bound water molecules in different geometric environments [15]. At low concentrations of < 1 M, one of the dominant roles in the solution is played by $Zn(H_2O)_6^{2+}$ complexes [16]. The theoretical zinc K-edge XANES spectra were calculated for this complex (Fig. 3a). According to various sources, Zn-O interatomic distances in the $Zn(H_2O)_6^{2+}$ complex range from 2.05 to 2.14 Å. Figure 3 shows the sensitivity of the XANES spectra to changes in the closest symmetry of the Zn^{2+} environment. The deviation from the octahedral geometry of the zinc environment with H_2O ligands towards the distorted octahedron resulted in a more pronounced peak B in the spectrum and a change in the shape of the main peak. The distortions in the octahedron included elongation of the axial distances to 2.7 Å as compared to distances typical of the $Zn(H_2O)_6^{2+}$ aqueous complex. Next, calculations were made for a structural model in which the OH hydroxyl group of the carboxyl group of arachidic acid replaced the water molecule at the octahedron's vertex (Fig. 3b). In this case, the Zn–OH interatomic distances were also 2.7 Å. This model was used to consider the possibility of forming intramolecular Zn···O spodium bonds between the zinc cation and the OH group of arachidic acid when the interatomic distances exceed the sum of the covalent radii. This type of interaction is an alternative to hydrogen bonding and was observed in Zn^{2+} complexes [17]. This model was in good agreement with the experiment. It should be noted that a longer interaction of arachidic acid with a $ZnCl_2$ solution resulted in an increased trend of changing XANES spectra in the AA+$ZnCl_2$ system, which may indicate the presence of other types of binding in this system [18].

4. Conclusions

For the first time, zinc K-edge total external reflection X-ray absorption spectra were obtained for the system of a arachidic acid monolayer on the $ZnCl_2$ solution surface of various concentrations ($6{\cdot}10^{-4}$, $6{\cdot}10^{-5}$, $3{\cdot}10^{-6}$ M). The analysis of the XANES spectra indicated that the local environment of zinc ions changed immediately after the formation of the Langmuir monolayer and depended even on minor changes in concentration. The analysis of theoretical XANES spectra allowed assuming that one of the ways of interaction of arachidic acid with aqueous Zn^{2+} complexes is an intramolecular interaction resulting in the formation of spodium bonds between the zinc cation and the OH carboxyl group of arachidic acid. In this case, the symmetry of the zinc environment changes from an octahedron to a distorted octahedron with an

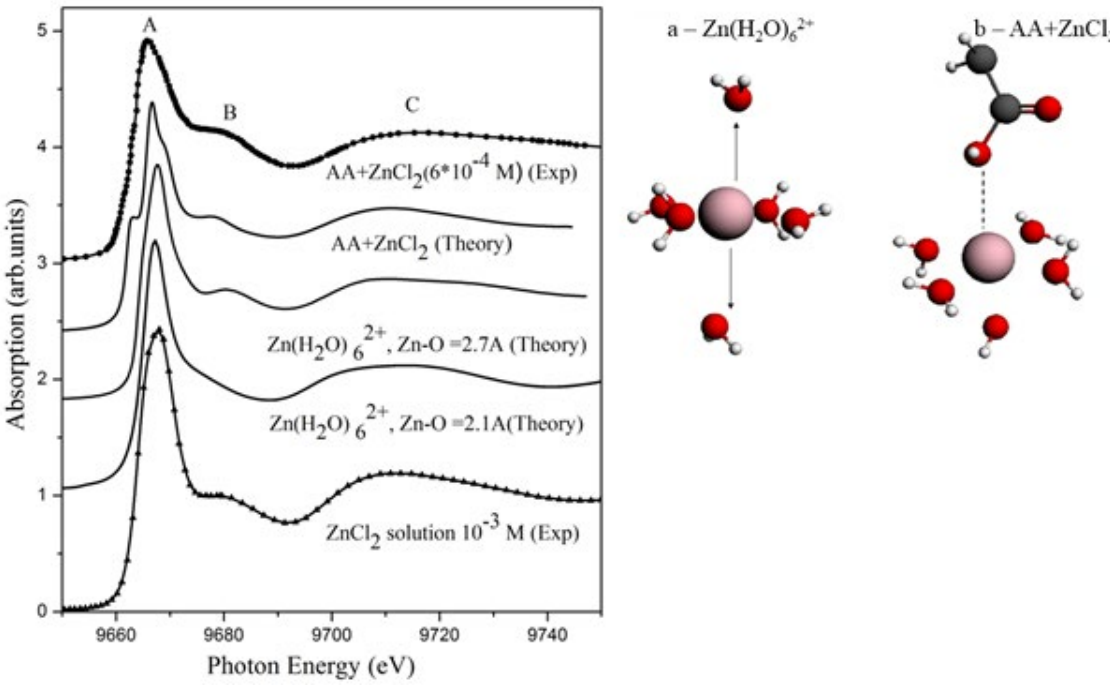

Fig. 3. Comparison of the theoretical Zn K-edge XANES (solid line) for the model $Zn(H_2O)_6^{2+}$ (a) and $AA+ZnCl_2$ (b) with the experimental spectra (symbol) of a solution of $ZnCl_2$ and $AA+ZnCl_2$ ($6{\cdot}10^{-4}$ M)

increased Zn–OH axial distance. Differences in the degree of changes in the local structure of zinc in the system "the monolayer of arachidic acid - a $ZnCl_2$ solution" at different concentrations can be due to the number of the interacted molecules of arachidic acid or to another type of interaction.

Contribution of the authors

V. Yu. Lysenko – theoretical modelling of XANES X-ray absorption spectra, study of literature. M. A. Kremennaya – construction and substantiation of structural models. S. N. Yakunin – development of methods, measuring of XANES X-ray absorption spectra in fluoresce mode under total external reflection using synchrotron radiation. A. V. Rogachev - measuring XANES X-ray absorption spectra in fluorescent mode under total external reflection using synchrotron radiation. G. E. Yalovega – analysis of literary sources, analysis and interpretation of experimental and theoretical XANES spectra, substantiation of results and conclusions.

Conflict of interests

The authors declare that they have no known competing financial interests or personal relationships that could have influenced the work reported in this paper.

References

1. Watson H. Biological membranes. *Essays in Biochemistry*. 2015;59: 43–69. https://doi.org/10.1042/bse0590043

2. Mukhomedzyanova S., Pivovarov Y., Bogdanova O., Dmitrieva L., Shulunov A. The lipids of biological membranes (Literature review). *Acta Biomedica Scientifica*. 2017;2(5(1)): 43–49. https://doi.org/10.12737/article_59e8bcd3d6fcb1.49315019

3. Wiśniewska-Becker A., Gruszecki W. I. 2 – Biomembrane models. In: *Drug – biomembrane interaction studies*. Woodhead Publishing. 2013: 47–59. https://doi.org/10.1533/9781908818348.47

4. Sandstead H. H. *Handbook on the Toxicology of Metals, 4th ed*. Elsevier. 2014: 1369–1386.

5. Pipan-Tkalec Z., Drobne D., Jemec A., Romih T., Zidar P., Bele M. Zinc bioaccumulation in a terrestrial invertebrate fed a diet treated with particulate ZnO or $ZnCl_2$ solution. *Toxicology*. 2010;269(2-3): 198–203. https://doi.org/10.1016/j.tox.2009.08.004

6. Li S., Du L., Wei Z., Wang W. Aqueous-phase aerosols on the air-water interface: Response of fatty acid Langmuir monolayers to atmospheric inorganic ions. *Science of the Total Environment*. 2017;580: 1155–1161. https://doi.org/10.1016/j.scitotenv.2016.12.072

7. Bokhoven J. A., Lamberti C. (eds.). *X-Ray absorption and X-Ray emission spectroscopy: Theory and Applications*. John Wiley & Sons. 2016. https://doi.org/10.1002/9781118844243

8. Shmatko V. A., Mysoedova T. N., Mikhailova T. A., Yalovega G. E. Features of the electronic structure and chemical bonds of polyaniline-based composites obtained by acid-free synthesis. *Condensed Matter and Interphases*. 2019;4(4): 567–578. https://doi.org/10.17308/kcmf.2019.21/2367

9. Konovalov O. V., Novikova N. N., Kovalchuk M. V., ... Yakunin S. N. XANES measurements for studies of adsorbed protein layers at liquid interfaces. *Materials*. 2020;13(20): 4635. https://doi.org/10.3390/ma13204635

10. Novikova N. N., Yakunin S. N., Koval'chuk M. V., ... Topunov A. F. Possibilities of X-ray absorption spectroscopy in the total external reflection geometry for studying protein films on liquids. *Crystallography Reports*. 2019;64(6): 952–957. https://doi.org/10.1134/S1063774519060130

11. Joly Y. X-ray absorption near-edge structure calculations beyond the muffin-tin approximation. *Physical Review*. 2001;63: 125120. https://doi.org/10.1103/physrevb.63.125120

12. Sujak A., Gagos M., Serra M. D., Gruszecki W. I. Organization of two-component monomolecular layers formed with dipalmitoylphosphatidylcholine and the carotenoid pigment, canthaxanthin. *Molecular Membrane Biology*. 2007;24(5-6): 431–41. https://doi.org/10.1080/09687860701243899

13. Hereć M., Gagoś M., Kulma M., Kwiatkowska K., Sobota A., Gruszecki W. I. Secondary structure and orientation of the pore-forming toxin lysenin in a sphingomyelin-containing membrane. *Biochim Biophys Acta*. 2008;1778(4): 872-9. https://doi.org/10.1016/j.bbamem.2007.12.004

14. Alloteau F., Valbi V., Majérus O., Biron I., Lehuede P., Caurant D., Seyeux A. Study of a surface treatment based on zinc salts to protect glasses from atmospheric alteration: Mechanisms and application to ancient glass objects in museum. In: *Glass Atmospheric Alteration: Cultural Heritage, Industrial and Nuclear Glasses*. Paris (France): Hermann edition, 2019. pp. 192–202.

15. Silber H. B., Simon D., Gaizer F. Octahedral-tetrahedral geometry changes for zinc(II) in the presence of chloride ions. *Inorganic Chemistry*. 1984;23(18): 2844–2848. https://doi.org/10.1021/ic00186a026

16. Parchment O. G., Vincent M. A., Hillier I. H. Speciation in aqueous zinc chloride. An *ab initio* hybrid microsolvation/continuum approach. *The Journal of Physical Chemistry A*. 1996;100(23): 9689–9693. https://doi.org/10.1021/jp960123z

17. Karmakar M., Frontera A., Chattopadhyay S., Mooibroek T., Bauzá A. Intramolecular spodium bonds in Zn(II) complexes: insights from theory and experiment. *International Journal of Molecular Sciences*. 2020;21(19): 7091. https://doi.org/10.3390/ijms21197091

18. Kremennaya M. A., Lysenko V. Y., Novikova N. N., Yakunin S. N., Rogachev A. V., Yalovega G. E. X-ray spectral diagnostics of the local environment of zinc in the arachidic acid layers. *Journal of Physics: Conference Series*. 2021;2103: 012171. https://doi.org/10.1088/1742-6596/2103/1/012171

Information about the authors

Victoria Yu. Lysenko, 2nd year master student of the Faculty of Physics, Southern Federal University (Rostov-on-Don, Russian Federation).
https://orcid.org/0000-0002-0538-7772
viktoriya.250699@mail.ru

Maria A. Kremennaya, Cand. Sci. (Phys.–Math.), Senior Lecturer, Faculty of Physics, Southern Federal University (Rostov-on-Don, Russian Federation).
https://orcid.org/0000-0002-0894-5733
kremennayamariya@gmail.com

Sergey N. Yakunin, Cand. Sci. (Phys.–Math.), First Deputy Head of the Kurchatov Complex for Synchrotron-Neutron Research of the National Research Center "Kurchatov Institute" (Moscow, Russian Federation).
s.n.yakunin@gmail.com

Alexander V. Rogachev, Researcher, National Research Center "Kurchatov Institute" (Moscow, Russian Federation).
https://orcid.org/0000-0001-6026-1534
a.v.rogachev@ya.ru

Galina E. Yalovega, Dr. Sci. (Phys.–Math.), Head of the Department of Physics of Nanosystems and Spectroscopy, Faculty of Physics, Southern Federal University (Rostov-on-Don, Russian Federation).
https://orcid.org/0000-0002-0157-6955
yalovega@sfedu.ru

Received 14.12.2022; approved after reviewing 22.12.2022; accepted for publication 26.12.2022; published online 25.09.2023.

Translated by Irina Charychanskaya

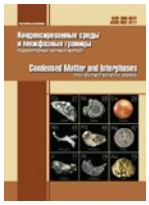

ISSN 1606-867X (Print)
ISSN 2687-0711 (Online)
Condensed Matter and Interphases
Kondensirovannye Sredy i Mezhfaznye Granitsy
https://journals.vsu.ru/kcmf/

Original articles

Research article
https://doi.org/10.17308/kcmf.2023.25/11261

Hydrogen permeability of 48Cu52Pd cold-rolled alloy foil and different methods of its surface pretreatment

N. B. Morozova[1]✉, L. E. Sidyakina[1], A. I. Dontsov[1,2], A. V. Vvedenskii[1]

[1]*Voronezh State University,*
1 Universitetskaya pl., Voronezh 394018, Russian Federation

[2]*Voronezh State Technical University,*
20 letiya Oktyabrya st., 84, Voronezh 394006, Russian Federation

Abstract

The process of atomic hydrogen penetration into the metal phase is complicated by the phase-boundary transition from the liquid and/or gas phase. That is why the cleanliness of metal and alloy surfaces is of particular importance. The purpose of this work was to determine the effect of surface pretreatment using photon pulses, ultrasound, and potential cycling on the parameters of hydrogen permeability for 48Cu52Pd metal cold-rolled membranes.

The study was focused on a foil of copper-palladium homogeneous alloy with 48 at. % Cu and 52 at. % Pd composition. The studied samples were obtained by cold rolling and their thickness were 10 and 16 μm. Surface pretreatment included rinsing in acetone, using ultrasound, pulsed photon treatment, and quadruple potential cycling over a wide range of potentials. Electrochemical studies included cyclic voltammetry and cathode-anodic chronoamperometry in a deaerated 0.1 M H_2SO_4 solution. Hydrogen permeability was calculated using mathematical models for samples of finite and semi-infinite thickness.

It was found that the surface treatment of a 48Cu52Pd foil with photon pulses leads to both an increase in the ionisation rate of atomic hydrogen and an increase in the roughness of the foil surface. The diffusion coefficient of atomic hydrogen does not depend on the method of surface pretreatment with ultrasound and photon pulses. The extraction rate constant for the extraction of the atomic hydrogen after photon treatment increases, which facilitates the processes of both H introduction and ionisation due to the release of active centres of the surface. Electrochemical cleaning of the surface during the quadruple potential cycling contributes to the growth of the extraction rate constant for the extraction of atomic hydrogen.

Keywords: 48Cu52Pd foil, Cold rolling, Hydrogen permeability, Surface pretreatment, Pulsed photon treatment, Ultrasound

Funding: The work was supported by the Ministry of Science and Higher Education of the Russian Federation in the framework of the government order to higher education institutions in the sphere of scientific research for years 2023-2025, project No. FZGU-2023-0006.

For citation: Morozova N. B., Sidyakina L. E., Dontsov A. I., Vvedenskii A. V. Hydrogen permeability of 48Cu52Pd cold-rolled alloy foil and different methods of its surface pretreatment. C*ondensed Matter and Interphases*. 2023;25(3): 373–382. https://doi.org/10.17308/kcmf.2023.25/11261

Для цитирования: Морозова Н. Б., Сидякина Л. Е., Донцов А. И., Введенский А. В. Водородопроницаемость фольги из холоднокатаных сплавов 48Cu52Pd с различной предобработкой поверхности. *Конденсированные среды и межфазные границы*. 2023;25(3): 373–382. https://doi.org/10.17308/kcmf.2023.25/11261

✉ Natalia B. Morozova, e-mail: mnb@chem.vsu.ru

1. Introduction

The production of high-purity hydrogen is important not only for hydrogen energy engineering, but also for hydraulic cleaning, hydrocracking, the production of synthetic fuel, etc. [1]. Various materials, such as polymers, zeolites, carbon, and certain metals, have previously been investigated for the purpose of obtaining high-quality membranes to isolate H_2 from a mixture with other gases [2], however, most of these membranes have low selectivity. Palladium-based membranes have high permeability and selectivity to molecular hydrogen due to a high dissociation rate and a high rate of atomic hydrogen penetration into the metal phase [3]. The main requirement for such membranes is their ability to prevent surface fouling with sulphur and its compounds. For this, copper, gold, and silver are added to palladium, both individually and in various combinations [4–6].

In particular, Pd-Cu membranes are recognised as the most promising due to their relatively low cost, noticeable resistance to fouling, and higher hydrogen permeability as compared to other Pd-based membranes [5,7-10]. Over the entire concentration range, Pd-Cu crystalline alloys are a continuous series of solid solutions [11]. However, the Cu- Pd alloy with a palladium content of 47 at. % demonstrates the highest hydrogen permeability [12]. It is also cost-effective as the copper content is just over 50 at. % [5]. Such an alloy is characterised by a sharp maximum of hydrogen permeability and forms the β-phase of a Pd-Cu solid solution at equilibrium. It was noted [9] that despite the same ratios of components in the alloy, due to its dense structure its high-temperature phase with the FCC lattice (α-phase) demonstrates a significantly lower hydrogen permeability than the β-phase.

The process of the atomic hydrogen penetration into the metal phase is complicated by the phase-boundary transition from the liquid and/or gas phase [13], therefore, there are additional requirements for the cleanliness of metal and alloy surfaces. This is especially important when using metal membranes obtained by cold rolling. In particular, organic oils used during rolling considerably pollute the surface of the metal phase, which inhibits the penetration of atomic hydrogen into the metal. In addition, oils can form durable polymer films on the surface. When manufacturing thin membranes whose thickness is just several microns, mechanical cleaning of their surfaces is absolutely unacceptable. What is more, when alloy membranes are used, chemical etching is also out of question.

The most common safe methods for preparing surfaces of metal samples that can be used for alloys include: laser [14, 15] and ultrasonic [16, 17] cleaning, high-temperature annealing [18, 19], and electrochemical cleaning [20]. Most physical cleaning methods are quite effective at removing persistent surface contamination, however, excessive cleaning intensity results in surface damage. Whereas, the method of electrochemical cleaning allows, by selecting the potential and the optimal number of cycles, removing substances of different solubility from the surface of noble metals and alloys based on them without changing the surface morphology [21].

The purpose of this work was to determine the effect of surface pretreatment using photon pulses, ultrasound, and potential cycling on the parameters of hydrogen permeability for 48Cu52Pd metal cold-rolled membranes.

2. Experimental

The study was focused on a copper-palladium foil with a thickness *l* and a composition of 48 at. % Cu and 52 at. % Pd, which was obtained by cold rolling*. The surface of the foil was pretreated by different methods. The pretreatment conditions included rinsing in acetone (30 min) in an ultrasonic bath (ODA-LQ07 (Russia)) at an operating frequency of 40 kHz. This was followed by pulsed photon treatment (PPT) at a radiation energy of ~35 J·cm^{-2} using a UOLP-1 unit, in a vacuum of 10^{-3} Pa using powerful INP 16/250 pulse xenon lamps (radiation spectrum 0.2–1.2 μm), and subsequent annealing in a vacuum at 350 °C.

The thickness of the samples and the methods used for surface pretreatment are shown in Table 1.

Electrochemical measurements were taken using an IPC-Compact potentiostat. The working

* The samples of palladium alloys were produced at the Baikov Institute of Metallurgy and Materials Science.

Table 1. Studied objects and method of their surface treatment

Sample	*l*, μm	Pretreatment method		
		Acetone	US (30 min)	PPT duration, s ; *I* = 50 A
1	16	+	+	–
2	10	+	+	1.0·10 (one side)
3	10	+	+	0.7·10 (two side)
4	10	+	+	0.7·10 (one side)

electrode was a sample of a 48Cu52Pd metal foil attached with a conductive graphite adhesive to a spectrally pure graphite electrode. The studies were carried out in a deaerated 0.1M H_2SO_4 solution (extra-pure grade) in a three-electrode cell with anode and cathode spaces separated with a thin section. A copper-sulphate electrode (E = 0.298 V) was used as the reference electrode. The auxiliary electrode was a platinised platinum Pt(Pt) electrode. All potentials were recalculated relative to a standard hydrogen electrode and the current values were given per single unit of the visible surface. The area of the studied foil samples did not exceed 0.5 cm^2.

The methods included cyclic voltammetry and two-stage anodic-cathodic chronoamperometry.

Voltammograms (VAG) were obtained from preliminary quadruple cycling of the working electrode within the potential range from E_c = –0.27 V to E_a = 1.70 V with a scanning rate of 5 mV/s. Before cycling and between cycles, the electrode was pre-polarised in a working solution at a potential of E_{pp} ≈ 0.30 V for t_{pp} = 500 s. The electrode was not removed from the solution. It was found that an increase in the number of cycles did not lead to any significant changes in the shape of voltammograms.

The method of cyclic voltammetry also determined the ionisation potential of atomic hydrogen E_p as the peak potential of hydrogen ionisation in the fourth cyclogram. The value E_p was used to obtain the anode half-period of the chronoamperogram. It should be noted that the values of E_p slightly differed due to the heterogeneity of the alloy surface after rolling.

Before obtaining the *i,t*-dependences, the electrode was pre-polarised at a potential of E_{pp} ≈ 0.30 V, which corresponded to the values of cathodic current not exceeding 2–4 μA. Chronoamperograms were obtained at the cathode hydrogenation potential E_c = –0.08 V for t_s from 1 to 10 s, and the anode ionisation potential E_p for t_a = 500 s. The cathode half-period of the chronoamperogram characterised the process of atomic hydrogen injection, while the anode half-period described its extraction. The time of the sample hydrogenation was chosen to prevent the formation of the palladium hydride β-phase within the metal phase. Over t_s = 10 s, the α-phase of the Pd-H solid solution was formed in the alloy, which was characterised by the ratio H/Pd = 0.02. We assumed that recharging of the double electric layer took little time, therefore, the anodic current transient i_a, which was observed for at least 500 s, was mainly due to the Faraday effect on the ionisation of atomic hydrogen.

Micrographs of the studied samples were obtained using a Solver P47PRO atomic force microscope (Russia) in a semi-contact (intermittent-contact) scanning mode.

3. Results and discussion

2.1. Analysis of cyclic voltammograms and chronoamperograms

Cyclic voltammograms obtained during quadruple cycling of the studied samples are shown in Fig. 1. They are characterised by two main peaks. The peak on the anodic branch of the curve corresponded to the ionisation of atomic hydrogen at E ~ 0.2–0.4 V, while the peak on the cathodic branch at E ~ 0.55 V corresponded to the PdO reduction [22]. The absence of ionisation peaks on samples 1 and 3 during the first cycle indicated that the active centres on the surface remained blocked even after the application of ultrasound and the PPT. Therefore, the pre-treatment procedure used for these samples was not effective. It can be assumed that oil annealing products used during alloy rolling were not removed completely. Within the potential range from 1.1 to 1.3 V, a blurred electrooxidation (EO) peak was observed on the anodic branch of the curve, which could be

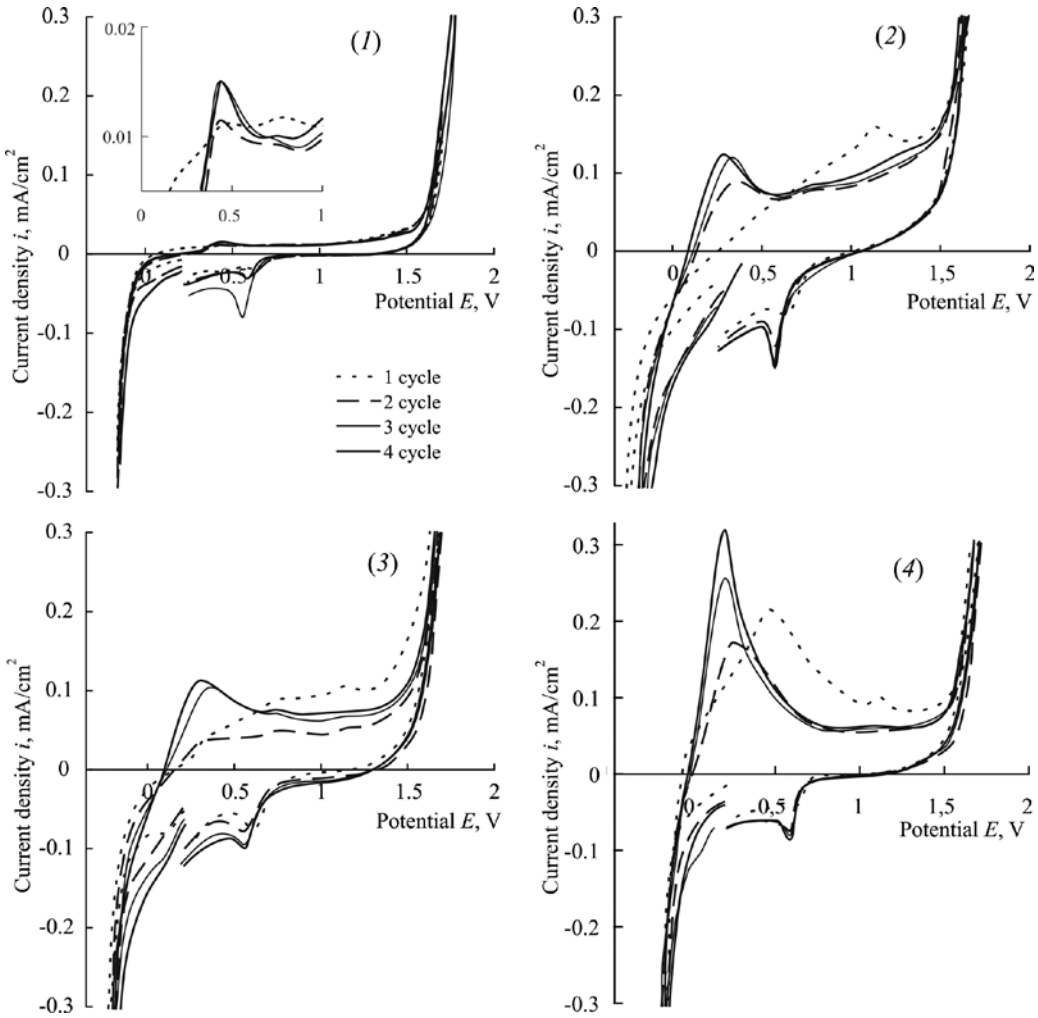

Fig. 1. Cyclic current-voltage curves with four-fold scanning of the potential of samples 1-4 of 48Cu52Pd alloy obtained in a 0.1M H_2SO_4 solution with a scanning rate of 5 mV/s

associated with the oxidation of traces of organic oils on the surface. However, in subsequent cycles, this peak was noticeably suppressed and, as a result, an ionisation peak of atomic hydrogen either appeared (samples 1, 3) or increased (samples 2, 4).

To find the parameters for the processes of introduction and ionisation of atomic hydrogen, two-stage cathodic-anodic chronoamperograms were obtained. For all chronoamperograms, the time of sample hydrogenation was t_c = 10 s. Both cathodic and anodic current transients in all samples were of the same nature. Cathodic current transients demonstrated a sharp decrease in the extraction rate in the first 3–4 seconds. For sample 4, there was a sharper transients than for samples 1-3. Anodic current transients also had a clear peak of H ionisation current, which decreased nonlinearly and completed a sharp decline after the first 10 s (Fig. 2).

The highest ionisation rates were observed in the fourth sample, and the lowest ionisation rates were in the first sample, which means that the PPT plays a significant role in eliminating oil products left after rolling and subsequent annealing of the sample. The comparison of the obtained results revealed that the highest ionisation rate was observed for the foil of the fourth sample, which had been rinsed in acetone and one side of which was exposed to ultrasound and photon treatment. The lowest ionisation peak was characteristic of the sample which hadn't been exposed to the PPT. Therefore, photon treatment of the surface contributed significantly to the surface cleaning of palladium and copper alloy samples after rolling and this effect was

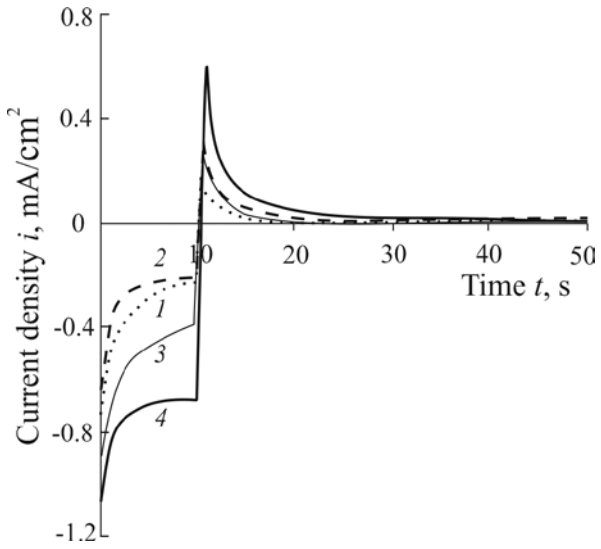

Fig. 2. Combined cathodic and anodic chronoamperograms of the studied samples (1-4) of 48Cu52Pd alloy obtained in a 0.1M H_2SO_4 solution after quadruple cycling at t_c = 10 s

noticeable in all samples which had been exposed to photon irradiation.

2.2. Microscopic examination of sample surfaces

The geometrical characteristics of the surfaces of 48Cu52Pd alloys both before and after the PPT were determined using atomic force microscopy (AFM). When comparing micrographs (Fig. 3), it can be seen that the PPT led to the appearance of globules on the surfaces of samples whose size reached ~700 nm. The globules were located on an initially even surface, which allows us to assume that they were formed as a result of the alloy's redeposition after the PPT procedure. The presence of these particles led to an increase in the total surface area of the studied samples. Also, the micrographs made before the PPT clearly showed the grain boundaries of the alloy, whose diameter was about 15–20 μm.

According to the results of AFM, the roughness of the alloy surface after the PPT increased by 3–5 times. It can be assumed that pulsed photon treatment of the surface not only removed the oil products used during rolling, but also led to the alloy redeposition being accompanied by the formation of globules. This resulted in the development of the alloy surface.

An increase in the rate of hydrogen ionisation on alloys after the PPT can also be associated with an increase in the surface area of the samples. However, even a five-fold increase (if we compare the peak heights of voltammograms of sample 1 without the PPT and samples 2–4) did not produce the results obtained for samples 2-4. This means that an increase in the rate of hydrogen ionisation should be associated not so much with an increase in the surface area of the alloy, but with a change in the state of its surface layer.

2.3. Calculating the parameters of hydrogen permeability

Two models for determining the parameters of hydrogen permeability were used to process

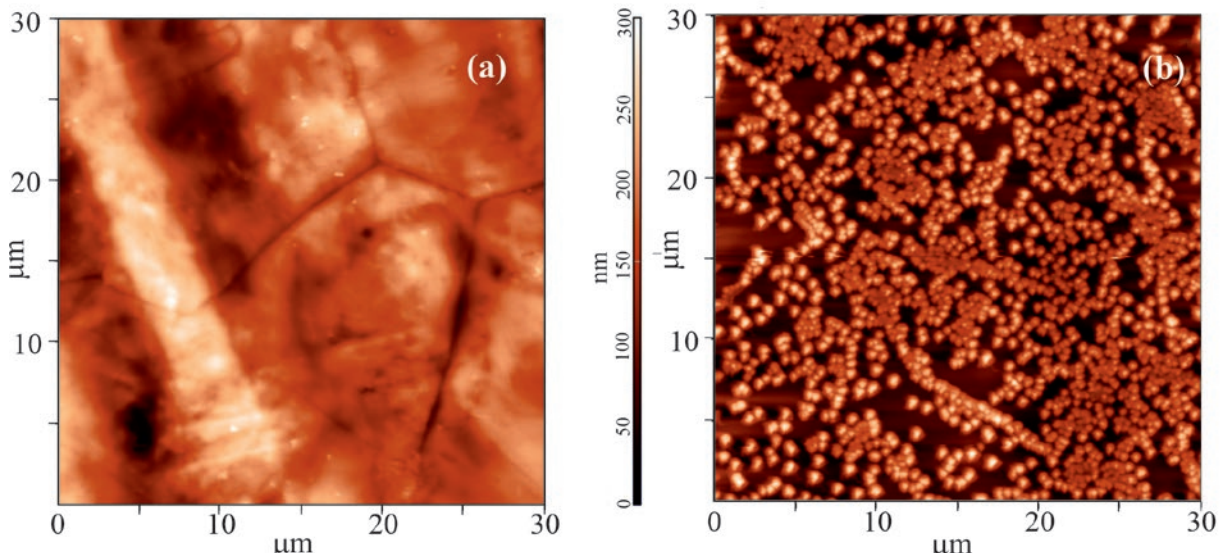

Fig. 3. AFM micrographs obtained for 48Cu52Pd alloy before (a) and after (b) the PPT

i,t-curves. The first model was valid for samples of semi-infinite thickness [13], for which the period of hydrogenation of 10 s was not enough for atomic hydrogen to cross the studied sample. Its application adequately described the processes of the introduction and ionisation of atomic hydrogen in samples with a thickness of more than 10 μm. The second model was applicable for samples of finite thickness which did not exceed 10 μm [24].

Since the thickness of sample 1 was 16 μm, we used the first model to calculate the parameters of hydrogen permeability. While the model of thin electrodes was used to process the current transients obtained for samples 2–4. This means that it was not possible to calculate the diffusion coefficient D_H for the first sample. For it, we could only determine a complex parameter, namely the hydrogen permeability coefficient K_D, which included the diffusion coefficient and the change in the concentration of atomic hydrogen in the film relative to its equilibrium value Δc_H:

$$K_D = \sqrt{D_H} \cdot \Delta c_H . \qquad (1)$$

The cathodic chronoamperograms revealed two areas of current transients. One was located at initial times $t \leqslant 3$ s, while the second was located at times $t > 4$ s. In the initial period of time, the stage that determined the rate was the stage of atomic hydrogen transition through the solution/metal interphase. Therefore, at the initial section, there was a phase-boundary control of the process of the atomic hydrogen introduction, which for electrodes with $l > 10$ μm was described by equation [13]:

$$i_c(t) = i_c(0) - \left[i_c(0) - i_c^{\infty} \right] \cdot \frac{2\overleftarrow{k}}{\pi^{1/2} \cdot D_H^{1/2}} \cdot t^{1/2}, \qquad (2)$$

and for samples with $l < 10$ μm by equation [23]:

$$\ln\left[i_c(t) - i_c^{\infty} \right] = \ln(F\overleftarrow{k}\Delta c_H) - \frac{\overleftarrow{k}t}{l}. \qquad (3)$$

Here, $i_c(0)$ and i_c^{∞} are the initial and stationary cathodic currents of the chronoamperograms, respectively, and $\overleftarrow{k}$ is the effective constant of the H extraction rate.

When hydrogenation times exceeded 4 s, the control was passed to the stage of solid-phase diffusion, and for samples with $l > 10$ μm it was described by the equation:

$$i_c(t) = i_c^{\infty} + \frac{FK_D}{\pi^{1/2} t^{1/2}}, \qquad (4)$$

whereas for samples with $l < 10$ μm it was described by the equation:

$$\ln\left[i_c(t) - i_c^{\infty} \right] = \ln\left(\frac{2FD}{l} \Delta c_H \right) - \frac{2D_H t}{l^2}. \qquad (5)$$

The parameters of hydrogen permeability determined by anodic current transients were also calculated using two mathematical models. However, due to a more complex mathematical solution of the equation describing the complete curve of anodic current transients, it was only possible to quantitatively consider the case of mixed phase-boundary diffusion kinetics. In that case, we considered sections of anodic chronoamperograms obtained at $t > 30$ s. Then, in models for electrodes of both semi-infinite and finite thickness, the linearisation equations for anodic current transients were as follows:

- for electrodes with $l > 10$ μm

$$i_a(t) = i_a^{\infty} - \frac{FK_D}{\pi^{1/2}} \left(\frac{1}{(t - t_c)^{1/2}} - \frac{1}{t^{1/2}} \right); \qquad (6)$$

- for electrodes with $l < 10$ μm

$$\ln\left(\frac{i_a(t) - i_a^{\infty}}{i_a(t_c) - i_a^{\infty}} \right) \approx -\frac{\pi^2 D_H (t - t_c)}{4l^2}. \qquad (7)$$

Here, $i_a(t_c)$ and i_a^{∞} are the initial and stationary anodic currents of the chronoamperograms, respectively.

Under these conditions, linearisation equations (2)–(7) could only be used to calculate the parameters D_H and Δc_H for thin samples, and parameter K_D for sample 1, which were found by the value of the slopes of the linearised dependencies. The obtained parameters are shown in Table 2.

It is important to note that surface treatment with photons pulses had nearly no effect on the diffusion coefficient of samples 2–4, which was primarily determined by the structural and chemical composition of the alloy. However, the concentration of atomic hydrogen in the alloy decreased linearly with a decrease in the irradiation intensity during the transition from the second sample to the fourth both at the initial stage, when phase-boundary control was

Table 2. Values of the parameters of hydrogen permeability calculated by cathodic and anodic chronoamperograms under kinetics with different controls

Sample			1	2	3	4
Cathodic process	Diffusion control	$D_H \cdot 10^8$, cm²/s	–	3.24 ±1.96	4.33±0.69	3.83±0.11
		$\Delta c_H \cdot 10^5$, mol/cm³	–	5.26±1.95	4.06±0.05	2.48±0.53
	Phase boundary control	$\overleftarrow{k} \cdot 10^4$, cm/s	3.16±0.05	4.66 ±1.51	5.12±0.78	6.74±1.41
		$\Delta c_H \cdot 10^5$, mol/cm³	–	1.93±0.94	1.48±0.48	1.02±0.25
		$K_D \cdot 10^9$, mol/cm²·s$^{1/2}$	6.24±0.05	8.90±0.54	6.68±0.63	4.86±1.02
Anodic process		$D_H \cdot 10^8$, cm²/s	–	1.02±0.01	1.70±0.20	1.34±0.07
		$\Delta c_H \cdot 10^5$, mol/cm³	–	0.44±0.20	0.32±0.21	1.69±1.13
		$K_D \cdot 10^9$, mol/cm²·s$^{1/2}$	0.39±0.11	0.44±0.08	0.42±0.12	1.70±0.21

implemented, and at longer times, when diffusion control dominated.

The value of the effective constant of the extraction rate of atomic hydrogen, on the $\overleftarrow{k}$ contrary, increased. Since the rate constant characterises the phase-boundary transition of H and surface processes, in particular, the extraction of atomic hydrogen from the alloy, it must be sensitive to the surface cleanliness. This means the higher $\overleftarrow{k}$, the cleaner the surface should be, therefore, the surface was cleaned during the transition from sample 1 to sample 4. The obtained data explain an increase in the ionisation peak in voltammograms and the presence of maximum ionisation currents in chronoamperograms during the transition from sample 1 to sample 4. The hydrogen permeability constant K_D changed in the same way as the concentration of atomic hydrogen in the alloy. However, for sample 1, the hydrogen permeability was lower than for samples 2 and 3 and higher than for sample 4.

According to (1), the concentration of atomic hydrogen contributed more to the value K_D rather than its diffusion coefficient. The comparison of the obtained results for cathodic and anodic current transients revealed that the values of the diffusion coefficient D_H determined by anodic transients were almost twice smaller than for the cathodic transients. This may be due to the fact that part of atomic hydrogen was captured in trap defects of the alloy, that is why the time of the experiment (500 s) did not allow completely extracting all the injected atomic hydrogen.

2.4. *The role of electrochemical pretreatment of the surface*

Suppression of the anodic peak of electrooxidation during the transition from the first to the fourth cycle of voltammograms (Fig. 1) occurred as a result of multiple cycling of the electrode potential. Therefore, it is interesting to understand the role of electrochemical surface pretreatment in the overall cleaning procedure. For this study, we chose the sample with the highest atomic hydrogen ionisation rate, i.e. sample 4. Chronoamperograms were obtained for this sample without preliminary quadruple potential cycling and after the cycling (Fig. 4). Sample 4 that had not been exposed to preliminary cycling was designated as 4′.

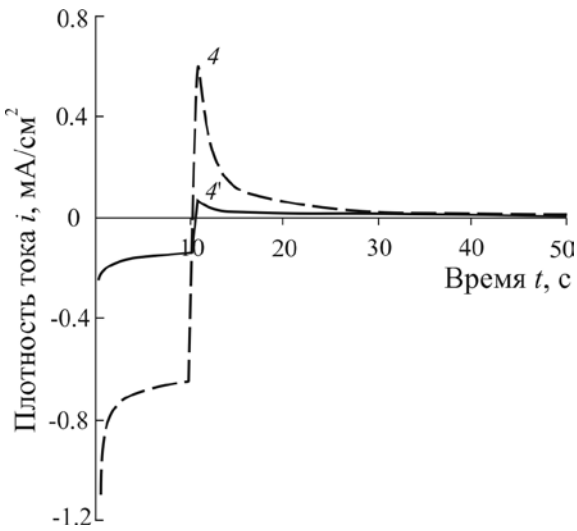

Fig. 4. Chronoamperograms for 48Cu52Pd alloy sample 4 obtained in a 0.1M H_2SO_4 solution without (*4′*) and after preliminary quadruple potential cycling (*4*)

The comparison of the *i,t*-curves obtained for sample 4' with the curves obtained for sample 4 revealed that the introduction rate was about 5 times lower and the ionisation rate was almost 10 times lower. For these samples, we only calculated the parameters of hydrogen permeability by cathodic current transients since they are more informative.

The comparison of parameters calculated for samples 4′ and 4 showed that the diffusion coefficient of atomic hydrogen for both samples coincided within the limits of experimental error (Table 3). However, the extraction rate constant decreased by almost 2 times, which suggests that the phase-boundary transition for the alloy without electrochemical pretreatment was inhibited. The concentration of atomic hydrogen in the alloy both at the stage of phase-boundary exchange and at the diffusion stage decreased. However, the concentration of H at the stage of phase-boundary exchange decreased to a greater extent for the sample which had not been exposed to preliminary potential cycling. In our opinion, this can be due to inhibited process of the atomic hydrogen penetration through the metal/solution interface. Sample 4' was characterised by lower values of the parameters of hydrogen permeability, except for the diffusion coefficient.

4. Conclusions

1. The methods of voltammetry and chronoamperometry allowed establishing that for the foil made from a cold-rolled 48Cu52Pd alloy, surface treatment with photon pulses leads to an increase in the ionisation rate of atomic hydrogen by 15-25 times depending on the sample. This results in the cleaning of the sample surface and in an increase of its roughness (3–5 times), which most likely happens due to the redeposition of the alloy during photon treatment.

2. The diffusion coefficient of atomic hydrogen for samples with a thickness of $l = 10$ μm is about $4 \cdot 10^{-8}$ cm^2/s and does not depend on the method of surface pretreatment with ultrasound and photon pulses. However, extraction rate constant for the extraction of the atomic hydrogen, which characterises the rate of the phase-boundary transition, slightly increases during the transition from sample 1 to sample 4 from $3.16 \cdot 10^{-4}$ to $6.74 \cdot 10^{-4}$ cm/s, respectively. This fact suggests that the processes of both introduction and ionisation are facilitated due to the release of active centres of the surface.

3. Electrochemical cleaning of the surface by means of quadruple potential cycling within a wide range of values contributes to the growth of the extraction rate constant from $3.29 \cdot 10^{-4}$ to $6.74\ 10^{-4}$ cm/s.

Contribution of the authors

The authors contributed equally to this article.

Conflict of interests

The authors declare that they have no known competing financial interests or personal relationships that could have influenced the work reported in this paper.

References

1. Babak V. N., Didenko L. P., Kvurt Y. P., Sementsova L. A. Studying the operation of a membrane module based on palladium foil at high temperatures. *Theoretical Foundations of Chemical Engineering*. 2018;52(2): 181–194. https://doi.org/10.1134/S004057951802001X

2. Han Z., Xu R., Ningbo N., Xue W. Theoretical investigations of permeability and selectivity of Pd-Cu and Pd-Ni membranes for hydrogen separation. *International Journal of Hydrogen Energy*. 2021;46: 23715. https://doi.org/10.1016/j.ijhydene.2021.04.145

3. Liu J., Bellini S., Niek C. A. de Nooijer, ... Caravella A. Hydrogen permeation and stability in ultra-thin Pd-Ru supported membranes. *International*

Table 3. Parameters of hydrogen permeability obtained for samples 4 and 4′

Sample	Cathodic process				
	Diffusion control		Phase boundary control		$K_D \cdot 10^9$, mol/cm^2·s$^{1/2}$
	$D \cdot 10^8$, cm^2/s	$\Delta c_H \cdot 10^5$, mol/cm^3	$\overleftarrow{k} \cdot 10^4$, cm/s	$\Delta c_H \cdot 10^5$, mol/cm^3	
4	3.83±0.11	2.48±0.53	6.74±1.41	1.02±0.25	4.86±1.02
4′	3.79±0.18	1.41±0.65	3.29±1.23	0.55±0.01	2.74±0.84

Journal of Hydrogen Energy. 2020;45(12): 7455–7467. https://doi.org/10.1016/j.ijhydene.2019.03.212

4. Bosko M. L., Fontana A. D., Tarditi A., Cornaglia L. Advances in hydrogen selective membranes based on palladium ternary alloys. *International Journal of Hydrogen Energy*. 2021;46(29): 15572–15594. https://doi.org/10.1016/j.ijhydene.2021.02.082

5. Endo N., Furukawa Y., Goshome K., Yaegashi S., Mashiko K., Tetsuhiko M. Characterization of mechanical strength and hydrogen permeability of a PdCu alloy film prepared by one-step electroplating for hydrogen separation and membrane reactors. *International Journal of Hydrogen Energy*. 2019;44(16): 8290–8297. https://doi.org/10.1016/j.ijhydene.2019.01.089

6. Nooijer N., Sanchez J., Melendez J. Influence of H_2S on the hydrogen flux of thin-film PdAgAu membranes. *International Journal of Hydrogen Energy*. 2020;45 (12): 7303–7312. https://doi.org/10.1016/j.ijhydene.2019.06.194

7. Lee Y-H., Jang Y., Han D. Palladium-copper membrane prepared by electroless plating for hydrogen separation at low temperature. *Journal of Environmental Chemical Engineering*. 2021;9(6): 106509. https://doi.org/10.1016/j.jece.2021.106509

8. Yuna S., Oyama S. T. Correlations in palladium membranes for hydrogen separation: A review. *Journal of Membrane Science*. 2011;375(1-2): 28–45. https://doi.org/10.1016/j.memsci.2011.03.057

9. Decaux C., Ngameni R., Solas D. Time and frequency domain analysis of hydrogen permeation across PdCu metallic membranes for hydrogen purification. *International Journal of Hydrogen Energy*. 2010;35(10): 4883–4892. https://doi.org/10.1016/j.ijhydene.2009.08.100

10. Zhaoa P., Goldbacha A., Xu H. Low-temperature stability of body-centered cubic PdCu membranes. *Journal of Membrane Science*. 2017;542: 60–67. http://dx.doi.org/10.1016/j.memsci.2017.07.049

11. Ievlev V. M., Roshan N. R., Belonogov E. K., ... Glazunova Yu. I. Hydrogen permeability of foil of Pd-Cu, Pd-Ru and Pd-In-Ru alloys received by magnetron sputtering. *Condensed Matter and Interphases*. 2012;14(4): 422–427. Available at: https://www.elibrary.ru/item.asp?id=18485336

12. *Hydrogen in Metals* / Alefeld and J. Volkl (eds.). Berlin; New York: Springer-Verlag; 1978. V.2. 332 p.

13. Morozova N. B., Vvedenskii A. V., Beredina I. P. The phase-boundary exchange and the non-steady-state diffusion of atomic hydrogen in Cu-Pd and Ag-Pd alloys. Part I. Analysis of the model. *Protection of Metals and Physical Chemistry of Surfaces*. 2014;50(6): 699–704. https://doi.org/10.1134/S2070205114060136

14. Francia E. D., Lahoz R., Neff D., Caro T. D., Angelini E., Grassini S. Laser-cleaning effects induced on different types of bronze archaeological corrosion products: chemical-physical surface characterization. *Applied Surface Science*. 2022;573: 150884 https://doi.org/10.1016/j.apsusc.2021.150884

15. Liu Y., Liu W. J., Zhang D. Experimental investigations into cleaning mechanism of ship shell plant surface involved in dry laser cleaning by controlling laser power. *Applied Physics A*. 2020;126: 866. https://doi.org/10.1007/s00339-020-04050-y

16. Mao H., Fan W., Cao H., Chen X., Qiu M., Verweij H., Fan Y. Self-cleaning performance of in-situ ultrasound generated by quartz-based piezoelectric membrane. *Separation and Purification Technology*. 2022;282(B): 120031. https://doi.org/10.1016/j.seppur.2021.120031

17. Chong W. Y., Secker T. J., Dolder P. N., The possibilities of using ultrasonically activated streams to reduce the risk of foodborne infection from salad. *Ultrasound in Medicine and Biology*. 2021;47(6): 1616-1630. https://doi.org/10.1016/j.ultrasmedbio.2021.01.026

18. Zhang H., He F., Che Y., Song Y., Zhou M., Ding, D. Effect of annealing treatment on response characteristics of Pd-Ni alloy based hydrogen sensor. *Surfaces and Interfaces*. 2023;36: 102597 https://doi.org/10.1016/j.surfin.2022.102597

19. Yin Z., Yang Z., Du M., ... Li S. Effect of annealing process on the hydrogen permeation through Pd–Ru membrane. *Journal of Membrane Science*. 2022;654: 120572 https://doi.org/10.1016/j.memsci.2022.120572

20. Yang H., Tang Y., Zou S. Electrochemical removal of surfactants from Pt nanocubes. *Electrochemistry Communications*. 2014;38: 134–137. https://doi.org/10.1016/j.elecom.2013.11.019

21. Pu H., Dai H., Zhang T. Metal nanoparticles with clean surface: The importance and progress. *Current Opinion in Electrochemistry*. 2022;32: 100927. https://doi.org/10.1016/j.coelec.2021.100927

22. Uluc A. V., Moa J. M. C., Terryn H., Bottger A. J. Hydrogen sorption and desorption related properties of Pd-alloysdetermined by cyclic voltammetry. *Journal of Electroanalytical Chemistry*. 2014;734(15): 53–60. https://doi.org/10.1016/j.jelechem.2014.09.021

23. Morozova N. B., Vvedenskii A. V. Phase-boundary exchange and non-stationary diffusion of atomic hydrogen in metal film. I. Analysis of current transient. Condensed *Matter and Interphases*. 2015;17(4): 451-458. https://journals.vsu.ru/kcmf/article/view/91/194

24. Fedoseeva A. I., Morozova N. B., Dontsov A. I., Kozaderov O. A., Vvedenskii A. V. Cold-rolled binary palladium alloys with copper and ruthenium: injection and extraction of atomic hydrogen. *Russian Journal of Electrochemistry*. 2022;58(9): 812-822. https://doi.org/10.1134/S1023193522090051

Information about the authors

Natalia B. Morozova, Cand. Sci. (Chem.), Associate Professor, Department of Physical Chemistry, Voronezh State University (Voronezh, Russian Federation).
https://orcid.org/0000-0003-4011-6510
mnb@chem.vsu.ru

Lidiya E. Sidyakina, 2th year undergraduate student of the Department of Physical Chemistry, Voronezh State University (Voronezh, Russian Federation).
https://orcid.org/0000-0001-6002-1434
sidykina_lidia98@mail.ru

Alexey I. Dontsov, Cand. Sci. (Phys.–Math.), Associate Professor, Department of Materials Science and Industry of Nanosystems, Voronezh State University; Associate Professor of the Department of Physics, Voronezh State Technical University (Voronezh, Russian Federation).
https://orcid.org/0000-0002-3645-1626
dontalex@mail.ru

Vvedenskii Alexander V., Dr. Sci. (Chem.), Full Professor, Department of Physical Chemistry, Voronezh State University (Voronezh, Russian Federation).
https://orcid.org/0000-0003-2210-5543
alvved@chem.vsu.ru

Received 28.03.2023; approved after reviewing 03.04.2023; accepted for publication 15.05.2023; published online 25.09.2023.
Translated by Irina Charychanskaya

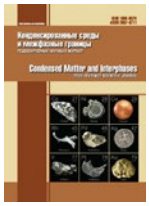

ISSN 1606-867X (Print)
ISSN 2687-0711 (Online)
Condensed Matter and Interphases
Kondensirovannye Sredy i Mezhfaznye Granitsy
https://journals.vsu.ru/kcmf/

Original articles

Research article
https://doi.org/10.17308/kcmf.2023.25/11262

Composition and thermoelectric properties of structures based on iron silicide grown by pulse laser deposition

D. E. Nikolichev✉, R. N. Kriukov, A. V. Nezhdanov, A. V. Zdoroveyshchev, Yu. M. Kuznetsov, V. P. Lesnikov, D. A. Zdoroveyshchev, M. V. Dorokhin, P. B. Demina, A. A. Skrylev

Lobachevsky University,
23 Gagarin av., Nizhny Novgorod 603022, Russian Federation

Abstract

Silicon compounds have a wide range of electrical properties. In particular, the possibility of creating thermoelectric converters based on them looks extremely attractive. The use of most silicides as thermoelectrics today is limited by their low efficiency. The development of approaches consisting in the creation of low-dimensional structures using non-equilibrium formation methods is one of the priority directions for improving the properties of thermoelectric generators. Determination of the effect of technological regimes on the structure, phase-chemical composition and thermoelectric properties of metal-silicide structures is a key task, the solution of which will allow creating highly efficient thermoelectric generators based on them.

Thin-film structures with a layer thickness of ~50 nm formed at different growth temperatures by pulsed laser deposition on two types of substrates: sapphire and gallium arsenide coated with an Al_2O_3 nanolayer were studied in this work. On the formed samples, a chemical analysis and a study of the phase composition were performed. Chemical analysis was carried out by X-ray photoelectron spectroscopy with the chemical composition depth profiling. The phase composition was studied by Raman spectroscopy. In addition, analysis of the elements in the films was carried out by X-ray spectral microanalysis based on a scanning electron microscope. To determine the thermoelectric properties of the formed thin-film structures, the temperature dependences of the Seebeck coefficient and the electrical conductivity coefficient were recorded.

The dependence of the thermoelectric characteristics of iron silicide films on the phase composition is analyzed. In particular, measurements of the thermoelectric properties of $FeSi_x$ thin-film structures registered the manifestation of a strong thermoelectric effect in layers with the maximum number of chemical bonds between iron and silicon. The parameters of the growth process at which the most effective formation of iron-silicon chemical bonds is achieved were determined using the method of X-ray photoelectron spectroscopy. Line shifts from the beta phase of iron disilicide were found in the Raman spectra and the reasons for their appearance were proposed.

Keywords: Iron silicide, Thermoelectric, Pulsed laser deposition, Composition, X-ray photoelectron spectroscopy, Raman spectroscopy

Funding: The work was carried out within the framework of the project N-487-99 under the program of strategic academic leadership «Priority-2030».

For citation: Nikolichev D. E., Kriukov R. N., Nezhdanov A. V., Zdoroveyshchev A. V., Kuznetsov Yu. M., Lesnikov V. P., Zdoroveyshchev D. A., Dorokhin M. V., Demina P. B., Skrylev A. A. Composition and thermoelectric properties of structures based on iron silicide grown by pulse laser deposition. *Condensed Matter and Interphases*. 20223;25(3): 383–391. https://doi.org/10.17308/kcmf.2023.25/11262

Для цитирования: Николичев Д. Е., Крюков Р. Н., Нежданов А. В., Здоровейщев А. В., Кузнецов Ю. М., Лесников В. П., Здоровейщев Д. А., Дорохин М. В., Демина П. Б., Скрылев А. А. Состав и термоэлектрические свойства структур на основе силицида железа, выращенных методом импульсного лазерного осаждения. *Конденсированные среды и межфазные границы*. 2023;25(3): 383–391. https://doi.org/10.17308/kcmf.2023.25/11262

✉ Dmitry E. Nikolichev, e-mail: nikolitchev@phys.unn.ru

1. Introduction

The high potential for the practical application of thermoelectric materials is of considerable interest to scientific groups. Materials based on tellurides and selenides of lead and bismuth today are among the champions in terms of the efficiency of thermoelectric conversion [1-2]. At the same time, there is an active search and development of thermoelectric generators based on silicides of transition *d*-metals (Mn, Fe, Co, etc.) [3]. Interest in thermoelectrics based on silicides is caused, first of all, by the presence of well-established technical processes for creating silicon systems. The variety of phases in metal silicides makes it possible to vary their electronic and photonic properties over a wide range [4-6]. This applies to the same extent to thermoelectric properties.

The dimensionless value of the thermoelectric quality factor $ZT = (\alpha^2\sigma T)/\chi$ determines the efficiency of converting thermal energy into electrical energy at an average absolute temperature T. Due to the high complexity of the experimental determination of thermal conductivity in films, another characteristic is often used that determines the efficiency of a thermoelectric generator: it is the power factor $W = \alpha^2\sigma$ [μW/K²·m].

The main problem of increasing the efficiency of the thermoelectric parameters of the material is that the thermoelectric quality factor ZT is proportional to the electrical conductivity σ and inversely proportional to the thermal conductivity coefficient χ of the material. Wherein the coefficients σ and χ of the material cannot change independently. An increase in electrical conductivity simultaneously reduces the thermo-EMF coefficient α and leads to an increase in the thermal conductivity of the material.

To reduce the thermal conductivity, the phonon contribution is usually suppressed using defect engineering: 1) the introduction of a high concentration of a substitutional impurity with the creation of a large number of defects due to interstitial atoms [7]; 2) the formation of a nanocrystalline structure with a decrease in thermal conductivity due to the presence of a high concentration of grain boundaries on which phonon vibrations [8] are effectively scattered; 3) the formation of thin films or multilayer structures. In the last two cases the thickness of the crystallite or film becomes an additional degree of freedom in controlling the value of ZT.

In this work, thin films of iron silicides with different Fe content grown at different temperatures are considered. As a method of film formation, we used the method of pulsed laser deposition (PLD) in a vacuum, which has proven itself as a cheap, versatile, and productive method for creating thin-film materials [9]. The study of iron silicides seems promising due to the significant difference in the properties of their phases. Interest in the β-$FeSi_2$ phase in addition to its direct and small band gap [10] arises when this material is used as a thermoelectric energy converter for the range near and below room temperature [11].

At the moment, the maximum ZT for materials based on iron silicides is 0.4 and 0.2 for *n*- and *p*-type semiconductors, respectively. [12]. It is also known that the presence of nanoclusters of this phase formed in epitaxial layers leads to a decrease in the thermal conductivity [13]. The complex of phases of iron silicides (Fe_3Si, FeSi and $FeSi_2$) in the future may have better thermoelectric properties than these phases separately. Structures with thin films, in which the set and content of iron silicide phases are balanced, can potentially act as an efficient thermoelectric converter. Thus, the necessary objective is to determine the phase-chemical composition of thermoelectric systems based on $FeSi_x$.

2. Experimental technique

The structures were formed by pulsed laser deposition in a vacuum chamber with a residual gas pressure of ~ $1\cdot10^{-6}$ Torr.

The composite target was sputtered from the Si and Fe sectors by an LQ-529A pulsed YAG:Nd laser operating at the second harmonic with λ = 0.532 μm. The laser radiation power was ~200 mJ and the pulse duration was 10 ns with a frequency of 10 Hz. The size of the silicon and iron sectors determined the total content of each of the elements in the resulting film. During the first stages, films with a high content of Fe were created, when the angles of the iron sector were ∠ Fe = 240° and ∠ Fe = 120°. Then the angle was reduced to ∠ Fe = 90°. Sputtering was performed

at substrate temperatures of 200, 400, 500, and 550 °C for 40 minutes. The material deposition rate was 1 – 2 nm/min, the average film thickness was ~ 60 nm. The deposition was carried out on two types of substrates: a sapphire (R-cut) and a GaAs (100) substrate with a 20-nm Al_2O_3 layer deposited by vacuum electron evaporation. The choice of substrates is determined by two factors. Firstly, the sapphire substrate does not allow diffusion of material, primarily *d*-metal [14]. Coating the gallium arsenide substrate with a layer of Al_2O_3 also effectively stops this process. [15]. Second, phase states were originally supposed to be recorded by Raman spectroscopy (RS), but the use of a cheap silicon substrate complicates the applying of RS due to the presence of a high-intensity silicon signal from the substrate. As a result, films on a sapphire substrate were used as reference films, while films on a gallium arsenide substrate with an Al_2O_3 layer were used to assess the possibility of forming layers on a semiconductor.

The chemical analysis of the $FeSi_x$/sapphire and $FeSi_x/Al_2O3$/GaAs structures was carried out by X-ray photoelectron spectroscopy (XPS). The spectrometer is part of the Multiprobe RM ultra-high vacuum measuring complex (Omicron Nanotechnology GmbH, Germany). To excite the emission of photoelectrons, Mg K_α radiation was used, and Fe 2*p*, Si 2*s*, Si 2*p*, O 1*s*, C 1*s* photoelectron (PE) lines were recorded. The analysis area diameter was 3 mm. The depth profiling of the composition was carried out by sputtering the layers with Ar^+ ions with an energy of 1 keV at an angle of 45° relative to the sample surface. The numerical values of the concentrations were calculated in accordance with the previously developed method [16].

The chemical shift for the bonding of iron with silicon is not recorded by XPS and this is a serious obstacle in the interpretation of PE lines. The determination of the presence of iron silicide compounds was carried out using the approaches given in [17-18]. To determine the presence of a phase related to iron silicides we used the peaks of photoelectron energy losses on plasmon oscillations, which are recorded for silicides to the left of the main Fe 2*p* doublet at an energy of ~ 730 eV and are absent in the PE spectrum for metallic iron. The intensity ratio of the plasmon loss lines and the main Fe 2*p* doublet is approximately 1:2. This feature made it possible to estimate the concentration of iron in chemical bonding with silicon.

Raman spectra were recorded on an NTEGRA Spectra Raman spectroscopy complex (NT-MDT, Zelenograd) using lasers with a wavelength of 473 nm. The radiation was focused by a 100× objective lens with a numerical aperture of NA = 0.9. The power of unfocused laser radiation measured with a silicon photodetector 11PD100-Si (Standa Ltd, Lithuania) varied in the range from 1 mW to 1 μW. The Raman scattering spectra were recorded in the reflection scheme at room temperature. RS was carried out in the range of 50–900 cm^{-1} with a resolution of 0.7 cm^{-1}.

Electron microscopic imaging, elemental analysis, and element mapping were carried out on a SEM JSM IT-300LV (JEOL, Japan) with an X-MaxN 20 X-ray energy-dispersive spectroscopy set (Oxford Instruments, UK). The measurements were carried out under high vacuum conditions with an electron probe energy of 20 keV. In addition to SEM the surface topography of $FeSi_x$ film was studied using a SolverPro atomic force microscope (NT-MDT, Zelenograd) in semicontact mode.

The temperature dependences of the Seebeck coefficient α and conductivity σ were measured in a Janis CCS-300S/202 closed-loop cryostat with a temperature range of 10–400 K. The sample was pressed with one face to the heater resistor and the other was pressed against a massive heat sink connected to the cooled cryostat rod. To heat up the resistor a Keithley 6221 current source-meter with a current measurement/maintenance accuracy of ~ 2 nA was used. The temperature gradient was stabilized with a LakeShore 335 temperature controller with feedback. The temperature gradient was 10 K with an accuracy of 0.1 K. The thermo-EMF signal was measured using a Keithley 2000 meter [19].

3. Results and discussion

The behaviour of the depth distribution profiles of chemical elements (Fig. 1) demonstrates that, at high Fe concentrations, spatial separation of Si and Fe occurs. It can be seen from Fig. 1a that near the heterointerface the Fe/Si ratio is greater than one and vice versa on the surface.

This circumstance can be explained by the inhomogeneity of the flow of atoms over time during laser deposition. With a decrease in the proportion of metal this inhomogeneity decreases (Fig. 1 b). At the same time a large number of Fe atoms in the layer facilitates the penetration of oxygen atoms into the system (Fig. 1 a). At a lower Fe concentration, the presence of oxygen is not detected. This indicates the concentration dependence of the efficiency of diffusion of oxygen atoms deep into the sample.

It can also be concluded from the behaviour of the Al, O, Si, and Fe profiles at the layer/substrate heterointerface that the Al_2O_3 layer effectively functions as a diffusion barrier. Subsequently, it was determined that the phase distribution is the same for both substrates.

At the same time, the presence of Fe oxide at the film/Al_2O_3 heterointerface (Fig. 1a) indicates the redundancy and physical adsorption of O atoms to Al_2O_3 layers. The composition of the $SiFe_x$ film itself mainly consists of iron silicides which is determined by the distribution profiles of the Fe-Si chemical bond. At the same time, the presence of elemental iron (Fe-Fe bonds) is also recorded and its volume fraction depends on the concentration. At a Fe concentration of 55 at.% only about 30 at.% is spent on the formation of Fe-Si bonds which is about 54 % of the total number of metal atoms. In turn, a decrease in the Fe concentration to 40 at.% leads to the fact that already about 90 % of iron atoms form a chemical bond with Si atoms.

The nonequilibrium process of pulsed laser deposition leads to fluctuations in the distribution profiles of Fe-Fe and Fe-Si chemical bonds. In addition, the applied film formation technology is characterized by the presence of defects on the surface [20]. Drop-like defects are formed due to the presence in the flow of large particles of the substance emitted from the target. Using the method of X-ray spectral analysis performed on the basis of SEM (Fig. 2 a) it was determined that the droplets on the surface consist of both iron and silicon (Fig. 2 b, c). The average size of objects consisting of Si significantly exceeds the diameter of objects consisting of Fe atoms (Fig. 2 b, c) which is caused by different thermodynamic conditions of laser evaporation of the combined Si/Fe target.

Further studies were aimed at studying the phase composition of thin-film structures of iron silicides created by the PLD method with the angle of the iron sector of the sample ∠ Fe = 90° since they demonstrated the almost complete combination of iron with silicon, on the one hand, and still a high concentration of additional phases, providing in the future a decrease in the phonon part of the thermal conductivity, on the other hand. Raman spectra were recorded for $FeSi_x$ films obtained at different temperatures of the Al_2O_3/GaAs substrate (Fig. 3). In all presented Raman spectra one can distinguish peaks related

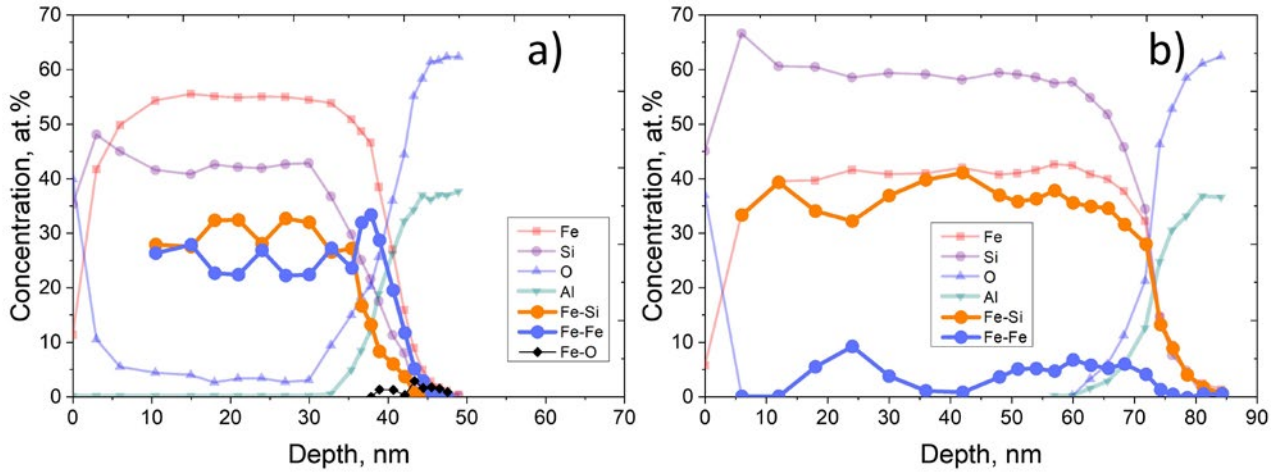

Fig. 1. Depth distribution profile of the concentration of chemical elements and chemical bonds in an $SiFe_x$ film grown on an Al_2O_3/GaAs substrate supersaturated with iron with an iron sector angle of ∠ Fe = 240° (a) and with a reduced iron content with an iron sector angle of ∠ Fe = 90° (b)

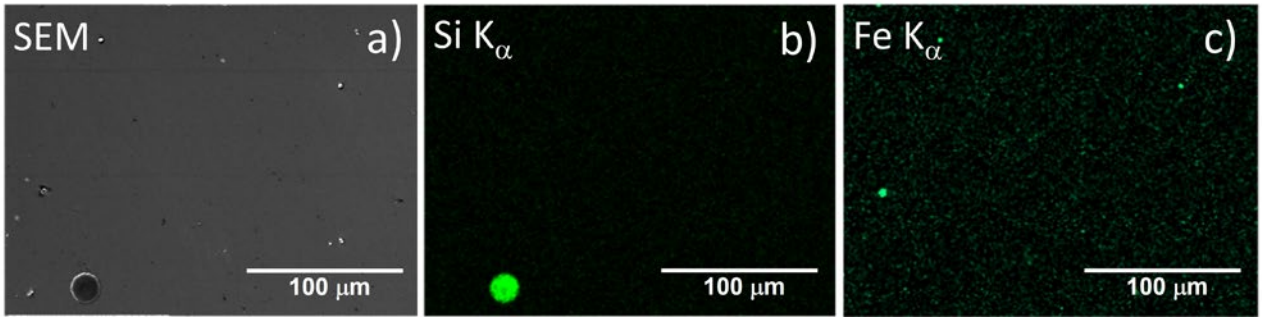

Fig. 2. Topography and elemental composition of the $FeSi_x$ film surface grown at a substrate temperature of 500°C: a) SEM surface image; b) Si distribution map in the Si $K_{\alpha1}$ emission line; and c) Fe distribution map in the Fe $K_{\alpha1}$ emission line

to the GaAs substrate: one of them is located at 268 cm^{-1} and corresponds to the transverse optical component (TO-mode), the second at 291 cm^{-1} belongs to the longitudinal optical component (LO-mode) [21]. Their presence is associated with a small thickness of the film and Al_2O_3 stop layer, as a result of which the signal is detected from the gallium arsenide substrate.

Depending on the substrate temperature during the formation of $FeSi_x$ films, significant changes are observed in the Raman spectra. At a substrate temperature of 200 °C the main contribution to the spectrum is made by a wide continuum related to amorphous silicon in which broad lines can be distinguished in the region of 180 cm^{-1} related to the transverse acoustic mode (TA) and in the region of 480 cm^{-1} related to the transverse optical mode (TO) [22]. The remaining modes from amorphous silicon are weakly expressed, in particular, at 300 cm^{-1} a longitudinal acoustic LA mode is recorded and at 410 cm^{-1} a longitudinal optical LO mode can be found [22]. Also, on the spectrum, there is a weakly pronounced shoulder at 160 cm^{-1} related to the vibrations of the Fe-Fe bonds [23].

Increasing the substrate temperature to 400 °C leads to the appearance of clearly defined lines at frequencies: 193 cm^{-1} with a nearby shoulder at ~ 180 cm^{-1}, ~ 246 cm^{-1} and weakly pronounced broad lines in the regions of 340 cm^{-1} and 385 cm^{-1}. There is also a broad maximum at ~480 cm^{-1} which is related to the transverse optical mode (TO) in amorphous silicon. The presence of lines related to vibrations of Fe-Fe bonds at 193 cm^{-1} and 246 cm^{-1} in the Raman spectrum indicates the formation of a β-$FeSi_2$ crystalline phase in the film [23]. Lines in the regions of 340 cm^{-1} and 385 cm^{-1} may be present, on the one hand, due to the structural imperfection of the film by analogy with the observed peaks in nonstoichiometric $NiSi_2$ [24] and due to second-order scattering, on the other hand [25].

A further increase in the substrate temperature, up to 550 °C leads to a narrowing and an increase in the intensity of the peaks at 193 cm^{-1} and 246 cm^{-1}, as well as to the appearance of a peak at ~ 521 cm^{-1} which belongs to the TO mode of crystalline silicon [26].

It is worth paying attention to the presence of a shift by 2 cm^{-1} in the position of the peak at 246 cm^{-1} related to β-$FeSi_2$. This shift was registered when comparing the spectra of films

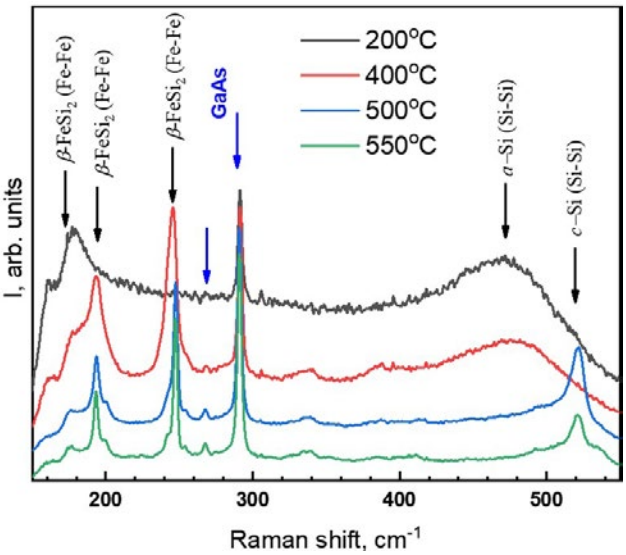

Fig. 3. Raman spectra recorded for $FeSi_x/Al_2O_3$/GaAs thin-film structures formed at different substrate temperatures in the PLD process

formed at 400 °C and 500 °C. One of the reasons for it can be defects, impurities, lattice distortions of the β-phase of iron disilicide [27]. Another circumstance leading to a shift may be the appearance of a nanocrystalline β-$FeSi_2$ phase by analogy with crystalline silicon [28].

The measurements of Seebeck coefficients, electrical conductivity and calculation of the power factor were carried out for all structures obtained at substrate temperatures of 200, 400, 500, and 550 °C. For all these structures a target with an iron sector ∠ Fe = 90° during the PLD process was used. The characteristic temperature dependences of these parameters are shown in Fig. 4 a–c. Additionally, measurements were made for structures supersaturated with iron in the range of medium temperatures (~ 300–600 °C). The temperature dependence of the power factor for specimens with iron attachment angles on the target ∠ Fe = 120° and ∠ Fe = 240° and a substrate growth temperature of 200 °C is shown in Fig. 4 d.

The electrical conductivity of $FeSi_x$ films at the same *x* depends significantly on the substrate temperature during growth and decreases as it increases. Presumably, this is due to the relaxation of the silicon lattice the formation of iron precipitates and iron silicides [29] in the layer which leads to an increase in the layer resistance. The highest value of the Seebeck coefficient α for samples in which an almost complete combination of iron and silicon has occurred (the angle of iron in the evaporated target ∠ Fe = 90°) is recorded in the low temperature region of about 100 K and its value is ~ 150 μV/K. At lower temperatures α could not be recorded due to a sharp increase in the electrical resistance of the film at temperatures

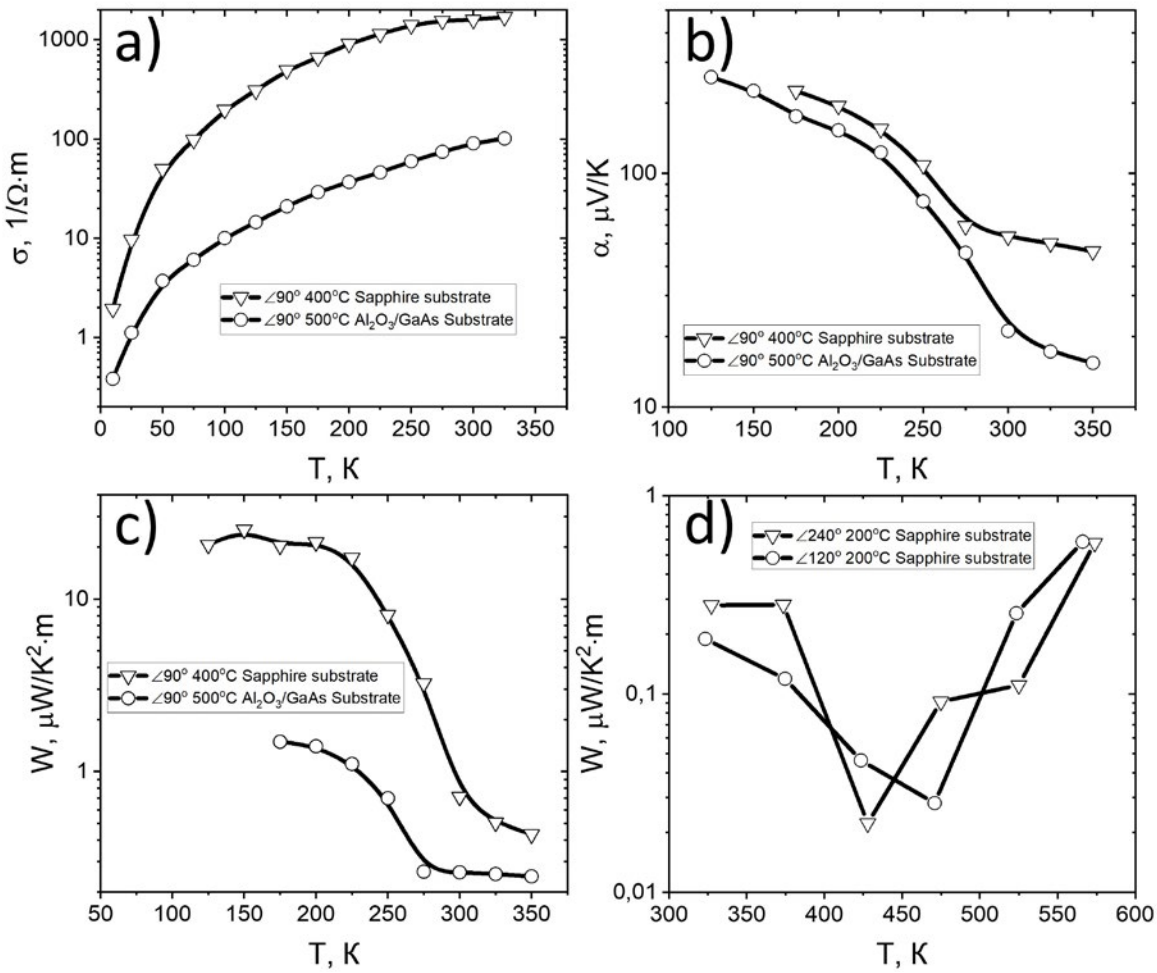

Fig. 4. Temperature dependence of the electrical conductivity coefficient, Seebeck coefficient and power factor for samples with iron sector on a target of ∠ Fe = 90° (a–c) and temperature dependence of the power factor for a Fe-supersaturated film with iron sectors on targets of ∠ Fe = 120° and ∠ Fe = 240° (d)

below 150 K. The maximum calculated value of the power factor *W* (Fig. 4 a) is ~ 20 μW/K²·m. Thus, a sufficiently high value of α is levelled by the low conductivity of thermoelectric films, formed when the iron angle in the evaporated target is ∠ Fe = 90°.

Despite the fact that the electrical conductivity of films supersaturated with iron is 4 orders of magnitude higher at temperatures of 300–600 K, the power factor reaches values only up to tenths of μW/K²·m (Fig. 4 d). This is due to the low efficiency of their thermoelectric conversion, when the maximum value of the Seebeck coefficient does not exceed 10 μV/K. The presence of a minimum in the temperature dependence of the power factor is due to the transition to intrinsic conductivity while the value of the Seebeck coefficient is minimal. Thus, a simple increase in electrical conductivity due to an increase in the iron content does not remove the problem of increasing the power factor, and the solution to this problem lies in the area of optimizing the content of metal-silicide compounds, when the Seebeck coefficient is directly proportional to their amount.

4. Conclusion

The application of X-ray photoelectron spectroscopy and Raman spectroscopy made it possible to find the parameters for the formation of $FeSi_x$ films by pulsed laser deposition, in which iron is almost completely combined with silicon, while the Fe concentration remains at a high level of 40 at.%. XPS depth profiling of the composition of thin-film structures made it possible to determine that an additional Al_2O_3 stop layer formed on a semiconductor substrate by high-vacuum electron evaporation effectively prevents the diffusion-active metal penetrating from the film into the substrate. This is an important technological aspect in the formation of structures under nonequilibrium conditions of the method of pulsed laser deposition and allows the use of a wide range of substrates for the creation of film and multilayer structures with high quality heterointerfaces. Thermoelectric measurements have shown that it is possible to obtain a high thermoelectric effect for films where the iron silicide phase is effectively formed. However, for such structures it is necessary to increase the thermoelectric conversion power factor by increasing the electrical conductivity. This can be facilitated by choosing the growth temperature or parameters of postgrowth annealing of structures that do not lead to the formation of undesirable inclusions in the film material, as well as additional doping of the films with other materials.

Contribution of the authors

The authors contributed equally to this article.

Conflict of interests

The authors declare that they have no known competing financial interests or personal relationships that could have influenced the work reported in this paper.

References

1. Tritt T. M., Subramanian M. A. Thermoelectric materials, phenomena, and applications: a bird's eye view. *MRS Bulletin*. 2006;31: 188–198. https://doi.org/10.1557/mrs2006.44

2. Belonogov E. K., Dybov V. A., Kostyuchenko A. V., Kuschev S. B., Sanin V. N., Serikov D. V., Soldatenko S. A. Modification of the surface of thermoelectric branches based on a Bi_2Te_3-Bi_2Se_3 solid solution by pulse photon treatment method. *Condensed Matter and Interphases*. 2017;19(4): 479–488. https://doi.org/10.17308/kcmf.2017.19/226

3. Rowe D. M. *Thermoelectrics Handbook. Macro to Nano*. New York: CRC Press; 2006. 1008 p. https://doi.org/10.1201/9781420038903

4. Chen L. J. *Silicide Technology for Integrated Circuits*. London: TheInstitution of Engineering and Technology; 2004. 279 p. https://doi.org/10.1049/PBEP005E

5. Wan Q., Wang T. H., Lin C. L. Synthesis and optical properties of semiconducting beta-FeSi2 nanocrystals. *Applied Physics Letters*. 2003;82: 3224–3226. https://doi.org/10.1063/1.1574845

6. Odkhuu D., Yun W. S., Hong S. C. Magnetocrystalline anisotropy energy and spin polarization of Fe3Si in bulk and on Si(001) and Si(111) substrates. *Thin Solid Films*. 2011;519: 8218–8222. https://doi.org/10.1016/j.tsf.2011.03.093

7. Feng X., Fan Y., Nomura N., Kikuchi K., Wang L., Jiang W., Kawasaki A. Graphene promoted oxygen vacancies in perovskite for enhanced thermoelectric properties. *Carbon*. 2017;112: 169–176. https://doi.org/10.1016/j.carbon.2016.11.012

8. Satyala N., Rad A. T., Zamanipour Z., Norouzzadeh P., Krasinski J. S., Tayebi L., Vashaee D. Reduction of thermal conductivity of bulk

nanostructured bismuth telluride composites embedded with silicon nano-inclusions. *Journal of Applied Physics*. 2014;115(4): 044304. https://doi.org/10.1063/1.4861727

9. Zvonkov B. N., Vikhrova O. V., Danilov Yu. A., ... Sapozhnikov M. V. Using laser sputtering to obtain semiconductor nanoheterostructures. *Journal Optical Technology*. 2008;75(6): 389–393. https://doi.org/10.1364/jot.75.000389

10. Liu Z., Osamura M., Ootsuka T., ... Tanoue H. Effect of a Fe_3Si buffer layer for the growth of semiconducting β-$FeSi_2$ thin film on stainless steel substrate. *Journal of Crystal Growth*. 2007;307(1): 82–86. https://doi.org/10.1016/j.jcrysgro.2007.06.007

11. Behr G., Werner J., Weise G., Heinrich A., Burkov A., Gladun C. Preparation and properties of high-purity β-$FeSi_2$ single crystals. *Physica Status Solidi (a)*. 1997;160(2): 549–556. https://doi.org/10.1002/1521-396x(199704)160:2<549::aid-pssa549>3.0.co;2-8

12. Lange H. Electronic properties of semiconducting silicides. *Physica Status Solidi B*. 1997;201(1): 3–65. https://doi.org/10.1002/1521-3951(199705)201:1<3::aid-pssb3>3.0.co;2-w

13. Chen Z.-G., Han G., Yang L., Cheng L., Zou J. Nanostructured thermoelectric materials: Current research and future challenge. *Progress in Natural Science: Materials International*. 2012;22(6): 535–549. https://doi.org/10.1016/j.pnsc.2012.11.011

14. Ohnuma I., Abe S., Shimenouchi S., Omori T., Kainuma R., Ishida K. Experimental and thermodynamic studies of the Fe–Si binary system. *ISIJ International*. 2012;52(4): 540–548. https://doi.org/10.2355/isijinternational.52.540

15. Bobrov A. I., Danilov Yu. A., Dorokhin M. V., ... Syed S. Application of cobalt in spin light Schottky diodes with InGaAs/GaAs quantum wells. *Surface. X-ray, synchrotron and neutron studies*. 2015;7: 57–60. https://doi.org/10.7868/S0207352815070057

16. Boryakov A. V., Surodin S. I., Kryukov R. N., Nikolichev D. E., Zubkov S. Yu. Spectral fit refinement in XPS analysis technique and its practical applications. *Journal of Electron Spectroscopy and Related Phenomena*. 2018;229: 132–140. https://doi.org/10.1016/j.elspec.2017.11.004

17. Ohtsu N., Oku M., Nomura A., Sugawara T., Shishido T., Wagatsuma K. X-ray photoelectron spectroscopic studies on initial oxidation of iron and manganese mono-silicides. *Applied Surface Science*. 2008;254: 3288–3294. https://doi.org/10.1016/j.apsusc.2007.11.005

18. Sidashov A. V., Kozakov A. T., Kolesnikov V. I., Manturov D. S., Yaresko S. I. Surface modification features of tool steels by laser radiation. *Journal of Friction and Wear*. 2020;41(6): 549–553. https://doi.org/10.3103/S1068366620060185

19. Dorokhin M. V., Demina P. B., Erofeeva I. V., ... Trushin V. N. Nanostructured SiGe:Sb solid solutions with improved thermoelectric figure of merit. *Nanosystems: Physics, Chemistry, Mathematics*. 2020;11(6): 680–684. https://doi.org/10.17586/2220-8054-2020-11-6-680-684

20. Demidov E. S., Zubkov S. Yu., Lesnikov V. P., Maksimov G. A., Nikolichev D. E., Podol'skii V. V. X-Ray photoelectron and auger spectroscopy analysis of Ge:Mn-based magnetic semiconductor layers. *Journal of Surface Investigation. X-ray, Synchrotron and Neutron Techniques*. 2008;2(4): 541–545. https://doi.org/10.1134/S1027451008040083

21. Volodin V. A., Sinyukov M. P. Anisotropy of long-wavelength optical phonons in GaAs/AlAs superlattices. *JETP Letters*. 2014;99: 396–399. https://doi.org/10.1134/S0021364014070121

22. Volodin V. A., Koshelev D. I. Quantitative analysis of hydrogen in amorphous silicon using Raman scattering spectroscopy. *Journal of Raman Spectroscopy*. 2013;44: 1760–1764. https://doi.org/10.1002/jrs.4408

23. Terai Y., Yamaguchi H., Tsukamoto H., Murakoso N., Hoshida H. Polarized Raman spectra of β-$FeSi_2$ epitaxial film grown by molecular beam epitaxy. *AIP Advances*. 2018;8: 105028. https://doi.org/10.1063/1.5042801

24. Li F., Lustig N., Klosowski P., Lannin J. S. Disorder-induced Raman scattering in $NiSi_2$. *Physical Review B*. 1990;41(14): 10210–10213. https://doi.org/10.1103/PhysRevB.41.10210

25. Guizzetti G., Marabelli F., Patrini M., Pellegrino P., Pivac B. Measurement and simulation of anisotropy in the infrared and Raman spectra of B single crystals. *Physical Review B*. 1997;55(21): 14290–14297. https://doi.org/10.1103/PhysRevB.55.14290

26. Spizzirri P., Fang J., Rubanov S., Gauja E., Prawer S. Nano-Raman spectroscopy of silicon surfaces. *Materials Forum*. 2008;34: 161–166. https://doi.org/10.48550/arXiv.1002.2692

27. Lefki K., Muret P., Bustarret E., ... Brunel M. Infrared and Raman characterization of beta iron silicide. *Solid State Communications*. 1991;80, 791–795. https://doi.org/10.1103/10.1016/0038-1098(91)90509-T

28. Doğan I., Van De Sanden M. C. M. Direct characterization of nanocrystal size distribution using Raman spectroscopy. *Journal of Applied Physics*. 2013;114: 134310. https://doi.org/10.1063/1.4824178

29. Terukov E. I., Kon'kov O. I., Kudoyarova V. Kh., Gusev O. B., Davydov V. Yu., Mosina G. N. The formation of β-$FeSi_2$ precipitates in microcrystalline Si. *Semiconductors*. 2002;36(11): 1235–1239. https://doi.org/10.1134/1.1521222

Information about the authors

Dmitri E. Nikolichev, Cand. Sci. (Phys.-Math), Associate Professor at the Department of Physics of Semiconductors, Electronics and Nanoelectronics, Lobachevsky University, (Nizhny Novgorod, Russian Federation).
https://orcid.org/0000-0002-0270-850X
nikolitchev@phys.unn.ru

Ruslan N. Kriukov, Cand. Sci. (Phys.-Math), Assistant at the Department of Physics of Semiconductors, Electronics and Nanoelectronics, Lobachevsky University (Nizhny Novgorod, Russian Federation).
https://orcid.org/0000-0001-6684-5899
kriukov@yandex.ru

Alexey V. Nezhdanov, Cand. Sci. (Phys.-Math), Associate Professor at the Department of Physics of Semiconductors, Electronics and Nanoelectronics, Lobachevsky University (Nizhny Novgorod, Russian Federation).
https://orcid.org/0000-0002-7484-106X
nezhdanov@phys.unn.ru

Anton V. Zdoroveyshchev, Cand. Sci. (Phys.-Math), Senior Research Fellow of Laboratory of Spin and Optical Electronics in Physical-Technical Research Institute, Lobachevsky University of (Nizhny Novgorod, Russian Federation).
https://orcid.org/0000-0002-8379-2263
zdorovei@nifti.unn.ru

Yuri M. Kuznetsov, Junior Research Fellow of Laboratory of Spin and Optical Electronics in Physical-Technical Research Institute, Lobachevsky University of Nizhny Novgorod (Nizhny Novgorod, Russian Federation).
https://orcid.org/0000-0001-9450-8953
yurakz94@list.ru

Daniil A. Zdoroveyshchev, Laboratory Technician of Laboratory of Spin and Optical Electronics in Physical-Technical Research Institute, Lobachevsky University of Nizhny Novgorod (Nizhny Novgorod, Russian Federation).
https://orcid.org/0000-0002-2877-4628
daniel.zdorov@nifti.unn.ru

Valery P. Lesnikov, Research Fellow of Laboratory of Spin and Optical Electronics in Physical-Technical Research Institute, Lobachevsky University (Nizhny Novgorod, Russian Federation).
lesnikov@nifti.unn.ru

Michael V. Dorokhin, Dr. Sci. (Phys.-Math), Leading Researcher of Laboratory of Spin and Optical Electronics in Physical-Technical Research Institute, Lobachevsky University (Nizhny Novgorod, Russian Federation).
https://orcid.org/0000-0001-5238-0090
dorokhin@nifti.unn.ru

Polina B. Demina, Junior Research Fellow of Laboratory of Spin and Optical Electronics in Physical-Technical Research Institute, Lobachevsky University (Nizhny Novgorod, Russian Federation).
https://orcid.org/0000-0003-3134-2268
demina@phys.unn.ru

Alexey A. Skrylev, Laboratory Technician of Laboratory of Functional Materials, Lobachevsky University of Nizhny Novgorod (Nizhny Novgorod, Russian Federation).
https://orcid.org/0000-0002-5399-6038
skrylev.lexa@mail.ru

Received 07.12.2022; approved after reviewing 19.12.2022; accepted for publication 26.12.2022; published online 25.09.2023.
Translated by author
Edited and proofread by Valentina Mittova

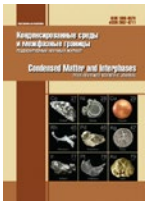

ISSN 1606-867X (Print)
ISSN 2687-0711 (Online)
Condensed Matter and Interphases
Kondensirovannye Sredy i Mezhfaznye Granitsy
https://journals.vsu.ru/kcmf/

Original articles

Research article
https://doi.org/10.17308/kcmf.2023.25/11263

Features of the resistive response to ozone of semiconductor PdO sensors operating in thermomodulation mode

S. V. Ryabtsev[1]✉, N. Yu. Obvintseva[2], V. V. Chistyakov[3], A. A. K. Al-Habeeb[1], A. V. Shaposhnik[4], S. Yu. Turishchev[1], E. P. Domashevskaya[1]

[1]*Voronezh State University,*
1 Universitetskaya pl., Voronezh 394018, Russian Federation

[2]*University of Science and Technology «MISIS»,*
4 Leninskiy pr., Moscow 119049, Russian Federation

[3]*Ioffe Institute,*
26 Polytekhnicheskaya st., St. Petersburg 194021, Russian Federation

[4]*Voronezh State Agrarian University named after Peter the Great*
1 Michurin st., Voronezh 394087, Russian Federation

Abstract

This work is dedicated to the issue of increasing the selectivity of semiconductor PdO sensors in case of ozone detection.

Thin PdO films were obtained using thermal sputtering of Pd and its subsequent oxidation. We characterised the obtained material using X-ray diffraction analysis and optical spectroscopy. We studied the gas-sensing properties of thin films in the mode of periodically changing temperature. The use of the thermal modulation mode allowed discovering the extremes of the resistive response of the PdO sensor in ozone, which helped to increase the selectivity of the sensor while detecting this gas.

We suggested a possible mechanism of ozone chemisorption, which determined the specific form of the thermally modulated PdO response. The studies of the resistive response of PdO sensors under the conditions of ultraviolet illumination confirmed the suggested mechanism of ozone chemisorption.

Keywords: Semiconductor gas sensors, Palladium oxide, Ozone, Thermal modulation mode, Features of resistive response of sensors, Oxygen chemisorption mechanism, Oxygen chemisorption under the conditions of UV illumination

Funding: The study was supported by the Russian Foundation for Basic Research, grant No. 20-03-00901; the Ministry of Education and Science of the Russian Federation in the framework of the state order to higher education institutions in the sphere of scientific research for years 2020–2022, project No. FZGU-2020-0036; the Ministry of Education and Science of the Russian Federation, agreement No. 075-15-2021-1351, regarding automation of electrophysical measurements.

For citation: Ryabtsev S. V., Obvintseva N. Yu., Chistyakov V. V., Al-Habeeb A. A. K., Shaposhnik A. V., Turishchev S. Yu., Domashevskaya E. P. Features of the resistive response to ozone of semiconductor PdO sensors operating in thermomodulation mode. *Condensed Matter and Interphases*. 2023;25(3): 392–397. https://doi.org/10.17308/kcmf.2023.25/11263

Для цитирования: Рябцев С. В., Обвинцева Н. Ю., Чистяков В. В., Аль-Хабиб А. А. К., Шапошник А. В., Турищев С. Ю., Домашевская Э. П. Особенности резистивного отклика на озон полупроводниковых сенсоров PdO, работающих в режиме термомодуляции. *Конденсированные среды и межфазные границы*. 2023;25(3): 392–397. https://doi.org/10.17308/kcmf.2023.25/11263

✉ Stanislav V. Ryabtsev, e-mail: ryabtsev@phys.vsu.ru

1. Introduction

The analysis of gas media is required in order to ensure safety in production, to control various technological processes, in environmental monitoring, scientific research, healthcare, etc. We believe that the devices based on semiconductor gas sensors (SCGS) may be the most suitable for these purposes. As compared to other gas analysers, their advantages include the low cost of manufacture, energy efficiency, high sensitivity, a lack of need for consumable products in the gas analysis process, and analysis continuity. The idea of their operation is changing the resistance of the oxide semiconductor material in the medium of a particular gas due to chemisorption. SCGS also have some disadvantages, among which is low selectivity in the detection of gas mixtures. There are several ways to neutralise this disadvantage, for example, by creating multi-sensor systems that consist of partially selective sensor elements. Signals from this array of sensors are processed using artificial neural networks, the principal component analysis, etc. Another known method of increasing selectivity is by modulating the operating temperature of sensors [1–4]. The sensor temperature can be changed according to a sinusoidal law or it may have another periodic form [5]. The informative value of the resistive response of the sensor in this mode of operation is significantly improved due to several reasons. The law of transformation of the gas adsorption effect into the resistive response of the sensor is of non-linear nature [1–4]. Therefore, the temperature-modulated resistive response may have typical features in the form of harmonics, the amplitude-frequency characteristics of which are discovered by the Fourier transformation of the sensor signal [1–5]. A change in the sensor temperature also leads to a shift in the adsorption-desorption equilibrium, which, in its turn, causes the formation of different charge states of particles on the sensor surface. For instance, the charge states of chemisorbed oxygen change in this way on the sensor surface in the course of heating or cooling [6]. This process is rather specific for each adsorbent-adsorbate pair and has an effect on the shape of the resistive response of the sensor. The problem of selectivity can be solved to some extent using the analysis of the sensor response forms in the course of thermal modulation.

The goal of this work was to identify the features and mechanisms of formation of the resistive response of sensors in the presence of ozone, which can ensure its selective detection. In this work we used semiconductor PdO films operating in the thermal modulation mode were used as sensors.

The research is relevant, on the one hand, due to by the widespread use of ozone in various technological processes, and on the other hand, due to its extreme toxicity (first hazard class) and the need for reliable control of the fact that ozone concentration must be controlled in the workplace.

2. Experiment

We used ~30 nm thick PdO films and determined their thickness using an LEF-757 ellipsometer. We obtained oxide films using air oxidation of metallic Pd layers deposited on dielectric substrates by thermal evaporation at a temperature of 550 °C. The dielectric substrates had platinum electrodes for measuring film resistance and a platinum heater which also served as a temperature sensor.

According to X-ray diffraction analysis, the obtained layers had a tetragonal structure (Fig. 1).

Using spectroscopic studies in the range of 300-900 nm (4.1–1.4 eV), we determined the band gap of PdO. Plotting the spectroscopic data in Tauc coordinates resulted in value E_g ~ 2.3 eV (Fig. 2).

The semiconductor nature of the conductivity of the obtained oxide layers was also confirmed by gas-sensor experiments. In the course of chemisorption of ozone (an electron acceptor gas), the resistance of PdO sensors decreased, which corresponded to the *p*-type semiconductor conductivity.

In the thermal modulation mode, the temperature of the PdO sensor varied from 50 to 300 °C according to a sinusoidal law with a period of 256 seconds. Over the course of the experiments, we recorded the current resistance of the sensors at a frequency of 16 measurements per second.

The sensors were tested in clean air and with an ozone concentration in the air of 250 ppb (1 ppb is 10^{-7} volume %) using a GS-024-25 ozone generator. The ozone generator included

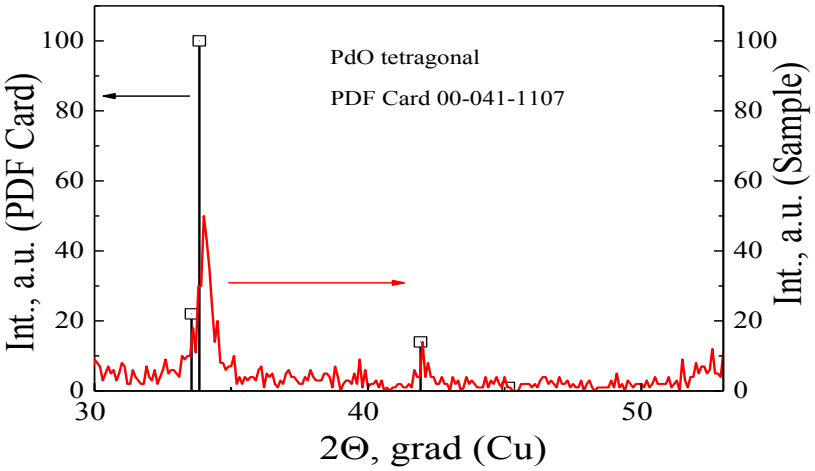

Fig. 1. The diffraction pattern of a PdO film

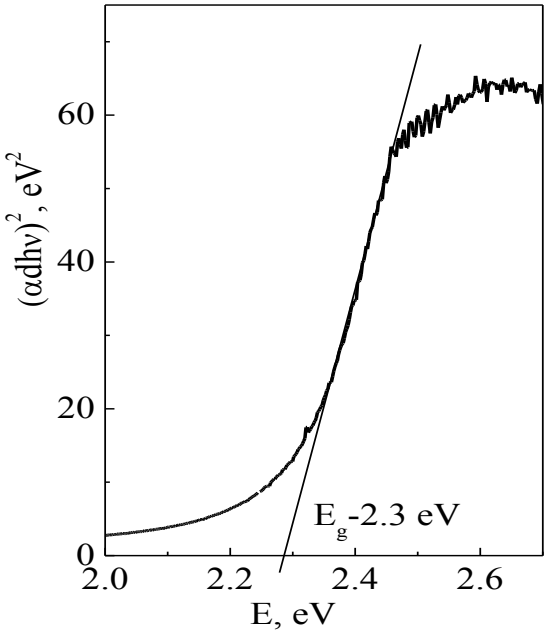

Fig. 2. Optical spectrum near the absorption edge of a thin PdO film

a special filter which lowered the background concentration of ozone that is always present in ordinary air to zero.

3. Results and discussion

Figure 3 shows the results of the experiment obtained using a thin-film PdO sensor operating in the thermal modulation mode of 50–300 °C. We are going to compare the resistive response of the sensor in clean air (the black curve) and in air with 250 ppb ozone (the blue curve).

After replacing the air in the measuring cell with an air-ozone mixture, transformation processes were observed for ~1 hour and included a change in the signal amplitude, its shape, and a signal shift along the resistance scale. Figure 3 shows the data for three periods of 256 seconds each, which were obtained after determining stationary values of the resistive response in air and in an air-ozone mixture.

The resistive response of the sensor with 250 ppb ozone was lower than the response in clean air, as ozone has a higher affinity to the electron than oxygen in the air. In the course of ozone chemisorption, an additional part of electrons was localised at its levels. For a *p*-type semiconductor, this resulted in a decrease in its resistance (Fig. 3.)

The shape of the signals is primarily determined by the dependence of the resistance of the semiconductor on its temperature (the resistance decreases for non-degenerate semiconductors with increasing temperature, since the concentration of charge carriers grows). Therefore, in vacuum or inert gases with sinusoidal thermal modulation, a resistive response of the sensor of the similar shape but antibatic in value should be observed.

In the presence of chemically active gases (air oxygen and ozone), the thermal signal of the sensor changed. This was due to the dependence of the adsorption-desorption equilibrium on temperature. Differences in the forms of signals (Fig. 3) from a purely "thermal sinusoid" were associated with this factor. The signal shape was specific for each adsorbent-adsorbate pair, as it was shown in our previous works [7, 8]. The

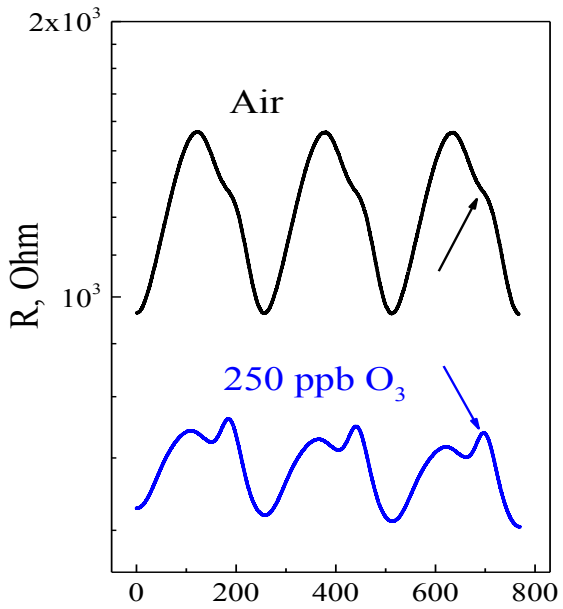

Fig. 3. Resistive response of a PdO sensor in thermal modulation mode in clean air and in air with 250 ppb ozone

resistive response of the PdO-O_3 pair among other oxides and gases that we studied [7, 8] had the greatest differences, which can be used to solve the issue of SCGS selectivity in ozone detection.

We will consider possible chemisorption forms of oxygen and ozone.

It is assumed that within the temperature range of 50–200 °C oxygen is chemisorbed in the molecular form O_2^-, at 150–450 °C in the atomic form O^-, and at >400 °C in the form of O^{2-} [5]. The temperature ranges of oxygen chemisorption in different charge states are rather conventional and differ in the existing literature.

Chemisorption of ozone on the sensor surface occurred in two forms: in molecular O_3^- and in atomic O^- [5]. The charge form O_3^- was unlikely or short-lived due to the fact that ozone rather quickly passed into a less active state on catalytically active surfaces.

Based on the above-studied chemisorption forms, it can be concluded that O^- form is common for both oxygen and ozone. Presumably, this form of chemisorption also determines the features of the plots marked with arrows (Fig. 3). The mentioned features of the air and ozone plots coincided regarding the time of the temperature rate and, as a result, regarding the temperature. In an ozone-containing media, the amount of O^- chemisorbed on the sensor surface increased as compared to air, which could explain the more pronounced feature in the ozone plot (the blue curve).

This mechanism can be confirmed by the experiments with the illumination of sensors using UV radiation with photon energy exceeding the PdO band gap energy (Figs. 4a, b).

An LED with a wavelength of 260 nm (4.8 eV) and an optical power of ~30 mW was used in the experiments. This illumination led to the generation of superequilibrium electron-hole pairs as follows:

$$h\nu \rightarrow e^- + h^+. \quad (1)$$

As a result of photoexcitation, the resistance of the PdO film should naturally decrease in vacuum or in an inert gas due to the appearance of additional charge carriers. However, in other gaseous media, the interaction between superequilibrium charge carriers and particles chemisorbed on the semiconductor surface must be taken into account.

In a medium that contains oxygen or ozone, a negative charge was localised on the surface of the semiconductor, associated with the chemisorption of oxygen in the form O^-, which resulted in surface bending of the semiconductor bands. A positive charge in the form of holes drifted towards it in order to compensate for the surface negative charge. Electrons, on the contrary, drifted into the bulk of the semiconductor, and the ionisation (chemisorption) of oxygen as follows:

$$O_{2(surf)} + 2e^- \rightarrow 2O^-_{(surf)} \quad (2)$$

was impeded [6,9,10]. Still, the holes easily interacted with the already chemisorbed oxygen, which was desorbed from the surface as a result of the reaction:

$$2O^-_{(surf)} + 2h^+ \rightarrow O_2\uparrow \quad (3).$$

In this case, the bending of the bands decreased until an equilibrium was reached between reaction (3) and (2) [6, 9, 10]. In accordance with this model, the resistance of the sensor in air (Fig. 4a) and in ozone (Fig. 4b) under UV illumination was higher than in the dark, as on the whole photodesorption of O^- from the sensor surface according to reaction (3) prevailed.

In order to substantiate our chemisorption model, we should also note that under UV

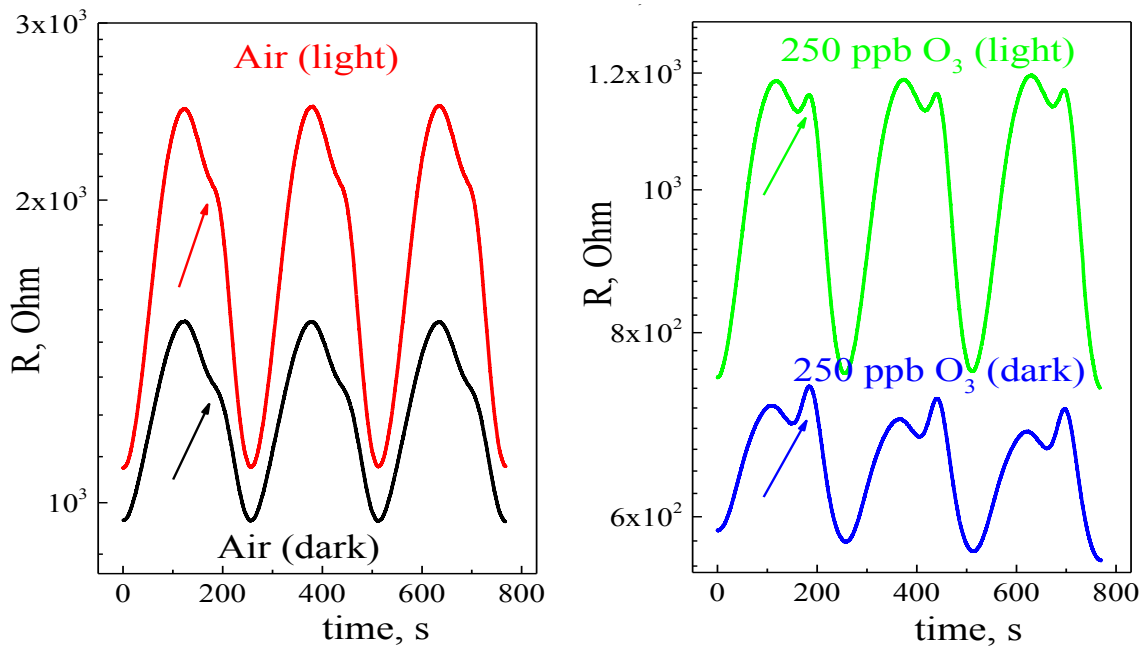

a b

Fig. 4. a) Resistive response of the sensor in air in the dark and under UV illumination; b) Resistive response of the sensor in air-ozone media in the dark and under UV illumination

illumination, the peak on the ozone curve indicated by the arrow (Fig. 4b) decreased. As it was assumed above, this was associated with chemisorbed oxygen in the form of O^-.

4. Conclusions

We studied the resistive response of PdO sensors in an ozone-air mixture in the thermal modulation mode. We discovered specific forms of the resistive response of PdO sensors in the presence of ozone, which can be used to solve the issue of its selective detection.

Possible mechanisms of oxygen and ozone chemisorption were studied. As a result of the analysis of data obtained in pure air and 250 ppb ozone, we assumed that the features of the resistive response of the PdO sensor in both gaseous media were determined using the chemisorption of oxygen in the form of atomic O^- ions.

The results of studying the resistive response of the PdO sensor under UV illumination with photon energies exceeding the band gap of PdO were consistent with the suggested chemisorption mechanism.

Contribution of the authors

The authors contributed equally to this article.

Conflict of interests

The authors declare that they have no known competing financial interests or personal relationships that could have influenced the work reported in this paper.

References

1. Nakata S. *Chemical analysis based on nonlinearity*. New York: Nova Science Publ. Inc.; 2003. 155 p.

2. Nakata S., Takahara N. Distinction of gaseous mixtures based on different cyclic temperature modulations. *Sensors Actuators: B*. 2022;359: 131615. https://doi.org/10.1016/j.snb.2022.131615

3. Nakata S., Hashimoto T., Okunishi H. Evaluation of the responses of a semiconductor gas sensor to gaseous mixtures under the application of temperature modulation. *The Analyst*. 2003;127: 1642. https://doi.org/10.1039/b208295k

4. Nakata S., Kashima K., Distinction between alcohols and hydrocarbons with a semiconductor gas sensor depending on the range and frequency of a cyclic temperature. *Analytical Methods*. 2012;4: 1126. https://doi.org/10.1039/c2ay05759j

5. He A., Yu J., Wei G., Chen Y., Wu H., Tang Z. Short-time fourier transform and decision tree-based pattern recognition for gas identification using temperature modulated microhotplate gas sensors. *Journal of Sensors*. 2016: 1–12 https://doi.org/10.1155/2016/7603931

6. Korotcenkov G., Brinzari V., Cho B. K. In_2O_3- and SnO_2-based ozone sensors: fundamentals. *Journal of*

Sensors. 2016: 1-31. https://doi.org/10.1155/2016/3816094

7. Ryabtsev S. V., Obvintseva L. A., Ghareeb D. A., Al-Habeeb A. A., Shaposhnik A. V., Domashevskaya E. P. Selective analysis of ozone with PdO semiconductor sensors in thermal modulation mode. *Sorbtsionnye I Khromatograficheskie Protsessy*. 2022;21(6): 888–893. https://doi.org/10.17308/sorpchrom.2021.21/3835

8. Ryabtsev S. V., Obvintseva N. Yu., Gkharib D. A. A., Al-Khabib A. A. K., Shaposhnik A. V., Turishchev S. Yu., Domashevskaya E. P. Thin-film oxide materials for ozone detection in the thermal modulation mode. *Inorganic Materials*. 2023, accepted for publication.

9. Kumar R., Liu X., Zhang J., Kumar M. Roomtemperature gas sensors under photoactivation: from metal oxides to 2D materials. *Nano-Micro Letters*. 2020;12(1): 164. https://doi.org/10.1007/s40820-020-00503-4

10. Zhang Q., Xie G., Xu M., Su Y., Tai H., Du H., Jiang Y. Visible light-assisted room temperature gas sensing with ZnO-Ag heterostructure nanoparticles. *Sensors and Actuators B*. 2017;259: 269. https://doi.org/10.1016/j.snb.2017.12.052

Information about the authors:

Stanislav V. Ryabtsev, Dr. Sci. (Phys.–Math.), Senior Researcher, Department of Solid State Physics and Nanostructures, Voronezh State University (Voronezh, Russian Federation).
https://orcid.org/0000-0001-7635-8162
ryabtsev@phys.vsu.ru

Nina Yu. Obvintseva, Cand. Sci. (Phys.–Math.), University of Science and Technology «MISIS» (Moscow, Russian Federation).
obvint@yandex.ru

Viktor V. Chistyakov, Cand. Sci. (Phys.–Math.), Senior Researcher, Ioffe Institute (St. Petersburg, Russian Federation).
https://orcid.org/0000-0003-4574-0857

Azl A. K. Al-Habeeb, postgraduate student, Department of Solid State Physics and Nanostructures, Voronezh State University (Voronezh, Russian Federation).
https://orcid.org/0009-0000-5642-1304

Aleksey V. Shaposhnik, Dr. Sci. (Chem.), Professor, Head of the Department of Chemistry, Voronezh State Agrarian University named after Peter the Great (Voronezh, Russian Federation).
https://orcid.org/0000-0002-1214-2730
ash@agrochem.vsau.ru

Sergey Yu. Turishchev, Dr. Sci. (Phys.-Math.), Associate Professor, Head of the General Physics Department, Voronezh State University (Voronezh, Russian Federation).
https://orcid.org/0000-0003-3320-1979
tsu@phys.vsu.ru

Evelina P. Domashevskaya, Dr. Sci. (Phys.–Math.), Full Professor, Department of Solid State Physics and Nanostructures, Voronezh State University (Voronezh, Russian Federation).
https://orcid.org/0000-0002-6354-4799
ftt@phys.vsu.ru

Received 29.12.2022; approved after reviewing 10.01.2023; accepted for publication 11.01.2023; published online 25.09.2023.

Translated by Marina Strepetova

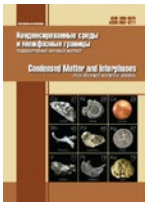

ISSN 1606-867X (Print)
ISSN 2687-0711 (Online)
Condensed Matter and Interphases
Kondensirovannye Sredy i Mezhfaznye Granitsy
https://journals.vsu.ru/kcmf/

Original articles

Research article
https://doi.org/10.17308/kcmf.2023.25/11264

Features of the molecular composition of dental biofilm in patients depending on the degree of caries and the method of its prevention: synchrotron FTIR spectroscopic studies

P. V. Seredin[1]✉, D. L. Goloschapov[1], V. M. Kashkarov[1], N. S. Builov[1], Yu. A. Ippolitov[2], I. Yu. Ippolitov[2], J. Vongsvivut[3]

[1]*Voronezh State University,*
1 Universitetskaya pl., Voronezh 394018, Russian Federation

[2]*Voronezh State Medical University,*
10 Studentcheskaya st., Voronezh 394036, Russian Federation

[3]*Australian Synchrotron (Synchrotron Light Source Australia Pty LTD),*
800 Blackburn Road, Clayton, Victoria 3168, Australia

Abstract

The article studies the molecular composition of dental biofilm in healthy people and patients with multiple caries lesions during several stages of exogenous and endogenous preventive measures.

The observed changes in the IR spectra registered during different stages of the experiment indicate a lack of balance between demineralisation and mineralisation of hard tissues resulting from different absorption mechanisms of agents applied exogenously and endogenously. All the observed changes result from the difference in the microbiota in healthy patients and patients with caries, as well as the difference in the microbiota caused by the impact of preventive agents on biofilm.

Keywords: Biofilm, Molecular properties, Endogenous and exogenous preventive methods, IR microspectroscopy, Synchrotron radiation

Funding: This study was supported by Russian Science Foundation, grant No. 23-15-00060.

Acknowledgements: Access to scientific equipment and methodology was provided by the Ministry of Education and Science of the Russian Federation, agreement No. 075-15-2021-1351.

The IRM studies were conducted by means of ANSTO's Australian Synchrotron.

For citation: Seredin P. V., Goloshchapov D. L., Kashkarov V. M., Buylov N. S., Ippolitov Yu. A., Ippolitov I. Yu., Vongsvivut J. Features of the molecular composition of dental biofilm in patients depending on the degree of caries and the method of its prevention: synchrotron FTIR spectroscopic studies. *Condensed Matter and Interphases*. 2023;23(3): 398–405. https://doi.org/10.17308/kcmf.2023.25/11264

Для цитирования: Середин П. В., Голощапов Д. Л., Кашкаров В. М., Буйлов Н. С., Ипполитов Ю. А., Ипполитов И. Ю., Vongsvivut J. Особенности молекулярного состава зубной биопленки у пациентов в зависимости от степени развитости кариеса и метода его профилактики: исследования с использованием синхротронной FTIR-спектроскопии. *Конденсированные среды и межфазные границы*. 2023;23(3): 398–405. https://doi.org/10.17308/kcmf.2023.25/11264

✉ Pavel V. Seredin, e-mail: paul@phys.vsu.ru

1. Introduction

Current approaches to pathological processes including demineralisation of bones, caries, erosion, dental fractures and chipping, as well as to the prevention methods, stress the importance of studying the molecular composition and phase transformations on the enamel-dental biofilm interface at both micro and nano scales [1–4]. The biofilm serves as a buffer on the surface of dental enamel. All exchange processes between the organomineral matrix of enamel apatite [1, 5] and oral fluid containing active remineralisation agents (phosphate and calcium complexes) are performed through this buffer [4, 6]. Quantitative studies and control over oral pathologies, with biofilm serving as an analyte, require precise determination of the changes in its molecular composition.

Fourier-transform infrared spectroscopy (FTIR) is an effective and a highly precise method used for the analysis of biological systems [7, 8]. FTIR has already been successfully used in the analysis of biofilms (namely, for detection and identification of bacteria contained in biofilm) and showed promising results [7–10]. An undeniable advantage of FTIR over genetic analysis is the fact that the latter does not always provide information corresponding to the cells' phenotypes, while FTIR makes it possible to monitor molecular biochemical changes taking place in the analyte, including over time [7–10].

Earlier we demonstrated that synchrotron-radiation FTIR is practical for studying the secondary structure of proteins in biological fluids of the oral cavity and occurring pathological processes. The protein secondary structure determines their spatial conformation and therefore, under certain conditions, can be connected with pathological processes in the human body.

We should note that there is hardly any information about the changes in the molecular composition of human dental biofilm depending on the dental caries degree and the prevention methods used.

Therefore, the purpose of our study was to analyse the specifics of molecular composition of dental biofilm in healthy people and in patients with pathologies using synchrotron-radiation FTIR.

2. Materials and methods

2.1. Research design

In our study, we used dental biofilm samples obtained from patients under various cariogenic conditions. The first group included healthy people without dental caries. The second group included patients with multiple carious lesions in enamel (ICDAS 1–2).

During the first stage of the experiment, we collected biofilm samples from both groups after mechanical tooth cleaning.

During the second stage of the experiment, we collected biofilm samples from all the participants after they cleaned their teeth with a toothpaste containing dicalcium phosphate.

During the third stage of the experiment, patients took a mineral complex containing dicalcium phosphate for three days. Biofilm samples were taken after mechanical tooth cleaning.

2.2. Experimental unit

Molecular compositions of biofilm samples were studied using the equipment of the Australian Nuclear Science and Technology Organisation (Melbourne, Australia). The spectra were registered in the spectral range of 3100–900 cm^{-1} with a spectral resolution of 4 cm^{-1}. In order to do this, we used a Bruker Vertex 80v IR spectrometer and a Bruker Hyperion 2000 IR microscope equipped with a diamond high pressure attachment for quantitative micro-analysis.

3. Results and discussion

The FTIR absorption spectra registered for biofilm samples from healthy patients and from patients with various degrees of caries, including the spectra registered during different stages of the experiment, are demonstrated in Figs. 1 and 2. Analysis of the results demonstrated that all the spectra, regardless of the experimental group and the stage of the experiment, had the same set of maxima that can be attributed to characteristic molecular bonds. Preliminary analysis of spectral sets of certain samples also demonstrated that the IR spectra of the sets are practically identical. Therefore, in this article we give the average IR absorption spectra of biofilm samples.

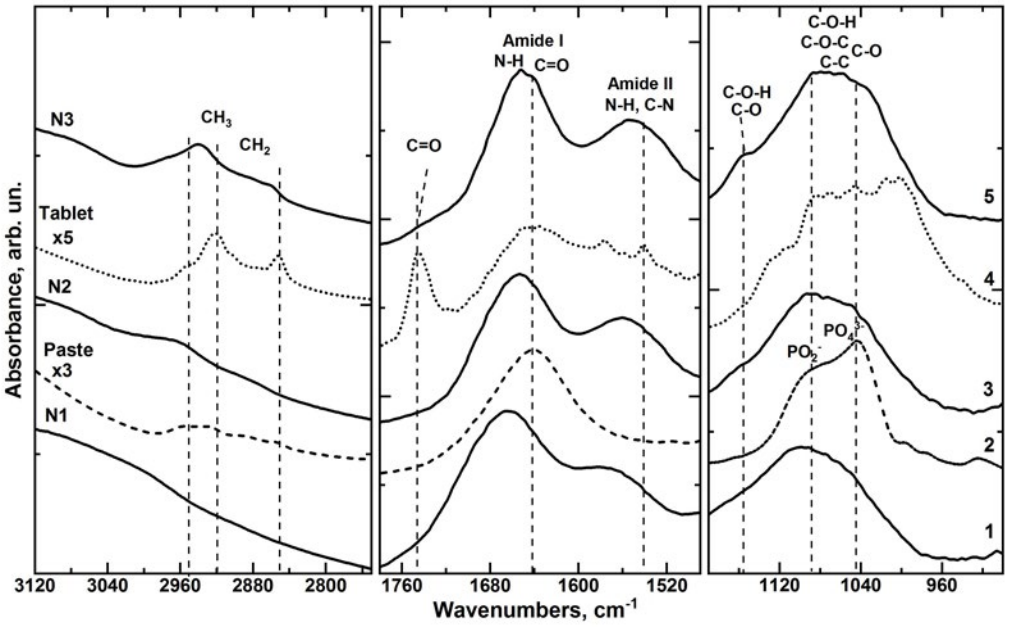

Fig. 1. IR absorption spectra of biofilm samples obtained from the enamel surface of healthy patients during different stages of the experiment: 1 – before applying preventive agents, 2 and 3 – after exogenous and endogenous preventive measures

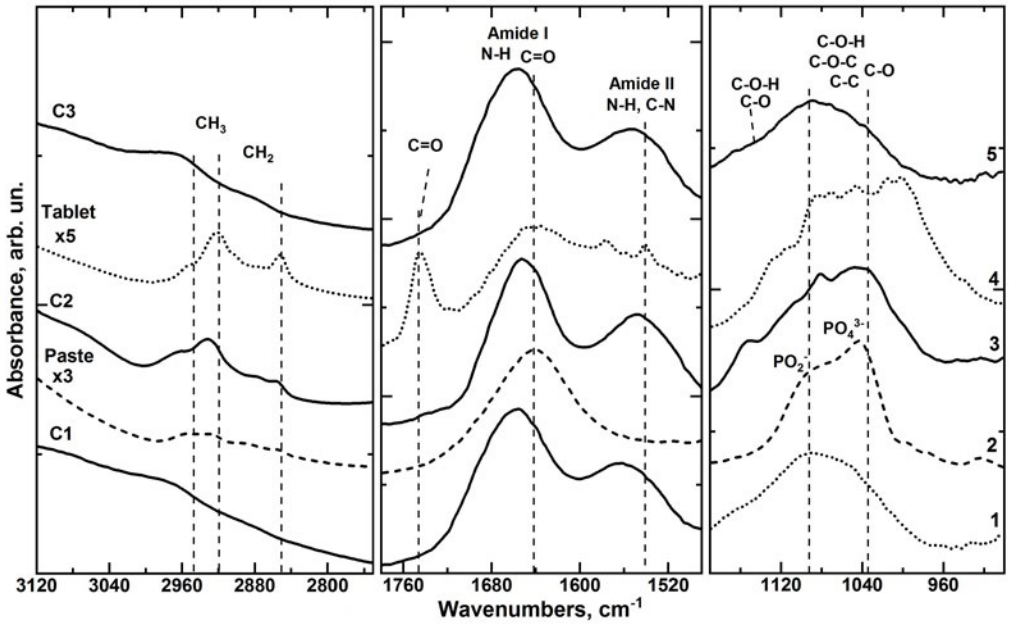

Fig. 2. IR absorption spectra of biofilm samples obtained from the enamel surface of patients with multiple caries lesions during different stages of the experiment: 1 – before applying preventive agents, 2 and 3 – after exogenous and endogenous preventive measures

The analysis of the experimental IR absorption spectra of biofilm samples was performed based on the existing data [7, 8, 11–15]. In these studies, vibrational IR spectroscopy was used to study the oral fluid, dental tissue, and biofilm in patients with various pathologies. The analysis demonstrated that the IR spectra of biofilm samples collected during different stages of the experiment have a set of characteristic vibrations, which can be attributed to molecular groups of various proteins, organic and inorganic agents, and oral microbiota.

The most significant changes in the relative intensities and profiles of the absorption bands observed in all the IR spectra of the biofilm samples were registered in the ranges 3120–2760, 1780–1500 cm^{-1}, and 1200–900 cm^{-1}. They are demonstrated in Fig. 1 and 2. When analysing the vibrational modes of the biofilm samples we noticed a group of bands localised in the range of 2950–2750 cm^{-1} and attributed to the vibrations of the C-H bonds of various fatty acids and lipids [7, 8]. We should note that the most significant changes in the relative intensity of these bands in the IR spectra of the biofilm samples were observed in the spectra registered for groups with different cariogenic situations (Fig. 2), when they used caries preventive agents. The analysis of the IR spectra of biofilm samples from healthy patients (fig. 1) demonstrated that the changes in the spectral region of 2950–2750 cm^{-1} are determined by the caries prevention method. This is easy to detect taking into account the characteristic spectral features of the preventive agents in the set range. At the same time, the IR spectra of biofilm samples from patients with multiple caries lesions (Fig. 2) demonstrated that significant changes in the molecular composition of biofilms occurred when putting preventive agents (toothpaste) into the oral cavity, while endogenous preventive methods did not have such an impact on the molecular composition of biofilms.

A similar tendency was observed when analysing the spectra in the range of 1200–900 cm^{-1}. A group of highly intense vibrations was observed associated with derivatives of phosphorus: phosphates, dicalcium phosphates, and phospholipids, which are important from the point of view of mineralisation processes [7, 8, 14]. We should note that the IR absorption spectra of biofilm samples demonstrated bands, whose occurrence and intensity in this range depend on the cariogenic situation and the stage of the experiment, i.e. the caries prevention method used. These modes include primarily the mode at 1082 cm^{-1} associated with PO_2^- by means of asymmetric and symmetric stretching vibrations of phosphate residues and phospholipids [7, 8, 14]. Another mode is located in the region of 1070–1020 cm^{-1}. It is presented as overlapping vibrational bands associated with organic derivatives of phosphates, dicalcium phosphate, and phosphatase by means of a C–O–P–O–C complex and cellular carbohydrate. Comparison of the results demonstrated that the use of a mineral complex in the form of pills or toothpaste leads to significant changes in the profile of the 1160–960 cm^{-1} band in biofilms obtained from healthy patients. In biofilms obtained from patients with multiple caries lesions, such changes were only observed immediately after applying the preventive agent whose composition results in significant changes in the molecular composition of biofilms in the given range. When a mineral complex in the form of pills was used, the molecular composition of biofilms did not change significantly after applying preventive agents (Fig. 3).

Another range of IR spectra that demonstrated significant changes was observed at 1780–1500 cm^{-1}. One of the spectral changes in the biofilm composition is the band at 1730 cm^{-1}, which can be attributed to bands (>C=O) of phospholipids, esters, and fatty acids, and corresponds to the characteristic region of proteins [7, 8, 11–13, 15]. At the same time, the most intense protein bands include the following: amide I vibrations (N–H, C=O) in the region of 1675–1615 cm^{-1}; amide II band (N–H and C–N) in the region of 1575–1520 cm^{-1}; according to [7, 8, 11–13, 15]. In the case of dental biofilms, these vibrational modes can also be attributed to peptides [7, 13].

We can see that the effect of preventive methods depending on the cariogenic situation is reflected by the position and shape of the amide I and amide II vibrational modes (Figs. 1 and 2). Thus, for the first (healthy) group, the use of a toothpaste and pills results in a significant (up to 14 cm^{-1}) shift of the amide I band towards the low-frequency region as compared to its position during the first stage of the experiment (without preventive agents). A similar tendency was observed for the group of vibration bands in the profile of the amide II. Here, for the healthy group, the use of a toothpaste and pills resulted in a significant (up to 25 cm^{-1}) shift of the band towards the low-frequency region as compared to its position during the first stage of the experiment (without preventive agents).

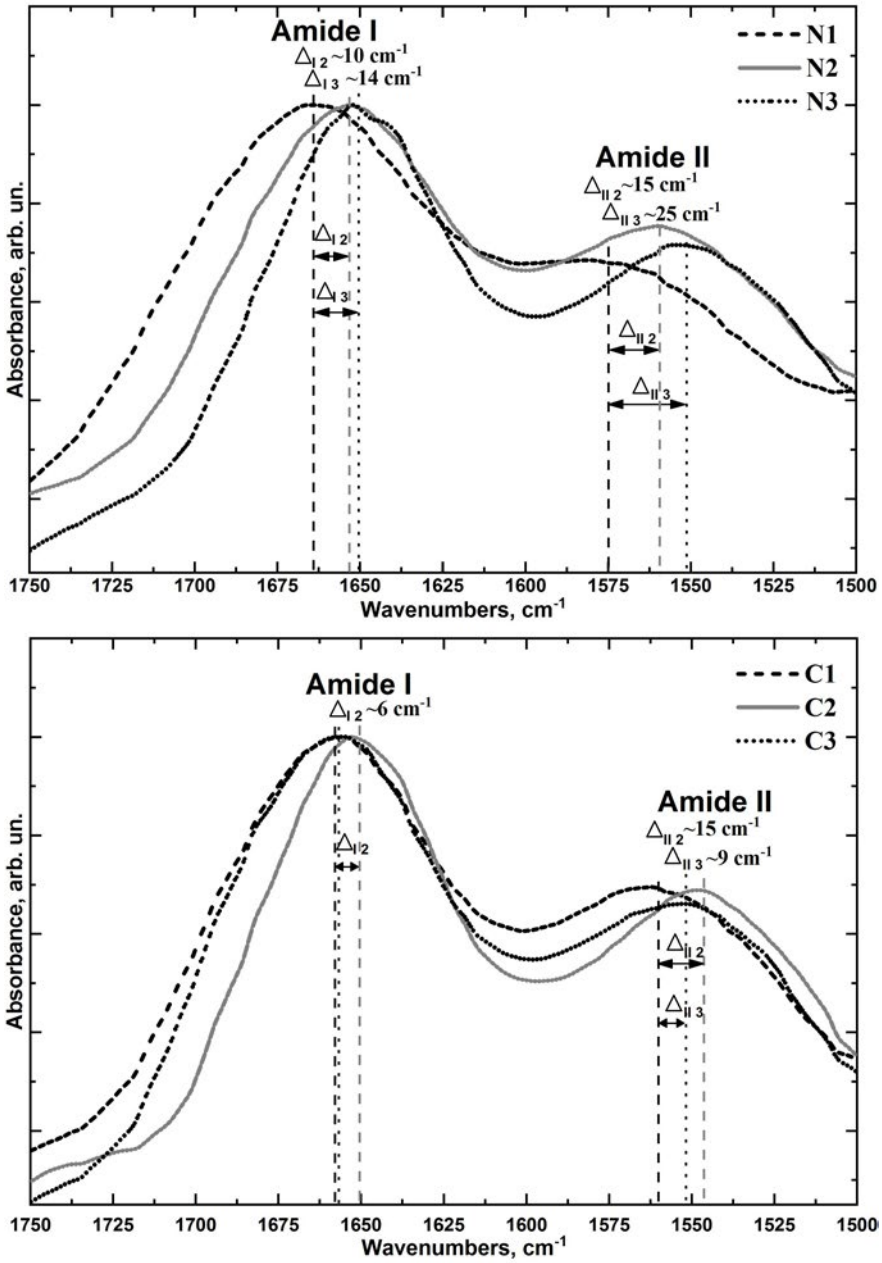

Fig. 3. Profiles of the amide I and amide II bands in the IR absorption spectra of the healthy (upper) and carious (down) group during different stages of the experiment: 1 – before applying preventive agents, 2 and 3 – after exogenous and endogenous preventive measures

For the group of patients with caries, these features were not that noticeable. Thus, a shift (up to 6 cm^{-1}) of the amide I band towards the low-frequency region was only registered during the second stage of the experiment (when toothpaste was used), while during the third stage (when pills were used) no shift was observed. At the same time, the shift of the maximum of the amide II band was 15 cm^{-1} during the second stage (when toothpaste was used), and only 9 cm^{-1} during the third stage (when pills were used).

The observed changes are caused by the changes in the biofilm molecular composition resulting from different cariogenic conditions and preventive methods used. Comparison of the results demonstrated that the changes in the profile of the amide II band (N–H and C–N) were greater than the changes in the profile of the amide I band. This corresponds to the

C–N vibrations, which can vary significantly depending on the factors affecting the molecular bonds.

The amide I band can be used to better monitor the changes in the protein secondary structure, because it is sensitive to such transformations. We should note that FTIR is often used to study protein conformation and aggregation processes *in vitro* [15, 16]. Based on the observed shifts in the frequency of the components of the secondary structure of the amide I band [11, 15, 17, 18] we can determine the impact of various factors on the protein conformation processes. Therefore, in our study we performed a precision comparative analysis of the IR spectroscopy data for the set frequency range of 1750–1500 cm^{-1}. A comparison of the spectra of biofilm samples obtained from both groups of patients demonstrated that the position and shape (half-width) of the high-frequency component of the amide I band in the region of 1700–1600 cm^{-1} depend on the cariogenic situation as well as on the preventive method. Thus, for the healthy patients, the use of a toothpaste and pills results in the shift of the amide I band towards the low-frequency region as compared to the first stage (without preventive agents), and to the reduction of the band's half-width from 55 cm^{-1} to 47 cm^{-1} and 37 cm^{-1} respectively. The shift and the reduction of the half-width were significantly greater, when pills were used. This is explained by the time the preventive agents spend in the oral cavity and the nature of their interaction with biofilm.

During the first stage of the experiment (without preventive agents), the IR spectra of patients with caries demonstrated that the position of the high-frequency component of the amide I band had already shifted by 7 cm^{-1} towards the low-frequency region as compared to that observed in the IR spectra of the healthy group. When toothpaste was used, there was a shift and a reduction in the half-width of the amide I band similar to that observed for the healthy group. However, when pills containing a mineral complex and dicalcium phosphate were used, there was no shift of the amide I band or any reduction in the half-width. More significant changes were observed for the amide II band. The spectral profile and the position of the band changed both when toothpaste and pills were used. We should note that when toothpaste was used, the shift of the amide II band was less significant, while the relative intensity of the maximum was lower than when pills were used. In the latter case the intensity was greater than the intensity of the spectral band of the samples obtained before using preventive agents.

The obtained spectral data indicated different conformation environment and secondary structure of biofilm proteins in patients with different cariogenic situations. The observed shift of the maximum of the high-frequency component of the amide I bands and the reduction of the half-width and redistribution of the intensity of components of the protein secondary structure was described in [11, 15, 19], namely as *random coil* (1648–1641 cm^{-1}) and α-helix (about 1660 см$^{-1}$). Changes in the molecular composition are also indicated by the changes in the relative intensity, frequency position, and spectral profile of the amide II band. All the observed changes result from the differences in the microbiota in healthy patients and patients with caries [20], when biofilm is affected by preventive agents [21].

The understanding of the changes in the molecular and phase compositions of dental tissues, oral fluid, and dental biofilm depending on the cariogenic situation and preventive methods makes it possible to take into account individual features of patients and perform effective treatment of caries, demineralisation, erosion, and dental attrition.

4. Conclusions

In our study, we used synchrotron-radiation FTIR to investigate the specifics of the molecular composition of dental biofilm after using exogenous and endogenous preventive methods in healthy patients and patients with multiple caries lesions.

The observed changes in the IR spectra indicate a lack of balance between demineralisation and mineralisation of hard tissues resulting from different absorption mechanisms of agents applied exogenously and endogenously. All the observed changes result from the difference in the microbiota in healthy patients and patients with caries, as well as the difference in the microbiota caused by the impact of preventive agents on biofilm.

Contribution of the authors

The authors contributed equally to this article.

Conflict of interests

The authors declare that they have no known competing financial interests or personal relationships that could have influenced the work reported in this paper.

References

1. García-Godoy F., Hicks M. J. Maintaining the integrity of the enamel surface: The role of dental biofilm, saliva and preventive agents in enamel demineralization and remineralization. *The Journal of the American Dental Association*. 2008;139: 25S–34S. https://doi.org/10.14219/jada.archive.2008.0352

2. Hicks J., Garcia-Godoy F., Flaitz C. Biological factors in dental caries: role of saliva and dental plaque in the dynamic process of demineralization and remineralization (part 1). *Journal of Clinical Pediatric Dentistry*. 2004;28(1): 47–52. https://doi.org/10.17796/jcpd.28.1.yg6m443046k50u20

3. Hara A. T., Zero D. T. The caries environment: saliva, pellicle, diet, and hard tissue ultrastructure. *Dental Clinics of North America*. 2010;54(3): 455–467. https://doi.org/10.1016/j.cden.2010.03.008

4. Odanaka H., Obama T., Sawada N., Sugano M., Itabe H., Yamamoto M. Comparison of protein profiles of the pellicle, gingival crevicular fluid, and saliva: possible origin of pellicle proteins. *Biological Research*. 2020;53(1): 3. https://doi.org/10.1186/s40659-020-0271-2

5. Lee Y. H., Zimmerman J. N., Custodio W., Xiao Y., Basiri T., Hatibovic-Kofman S., Siqueira W. L. Proteomic evaluation of acquired enamel pellicle during in vivo formation. *PLOS ONE. Public Library of Science*. 2013;8(7): e67919. https://doi.org/10.1371/journal.pone.0067919

6. Meyer F., Enax J., Epple M., Amaechi B.T., Simader B. Cariogenic biofilms: development, properties, and biomimetic preventive agents. *Dentistry Journal*. 2021;9(8): 88. https://doi.org/10.3390/dj9080088

7. Chirman D., Pleshko N. Characterization of bacterial biofilm infections with Fourier transform infrared spectroscopy: a review. *Applied Spectroscopy Reviews*. 2021;56(8–10): 673–701. https://doi.org/10.1080/05704928.2020.1864392

8. Gieroba B., Krysa M., Wojtowicz K., Wiater A., Pleszczyńska M., Tomczyk M., Sroka-Bartnicka A. The FT-IR and Raman spectroscopies as tools for biofilm characterization created by cariogenic streptococci. *International Journal of Molecular Sciences*. 2020;21(11): 3811. https://doi.org/10.3390/ijms21113811

9. Azam M. T., Khan A. S., Muzzafar D., Faryal R., Siddiqi S. A., Ahmad R., Chauhdry A. A., Rehman I. U. Structural, surface, in vitro bacterial adhesion and biofilm formation analysis of three dental restorative composites. *Materials*. 2015;8(6): 3221–3237. https://doi.org/10.3390/ma8063221

10. Cheeseman S., Shaw Z. L., Vongsvivut J., Crawford R. J., ... Truong V. K. Analysis of pathogenic bacterial and yeast biofilms using the combination of synchrotron ATR-FTIR microspectroscopy and chemometric approaches. *Molecules*. 2021;26(13): 3890. https://doi.org/10.3390/molecules26133890

11. Baldassarre M., Li C., Eremina N., ... Barth A. Simultaneous fitting of absorption spectra and their second derivatives for an improved analysis of protein infrared spectra. *Molecules*. 2015;20(7): 12599–12622. https://doi.org/10.3390/molecules200712599

12. Barth A., Haris P. I. *Biological and biomedical infrared spectroscopy*. IOS Press; 2009. 449 p.

13. Matthäus C., Bird B., Miljković M., Chernenko T., Romeo M., Diem M. Infrared and Raman microscopy in cell biology. *Methods in Cell Biology*. 2008: 275–308. https://doi.org/10.1016/S0091-679X(08)00610-9

14. Ren Z., Do L. D., Bechkoff G., ... Buchet R. Direct determination of phosphatase activity from physiological substrates in cells. *PLoS ONE*. 2015;10(3): e0120087. https://doi.org/10.1371/journal.pone.0120087

15. Yang S., Zhang Q., Yang H., Shi H., Dong A., Wang L., Yu S. Progress in infrared spectroscopy as an efficient tool for predicting protein secondary structure. *International Journal of Biological Macromolecules*. 2022: 175–187. https://doi.org/10.1016/j.ijbiomac.2022.02.104

16. Ripanti F., Luchetti N., Nucara A., Minicozzi V., Venere A. D., Filabozzi A., Carbonaro M. Normal mode calculation and infrared spectroscopy of proteins in water solution: Relationship between amide I transition dipole strength and secondary structure. *International Journal of Biological Macromolecules*. 2021;185: 369–376. https://doi.org/10.1016/j.ijbiomac.2021.06.092

17. Seredin P., Goloshchapov D., Ippolitov Y., Jitraporn Vongsvivut. Spectroscopic signature of the pathological processes of carious dentine based on FTIR investigations of the oral biological fluids. *Biomedical Optics Express*. 2019;10(8): 4050–4058. https://doi.org/10.1364/BOE.10.004050

18. Miller L. M., Bourassa M. W., Smith R. J. FTIR spectroscopic imaging of protein aggregation in living cells. *Biochimica et Biophysica Acta (BBA) - Biomembranes*. 2013;1828(10): 2339–2346. https://doi.org/10.1016/j.bbamem.2013.01.014

19. Seredin P., Goloshchapov D., Ippolitov Y., Vongsvivut J. Comparative analysis of dentine and gingival fluid molecular composition and protein

conformations during development of dentine caries: A pilot study. *Vibrational Spectroscopy*. 2020;108: 103058. https://doi.org/10.1016/j.vibspec.2020.103058

20. Kriebel K., Hieke C., Müller-Hilke B., Nakata M., Kreikemeyer B. Oral biofilms from symbiotic to pathogenic interactions and associated disease –connection of periodontitis and rheumatic arthritis by peptidylarginine deiminase. *Frontiers in Microbiology*. 2018;9. https://doi.org/10.3389/fmicb.2018.00053

21. Meyer F., Amaechi B. T., Fabritius H.-O., Enax J. Overview of calcium phosphates used in biomimetic oral care. *The Open Dentistry Journal*. 2018;12(1): 406–423. https://doi.org/10.2174/1874210601812010406

Information about of authors

Pavel V. Seredin, Dr. Sci. (Phys.–Math.), Full Professor, Chair of Department, Department of Solid State Physics and Nanostructures, Voronezh State University (Voronezh, Russian Federation).
https://orcid.org/0000-0002-6724-0063
paul@phys.vsu.ru

Dmitry L. Goloshchapov, Cand. Sci. (Phys.–Math.), Assistant Professor, Department of Solid State Physics and Nanostructures, Voronezh State University (Voronezh, Russian Federation).
https://orcid.org/0000-0002-1400-2870
goloshchapov@phys.vsu.ru

Vladimir M. Kashkarov, Cand. Sci. (Phys.–Math.), Senior Researcher, Department of Solid State Physic and Nanostructures, Voronezh State University (Voronezh, Russian Federation).
https://orcid.org/0000-0001-9460-9244
vmkashkarov@gmail.com

Nikita S. Buylov, Cand. Sci. (Phys.–Math.), Lecturer, Department of Solid State Physics and Nanostructures, Voronezh State University (Voronezh, Russian Federation).
https://orcid.org/0000-0003-1793-4400
buylov@phys.vsu.ru

Yury A. Ippolitov, Dr. Sci. (Med.), Full Professor, Head of Dentistry Institute of Postgraduate Medical Education Department, Voronezh State Medical University (Voronezh, Russian Federation).
https://orcid.org/0000-0001-9922-137X
dsvgma@mail.ru

Ivan Yu. Ippolitov, Cand. Sci. (Med.), Assistant, Department of Orthopedic Dentistry, Voronezh State Medical University (Voronezh, Russian Federation).
https://orcid.org/0000-0003-0012-6482
dsvgma@mail.ru

Jitraporn (Pimm) Vongsvivut, Senior Beamline Scientist – Infrared Microspectroscopy, Australian Synchrotron, Synchrotron Light Source Australia Pty LTD (Melburn, Australia).
jitrapov@ansto.gov.au
https://orcid.org/0000-0003-0699-3464

Received 27.12.2022; approved after reviewing 25.05.2022; accepted for publication 15.06.2022; published online 25.09.2023.

Translated by Yulia Dymant

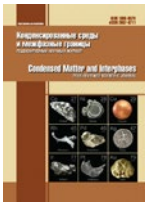

ISSN 1606-867X (Print)
ISSN 2687-0711 (Online)
Condensed Matter and Interphases
Kondensirovannye Sredy i Mezhfaznye Granitsy
https://journals.vsu.ru/kcmf/

Original articles

Research article
https://doi.org/10.17308/kcmf.2023.25/11265

Heat capacities and thermal expansion coefficients of iron triad metals

S. V. Terekhov✉

Galkin Donetsk Institute for Physics and Engineering
72 R. Luxembourg st., Donetsk 83114, Russian Federation

Abstract

One of the complex problems relating to the thermodynamics of a substance is creating an adequate description of its thermal properties. For example, the Einstein and Debye models (as well as in various modifications of these models) the heat capacity is calculated only when mechanical vibrations of the lattice are taken into account. This leads to the impossibility of describing the increase in heat capacity with increasing temperature for most substances, including iron triad metals. In addition, there is not a single theoretical construction capable of calculating the temperature dependences of the heat capacity and thermal expansion coefficient during polymorphic transformations and structural, magnetic and other phase transitions in the system. They appear on the charts in the form of final jumps, peaks and holes. As a result, there is a need to develop a new approach to the calculation of thermal characteristics. It should take into account the occurrence of local equilibrium in small areas in initially non-equilibrium metal samples for research. The nonequilibrium of a sample can be caused by the presence of impurity atoms, defects, volatile components in it, residual stresses, the occurrence of irreversible processes, etc. For the analytical description of arrays of measured values, experimenters use different exponential expressions in different temperature intervals, sometimes with negative powers. Such theoretical and experimental approaches cannot be considered satisfactory. Therefore, for the creation of the new model, it is necessary to choose such values that would be sensitive to changes in the state of the system. Within the framework of the proposed model of a two-phase locally equilibrium region, such quantities are the absolute temperature of the system, the order parameter in the form of the difference in volume fractions of coexisting ideal phases, the phase composition of the ordering phase, and its derivative with respect to temperature. The developed model allows to calculate the temperature dependences of the heat capacities and coefficients of thermal linear expansion of the iron triad metals (Fe, Co, Ni) with a change in the aggregation state (crystal - liquid), the presence of structural, magnetic and other phase transitions.

It has been shown that the used expressions adequately describe the experimental data in a wide temperature range, and also allow to extend the plotted curves to experimentally unexplored regions. A possible structural transition in cobalt at a temperature of about 1600 K, the existence of which requires additional experiments, was established. The obtained expressions are distinguished by their simplicity and universality of applicability; they can be used to create an automatic calculation of the thermophysical properties of not only iron triad metals, but also other solid substances.

Keywords: Thermodynamic model, Order parameter, Structural rearrangement, Polymorphic transformations, Transition metal

For citation: Terekhov S. V. Heat capacities and thermal expansion coefficients of iron triad metals. *Condensed Matter and Interphases*. 2023;25(1): 406–414. https://doi.org/10.17308/kcmf.2023.25/11265

Для цитирования: Терехов С. В. Теплоемкости и коэффициенты теплового расширения металлов триады железа. *Конденсированные среды и межфазные границы*. 2023;25(3): 406–414. https://doi.org/10.17308/kcmf.2023.25/11265

✉ Sergey V. Terekhov, e-mail: svlter@yandex.ru

1. Introduction

Iron triad elements are transition metals: iron Fe, cobalt Co, and nickel Ni. At room temperature, the elements form structures: Fe – BCC, Co – HCP, Ni – FCC. They are used in the production of structural steels, metallic glasses, ferromagnetic materials (for Fe, the Curie temperature T_C = 1041 K, for Co - 1390 K, for Ni – 631 K), etc.

Products made from them may be subject to seasonal temperature variations or a change in operating mode, therefore it is important to know the temperature dependence of the thermophysical properties of the components. The internal reaction of the alloy to a change in the temperature of the external medium can be accompanied by rearrangements of the electronic, atomic, phonon, vacancy, and other subsystems of quasiparticles with the possible nucleation of new phases in them. Important thermal characteristics of pure metals, sensitive to changes in the internal state of the system, are the heat capacity and the coefficient of thermal linear expansion. The course of the phase transition is reflected in their temperature dependences in the form:

– final jump (structural transition) of the baseline (see explanation in the text after formula (12));

– narrow in width, sharp and large peak (magnetic transition);

- symmetric or asymmetric peaks/pits with a rounded top, depending on the sign of the transition enthalpy or other physical quantity (polymorphic and aggregate transitions). The asymmetry of these graphical features is probably associated with a succession of phase transitions in the atomic system and subsystems of quasiparticles.

The evolution of the internal structure can occur by local nucleation of new phases (first-order phase transitions) or by creating conditions for the simultaneous appearance of a new phase in the entire volume (second-order phase transitions) both in the system itself and in its subsystems. Thus, internal phenomena and processes affect the measuring equipment.

The scatter of experimental values, for example, the heat capacities of Fe, Co, and Ni [1–8] depends on the temperature range in which they were obtained, the chosen research method, the equipment used, the atmosphere in it, the chemical indifference of the crucible, sample pretreatment, and internal processes in it. Such kinetic phenomena include [9]: structure rearrangement, redistribution of atoms over positions in the unit cell, thermal expansion, transition of volatile impurities into the atmosphere of the calorimeter, etc. In this case, the thermal effects of a change in the internal state of the sample are summed up by the measuring equipment, which causes a discrepancy between the experimental data of different authors.

In the absence of phase transitions, experimental data on the temperature dependence, in particular, on the heat capacity of a substance, are often smoothed out by approximating functions [10–12], which contain a divergence at absolute zero temperature. The applied theoretical developments do not use one continuous function (or the sum of continuous functions) to describe the heat capacity graph of the system, especially in the presence of phase transitions [10, 13]. Therefore, there is a need to search for a new theoretical approach to describing the behaviour of the heat capacity of a solid in the temperature range from 0 K to the melting point.

The aim of this study was the description of the temperature dependences of the heat capacities and coefficients of thermal linear expansion of Fe, Co, Ni during the implementation of phase transitions of various nature in the studied temperature range using the ratios of the two-phase local equilibrium region model [14]. The model showed a fairly good agreement with the experimental data [14–19].

2. Heat capacities of iron, cobalt and nickel in the presence of structural, magnetic and aggregate phase transitions

2.1. Model of ideal phases (model of a two-phase locally equilibrium region)

Let us consider a locally equilibrium region of a condensed medium with a volume V, in which two ideal phases coexist, containing N_1 and N_2 elements with volumes ω_1 and ω_2 respectively [14]. In other words, phase 1 has the volume of $V_1 = \omega_1 N_1$, phase 2 has the volume of $V_2 = \omega_2 N_2$,

and the volume V of the region (with total number of elements $N = N_1 + N_2$) is equal to:

$$V_1 + V_2 = V. \quad (1)$$

It should be noted that one element of the local region accounts for the volume $\omega = V/N$, which depends on the concentration $c_i = N_i/N$ (i = 1, 2) of elements in phases. For simplicity of reasoning, we will further assume that the elements of the phases have the same or very close volumes, i.e., the condition $\omega_1 = \omega_2 = \omega$.

Dividing the equality (1) by the volume V, we obtain the ratio for the volume fractions of the phases:

$$x_1 + x_2 = 1, \quad (2)$$

where $x_i = V_i/V = N_i/N = c_i$ is the volume fraction of the phase i = 1,2.

Let us introduce the order parameter η according to the formula:

$$\eta = x_1 - x_2. \quad (3)$$

From (2) and (3) it follows that:

$$x_1 = (1+\eta)/2,\ x_2 = (1-\eta)/2. \quad (4)$$

Formulas (4) show that the order parameter η takes values from the interval from −1 to +1, since volume fractions x_i vary from 0 to 1.

Gibbs energy G of one mole of a substance (or per unit of dimensionless volume of the system) is equal to:

$$g = G/N = G\omega/V = \mu_1 x_1 + \mu_2 x_2, \quad (5)$$

where μ_{i0} are the chemical potentials of phase elements at temperature T, set by known formulas for an ideal system:

$$\mu_i = \mu_{i0} + k_B T \ln x_i, \quad (6)$$

Here μ_{i0} are the standard values of chemical potentials for each of the phases, which include a summand in the form $k_B T \ln N$, connected by the equation for the state of the medium with pressure and temperature, k_B is the Boltzmann constant. The extremum of the Gibbs energy (5) along the argument η, which corresponds to the local equilibrium value of the order parameter, is observed at:

$$(dg/d\eta)\big|_{\eta=\eta_0} = 0 \Rightarrow \eta_0 = -\mathrm{th}(\varphi/T), \quad (7)$$

where the argument is $\varphi = \Delta\mu_0/2k_B$, the function is $\Delta\mu_0 = \mu_{10} - \mu_{20}$. Therefore, the equilibrium fraction, for example, of the crystalline phase in an amorphous alloy during its isochronous crystallization is described by the function:

$$x_1 = [1 - \mathrm{th}(\varphi/T)]/2. \quad (8)$$

If we expand the function φ in a Taylor series near the extreme point of thermal effect of the phase transition T_x with only the linear terms of the series preserved, than:

$$\varphi/T = (\partial\phi/\partial T)(T - T_x)/T = \\ = a_0(q)[(T_x/T) - 1], \quad (9)$$

where parameter is $a_0(q) = -\partial\phi/\partial T$, q is the rate of sample heating. Model parameter $T_x(q)$, at which the maximum of the first derivative $u_x(q) = (dx_1/dT)\big|_{T=T_x}$ on the volume fraction of phase 1 and the extremum of the phase transition heat is observed, related to temperature by the ratio:

$$a_0(q) = 2T_x(q)u_x(q). \quad (10)$$

2.2. Heat capacity baseline (local heat capacity)

The local (partial) derivative of a function characterizes its changes in the vicinity of a single point. Thus, the entropy of the system at a fixed phase composition $x = x_1$ is defined by the formula [20]:

$$\sigma_x = -(\partial g/\partial T)_x = -\partial\mu_{20}/\partial T - x\partial(\Delta\mu_0)/\partial T - \\ -k_B[x\ln x + (1-x)\ln(1-x)] = \sigma_1 + \sigma_2 x + \sigma_3, \quad (11)$$

where entropy: mother phase $\sigma_1 = -\partial\mu_{20}/\partial T$, phase differences $\sigma_2 = -\partial(\Delta\mu_0)/\partial T$, and their mixing $\sigma_3 = -k_B[x\ln x + (1-x)\ln(1-x)]$. Then the local heat capacity of the system:

$$C_b = T(\partial\sigma_x/\partial T)_x = T(\partial\sigma_1/\partial T)_x + \\ +T(\partial\sigma_2/\partial T)_x x = k_1 T + k_2 x, \quad (12)$$

where coefficients $k_1 = T(\partial\sigma_1/\partial T)_x$ and $k_2 = T(\partial\sigma_2/\partial T)_x$ we considered to be constant. In this case, formula (12) describes within the experimental error *heat capacity baseline* of the substances (*temperature dependence of local heat capacity* calculated at a constant phase composition) [17, 19]. The first summand in (12) depends linearly on temperature and describes the contribution of the electron subsystem to the heat capacity of the substance, while the internal evolution of the substance is represented by the second term.

2.3. Substantial heat capacity (heat capacity of the test sample)

Unlike the partial derivative of a function, its total derivative describes the behaviour of the function at any point in the system and during the transition from one point to another. We will use this fact for the study of the heat capacity of the investigated sample (*substantial heat capacity* of locally-equilibrium region), i.e., substantive entropy:

$$\sigma = -(dg/dT) = \\ = -[(\partial g/\partial T)_x - (\partial g/\partial x)_T \partial(dx/dT)] = \\ = \sigma_x + \varepsilon_T u, \quad (13)$$

where is the density energy of phase coexistence:

$$\varepsilon_T = -(\partial g/\partial x)_T = -\Delta\mu_0 - k_B T \ln[x/(1-x)], \quad (14)$$

$u = dx/dT$ is "rate" of change in the phase composition x upon thermal transition to a new state. Thus, the local equilibrium entropy (11) coincides with its substantial definition (13) when the equation $\varepsilon_T = 0$ is satisfied, which generates formula (8).

Substantial heat capacity:

$$C = T\frac{d\sigma_x}{dT} = \\ = T\left[\left(\frac{\partial\sigma}{\partial T}\right)_{x,u} + \left(\frac{\partial\sigma}{\partial x}\right)_{T,u}\left(\frac{dx}{dT}\right) + \left(\frac{\partial\sigma}{\partial u}\right)_{T,x}\left(\frac{dx}{dT}\right)\right] = \\ = C_b + C_k + C_d. \quad (15)$$

The kinetics of the formation of a new phase affects the function (15), as was indicated in [9]. The "kinetic" component of heat capacity:

$$C_k = \{2\xi_T - Tu/[x(1-x)]\}Tu = k_3 Tu, \quad (16)$$

here $\xi_T = (\partial\varepsilon_T/\partial T)_{x,u}$, $k_3 = 2\xi_T - Tu/[x(1-x)]$. At a constant coefficient k_3 formula (16) describes the peaks ($k_3 > 0$) and pits ($k_3 < 0$) of polymorphic transformations, aggregate and magnetic transitions. "Dynamic" heat capacity component:

$$C_d = T\varepsilon_T w \quad (17)$$

where $w = du/dT$ for establishing local equilibrium ($\varepsilon_T = 0$) equals zero. Thus, the theoretical relation for calculating the temperature dependence of the heat capacity of a condensed medium upon reaching a local equilibrium state takes the form:

$$C = C_b + C_k. \quad (18)$$

2.4. Heat capacity of iron triad elements (Fe, Co, Ni)

Since when the temperature changes, the formation of a singularity β on the graph and the rearrangement of the subsystem i (fluctuation, vacancy, phonon, magnetic, etc.) substance can occur, the heat capacity C_b and C_k in formula (18) are calculated as:

$$C_b = k_1 T + \sum_{\beta,i} k_{2\beta i} x_{1\beta i}, \quad (19)$$

$$C_k = T\sum_{\beta,i} k_{3\beta i} u_{1\beta i}. \quad (20)$$

For the transition metals iron Fe, cobalt Co, and nickel Ni, the model parameters are shown in Table 1, and the calculation result is shown in Fig. 1. Fig. 1 demonstrates an adequate description of the experimental data using a single continuous function consisting of the sum of continuous values. As can be seen in Fig. 1, the above formulas describe quite well the temperature dependences

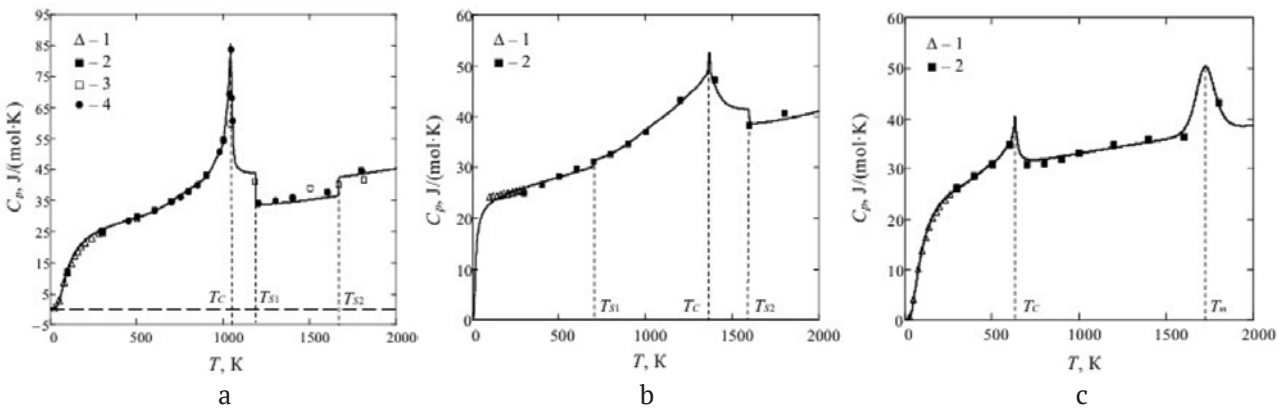

Fig. 1. Heat capacities of iron Fe (a), cobalt Co (b), and nickel Ni (c): *1* – data [1], *2* – [2], *3* – [3], *4* - [4]; solid line – theory

Table 1. Parameters of the theoretical model for calculating the heat capacities of metals

Parameters \ Metals		Fe (T_m = 1811 K [32])	Co (T_m = 1767 K [32])	Ni (T_m = 1728 K [2,32])
a_{01}		0.79	0.6	0.56
T_{x01}, K		140	27	156
$k_1 \cdot 10^4$		87	92	50
k_{201}		32.9	31	38.7
a_{02}	β → γ (Fe) α → β (Co)	T_{S1} = 1183 K [2] 2000	T_{S1} = ~ 700 K 2000	–
T_{x02}, K		1188 (T_{cubic} = 1189 K [2])	698	–
k_{202}		–10.1	1.2	–
a_{03}	γ → δ (Fe) α → ? (Co)	T_{S2} = 1665 K 2000	T_{S2} = ? 2000	–
T_{x03}, K		1667 (T_{S2} = 1667 K [2])	1600	–
k_{203}		6.0	–2.8	–
Phase transitions in subsystems				
a_{111}		3.1	4.0	1.9
T_{x11}, K		955 (T_C = 910 K [32] α_{amph}↔g)	1190	492
k_{211}		5.0	–	–
k_{311}		3.4	2.3	2.8
a_{121}		15	10	4.0
T_{x21}, K		997	1314	543
k_{321}		1.1	0.9	1.0
a_{131}		58	29	12
T_{x31}, K		1022	1350	603
k_{231}		–	0.1	
k_{331}		0.4	0.06	0.5
a_{141}		92	28	40
T_{x41}, K		1041	1368	632 (T_C = 631 K [32])
k_{341}		0.6	0.28	0.23
a_{151}		520	220	200
T_{x51}, K		1043 (T_C = 1043 K [2])	1369 (T_C = 1390 K [32])	633
k_{351}		0.027	0.04	0.023

of the heat capacities of the above metals for the structural (transition temperature T_s), magnetic (T_C) and aggregate (T_m) transitions. From Table 1 and Fig. 1b it can be seen that in cobalt at a temperature T = ~ 1600 K, a polymorphic transformation of the β phase may occur with a change in the structure of the metal occurs, which is reflected in its temperature dependence as the jump. Apparently, at this temperature, the premelting process starts, which destroys the β-structure of the metal, since the temperature of the aggregate transition of cobalt T_m = 1767 K.

It should also be noted that the obtained results coincide with the data provided for Fe in [5, 21 p. 30], cobalt Co – [5, 8] and nickel Ni – [5, 7, 22, 23].

3. Thermal expansion coefficients of iron triad elements

Isobaric coefficient of thermal (linear – $\alpha_L = (\partial L / \partial T)_P / L$ or volumetric - $\alpha_V = (\partial V / \partial T)_P / V$) expansion depends on the aggregate state of the object, its chemical and phase compositions, structure and other internal phenomena and processes. At the microlevel, an increase in temperature is accompanied by an increase in the mobility of atoms, the appearance of new degrees of freedom, rearrangement of the phonon subsystem, and evolution of other subsystems of quasiparticles [24]. At the macro level, these phenomena lead to: the appearance of singular points (kinks) on the temperature dependences of the measured quantities; the appearance of diffuse phase transitions [25, 26]; the growth of cracks in solids due to emerging elastic and thermal stresses, as well as other irreversible processes.

Relationship of isobaric coefficient α_V with specific heat capacity c_V was first obtained by Grüneisen (see, for example, [27, p. 13; 28, p. 26]):

$$\alpha_V / c_V = \gamma\beta / V_m \approx \text{const}, \quad (21)$$

where γ is the Grüneisen parameter from the interval [1.5; 2.5], $\beta = (\partial V / \partial P)_T / V$ is coefficient of isothermal compressibility of metal, V_m is molecular volume, which is practically independent of temperature. Formula (21) indicates the similarity of the temperature curves for $_V$ and specific heat capacity c_V.

On the other hand, in accordance with the mixing rule (see, for example, [29]), the thermal expansion coefficient of a two-phase locally equilibrium region is:

$$\alpha = \alpha_1 x + \alpha_2 (1 - x) = \alpha_2 + x\Delta\alpha, \quad (22)$$

here α_i (i = 1.2) is coefficient $_V$ (or $_L$) of phase i, $\Delta\alpha = \alpha_1 - \alpha_2$ is phase thermal difference coefficient. In study [30] the behaviour of metallic glass using the above formulas both during cooling of the melt and during heating of the amorphous alloy was simulated. It was demonstrated that the presence of kinks on straight lines is associated with the occurrence of a diffuse phase transition.

Equations (21) and (22) allow us to calculate the coefficient $\alpha_L \cdot 10^6$ according to the formula:

$$\alpha_L \cdot 10^6 = q_1 T + q_2 x + \sum_{\beta,i} q_{3\beta i} T u_{\beta i}. \quad (23)$$

The parameters of the theoretical model are shown in Table 2, and temperature dependences of the coefficients of linear thermal expansion

Table 2. Parameters of the theoretical model for calculating the linear thermal expansion coefficients

Parameters \ Metals	Fe	Co	**Ni**
a_0	0.756	0.96	0.735
T_{x0}	154	114	134
$q_1 \cdot 10^4$	80	32	57
q_2	14	15.8	16
Phase transitions in subsystems			
a_{011}	5.28	–	23.4
T_{x11}	1063 ($T_{\gamma\to\delta}$ = 1038 K [27])	–	639 (T_C = 633 K [27])
q_{311}	–1.68	–	1.06
a_{021}	9.3	–	12.2
T_{x21}	1810 (T_m = 1811 K [32])	–	670
q_{321}	–0.76	–	–0.5
a_{031}	–	–	3.4
T_{x31}	–	–	1728
q_{331}	–	–	2.0

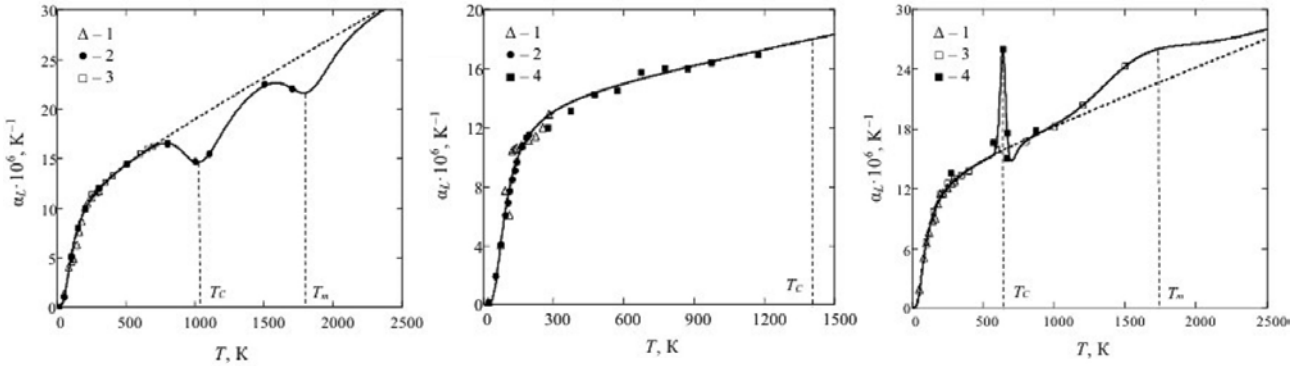

a b c

Fig. 2. Linear thermal expansion coefficients of iron Fe (a), cobalt Co (b), and nickel Ni (c): *1* – data [1], *2* – [27], *3* – [31], *4* – [32]; dotted line – base line, solid line – theory

of the iron triad elements are shown in Fig. 2. It should be noted that for iron the temperature T_{x11} is close to its Curie temperature T_C, and the temperature T_{x21} almost the same as the melting point T_m. Therefore, the proposed approach allows to analytically calculate not only the base lines of heat capacities and thermal expansion coefficients of iron triad elements, but also take into account the implementation of phase transformations in their subsystems.

Thus, the nonmonotonic and complex behaviour of the linear thermal expansion coefficient (Fig. 2b and *c*), for example, for nickel (Fig. 2c) did not receive an explanation during the experimental study [27, p. 203]. This study, taking into account "kinetic" additives allows to explain the non-monotonic nature of the temperature dependence curves by the occurrence of phase transitions. For iron (Fig. 2a) the presence of rounded extrema, probably, is associated with a series of polymorphic transformations, which are set with increasing temperature by rearrangements of atoms in the unit cells of the metal. For nickel, the sharp peak and the following minimum of the thermal expansion coefficient are determined by the successive implementation of the magnetic phase transition and polymorphic transformation in the temperature range from 500 to 800 K. A further increase in temperature causes a new transition: the system begins to rearrange into a new (liquid) aggregate state.

4. Discussion

The calculations carried out within the framework of the model of coexistence of two ideal phases in the local equilibrium region showed a fairly good agreement between the theoretical results and different experimental data arrays on the heat capacities and thermal expansion coefficients of iron triad elements. According to most experimental data, the relative calculation error does not exceed 5–7%, and for transition temperatures it does not exceed 3%. The use of total temperature derivatives of specific entropies and the second Grüneisen rule allow to describe the temperature graphs of the indicated values in the implementation of structural, magnetic, and aggregate transitions.

Unlike the CALPHAD method, which uses functionally different dependences with divergence at 0 K, the presented approach uses the sum of continuous functions. The presence of features on the graphs (jumps, peaks/pits with sharp and rounded peaks) is due to the influence of the "kinetic" additive associated with rearrangements of quasiparticle subsystems. Their implementation should be taken into account when developing materials with specific thermophysical properties and during the use of finished products.

5. Conclusions

The simplicity of the ratios obtained in the proposed model and the reliability of the calculated data allow us to hope for its use in the algorithms for designing new materials. In addition, the applicability of the theoretical construction to solids of different physical and chemical nature, demonstrated in other studies of the author, indicates the universal nature of the assumptions of the model.

Conflict of interests

The author declares that they has no known competing financial interests or personal relationships that could have influenced the work reported in this paper.

References

1. Novitsky L. A., Kozhevnikov I. G. *Thermophysical properties of materials at low temperatures**. Handbook. Moscow: Mashinostroenie Publ., 1975. 216 p. (in Russ.)

2. Zinoviev V. E. *Thermophysical properties of metals at high temperatures**. Handbook. Moscow: Metallurgiya Publ., 1989. 384 p. (in Russ.)

3. Dorogokupets P. I., Sokolova, T. S., Litasov K. D. Thermodynamic properties of bcc-Fe to melting temperature and pressure to 15 GPa. *Geodynamics & Tectonophysics*. 2014:5(4): 1033–1044. https://doi.org/10.5800/gt-2014-5-4-0166

4. Desai P. D. Thermodynamic properties of iron and silicon. *Journal of Physical and Chemical Reference Data*. 1986;15(3): 967–983. https://doi.org/10.1063/1.555761

5. Dinsdale A. T. SGTE data for pure elements. *Calphad*. 1991;15(4): 317–425. https://doi.org/10.1016/0364-5916(91)90030-n

6. Chen Q., Sundman B. Modeling of thermodynamic properties for bcc, fcc, liquid, and amorphous iron. *Journal of Phase Equilibria*. 2001;22(6): 631–644. https://doi.org/10.1007/s11669-001-0027-9

7. Gamsjäger H., Bugajski J., Gajda T., Lemire R. J., Preis W. Errata for the 2005 review on the chemical thermodynamics of nickel. In: Mompean F. J., Illemassène M. (Eds.) *Chemical Thermodynamics*. Vol. 6. Nuclear Energy Agency Data Bank, Organisation for Economic Co-operation and Development, North Holland Elsevier Science Publishers B.V., Amsterdam, The Netherlands. Amsterdam: Elsevier, 2005. 616 p. Available at: https://oecd-nea.org/dbtdb/pubs/Errata_Nickel.pdf

8. Li Z., Mao H., Selleby M. Thermodynamic modeling of pure Co accounting two magnetic states for the Fcc phase. *Journal of Phase Equilibria and Diffusion*. 2018;39(5): 502–509. https://doi.org/10.1007/s11669-018-0656-x

9. Bubnova R. S., Filatov S. K. *Thermoradiography of polycrystals. Part II. Determination of quantitative characteristics of the thermal expansion tensor**. St. Petersburg: S.-Pb. State University Publ., 2013. 143 p. (in Russ.)

10. Khodakovsky I. L. About new semi-empirical equations of temperature dependence of heat capacity and volume coefficient of thermal expansion of minerals*. In: Tsekhonya T. I., Sirotkina, E. A. (Eds.). Proceedings of the ASEMPG-2012. *Vestnik Otdelenia nauk o Zemle RAN*. 2012;4(9): NZ9001. (in Russ.). https://doi.org/10.2205/2012nz_asempg

11. Saunders N., Miodownik A. P. *CALPHAD* (*calculation of phase diagrams*): *a comprehensive guide*. V. 1. Pergamon: Elsevier Science Ltd, 1998. 479 p. https://doi.org/10.1016/s1470-1804(98)80034-5

12. Lukas H. L., Fries S. G., Sundman B. *Computational Thermodynamics*: *The Calphad Method*. Cambridge: Cambridge University Press The Edinburgh Building, 2007. 313 p.

13. Gilev S. D. Low-parametric equation of state of aluminum. *High Temperature*. 2020;58(2): 166–172. https://doi.org/10.1134/s0018151x20020078

14. Terekhov S. V. Thermodynamic model of a blurred phase transition in the $Fe_{40}Ni_{40}P_{14}B_6$ glass. *Physics and High Pressure Technology*. 2018;28(1): 54–61. (in Russ.). Available at: https://www.elibrary.ru/item.asp?id=32664811

15. Terekhov S. V. Blurred phase transition in the $Fe_{40}Ni_{40}P_{14}B_6$ amorphous alloy: thermodynamics of phases and kinetics of crystallization. *Physics and High Pressure Technology*. 2019;29(2): 24–39. (in Russ.). Available at: https://www.elibrary.ru/item.asp?id=38479797

16. Terekhov S. V. Single- and multistage crystallization of amorphous alloys. *Physics of Metals and Metallography*. 2020;121(7): 664–669. https://doi.org/10.1134/s0031918x20070108

17. Terehov S. V. Thermal properties of matter within the model of a two-phase system. *Physics of the Solid State*. 2022;64(8): 1089. https://doi.org/10.21883/pss.2022.08.54631.352

18. Terehov S. V. Iffuse phase transition and heat capacity of a solid. *Physics and High Pressure Technology*. 2022;32(2): 36–51. (in Russ.). Available at: https://www.elibrary.ru/item.asp?id=48746674

19. Terekhov S. V. *Heat capacity and thermal expansion of matter**. Handbook. Donetsk: DonFTI im. A. A. Galkina Publ., 2022. 168 p. (in Russ.)

20. Kubo R. *Thermodynamics*. North-Holland Publishing Company: 1968. 310 p.

21. Livshits B. G., Kraposhin V. S., Lipetsky Ya. L. *Physical properties of metals and alloys**. Moscow: Metallurgiya Publ., 1980. 320 p. (in Russ.)

22. Meschter P. J., Wright J. W., Brooks C. R., Kollie T. G. Physical contributions to the heat capacity of Nickel, *Journal of Physics and Chemistry of Solids*. 1981;42(9): 861–871. https://doi.org/10.1016/0022-3697(81)90174-8

23. Bodryakov V. Yu. (2020). Isolation of the magnetic contribution to the thermal expansion of nickel at ferromagnetic transformation on the base of analysis of β(CP) correlation dependence. *High Temperature*. 2020;58(2): 213–217. https://doi.org/10.1134/s0018151x20020042

24. Kittel C. *Elementary solid state physics: A short course*. N.Y., London: John Wiley & Sons Publ., 1962. 339 p.

25. Rolov B. N., Yurkevich V. E. *Physics of diffuse phase transitions**. Rostov-on-Don: RGU Publ., 1983. 320 p. (in Russ.)

26. Aliyev S. A. *Blurring of phase transitions in semiconductors and high-temperature superconductors**. Baku: Elm Publ., 2007. 286 p. (in Russ.)

27. Novikova S. I. *Thermal expansion of solid**. Moscow: Nauka Publ., 1974. 292 p. (in Russ.)

28. Epifanov G. I. *Solid state physics**. Moscow: Vysshaya shkola Publ., 1977. 288 p. (in Russ.)

29. Kingery W. D. *Introduction to ceramics*. New York: Wiley, 1960. 1065 p.

30. Terekhov S. V. Thermal changes in the state of metal glasses. *Physics and High Pressure Technology*. 2020;30(1): 5–16. (in Russ.) Available at: https://www.elibrary.ru/item.asp?id=42627413

31. Sheludyak Yu. E., Kashporov L. Ya., Malinin L. A., Tsalkov V. N. *Thermophysical properties of combustible system components**. Handbook. Moscow: NPO «Informatsiya i tekhniko-ekonomicheskie issledovaniya» Publ., 1992. 184 p. (in Russ.)

32. *Element properties**. Handbook. M. E. Dritz (ed.). Moscow: Metallurgiya, 1985. 672 p. (in Russ.)

* *Translated by author of the article.*

Information about the author

Sergey V. Terekhov, Dr. Sci. (Phys.–Math.), Associate Professor, Leading Researcher of the Department of Electronic Properties of Metals, Galkin Donetsk Institute for Physics and Engineering (Donetsk, Russian Federation).

https://orcid.org/0000-0003-3037-7258

svlter@yandex.ru

Received 10.01.2023; *approved after reviewing 25.03.2023*; *accepted for publication 15.04.2023*; *published online 25.09.2023.*

Translated by Valentina Mittova

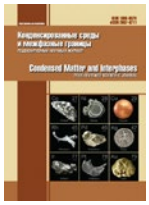

ISSN 1606-867X (Print)
ISSN 2687-0711 (Online)
Condensed Matter and Interphases
Kondensirovannye Sredy i Mezhfaznye Granitsy
https://journals.vsu.ru/kcmf/

Original articles

Research article
https://doi.org/10.17308/kcmf.2023.25/11266

Temperature influences of the interfacial layer in MOS ($Pt/TiO_2/Si$) structures

H. D. Chandrashekara✉, **P. Poornima**

Government science college (Autonomous), Department of Physics,
Hassan 573201, Karnataka, India

Abstract

In this paper present *I-V* and *C-V* electrical characteristics of MOS ($Pt/TiO_2/Si$) were reported. In the *I-V* characteristics the various electric parameter estimated such as the ideality factor (n), barrier height (Φ_B), leakage current (I_c) and saturation current (I_o) were estimated and further analyzed with Cheung functions.

These electrical parameters were observed to be varying with heat treatment. The *C-V* characteristics, flat band voltage (V_{FB}), interface trap density (D_{it}), effective charge density (N_{eff}) and oxide trapped charge (Q_{ot}) were estimated and analyzed. The variation of these values with annealing temperature was correlated with restructuring and rearrangement of TiO_2/SiO_2 atoms at the metal/silicon interface. The hysteresis loop in counter clock wise voltage between -1 V to 1 V at 1 MHz frequency, after 600 °C heat treatment show the strong accumulation region, this may be due to the reduced interface trapped charge and dangling bond.

Keywords: Leakage current, Ideality factor, Flat band voltage, Oxide trapped charge

Acknowledgement: Authors would like to thank Indian Nano electronics User's Programme, Centre for Nano Science and Engineering (CeNSE). One of the author (HDC) thank all the staff of GSC, Hassan, for their moral support to do the research work.

For citation: Chandrashekara H. D., Poornima P. Temperature influences of the interfacial layer in MOS ($Pt/TiO_2/Si$) structures. *Condensed Matter and Interphases*. 20223;25(3): 415–423. https://doi.org/10.17308/kcmf.2023.25/11266

Для цитирования: Чандрашекхара Х. Д., Пурнима П Влияние температуры на межфазный слой в МОП-структурах ($Pt/TiO_2/Si$). *Конденсированные среды и межфазные границы*. 2023;25(3): 415–423. https://doi.org/10.17308/kcmf.2023.25/11266

✉ H. D. Chandrashekara, chandruhdcs@gmail.com

1. Introduction

The band gap of SiO_2 about 9 eV and trap density of the bulk material is low, so that current passing through dielectric layer low. These oxide thickness increase with decreasing leakage current density. Other oxide materials with higher dielectric constant are suitable for optimising the leakage current, trap density and dangling bonds. Titanium dioxide (TiO_2) many interesting properties and various applications, such as in photo-catalytic activity, gas sensing, gate insulator and solar cells. TiO_2 thin films deposited on silicon/SiO_2 surface is very simple and significant role in all semiconductor devices. However, TiO_2 as a gate insulator shows higher leakage current due to higher band gap and high band offset than SiO_2 and silicon substrate. The anatase phase can be obtained at a temperature of 350 °C and it undergoes phase transformation to the more stable rutile phase at a higher temperature of 800 °C [1]. The phase transformation, from amorphous to crystalline anatase, can take place in the deposited films after annealing due to changes in grain boundary, packing density and defects [2, 3]. The TiO_2 thin films have been deposited using wide variety of techniques, like CVD [4], radio-frequency sputtering [5], atomic layer deposition [6], Sol-gel [7], Sputtering [8], pulsed laser deposition [9,] and spray pyrolysis [10, 11]. Among all the aforementioned methods of TiO_2 film synthesis, spray pyrolysis is quite widespread used technique due to its simplicity, commercial viability, potential for cost-effective, mass production and easier usage. The MOS structures constitute a kind of capacitor, which stores the electric charge by virtue of the dielectric property of insulating layers. Due to the presence of oxide layer and two surface-charge regions, MOS physics is more complicated than semiconductor surface physics. The importance in Silicon technology, the semiconductor/insulator (Si/TiO_2) interface and defects on its neighbourhood have been extensively studied in the past four decades. In general, there are several possible sources of error, which cause deviations from the ideal MOS behaviour such as electrical properties, must be taken into account. The study of *I-V* and *C-V* characteristics obtained at room temperature does not provide the detailed information about the charge transport process at the Si/TiO_2 interface. The temperature dependent electrical characteristics provide the information regarding the charge transport process through MOS contacts and also give a better picture of the conduction mechanisms [12]. The leakage current density of TiO_2 thin films can be further reduced by annealing in various gas environments such as O_2, N_2O and N_2, among these the common annealing process was in air ambience because it improves the structural order, dielectric constant and the reduction of defect states. This paper deals with the TiO_2 thin film deposition and annealing studies [13]. Due to the presence of oxide layer (TiO_2/SiO_2) and two region of interfaces metal/oxide and silicon/oxide have been extensively studied in the past four decades. The epitaxial growth of TiO_2 thin films deposited by Pulsed laser ablation, further improved the thin films as MOS Ni/*n*-TiO_2/*p*-Si for rectifying contact [14].The MOS structures of Pt/TiO_2/Si present that the dielectric constant of the TiO_2 thin film deposited between the Silicon substrate and platinum electrode. The growth of the interfacial layer seems to be reduction of oxygen vacancies. The MOS device different appearance as compared to the ideal case due to the presence of interface trapped density, effective oxide charge density and localized interface states. Then the leakage current mechanism in MOS (Pt/TiO_2/Si) structures capacitor at high electric field and at high temperature is due to Schottky emission.

2. Experimental

The TiO_2 thin films were prepared by spray pyrolysis technique under optimum conditions using Titanium (IV) Isopropoxide as a source material, Acetyl Acetonate as a complexing agent and Absolute ethanol as solvent. Before deposition, the silicon (100) wafers were cleaned using RCA-1 and RCA-2 [15]. TiO_2 thin films were deposited at a substrate temperature of 350 °C using 0.1 mol TiO_2 precursor solution. After deposition, isochronal annealing studies were carried out at various temperatures of 400, 500 and 600 °C for constant time of 30 min under air ambient. Electrical studies were made

by analyzing *C-V* and *I-V* characteristics of the deposited films. The electrical contacts were made by depositing platinum via a shadow mask on the surface of the TiO_2 layer using sputtering technique. The area of the dot diameter 7.5×10^{-4} cm². Other hand the back contact were made aluminum layer deposited of the silicon (100) wafer using thermal evaporation technique (Hindhivac vacuum coating unit Model 15F6). The devices were electrically characterized by Agilent Technologies B1500A Semiconductor device analyzer for both *I-V* and *C-V* studies. The bias was applied to the back contact (Si substrate) while the top contact was kept at the ground potential. Positive and negative bias sweeps were applied across zero bias. This paper presents the study of *I-V*, *C-V* and C^{-2}-*V* (hysteresis loop) characteristics of MOS (Pt/TiO_2/Si) device were made and estimate the electrical properties.

3. Result and Discussion

3.1. I-V Characteristics

Fig. 1 shows the measured forward and reverse bias Current density-Voltage characteristics of the fabricated MOS (Pt/TiO_2/*p*-Si) capacitor using as deposited at 300 °C and annealed TiO_2 thin films at 400, 500 and 600 °C. The applied voltage was varied from –1 V to +1 V, these devices are presented rectifying behaviour. Ideality factor *n* (*I-V*) for the MOS capacitor was obtained from the linear region of the forward characteristics ln (*I*) versus voltage using equation [16]. Where *k* is the Boltzman constant, *T* is the temperature and *q* is the electronic charge:

$$n=\frac{q}{kT}\left(\frac{dV}{d\ln I}\right). \qquad (1)$$

Various electrical parameters such as ideality factor (*n*), barrier height (Φ_B), saturation current (I_0), leakage current (I_C), series resistance (R_C) were calculated and estimated values are tabulated in Table 1. It can be observed that the decrease in ideality factor with increase in heat treatment may be attributed to the potential drop across the interfacial insulating layer of TiO_2 at the metal/semiconductor interface. The values of the saturation current were calculated by extrapolating the linear region to the ordinate and estimated as shown in the Table 1. The large value of the leakage current density (at –1 V) decrease with increase in annealing temperature, which may be attributed to the fabrication

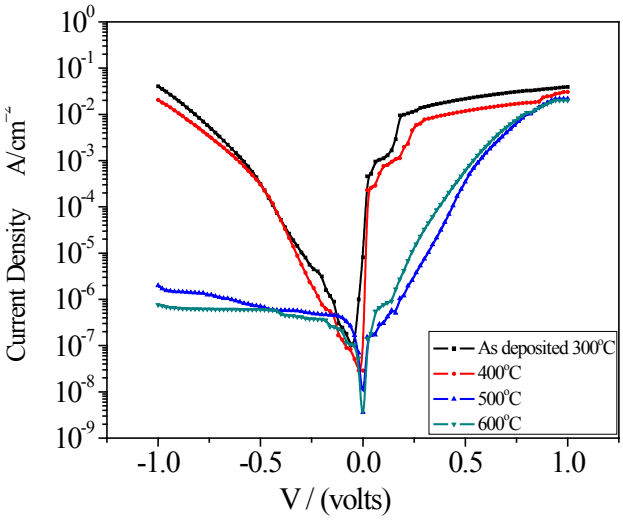

Fig. 1. Current–Voltage characteristics of Pt/TiO_2/Si for as deposited and annealed at different temperatures

Table 1. Electrical parameters of Pt/TiO_2/Si (MOS) structure from Current–Voltage

Sample	As deposited 300 °C	Annealing 400 °C	Annealing 500 °C	Annealing 600 °C
$n_{(FB\ I\text{-}V)}$	3.014	2.78	2.64	2.24
Jc, A/cm² at 1 V	$1.19\cdot10^{-4}$	$9.14\cdot10^{-5}$	$7.4\cdot10^{-5}$	$4.2\cdot10^{-5}$
$\Phi_{B(FB\ I\text{-}V)}$, eV	0.7004	0.7146	0.82879	0.840402
I_o, A	$5.89\cdot10^{-9}$	$1.02\cdot10^{-8}$	$7.15\cdot10^{-11}$	$4.56\cdot10^{-11}$
$n_{(dV/d\ln(I))}$	2.78	2.27	2.2	2.054
$\Phi_{B(H(I))}$	0.65	0.75	0.829	0.862
$R_{C\ (dV/d\ln(I))}$, Ω	129.59	139.5	168.109	194.102
$R_{C\ (H(I))}$, Ω	116.96	176.34	182.2	208,5

method and generation of the defects in the interface between silicon/TiO_2 and high series resistance of as deposited TiO_2 thin films and also the top electrode Pt acts as higher conductivity [17]. The barrier height is calculated from equation, where A^* is the effective Richardson constant (32 A/cm^{2}K^2) for *p*-type silicon, A is the area of the device (1.96e^{-3}cm^2), *T* is the room temperature (300 K), *q* is the electronic charge, *k* is the Boltzmann constant:

$$\Phi_{B0} = \left(\frac{KT}{q}\right)\ln\left(\frac{AA^*T^2}{I_0}\right). \quad (2)$$

The estimated values are tabulated in Table 1 and it is observed that the barrier height increases with increasing annealing temperature this may be due to immobilized radical are present in the metal/insulating layer interfaces. And also further analysed method developed by Cheung and Cheung's functions are given as [18,19]:

$$\frac{dV}{d\ln I} = IR_S + n\left(\frac{kT}{q}\right), \quad (3)$$

$$H(I) = n\Phi_B + IR_S = V - \frac{nkT}{q}\ln\left(\frac{I}{AA^*T^2}\right). \quad (4)$$

where *V* is voltage; R_S is series resistance; Φ_B is barrier height

Figs. 2 and 3 show the plots of d*V*/d(ln*I*) versus *I* and *H*(*I*) versus *I* corresponding to Cheung functions of below equations extracted from experimental forward *I-V* characteristics data. In Fig. 2 the obtained slope gives the series resistance, while the intercept on *y*-axis is the ideality factor which is nearer to those obtained from the ln(*I*)-*V* plot. The series resistance (R_S) plays a crucial role in the forward *I-V* characteristics of the MOS structure at higher applied voltage. Thus, Fig. 3 also gives the straight line with current axis intercept equal to the barrier height. The slope of this straight line provides the series resistance (R_s), which can be used to check the consistency of this approach. The estimated values of *n*, Φ_B and (R_s) from Cheung functions are tabulated in table 1, which are close to those obtained from *I-V* forward region. The series resistance (*R*s) was found to increase with increase in temperature, this may be due to increased effective oxide thickness of TiO_2 film with increased annealing temperature.

3.1. C-V Characteristics

Fig 4. presented the *C-V* characteristics of MOS (Pt/TiO_2/Si) devices, the voltage sweep from –1 V to +1 V at 1 MHz and its shows accumulation, inversion and depletion regions. It is observed that a strong accumulation is observed with high value of capacitance for the device annealed at 600 °C, which is attributed to the variation of the interface states density and dangling bonds which are associated with silicon/Oxide and metal/oxide interface. The capacitance becomes up and down in inversion and accumulation region as gate voltage

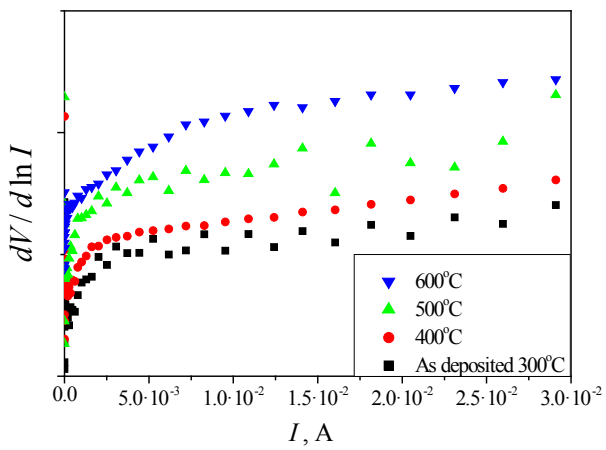

Fig. 2. dV/dln(I)-I characteristics of Pt/TiO_2/Si for as deposited and annealed at different temperatures

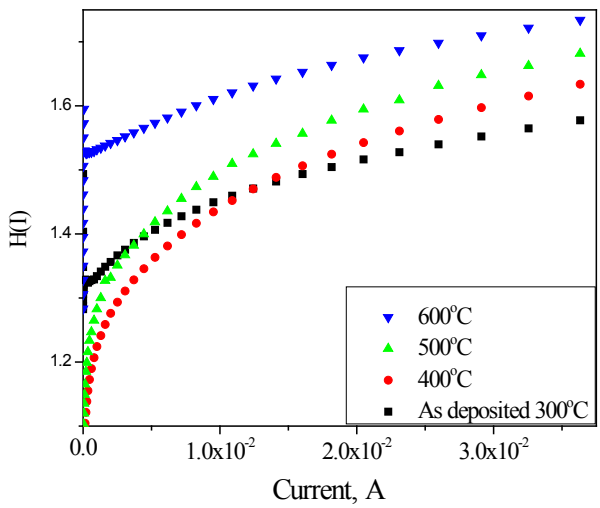

Fig. 3. H(I)-I characteristics of Pt/TiO_2/Si for as deposited and annealed at different temperatures

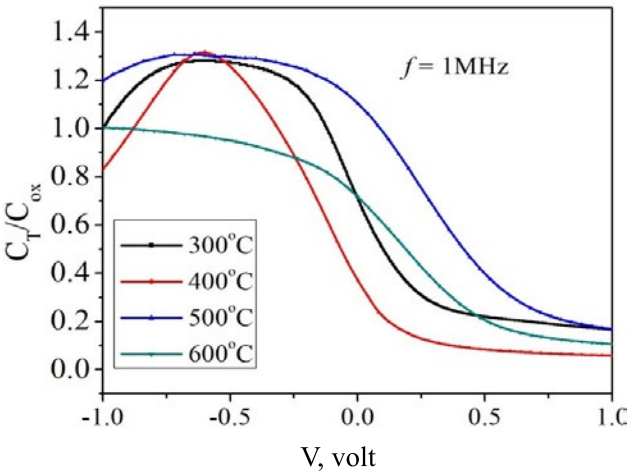

Fig. 4. *C-V* characteristics of Pt/TiO_2/Si for as deposited and different annealing temperature

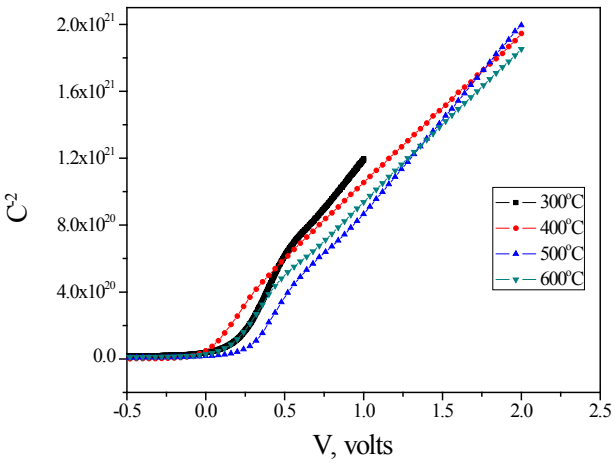

Fig. 5. C^{-2}-V characteristics of Pt/TiO_2/Si for as deposited and annealed at different temperatures

increase, which is attributed due to higher leakage current in TiO_2/Si interface. The slope estimated from the C^{-2}-V plot (Fig. 5) of device is substituted in below equation, which gives the oxide charge concentration as tabulated in Table 2:

$$\left(\frac{dC^{-2}}{dV}\right)=\left(\frac{2}{\varepsilon_s q A^2 N_D}\right), \quad (5)$$

where ε_s dielectric constant of semiconductor (silicon) $\varepsilon_s = 11.8\varepsilon_0$ (ε_0 is $8.85\cdot10^{-14}$ F/cm), A is area and q is charge, N_D is doping concentration.. It can be observed from the C^{-2}-V plot that the intercept on voltage axis gives the flat band voltage and are tabulated in Table 2. The increasing temperature of films under air ambient which leads to increase in oxygen vacancies and acceptor trap density which leads to the flat band voltage shifts towards positive. It can be seen that the oxide charge concentration at 400 °C with the annealing temperature, which may be due to the reduction of the interface trapped charges as seen in Table 2. It appears that drastic variation of Capacitance (C_{ox}) per unit area at 400 °C, this attributed that, between silicon/oxide interface the impurity concentration randomly variation takes place. And also the most interface trap density neutralised at this particular temperature. The similar study of MOS in *C-V* plot reported [20, 21]. The *C-V* hysteresis loop of MOS devise measured in counter clockwise at frequency of 1 MHz for different annealing temperatures is shown in Fig. 6. Presents *C-V* hysteresis loop the dc voltage swept sufficiently slowly to allow the inversion charge to form but the ac probe frequency is too high for the inversion charge to be able to responds, then high frequency curve is

Таблица 2. Электрические параметры структуры Pt/TiO_2/Si (МОП) по данным ВФХ

Sample	As deposited at 300 °C	Annealed at 400 °C	Annealed at 500 °C	Annealed at 600 °C
$C_{ox}\cdot10^{-7}$, f/cm^2	1.195	8.16	2.05	1.68
V_{FB}, B	–0.0705	–0.2148	–0.225	0.00992
∇V_{FB}, , V	0.0466	0.07372	0.13766	0.0089
ΔC, f	$2.23\cdot10^{-9}$	$4.19\cdot10^{-9}$	$1.01\cdot10^{-8}$	$1.01\cdot10^{-12}$
D_{it}, cm^{-1}eV^{-1}	$1.36\cdot10^{10}$	$2.54\cdot10^{10}$	$6.30\cdot10^{10}$	$6.3\cdot10^{6}$
N_{eff}, cm^{-3}	$8.02\cdot10^{11}$	$6.07\cdot10^{12}$	$1.23\cdot10^{12}$	$1.19\cdot10^{12}$
Q_{OT}, f/cm^2	$3.71\cdot10^{11}$	$1.76\cdot10^{11}$	$3.46\cdot10^{10}$	$9.37\cdot10^{09}$
N_{ox}, cm^{-3}	$2.34\cdot10^{15}$	$2.85\cdot10^{15}$	$3.15\cdot10^{15}$	$3.32\cdot10^{15}$

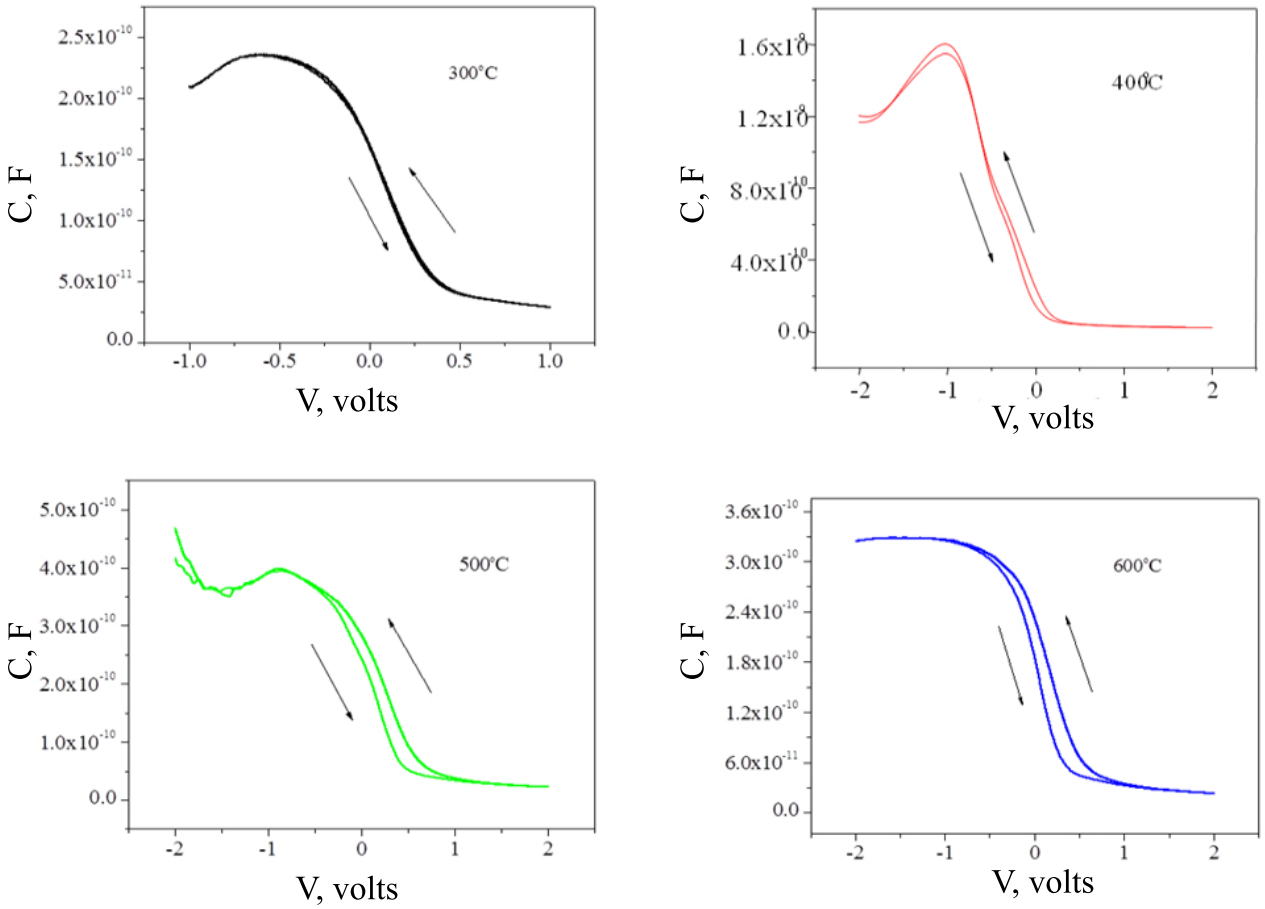

Fig. 6. *C-V* hysteresis loop of Pt/TiO_2/Si for as deposited and annealed at different temperatures

obtained. The hysteresis loop found to improve for all bias modes of accumulation, depletion and inversion as a function of heat treatment, which may be attributed to the decrease in leakage current and reduction of the interface trap density. In the *C-V* hysteresis, the voltage sweep in counter clock wise direction (–1 V to +1 V to –1 V) does not trace the same path as that of clock wise and shifted to lower voltages due to effective charge densities present in the interface between metal and silicon. The strong bias mode loop was observed at annealing temperature of 600 °C which may be due to lower value of interface trapped charge i.e., $6.3 \cdot 10^6$ $cm^{-1}eV^{-1}$ and reduction in the dangling bonds [22, 23]. Interface trap density, it is defined as the dangling bands at the surface of a semiconductor are responsible for distributed energy level called surface states or interface states density within the forbidden gap at the surface of the semiconductor, which is calculated using *C-V* characteristics in following relation [24]:

$$D_{\text{it}} = \frac{dC}{q}\left(1 - \frac{C_{HF} + \Delta C}{C_{\text{ox}}}\right)\left(1 - \frac{C_{HF}}{C_{\text{ox}}}\right), \quad (6)$$

where $\Delta C = C_{HF} - C_{LF}$, C_{LF} and C_{HF} *are* lower frequency region (lesser than the 1 KHz) and higher frequency region (greater than 1 MHz), C_{ox} is the Capacitance per unit area from and q is charge ($1.69 \cdot 10^{-19}$ C). The interface trap density D_{it} values are tabulated in Table 2 and values are found to be lower as compared to SiO_2. During annealing, the TiO_2 thin films gets oxidized which leads to the variation in dangling bonds. It is also observed that, annealing at 600 °C, the interface trapped density of TiO_2 thin films suddenly reduced by 4 order of magnitude ($6.3 \cdot 10^6$ $cm^{-1}eV^{-1}$) as compared to those of lower temperature annealed films. This may be due to the increased crystallinity of the TiO_2 thin films and reduced leakage current ($4.2 \cdot 10^{-5}$A). The

effective charge density (N_{eff}) is related to fixed oxide charge (Q_F), mobile ionic charge (Q_M) and oxide trapped charge (Q_{OT}) as in equation:

$$N_{eff} = \frac{Q_F + Q_M + Q_{OT}}{q}. \quad (7)$$

For the calculation of the effective oxide charge density, the expression by Nicollian and Brews [25]. It was found that the N_{EEF} was related to metal (Platinum) - Semiconductor junction and flat band voltage by,

$$N_{eff} = \frac{C_{ox}(\varphi_{MS} - V_{FB})}{Aq}, \quad (8)$$

where A is the area, C_{ox} is the capacitance per unit area and q is charge of an electron ($1.69 \cdot 10^{-19}$ C), V_{FB} is the flat band voltage and φ_{MS} is the metal semiconductor work function difference. The estimated values of N_{eff} are tabulated in Table 2 and it is found to decrease with annealing temperature, which is attributed to the increase in leakage current upon electrical stress. This suggests that near interface states creates neutral trapped charges in insulating layer. The oxide trapped charges are not located at the silicon/oxide interface but are distributed throughout oxide. The distribution of Q_{OT} must be known for proper interpretation of C–V curves. These are not introduced during the device fabrication, but in C-V characteristics during the gate voltage sweeping process electron or holes can be injected from gate or substrates. The oxide trapped charge distribution in oxide was estimated using the equation [26]:

$$Q_{OT} = \left(\frac{C_{ox} \nabla V_{FB})}{q} \right), \quad (9)$$

where ∇V_{FB} are flat band voltage shifts, C_{ox} is the Capacitance per unit area from and q is charge ($1.69 \cdot 10^{-19}$ C). The value of Q_{OT} tabulated in Table 2. These values are found to decrease with increase in heat treatment which may be attributed to the ionizing radiation, avalanche injection, Schottky emission, Fowler–Nordheim tunneling, or other mechanisms.

4. Conclusion

It is found that interfacial layer has crucial effect on electrical properties role MOS structures of Pt/TiO_2/Si. From I-V characteristics estimated parameter such as ideality factor (n) and barrier height (Φ_B) were found to be comparable as estimated from the model using Cheung functions. The estimated values of the barrier height increases with increasing annealing temperature, this may be potential drop across the interfacial insulating layer of TiO_2 at the metal/semiconductor interface. The series resistance (Rs) of device found to increase with increase in heat treatment. The observed decrease in leakage current with annealing temperature was attributed to the decrease in dangling bonds. From C-V characteristics, the oxide charge concentration (N_{ox}), flat band voltage (V_{FB}), interface trap density (D_{it}) and effective charge density (N_{eff}) were estimated. These values were found to decrease with the annealing temperature, due to the reconstruction and rearrangement of Ti and O atoms. From C-V hysteresis loop, in the counter clock wise direction, it is observed that hysteresis shifted to lower voltages due to effective charge densities present in the MOS structure and the strong accumulation region was obtained for higher temperature annealed TiO_2 film may be due to the reduction of interface trapped charge and oxide trapped charge density.

Contribution of the authors

The authors contributed equally to this article.

Conflict of interests

The authors declare that they have no known competing financial interests or personal relationships that could have influenced the work reported in this paper.

Reference

1. Nakaruk A., Ragazzon D., Sorrel C. C. Anatase–rutile transformation through high-temperature annealing of titania films produced by ultrasonic spray pyrolysis. *Thin Solid Films*. 2010;518(14): 3735–3742. https://doi.org/10.1016/j.tsf.2009.10.109

2. Li W., Ni C., Lin H., Huang C. P., Ismat Shah S. Size dependence of thermal stability of TiO_2 nanoparticles. *Journal of Applied Physics*. 2004;96(11): 6663–6668. https://doi.org/10.1063/1.1807520

3. Murad E. Raman and X-ray diffraction data on anatase in fired kaolins. *Clays and Clay Minerals*.2003;51(6); 689–692. https://doi.org/10.1346/cmn.203.0510611

4. Rausch N., Burte E. P. Thin TiO_2 films prepared by low pressure chemical vapor deposition. *Journal of*

The Electrochemical Society. 1993;140(1): 145–149. https://doi.org/10.1149/1.2056076

5. Kemell M., Pore V., Ritala M., Leskelä M., LindénM. Atomic layer deposition in nanometer-level replication of cellulosic substances and preparation of photocatalytic TiO_2/cellulose composites. *Journal of the American Chemical Society*. 2005;127(41): 14178–14179. https://doi.org/10.1021/ja0532887

6. Kim D. J., Hahn S. H., Oh S. H., Kim E. J. Influence of calcination temperature on structural and optical properties of TiO_2 thin films prepared by sol–gel dip coating. *Materials Letters*. 2002;57(2): 355–360. https://doi.org/10.1016/s0167-577x(02)00790-5

7. Suda Y., Kawasaki H., Ueda T., Ohshima T. Preparation of high quality nitrogen doped TiO_2 thin film as a photocatalyst using a pulsed laser deposition method. *Thin Solid Films*. 2004;453–454: 162–166. https://doi.org/10.1016/j.tsf.2003.11.185

8. Wang H., Chen L., Wang J., Sun Q., Zhao Y. A micro oxygen sensor based on a nano sol-gel TiO_2 thin film. *Sensors*. 2014;14(9): 16423–16433. https://doi.org/10.3390/s140916423

9. Kikuchi H., Kitano M., Takeuchi M., Matsuoka M., Anpo M., Kamat P. V. Extending the photoresponse of TiO_2 to the visible light region: photoelectrochemical behavior of TiO_2 thin films prepared by the radio frequency magnetron sputtering deposition method. *The Journal of Physical Chemistry B*. 2006;110(11): 5537–5541. https://doi.org/10.1021/jp058262g

10. Chandrashekara H. D., Angadi B., Shashidhar R., Murthy L. C. S., Poornima P. Optical properties of pseudo binary oxides $(TiO_2)_{1-x}$-$(Al_2O_3)_x$ thin films prepared by spray pyrolysis technique. *Materials Today: Proceedings*. 2006;3(6): 2027–2034. https://doi.org/10.1016/j.matpr.2016.04.105

11. Khan M. I., Imran S., Shahnawaz Saleem M., Ur Rehman S. Annealing effect on the structural, morphological and electrical properties of TiO_2/ZnO bilayer thin films. *Results in Physics*. 2018;8: 249–252. https://doi.org/10.1016/j.rinp.2017.12.030

12. Ramana C., Becker U., Shutthanandan V., Julien C. Oxidation and metal-insertion in molybdenite surfaces: evaluation of charge-transfer mechanisms and dynamics. *Geochemical Transactions*. 2008;9(1). https://doi.org/10.1186/1467-4866-9-8

13. Chandrashekara H. D., Angadi B., Shashidhar R., Murthy L. C. S., Poornima P. (2016). Isochronal effect of optical studies of TiO_2 thin films deposited by spray pyrolysis technique. *Advanced Science Letters*.2016; 22(4): 739–744. https://doi.org/10.1166/asl.2016.6975

14. Kumar A., Sharma K. K., Chand S., Kumar A. Investigation of barrier inhomogeneities in I-V and C-V characteristics of Ni/n-TiO_2/*p*-Si/Al heterostructure in wide temperature range. *Superlattices and Microstructures*. 2018;122: 304–315. https://doi.org/10.1016/j.spmi.2018.07.034

15. Kern W. *Hand book of semiconductor cleaning technology*. Noyes Publications; 1993. 623 p.

16. Sze S. M. *Physics of semiconductor devices*. New York: John Wiley and Sons; 1981. 868 p.

17. Gümüş A., Türüt A., Yalçin N. Temperature dependent barrier characteristics of CrNiCo alloy Schottky contacts on n-type molecular-beam epitaxy GaAs. *Journal of Applied Physics*. 2002;91(1): 245–250. https://doi.org/10.1063/1.1424054

18. Pakma O., Serin N., Serin T., Altındal Ş. The effects of preparation temperature on the main electrical parameters of Al/TiO_2/*p*-Si (MIS) structures by using sol–gel method. Journal of Sol-Gel Science and Technology. 2009;50(1): 28–34. https://doi.org/10.1007/s10971-009-1895-4

19. Yen C.-F., Lee M.-K. Low equivalent oxide thickness of TiO_2/GaAs MOS capacitor. *Solid-State Electronics*. 2012;73: 56–59. https://doi.org/10.1016/j.sse.2012.03.007

20. Rathee D., Kumar M., Arya S. K. (2012). Deposition of nanocrystalline thin TiO_2 films for MOS capacitors using Sol–Gel spin method with Pt and Al top electrodes. *Solid-State Electronics*. 2012;76: 71–76. https://doi.org/10.1016/j.sse.2012.04.041

21. Wei D., Hossain T., Garces N. Y., ... Edgar J. H. Influence of atomic layer deposition temperatures on TiO_2/*n*-Si MOS capacitor. *ECS Journal of Solid State Science and Technology*. 2013;2(5): N110–N114. https://doi.org/10.1149/2.010305jss

22. Chiu H.-C., Lin C.-K., Lin C.-W., Lai C.-S. Investigation of surface pretreatments on GaAs and memory characteristics of MOS capacitors embedded with Au nano-particles. *Microelectronics Reliability*. 2012;52(11): 2592–2596. https://doi.org/10.1016/j.microrel.2012.05.002

23. Murray H., Martin P. A unified channel charges expression for analytic MOSFET modeling. *Active and Passive Electronic Components*. 2012; 1–12. https://doi.org/10.1155/2012/652478

24. Yen C.-F., Lee M.-K. Low equivalent oxide thickness of TiO_2/GaAs MOS capacitor. *Solid-State Electronics*. 2012;73: 56–59. https://doi.org/10.1016/j.sse.2012.03.007

25 Nicollian E. H, Brews J. R. *MOS (Metal Oxide Semiconductor) physics and pechnology.* John Wiley & Sons; 1982. 928 p.

26. Schroder D. K. *Semiconductor material and device characterization*. John Wiley & Sons; 2006. 800 p.

Information about the authors

H. D. Chandrashekara, PhD, Assistant Professor, Department of Physics, Government Science College, Hassan (Karnataka, India).
https://orcid.org/0000-0001-9976-3128
chandruhdcs@gmail.com

P. Poornima, Assistant Professor, Department of Physics, Government Science College, Hassan (Karnataka, India).
https://orcid.org/0000-0001-7685-6778
poornimaputtegowda81@gmail.com

Received 08.12.2022; approved after reviewing 18.01.2023; accepted for publication 15.05.2023; published online 25.09.2023.

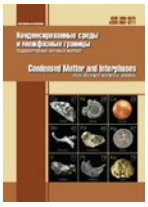

ISSN 1606-867X (Print)
ISSN 2687-0711 (Online)
Condensed Matter and Interphases
Kondensirovannye Sredy i Mezhfaznye Granitsy
https://journals.vsu.ru/kcmf/

Original articles

Research article
https://doi.org/10.17308/kcmf.2023.25/11391

Sedimentation of bentonite suspensions under the influence of low molecular weight polymers based on amino ester salts

D. Yu. Vandyshev[1]✉, O. V. Sleptsova[1], V. Yu. Gazin[1], S. A. Malyutin[2], N. R. Malkin[2], Kh. S. Shikhaliev[1]

[1]*Voronezh State University,*
1 Universitetskaya pl., Voronezh 394018, Russian Federation

[2]*JSC Petrochem,*
14, Rabochaya st., Belgorod 308017, Russian Federation

Abstract

Among the available technologies for treating natural and wastewater from clay materials, coagulation/flocculation is the most common method due to its high efficiency, simplicity, and cost-effectiveness. Inorganic coagulants such as aluminum sulfate and ferric chloride, widely used as destabilizing agents for colloidal particles, have several significant drawbacks: low efficiency and toxicity. Organic reagents of both natural and synthetic origin are a good alternative.

This work is devoted to the evaluation of the flocculation action of new reagents, which are low molecular weight polymers based on amino ester salts on clay suspensions, as well as the selection of their optimal concentration, providing the maximum sedimentation rate.

Studies have shown that amino ester salts can be effectively used for the treatment of water-clay suspensions. An important factor is the nature of the anion used, which has a significant influence on the coagulation ability of esters. Thus, 40–50 % (wt.) aqueous solutions of amino ester chlorides added to clay suspensions in an amount not exceeding 0.1% (vol.) can be used to thicken clay suspensions. At the same time, aqueous solutions of amino ester bromides regardless of the concentration, introduced into bentonite suspensions of 0.1–0.4 % (vol.), contribute to improved sedimentation, reducing viscosity, and increasing filtration capacity. These results allow us to recommend the use of amino ester chlorides as a thickener in the preparation of drilling muds for strengthening the walls of wells during drilling, and bromides – for flocculation of bentonite suspensions in oil production.

Keywords: Flocculation, Coagulation, Amino esters, Sedimentation rate, Rheological properties, Bentonite, Drilling fluid

Funding source: The results were obtained as part of the work supported by the Ministry of Science and Higher Education of the Russian Federation within the framework of the state assignment to universities in the field of scientific activity for 2022-2024, project No. FZGU-2022-0003.

Acknowledgments: Research results were partially obtained on the equipment of the Collective Use Centre of Voronezh State University. URL: http://ckp.vsu.ru

For citation: Vandyshev D. Yu., Sleptsova O. V., Gazin V. Yu., Malyutin S. A., Malkin N. R., Shikhaliev Kh. S. Sedimentation of bentonite suspensions under the influence of low molecular weight polymers based on aminoether salts. *Condensed Matter and Interphases*. 20223;25(3): 424–434. https://doi.org/10.17308/kcmf.2023.25/11391

Для цитирования: Вандышев Д. Ю., Слепцова О. В., Газин В. Ю., Малютин С. А., Малкин Н. Р., Шихалиев Х. С. Седиментация бентонитовых суспензий под влиянием низкомолекулярных полимеров на основе солей аминоэфиров. *Конденсированные среды и межфазные границы*. 2023;25(3): 424–434. https://doi.org/10.17308/kcmf.2023.25/11391

✉ Dmitriy Yu. Vandyshev, e-mail: francy_2007@mail.ru

1. Introduction

Bentonite consists of clay minerals based on hydrous aluminosilicate such as montmorillonite, illite, quartz, pyrite, and other minerals [1, 2]. In water, bentonite clay is dispersed to a colloidal state in which the particles acquire a negative surface charge and consequently a negative zeta potential (ξ < -35 mV) due to the isomorphic substitution of aluminum ions for magnesium and iron ions (Mg^{2+} and Fe^{2+}) and silicon ions for Al^{3+} occurring in the octahedral and tetrahedral layers, respectively [3]. This explains the fact that when dispersed in water, bentonite forms a highly stable colloidal suspension, mutual repulsion of particles which prevents their aggregation and sedimentation [4–6].

Bentonite particles have a lamellar shape with a small average diameter (D_{50} < 5 μm), which causes a high surface area of the dispersed phase. At the same time, the value of the negative charge on different parts of the particle surface is not equal, the charge on the protruding curved areas depends on the pH of the dispersion medium. Therefore, the degree of flocculation of bentonite suspension and the structure of the formed precipitates strongly depends on the pH of the medium [5].

Bentonite has a number of useful properties such as non-toxicity, high ion exchange capacity, swelling ability, and large surface area with excess free surface energy [7]. It can be applied directly in its natural form or pre-treated by various chemical and physical activation methods [8]. The composition and desirable consumer properties of clay minerals have caused the popularity of bentonite as a raw material in the industrial sector [2]. However, its use in food, petroleum, wine, construction, and agriculture produces wastewater containing fine colloidal clay particles. The resulting colloidal suspensions require special treatment and separation of solid pollutants from water [9]. Direct discharge of stable colloidal suspension into water bodies is prohibited, as it causes a significant increase in turbidity and leads to serious problems for aquatic life [10]. Therefore, it is crucial to properly treat the generated wastewater before its discharge into water bodies [9, 11]. This issue is particularly acute in oil and gas production. Well formation in the oil and gas industry is accompanied by environmental pollution with drilling muds, their spent or waste part, drilling cuttings, etc. Waste drilling muds accumulate due to the duration of sedimentation of the drilled predominantly clayey rock during sedimentation in mud pits.

Various solid-liquid separation methods, including physical and chemical methods, are used to purify colloidal suspensions. There are several technologies such as electrocoagulation, membrane filtration, electroosmosis, and thermomechanical dewatering [12–15], but these methods are require a high expenditure of energy and finances [16]. Coagulation/flocculation is one of the most commonly used processes for water and wastewater treatment, especially for the separation of suspended colloidal particles. This method is highly efficient, economical, cheap, and non-energy consuming [17–20]. The key principle of coagulation and flocculation processes is to reduce the net negative charge of particles and to stimulate the van der Waals attraction forces between them [17]. Coagulation is aimed at destabilization of colloidal particles and formation of microaggregates, while flocculation is aimed at further agglomeration of particles and formation of larger floccules [17]. Thus, the formed aggregates are deposited by gravity, resulting in a relatively clear supernatant. Various chemicals including metal salts (coagulants) and polyelectrolytes (flocculants) are used to destabilize the colloidal suspension [20]. Aluminum sulfate as well as iron and aluminum chlorides are common coagulants, but their utilization is limited due to low removal efficiency, environmental and health concerns associated with the presence of residual metal in the supernatant, and the formation of toxic sludge [18]. Therefore, there is an ongoing search for environmentally friendly and economical alternative coagulants.

In recent years, the use of polyelectrolytes as flocculants has become a common practice due to their effectiveness in treating colloidal suspensions through a bridging mechanism [17]. Flocculation of fine colloidal particles with the employment of polyelectrolytes such as polyelectrolyte (PAA) can occur by various mechanisms including adsorption and binding of the polymer, charge neutralization, particle-surface complex formation, and depletion flocculation, or a combination of these

mechanisms [6, 21–24]. Cationic polyacrylamide (CPAA) is most commonly used for destabilization and separation of stable colloidal drilling fluid suspension. The destabilization process with the help of CPAA is carried out due to the adsorption of cationic polymer chains due to the formation of hydrogen bonds between the particle surface and the primary amide functional groups of the polymer. Thus, charge neutralization becomes the main mechanism by which CPAA locally changes the charge of the particle surface [17]. The main characteristic of CPAA responsible for its function as a destabilizing agent is determined by the presence of a quaternary ammonium salt carrying a positive charge. The same is true for a cheap low molecular weight flocculant/coagulant, choline chloride (ChCl). It is also worth noting that ChCl exhibits its flocculating properties only at significantly high concentrations in relation to clay suspensions. Therefore, it is more often used as a thickener and stabilizer (coagulant property) in an individual form or as part of a mixture with inorganic and high molecular weight reagents [25–26]. However, it is important to note that the potential hazard of these reagents is determined by the content of monomers, residues of initial halogen derivatives of hydrocarbons involved in their synthesis, and other impurities. Therefore, their application requires additional purification stages. In this case, the search for simple in terms of synthesis methodology, environmentally safe and effective alternatives to traditional coagulants/flocculants becomes highly relevant.

From this point of view, amino esters are promising, the advantage of which is biodegradability and nontoxicity. This class of compounds has found wide application in the production of biologically active substances (BAS) [27], polyurethanes [28–30], catalysts and modifiers [31], emulsifiers of inverse emulsions [32–33], fabric softeners [34], and in the field of microelectronics [35–40]. However, their application for wastewater treatment, in particular, drilling muds, has not been previously considered.

In this regard, this work aimed to evaluate the flocculation action of new reagents, which are low molecular weight polymers based on amino ester salts, on clay suspensions, as well as the selection of their optimal concentration, providing the maximum sedimentation rate.

2. Experimental

The following raw materials and reagents were used in the work:

1) Bentonite clay with particle sizes in the range of 5–75 μm.

2) Flocculants/coagulants in the form of low molecular weight polymers based on hydrochlorides (AE-1) and hydrobromides (AE-2) of amino esters, which were synthesized at the Department of Organic Chemistry of Voronezh State University using reagents of "chemically pure" grade. The structure of the compounds was proved by a complex of physicochemical methods such as:

– ^{1}H NMR (spectra recorded on a Bruker DRX-500 instrument (500.13 MHz) in DMSO-d6 and an internal standard Me_4Si);

– HPLC-MS (spectra were recorded on Agilent Infinity 1260 chromatograph with Agilent 6230 TOF LC/MS interface. Separation conditions: mobile phase MeCN/H_2O + 0.1% FA (formic acid), gradient elution, column – Poroshell 120 EC-C18 (4.6×50 mm, 2.7 μm), thermostat 23–28 °C, flow rate 0.3-0.4 ml/min. Ionisation – electrospray (capillary –3.5 kV; fragmentor +191 V; OctRF +66 V – positive polarity);

– To study sedimentation stability, we used a combined technique based on the works of A. A. Shkop. A. [41] and Averkina E. V. B. [42], which consisted of the following stages:

1. ***Preparation of bentonite suspension (BS).*** 100 ml of distilled water and clay stabilizer (ChCl), the concentration of which was 0.2 % (vol.), were placed in a 250 ml flask. 1.7 g of bentonitic clay was added to the obtained solution, the flask was tightly corked and stirred on a vibration table VB 1.1 (2 vibration frequencies 3000, 6000 min^{-1}, vibration amplitude controller, vibration arc, working table 185×135 mm) for uniform distribution of clay in the liquid volume due to dispersion of agglomerates. The resulting mixture was left to swell the clay particles for 24 hours. After soaking, the flask was shaken thoroughly to obtain stable BS.

2. ***Estimation of the deposition rate.*** The obtained BS was transferred into a 100 ml measuring cylinder (30 mm diameter and 230 mm height) and a certain amount (0.1–0.6 % (vol.)) of the test reagent solution (AE-1 or AE-2) with different concentrations of 40, 50, 60, 70 % (wt.)

was added. The range of reagent concentrations was selected based on the analysis of the available market of flocculants/coagulants close in chemical structure. After introducing a portion of the reagent, the contents of the cylinder were stirred by tilting it ten times slowly. The time interval during which the interface between the clarified liquid layer, presumably containing no clay particles, and the compacted suspension layer passes the path corresponding to the zone of free sedimentation of particles, was determined. According to the experimental data obtained, the flocculus sedimentation rate (V, mm/min) was calculated to the time of flocculus passage along this path. The primary results of the experiment were graphically represented as points in the coordinates "flocculus settling velocity V – the amount of reagent solution N". Each point represented the average value of the results of three or four experiments. The relative deviation of experimental data from the average value did not exceed 4.5 %.

To assess the flocculation quality of the BS (mechanical strength of the aggregates), after completion of the flocculation process and measurement of the sedimentation rate V_1, the sample was stirred again with a mechanical stirrer at 600 rpm for 40 s in a chemical beaker. The contents were then transferred back into the measuring cylinder and the sedimentation rate of suspended particles in the sample was determined (V_2, mm/min).

3) After each measurement of sedimentation rate, samples were taken to ***control the size of formed particles***. To qualitatively assess the size of the formed agglomerates, a Biomed-6 microscope equipped with a digital camera which was used at a magnification of 40 times. The microscope was equipped with an achromatic lens 40×0.65, halogen illuminator with smooth brightness control.

4) ***Viscosity measurements*** of the tested suspensions were carried out on an A&D SV-100A vibro viscometer. The principle of operation of the device was based on the dependence of power, which was used to excite the vibration of two thin sensor plates with a frequency of 30 Hz and a constant amplitude of about 1 mm, on the product of dynamic viscosity by suspension density (ν). The measurements were carried out at a constant temperature of 25 °C by a number of at least three repetitions. The instrument was standardized and calibrated with distilled water before each new measurement.

The pycnometric method was used to determine the density of BS and the resulting systems. The obtained values were the average of three measurements performed at a constant temperature of 25 °C.

5) ***Determination of the acidity of the medium*** pH-meter "Ionometer I-160 MI" was used. Operating conditions of the device correspond to the values for devices of group 2 according to GOST 22261-94. The device complies with TU 4215-053-89650280-2009. Measurements were carried out at a constant temperature of 25 °C, the number of at least 3 repetitions.

3. Results and discussion

In order to select a flocculant/coagulant for BS with the best flocculation characteristics, the experiments were carried out in two stages.

The first stage consisted in comparison of sedimentation rates in free conditions of BS samples containing additives of reagents AE-1 and AE-2.

The second stage of the experiments included mechanical impact on the resulting systems, simulating the movement of the flocculated suspension from the thickening apparatus (settling tank) to the dewatering apparatus (centrifuge or filter press). The residual sedimentation velocity V_2 after mechanical action characterized the sedimentation ability of the BS, determined by the size of the aggregates formed, and hence the strength of the initial floccule. Identification of the optimal concentration of additives was carried out on the basis of the graphical plots obtained by analogy with the first stage.

The structure, stability, purity of the BS filtrate, and water separation were visually assessed during each test. In addition, the viscosity, density of the suspension, pH of the dispersion medium, and the size of the aggregates formed were analyzed.

According to the data obtained by measuring the sedimentation rate before mechanical action (Fig. 1a and 2a), additives AE-1 and AE-2 have a flocculation effect, causing the coagulation

and sedimentation processes. The maximum sedimentation rate is observed when using 70 % (wt.) aqueous solution of the flocculating agent in the amount of 0.6 % (vol.) and is 0.73 mm/min for AE-1 and 3.56 mm/min for AE-2. On visual evaluation, agglomerate formation is noted for both additives, but when AE-2 is introduced into the BS, much larger aggregates are formed almost immediately and the supernatant becomes transparent. Over time, the flocculates formed almost completely settle to the bottom of the measuring cylinder. That is, the reagent AE-2 under equal conditions to a greater extent disrupts the aggregative and sedimentation stability of BS and, therefore, has a more pronounced flocculating effect, leading to accelerated sedimentation. At the introduction of AE-1 the formation of agglomerates is accompanied by the thickening of clay suspension, and the height of the clarified layer after the thickening

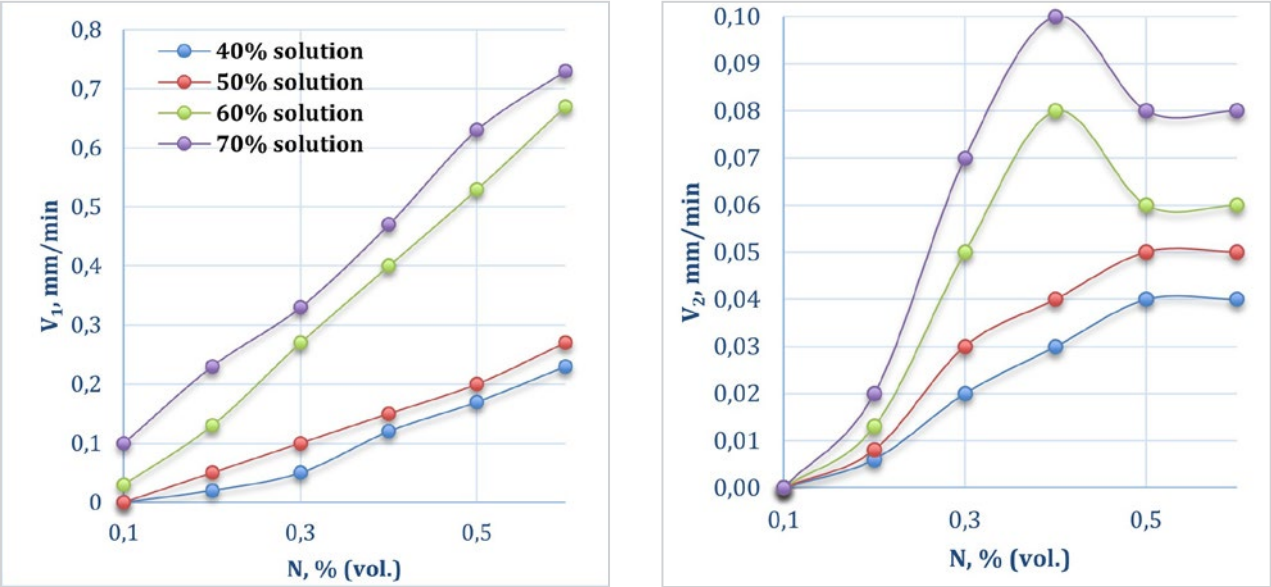

a b

Fig. 1 Dependence of flocculus sedimentation rate (V) on the amount (N) of injected solution of reagent AE-1 before (a) and after (b) mechanical impact

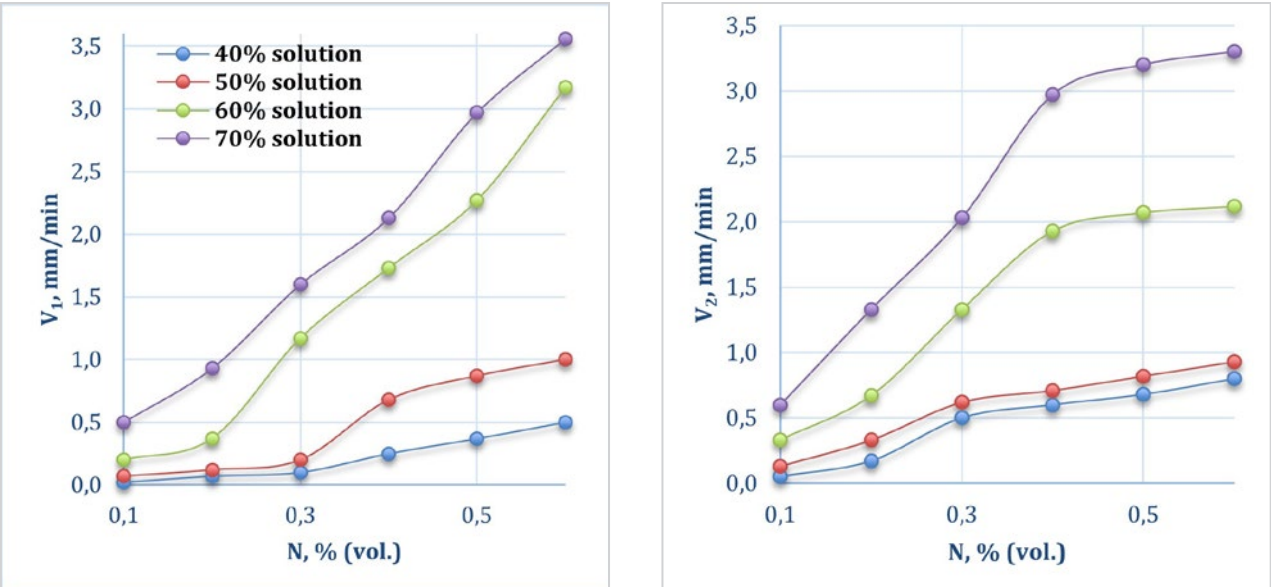

a b

Fig. 2. Dependence of flocculus sedimentation rate (V) on the amount (N) of injected AE-2 reagent solution before (a) and after (b) mechanical impact

of compacted layer of suspension practically does not change for several days. Probably, the reason of thickening is structure formation in the thickened layer of suspension, which is also based on coagulation and flocculation processes with the participation of the introduced reagent. Obviously, the mechanism of these processes at the introduction of investigated additives is somewhat different.

Of practical interest is the change in the sedimentation rate of flocculated clay after mechanical action on the suspension (Figs. 1b and 2b), which allows us to assess the strength of aggregates formed at the first stage of research. The residual sedimentation rate of BS samples containing AE-1 decreases significantly, almost by an order of magnitude (Fig. 1). The almost linear dependence of sedimentation rate on the amount of the introduced reagent is broken, which indicates the transition of sedimentation from free conditions to constricted conditions. Broken floccule visually acquires a shapeless appearance. In contrast to the first stage of tests, the clarified liquid after repeated sedimentation of the suspension becomes turbid, this is caused by the increase in the dispersibility of the system, subjected to mechanical influence, and the appearance of colloidal particles resistant to sedimentation due to their small size.

Mechanical impact on the flocculated BS sample containing AE-2 reagent practically does not change the rate of re-sedimentation of agglomerates. Only at high concentrations of AE-2 sedimentation rate ceases to depend on the amount of the introduced reagent, which may be due to the transition of the sedimentation process in the compacted layer in constricted conditions. It should be noted that for all BS with introduced AE-2 the liquid above the compacted layer remains transparent regardless of the mechanical influence.

The observed difference in the course of sedimentation processes in BS at the introduction of reagents AE-1 and AE-2 before and after mechanical action confirms assumptions about different mechanisms of coagulation-flocculation processes with the participation of these additives.

In addition to the observed regularities of macroscopic processes of particle deposition, we evaluated the dimensional characteristics of BS agglomerates using optical microscopy. The images obtained with 40× magnification (Fig. 3, 4) show that the introduction of reagents AE-1 and AE-2 into the BS causes coagulation process, i.e. clay particles sticking together to form agglomerates (images F1). When using the AE-1 additive, a structure with a more uniform distribution of agglomerates and inclusion of water in the structural grid is observed (Fig. 3). Probably, the introduction of the AE-1 additive leads to the formation of a coagulation structure with fragile contacts through the dispersion medium interlayers. Such contacts are easily destroyed by mechanical action, as shown by the F2 image (Fig. 3). The previously observed thickening effect and some sedimentation stability of the thickened layer of suspension are possible when AE-1 molecules are fixed on one particle and structured polyelectrolyte layers of amino ester in Cl-form are formed.

When AE-2 is used as a flocculation agent, the formation of larger and stronger aggregates that are not destroyed by mechanical action occurs (Fig. 4). Most likely, when AE-2 is used, the formation of some number of phase contacts occurs as a result of a decrease in the ionic-electrostatic stability factor provided by the negative surface charge of clay particles. The coagulated particles may also bind due to “bridging” fixation by the introduced AE-2 reagent, and the dispersion medium will be in a free state in the space between agglomerates.

Viscometric studies confirmed the viscosity increase observed visually with increasing concentration of AE-1 (Fig. 5a) and viscosity decrease with increasing concentration of AE-2 in BS (Fig. 5b), associated with the formation of different structures during coagulation and flocculation processes involving the studied reagents. Obviously, the adsorption layers of polyelectrolytes based on hydrochlorides (AE-1) and hydrobromides (AE-2) of amino esters, in which Cl^- and Br^- act as counterions of the electric double layer, have a determining influence on these processes. Br^- has a larger ionic radius compared to Cl^-, the lower degree of hydration and higher adsorption capacity, and hence will preferentially reside in the dense adsorption part of the electrical double layer. This will lead to a decrease in the ξ-potential and, as

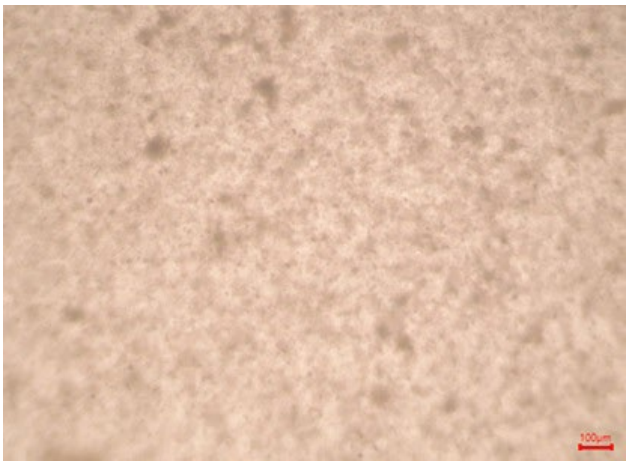

a

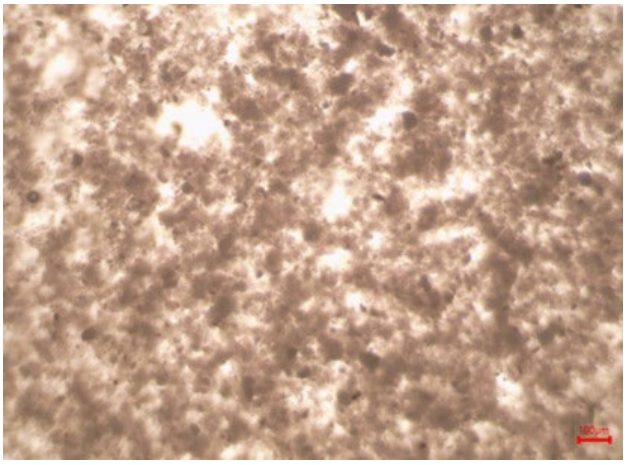

b

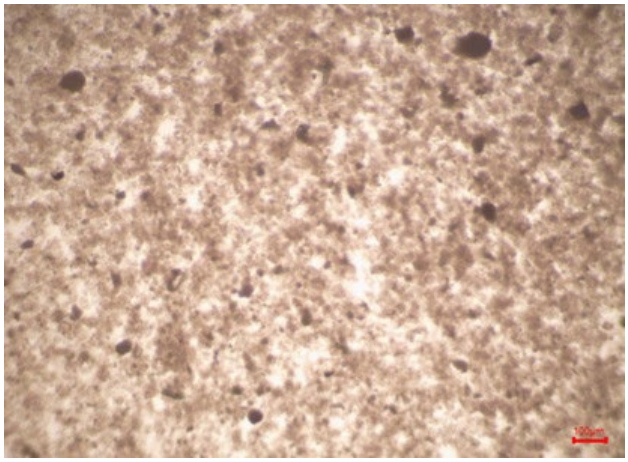

c

Fig. 3. View of the BS without additive (a), before (b) and after (c) mechanical action at introduction of 40 % (wt.) solution of AE-1 reagent in the amount of 0.1 % (vol.)

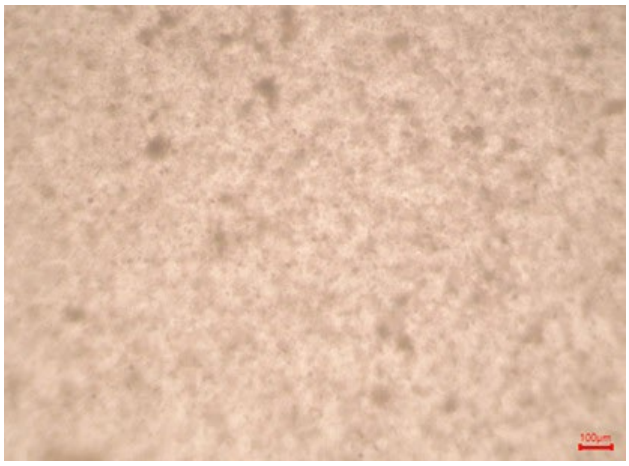

a

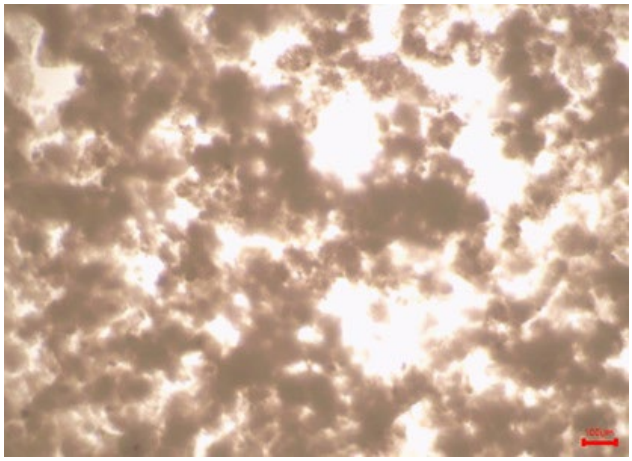

b

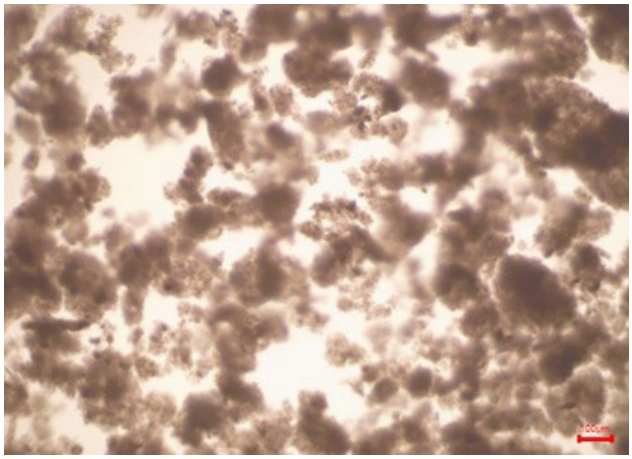

c

Fig. 4. View of the BS without additive (a), before (b) and after (c) mechanical action at introduction of 60 % (wt.) solution of reagent AE-2 in the amount of 0.4 % (vol.)

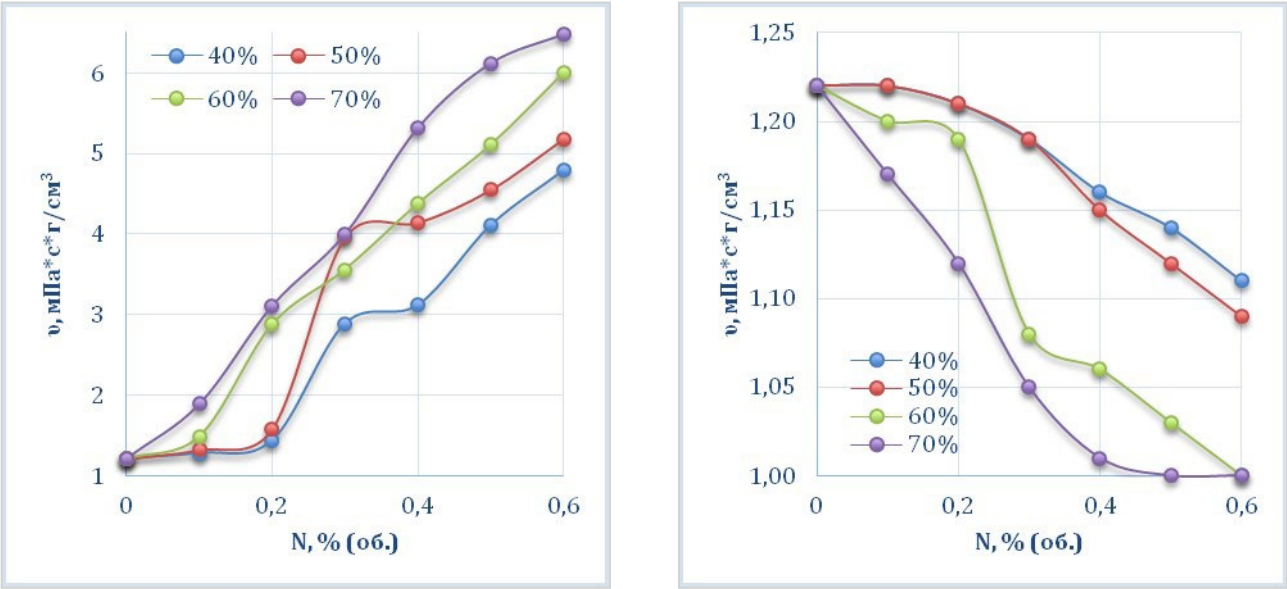

a b

Fig. 5. Dependence of viscosity (υ) on the amount (N) of injected reagent solution AE-1 (a) and AE-2 (b)

a consequence, a decrease in the aggregative stability of the BS as a result of the formation of rather strong aggregates - floccules. Therefore, amino ester bromide oligomers (reagent AE-2) have pronounced flocculating properties and can be used as flocculants of BS.

Cl^- ion of amino ester hydrochlorides (AE-1), which has higher mobility, participates mainly in the formation of the diffuse part of the electric double layer, providing a sufficiently high value of ξ-potential, and therefore will act as a stabilizer and thickener of the suspension. Anisometric (lamellar) clay particles at the introduction of AE-1 will be able to interact with their protruding parts through water layers, forming unstable coagulation contacts, easily destroyed as a result of mechanical impact. Formation of the coagulation structure (grid), as well as the participation of water molecules in this process (its binding), leads to the thickening of suspension and increasing its sedimentation stability. The ability of AE-1 to fulfill the function of a thickener can be used in the preparation of drilling muds to strengthen the borehole walls during drilling.

The use of AE-1 can be limited by hydrolysis of amino ester salts. For example, increasing the concentration of AE-1 in the BS leads to a significant decrease in the pH of the dispersion medium (Fig. 6a). This parameter limits the use of AE-1, and 40-50 % (wt.) aqueous solutions introduced in amounts not exceeding 0.1 % (vol.) are optimal as BS thickeners. For AE-2, a decrease in pH is also observed, but it is within acceptable limits (Fig. 6b).

It is also worth noting that regardless of the observed phenomena, the viscosity of the system, and pH, the density of BS was unchanged and was 1.023 g/cm^3. The change of physicochemical parameters after mechanical action on BS was not significant (within 10^{-3}).

4. Conclusions

As a result of the research, it is shown that the salts of amino esters obtained by us can be effectively used in the processes of water-clay suspension treatment. The nature of the used anion has a significant influence on the coagulating ability of esters: amino ester chlorides AE-1 can be used in the form of 40–50 % (wt.) aqueous solutions introduced in amounts not exceeding 0.1 % (vol.) for thickening of clay suspensions. At the same time, aqueous solutions of bromides of AE-2 amino esters introduced into bentonite suspensions in the amount of 0.1–0.4 % (vol.), regardless of the concentration, contribute to improved sedimentation. On this basis, we can conclude that the obtained results allow us to recommend to use of AE-1 as a thickener in preparation of drilling muds for strengthening of

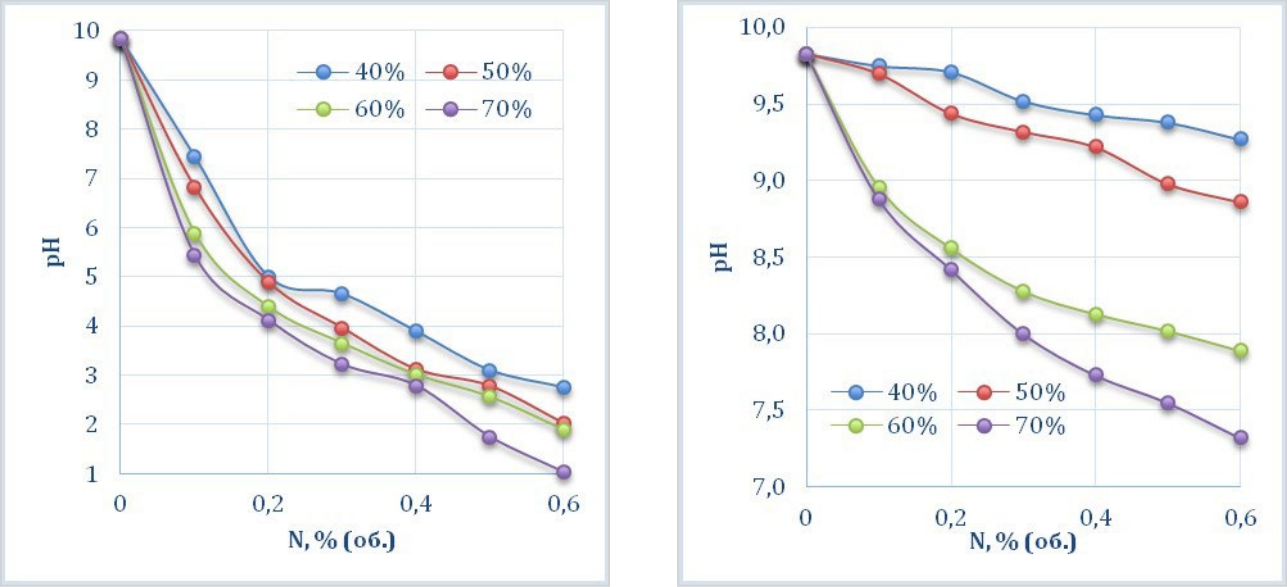

а б

Fig. 6. Dependence of BS pH on the amount (N) of injected solution of reagent AE-1 (a) and AE-2 (b)

borehole walls during drilling, where AE-2 – for flocculation of bentonite suspensions during oil production. Both additives are characterized by low consumption, which makes them economically attractive for practical use.

Contribution of the authors

All authors made equivalent contributions to the publication.

Conflict of interest

The authors declare that they have no known financial conflicts of interest or personal relationships that could influence the work presented in this article.

Reference

1. Abu-Jdayil B. Rheology of sodium and calcium bentonite-water dispersions: Effect of electrolytes and aging time. *International Journal of Mineral Processing*. 2011;98(3-4): 208–213. https://doi.org/10.1016/j.minpro.2011.01.001

2. Karnland O. *Chemical and mineralogical characterization of the bentonite buffer for the acceptance control procedure in a KBS-3 repository*. Stockholm: Clay Technology AB; Technical Report, SKB-TR-10-60, 2010. 25 p.

3. Duman O., Tunç S. Electrokinetic and rheological properties of Na-bentonite in some electrolyte solutions. *Microporous Mesoporous Materials*. 2009;117(1-2): 331–338. https://doi.org/10.1016/j.micromeso.2008.07.007

4. Tchobanoglous G., Burton F. L., Stensel H. D. *Wastewater engineering: treatment and reuse*. Metcalf & Eddy Inc., McGraw-Hill Education, Boston; 2003. 1819 p.

5. Shaikh S. M. R., Nasser M. S., Hussein I. A., Benamor A. Investigation of the effect of polyelectrolyte structure and type on the electrokinetics and flocculation behavior of bentonite dispersions. *Chemical Engineering Journal*. 2017;311: 265–276. https://doi.org/10.1016/j.cej.2016.11.098

6. Zhang B., Su H., Gu X., X. Huang. Wang H. Effect of structure and charge of polysaccharide flocculants on their flocculation performance for bentonite suspensions. *Colloids and Surfaces A: Physicochemical and Engineering Aspects*. 2013;436: 443–449. https://doi.org/10.1016/j.colsurfa.2013.07.017

7. Carlson L. *Bentonite Mineralogy. Working Report*. POSIVA OY, Finland. 2004. 189 p.

8. Karimi L., Salem A. The role of bentonite particle size distribution on kinetic of cation exchange capacity. *Journal of Industrial and Engineering Chemistry*. 2011;17(1): 90–95. https://doi.org/10.1016/j.jiec.2010.12.002

9. Nasser M. S., Twaiq F. A., Onaizi S. A. Effect of polyelectrolytes on the degree of flocculation of papermaking suspensions. *Separation and Purification Technology*. 2013;103: 43–52. https://doi.org/10.1016/j.seppur.2012.10.024

10. Yousefi S. A., Nasser M. S., Hussein I. A., Benamor A., El-Naas M. H. Influence of polyelectrolyte structure and type on the degree of flocculation and rheological behavior of industrial MBR sludge. *Separation and Purification Technology*, 2020;233: 116001. https://doi.org/10.1016/j.seppur.2019.116001

11. Chatterjee T., Chatterjee S., Woo S. H. Enhanced coagulation of bentonite particles in water by a modified chitosan biopolymer. *Chemical Engineering Journal*. 2009;148(2-3): 414–419. https://doi.org/10.1016/j.cej.2008.09.016

12. Ghernaout D., Ghernaout B., Boucherit A. Effect of pH on electrocoagulation of bentonite suspensions in batch using iron electrodes. *Journal of Dispersion Science and Technology*. 2008;29(9): 1272–1275. https://doi.org/10.1080/01932690701857483

13. Hilal N., Ogunbiyi O. O., Al-Abri M. Neural network modeling for separation of bentonite in tubular ceramic membranes. *Desalination*. 2008;228(1-3): 175–182. https://doi.org/10.1016/j.desal.2007.10.006

14. Ju S., Weber M. E. Mujumdar A. S. Electroosmotic dewatering of bentonite suspensions. *Separations Technology*. 1991;1(4): 214–221. https://doi.org/10.1016/0956-9618(91)80016-s

15. Mahmoud A., Fernandez A., Chituchi T. M., Arlabosse P. Thermally assisted mechanical dewatering (TAMD) of suspensions of fine particles: Analysis of the influence of the operating conditions using the response surface methodology. *Chemosphere*. 2008;72(11): 1765–1773. https://doi.org/10.1016/j.chemosphere.2008.04.075

16. Shaikh S. M. R., Nasser M. S., Magzoub M., Benamor A., Hussein I. A., El-Naas M. H. Qiblawey H. Effect of electrolytes on electrokinetics and flocculation behavior of bentonite-polyacrylamide dispersions. *Applied Clay Science*. 2018;158: 46–54. https://doi.org/10.1016/j.clay.2018.03.017

17. Shaikh S. M. R., Nasser M. S., Hussein I., Benamor A., Onaizi S. A., Qiblawey H. Influence of polyelectrolytes and other polymer complexes on the flocculation and rheological behaviors of clay minerals: A comprehensive review. *Separation and Purification Technology*. 2017;187: 137–161. https://doi.org/10.1016/j.seppur.2017.06.050

18. Lee C. S., Robinson J., Chong M. F. A review on application of flocculants in wastewater treatment. *Process Safety and Environmental Protection,* 2014;92(6): 489–508. https://doi.org/10.1016/j.psep.2014.04.010

19. Lin J. L., Huang C., Chin C. J. M., Pan J. R. Coagulation dynamics of fractal flocs induced by enmeshment and electrostatic patch mechanisms. *Water Research*. 2008;42(17): 4457–4466. https://doi.org/10.1016/j.watres.2008.07.043

20. Barbot E., Dussouillez P., Bottero J. Y., Moulin P. Coagulation of bentonite suspension by polyelectrolytes or ferric chloride: Floc breakage and reformation. *Chemical Engineering Journal*. 2010;156(1): 83–91. https://doi.org/10.1016/j.cej.2009.10.001

21. Daifa M., Shmoeli E., Domb A. J. Enhanced flocculation activity of polyacrylamide-based flocculant for purification of industrial wastewater. *Polymers for Advanced Technologies*. 2019;30: 2636–2646. https://doi.org/10.1002/pat.4730

22. Ma J., Shi J., Ding L., ... Fu K. Removal of emulsified oil from water using hydrophobic modified cationic polyacrylamide flocculants synthesized from low-pressure UV initiation. *Separation and Purification Technology*. 2018;197: 407–417. https://doi.org/10.1016/j.seppur.2018.01.036

23. Liu T., Ding E., Xue F. Polyacrylamide and poly(N.N-dimethylacrylamide) grafted cellulose nanocrystals as efficient flocculants for kaolin suspension. *International Journal of Biological Macromolecules*. 2017;103: 1107–1112. https://doi.org/10.1016/j.ijbiomac.2017.05.098

24. Nasser M. S., James A. E. The effect of polyacrylamide charge density and molecular weight on the flocculation and sedimentation behaviour of kaolinite suspensions. *Separation and Purification Technology*. 2006;52: 241–252. https://doi.org/10.1016/j.seppur.2006.04.005

25. Smith E. L., Abbott A. P., Ryder K. S. Deep eutectic solvents (DESs) and their 186 applications. *Chemical Reviews*. 2014;114(21): 11060–11082. https://doi.org/10.1021/cr300162p

26. Zhang Q., De Oliveira Vigier K., Royer S., Jérôme F. Deep eutectic solvents: Syntheses. properties and applications. *Chemical Society Reviews*. 2012;41(21): 7108–7146. https://doi.org/10.1039/c2cs35178a

27. Shomurodov A., Makhsumov A., Ismailov B., Obidov S. B. N-diethanoloiloamino-(butin-2-il)-sorbinate and its physico-chemical properties. *Universum: Chemistry & Biology*. 2021;6(84): 20–24. (In Russ., abstract in Eng.). https://doi.org/10.32743/UniChem.2021.84.6.11856

28. Davletbaeva I. M., Dulmaev S. E., Sazonov O. O., Gumerov A. M., Ibragimov R. G., Davletbaev R. S., Valiullin L. R. Polyurethanes based on modified amino ethers of boric acid. *Polymer Science, Series B*. 2020;62(4): 375–384. https://doi.org/10.1134/S156009042004003X

29. Nizamov A. A., Myasnikov G. V., Davletbaev R. S.,... Davletbaeva, I. M. Polyurethane gel electrolytes based on phthalic anhydride-modified amino ethers of ortho-phosphoric acid. *Herald of Technological University*. 2022;25(8): 121–125. (In Russ., abstract in Eng.). https://doi.org/10.55421/1998-7072_2022_25_8_121

30. Sazonov O. O., Zakirov I. N., Davletbaev R. S., Korobkina A. A., Sidorova M. I., Davletbaeva I. M. Thermal sensitive vapor permeable polyurethanes based on amino esters of ortho-phosphoric acid. *Herald of Technological University*. 2021;22(1): 37–40. (In Russ., abstract in Eng.). Available at: https://elibrary.ru/item.asp?id=44548999

31. Davletbaev R. S., Emelina O. Yu., Davletbaeva I. M., Gumerov A. M. Complexes of amino esters of

boric acid as modifiers of polydimethylsiloxanes. *Vestnik Kazanskogo tekhnologicheskogo universiteta.* 2012;10: 120–122. (In Russ., abstract in Eng.). Available at:https://elibrary.ru/item.asp?id=17788724

32. Tokunov V. I., Kheifets I. B. Hydrophobic-emulsion drilling fluids*. Moscow: Nedra Publ. 1983. 167 p.

33. *Drilling completion and workover fluids: Oil and gas technologies.* 2008;11 (Appendix). 63 p. 34.

34. Case R. O., Tawney K. J., Jefwerth J. L. *Quaternized MDEA complex esters with a high content of complex monoester mixed with quaternized complex ethers*. Patent RF, no. 2006100036/04. Publ. 06.27.2006, bull. no. 18. (In Russ.) Available at: https://patents.google.com/patent/RU2006100036A/en

35. Kuznetsova N. A., Chaltseva T. V., Norkina R. N., ... Koroleva N. A. *Negative photoresist for "explosive" photolithography.* Patent RF, no. 2017103195. Publ. 22.03.2018, bull. no. 9. Available at: https://patents.google.com/patent/RU2648048C1/en

36. Lemaire P. C., Oldham C. J., Parsons G. N. Rapid visible color change and physical swelling during water exposure in triethanolamine-metalcone films formed by molecular layer deposition. *Journal of Vacuum Science & Technology A: Vacuum. Surfaces. and Films*. 2016;34(1): 01A134. https://doi.org/10.1116/1.4937222

37. Dutta S., Karak N. Synthesis. Characterization of poly(urethane amide) resins from nahar seed oil for surface coating applications. *Progress in Organic Coatings*. 2005;53(2): 147–152. https://doi.org/10.1016/j.porgcoat.2005.02.003

38. Ashraf S. M., Ahmad S., Riaz U. Development of novel conducting composites of linseed-oil-based poly(urethane amide) with nanostructured poly(1-naphthylamine). *Polymer International.* 2007;56(9): 1173–1181. http://dx.doi.org/10.1002/pi.2265

38. Yadav S., Zafar F., Hasnat A., Ahmad S. Poly (urethane fatty amide) resin from linseed oil – a renewable resource. *Progress in Organic Coatings.* 2009;64(1): 27–32. https://doi.org/10.1016/j.porgcoat.2008.07.006

39. Lee C. S., Ooi. T. L., Chuah C. H., Ahmad S. Rigid polyurethane foam production from palm oil-based epoxidized diethanolamides. *Journal of the American Oil Chemists' Society*. 2007;84: 1161–1167. https://doi.org/10.1007/s11746-007-1150-5

40. Palanisamy A., Rao. B. S., Mehazabeen S. Diethanolamides of castor oil as polyols for the development of water-blown polyurethane foam. *Journal of Polymers and the Environment*. 2011;19: 698–705. https://doi.org/10.1007/s10924-011-0316-2

41. Shkop A., Tseitlin M., Shestopalov O. Exploring the ways to intensify the dewatering process of polydisperse suspensions. *Eastern-European Journal of Enterprise Technologies.* 2016;6(10 (84)): 35–40. https://doi.org/10.15587/1729-4061.2016.86085

42. Averkina E., Shakirova E., Butakova L. Influence of flocculant reagents on the parameters of clay suspensions. *Earth Sciences and Subsoil Use*. 2020;43(2); 230–241. https://doi.org/10.21285/2686-9993-2020-43-2-230-241

Information about the authors

Dmitriy Yu. Vandyshev, Cand. Sci. (Chem.), Associate Professor of the Department of Organic Chemistry, Voronezh State University (Voronezh, Russian Federation).
https://orcid.org/0000-0001-8606-458X
francy_2007@mail.ru

Olga V. Sleptsova, Cand. Sci. (Chem.), Associate Professor of the Department of High Molecular Compounds and Colloidal Chemistry, Voronezh State University (Voronezh, Russian Federation).
https://orcid.org/0009-0006-7467-275X
slepts@gmail.com

Vladislav Yu. Gazin, Master's student of the 2nd year of the Department of Organic Chemistry, Voronezh State University (Voronezh, Russian Federation).
https://orcid.org/0009-0009-4000-6638
gazin2000@gmail.com

Stanislav A. Malyutin, Cand. Sci. (Tech.), General Director of JSC Petrochem (Belgorod, Russian Federation).
https://orcid.org/0009-0006-0572-8545
malyutin@petrohim.ru

Naum R. Malkin, Chief Technologist of JSC Petrochem (Belgorod, Russian Federation).
https://orcid.org/0009-0006-9744-3044
n.malkin@petrohim.ru

Khidmet S. Shikhaliev, Dr. Sci. (Chem.), Professor, Head of the Department of Organic Chemistry, Voronezh State University (Voronezh, Russian Federation).
https://orcid.org/0000-0002-6576-0305
shikh1961@yandex.ru

Received 27.01.2023; approved after reviewing 07.03.2023; accepted for publication 15.04.2023; published online 25.09.2023.

Translated by Dmitriy Vandyshev

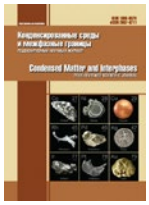

ISSN 1606-867X (Print)
ISSN 2687-0711 (Online)
Condensed Matter and Interphases
Kondensirovannye Sredy i Mezhfaznye Granitsy
https://journals.vsu.ru/kcmf/

Original articles

Research article
https://doi.org/10.17308/kcmf.2023.25/11393

Inhibitors of chloride corrosion of reinforcement steel in concrete based on derivatives of salts of carboxylic acids and dimethylaminopropylamine

O. A. Kozaderov✉, D. S. Shevtsov, M. A. Potapov, I. D. Zartsyn, S. N. Grushevskaya, A. A. Kruzhilin, E. A. Ilina, K. A. Tkachenko, Kh. S. Shikhaliev

Voronezh State University,
1 Universitetskaya pl., Voronezh 394018, Russian Federation

Abstract

In our study, we synthesised derivatives of salts of carboxylic acids and dimethylaminopropylamine: 3-(dimethylamino) propyl-1-ammonium acetate, 3-(dimethylamino)propyl-1-ammonium hexanoate, 3-(dimethylamino)propyl-1-ammonium octanoate, and 3-(dimethylamino)propyl-1-ammonium terephthalate. The structures of the molecules of the obtained substances were confirmed using physical methods: Fourier-transform infrared spectroscopy, NMR spectroscopy, and HPLC.

Electrochemical methods (voltammetry and electrochemical impedance spectroscopy) and quantum chemical modeling were used to assess the inhibitory effect of the synthesised substances with regard to 35GS reinforcement steel. Experiments were conducted in a water extract from a mortar simulating concrete pore solution in the presence of chlorides inducing pitting corrosion. 3-(dimethylamino)propyl-1-ammonium terephthalate is expected to have the highest degree of protection (up to 71%) at a concentration of 2.0 g·dm^{-3}. The highest degree of protection for the derivatives with alkyl radicals is 41–46% in a range of concentrations from 0.5 to 2.0 g·dm^{-3}. The results of potentiodynamic measurements and quantum chemical modeling were close. Average level of degree of protection can be explained by a high concentration of chlorides in the model solution (1.00 mol·dm^{-3}). The effectiveness of the obtained substances is to be further studied using fine-grained concrete. This will help to assess the impact of the additives on the capillary pore structure (permeability) of concrete and the concentration of chlorides.

Keywords: Reinforcement steel, Reinforced concrete, Corrosion inhibitors, Chlorides, Dimethylaminopropylamine derivatives

Funding: The study was supported by the Russian Science Foundation (RSF), project No. 22-23-01144, https://rscf.ru/en/project/22-23-01144/

For citation: Kozaderov O. A., Shevtsov D. S., Potapov M. A., Zartsyn I. D., Grushevskaya S. N., Kruzhilin A. A., Ilina E. A., Tkachenko K. A., Shikhaliev Kh. S. Inhibitors of chloride corrosion of reinforcement steel in concrete based on derivatives of salts of carboxylic acids and dimethylaminopropylamine. *Condensed Matter and Interphases*. 2023;25(3): 435–444 . https://doi.org/10.17308/kcmf.2023.25/11393

Для цитирования: Козадеров О. А., Шевцов Д. С., Потапов М. А., Зарцын И. Д., Грушевская С. Н., Кружилин А. А., Ильина Е. А., Ткаченко К. А., Шихалиев Х. С. Ингибиторы хлоридной коррозии арматурной стали в бетоне на основе производных солей карбоновых кислот и диметиламинопропиламина. *Конденсированные среды и межфазные границы*. 2023;25(3): 435–444. https://doi.org/10.17308/kcmf.2023.25/11393

✉ Oleg A. Kozaderov, e-mail: ok@chem.vsu.ru

1. Introduction

The design life of reinforced concrete structures should be at least 50–100 years depending on the area of application and design features [1]. This parameter can decrease significantly during operation, especially in highly corrosive environments. As a result, the first signs of distress appear during the early stages of operation [2]. Preventive maintenance and capital repairs using specialized fine-grained concrete are common practice [3]. However, this approach is often hard to implement. For instance, due to the continuity of the production process it is impossible to stop the operation of a certain structure without shutting down the whole production line. Considering the fact that large enterprises endure enormous financial losses because of long downtime, which exceed the cost of repair several times [4], it is important to make reinforced concrete structures as durable as possible.

The main cause of degradation of reinforced concrete structures is corrosion of reinforcement bars, with the contribution of processes induced by chlorides being over 65% [5]. Therefore, the structures most susceptible to chloride corrosion are those located on the coast, as well as transport infrastructure facilities and motorways coated with antifreeze reagents, chemical industry facilities producing mineral fertilizers, etc. Primary and secondary protection of reinforced concrete is used to prevent corrosion [6]. At the same time coatings, surface treatment, and other secondary protection methods require additional time and expenses [7]. Although secondary protection is the only way to ensure the required durability in certain environments (e.g. aggressive acids) [8], primary protection measures, i.e. finding the optimal composition of concrete, are generally the easiest to implement.

To increase the corrosion resistance of steel reinforcement bars in concrete, various additives reducing the permeability of concrete [9, 10] or corrosion inhibitors [11, 12] are used, which can reduce the rate of corrosion of steel and affect the physical and mechanical properties of concrete at the same time. To reduce the time of analysis of their effect, model liquid solutions are used: a saturated solution of $Ca(OH)_2$ [13–16], its modifications whose compositions are close to the actual composition of the concrete pore solution, and extracts obtained from cement and ground concrete [17, 18]. The concentration of chlorides (C_{Cl}) introduced to induce corrosion varies from 0.1 to 0.9 mol·dm^{-3} (5% wt.). This parameter affects the degree of protection: the higher the concentration of chlorides, the lower the protection degree.

We should note that experiments with model aqueous electrolyte solutions demonstrate only the true inhibitory effect of the studied substance on steel reinforcement. When used in actual concretes, the protective effect can be significantly greater due to the compaction of concrete (the plastification effect) or lower (due to increased permeability, air entrainment, etc.).

Therefore, it is important to determine the most effective inhibitors of corrosion of steel reinforcement in concrete affected by chlorides. At the moment, a large number of inorganic (nitrites, chromates, phosphates, etc. [16–18]), organic (amines and carboxylic acids [13, 19, 20], triazoles [21], salts of benzoic acid [22], hydroquinoline and pyrocatechol [23], siloxanes [24], etc.), natural compounds [25, 26], and compositions based on them [27–29] are being studied. Due to the great protective effect of carboxylic acids, including long-chain carboxylic acids, against corrosion of steel reinforcement bars in concrete, it is of great scientific and practical importance to study the inhibitory properties of their derivatives.

The purpose of our study was to synthesize and assess the inhibitory properties of new derivatives of salts of carboxylic acids and dimethylaminopropylamine with regard to low-carbon reinforcement steel in an aqueous solution simulating a concrete environment in the presence of chlorides.

2. Experimental

2.1. Synthesis and analysis of dimethylaminopropylamine derivatives

In our study, we obtained a series of ammonium salts of dimethylaminopropylamine with certain carboxylic acids (Table 1) with different lengths of the hydrocarbon radicals as potential inhibitors of chloride corrosion of steel reinforcement bars in reinforced concrete. All reagents used were purchased from Acros Organics.

The inhibitors were synthesised as follows: a mixture of 1 mol of acid, 1 mol of amine (2 mol for ***d***), and 50 ml of ethanol was boiled until

all the components dispersed completely. The completeness of the reaction was controlled using a universal indicator and thin-layer chromatography. After the neutralization, the obtained homogeneous solution was evaporated on a rotary evaporator until the solvent evaporated. The scheme of the process is presented below.

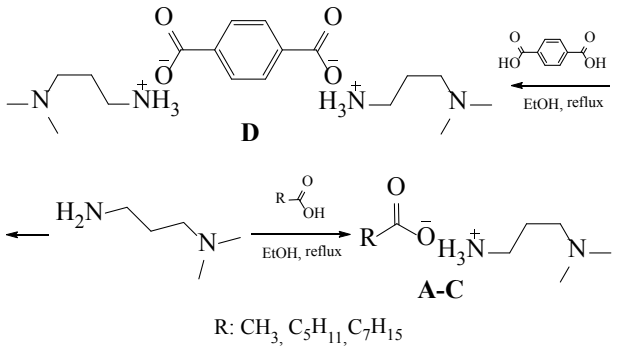

The obtained ammonium salts were analysed using high-performance liquid chromatography with high-resolution mass spectrometry (electrospray ionization, HPLC-HRMS-ESI) in combination with UV detection. The analyser unit included an Agilent 1269 Infinity chromatograph and an Agilent 6230 TOF LC/MS detector. Quantitative analysis was performed using an external standard method. 1H NMR spectra were recorded using a Bruker AV600 (600, 13 MHz) spectrometer in a DMSO-d6. TMS was used as the internal standard. The IR spectrum was recorded on Vertex 70 FT-IR spectrometer using a Platinum ATR (Bruker) ATR attachment equipped with a diamond prism in the frequency range from 4000 to 400 cm^{-1} with a resolution of 2 cm^{-1}. The result was obtained by averaging 16 scans.

The study demonstrated that in the absence of a catalyst, when equimolar amounts of dimethylaminopropylamine and carboxylic acids are boiled in ethanol, a neutralization reaction takes place with almost quantitative yields of the corresponding ammonium salts. This is confirmed by LC/MS spectrometry, 1H NMR spectrometry, and IR spectrometry.

3-(dimethylamino)propyl-1-ammonium acetate (***a***). 95% yield, amber viscous liquid. 1H NMR (δ): 1.84–1.91 (m, 2H $1CH_2$), 2.22 (s, 3H CH_3), 2.37–2.41 (s, 6H $2CH_3$), 2.60–2.67 (m, 2H $1CH_3$), 2.90–2.97 (*m*, 2H $1CH_2$). IR spectrum (cm^{-1}): 3300–3400 (OH + N^+-H), 2150–2200 (N^+-H), 1700–1750 (C=O), 1550–1600 (COO^- + C-O-H), 1550 (N^+H), 1400 (N^+H), 900–1150 (CH_2), 750–800 (CH_2). Determined, *m/z*: 163.1162 $[M+H]^+$. Calculated, *m/z* 163.1368 $[M+H]^+$.

3-(dimethylamino)propyl-1-ammonium hexanoate (***b***). 96% yield, amber viscous liquid. 1H NMR (δ): 0.89–0.90 (*t*, 3H CH_3), 1.20–1.23 (*m*, 6H $3CH_2$), 1.85–1.90 (m, 2H $1CH_2$), 2.35–2.43 (s, 8H $2CH_3$+βCH_2), 2.61–2.65 (m, 2H $1CH_2$), 2.91–2.92 (*m*, 2H $1CH_2$). IR spectrum (cm^{-1}): 3300–3400 (OH + N^+-H), 2150–2200 (N^+-H), 1700–1750 (C=O), 1550–1600 (COO^- + C-O-H), 1550 (N^+H), 1400 (N^+H), 900–1150 (CH_2), 750–800 (CH_2). Determined, *m/z*: 218.1862 $[M+H]^+$. Calculated, m/z: 218.1994 $[M+H]^+$.

Table 1. Studied inhibitors

Symbol	Name	Formula
a	3-(dimethylamino)propyl-1-ammonium acetate	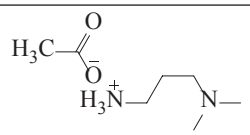
b	3-(dimethylamino)propyl-1-ammonium hexanoate	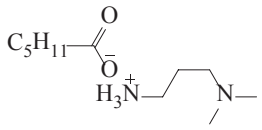
c	3-(dimethylamino)propyl-1-ammonium octanoate	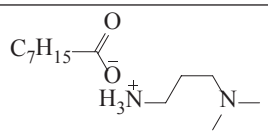
d	3-(dimethylamino)propyl-1-ammonium terephthalate	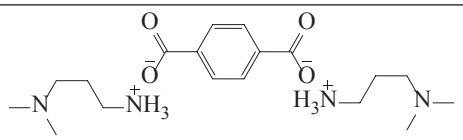

3-(dimethylamino)propyl-1-ammonium octanoate **(*c*)**. 94% yield, amber viscous liquid. 1H NMR (δ): 0.87–0.91 (*t*, 3H CH_3), 1.19–1.86 (*m*, 14H $5CH_2$+βCH_2+CH_2), 2.25–2.33 (s, 6H $2CH_3$), 2.60–2.63 (m, 2H CH_2), 2.92–2.94 (*m*, 2H CH_2). IR spectrum (cm^{-1}): 3300–3400 (OH + N^+-H), 2150–2200 (N^+-H), 1700–1750 (C=O), 1550–1600 (COO^- + C-O-H), 1550 (N^+H), 1400 (N^+H), 900–1150 (CH_2), 750–800 (CH_2), Determined, *m/z*: 246.3154 $[M+H]^+$. Calculated, m/z: 246.2307 $[M+H]^+$.

3-(dimethylamino)propyl-1-ammonium terephthalate **(*d*)**. 85% yield, white crystalline substance, mp = 273–275 °C. 1H NMR (δ): 1.84–1.91 (m, 4H $2CH_2$), 2.41–2.45 (m, 12H $6CH_3$), 2.64–2.71 (m, 4H $2CH_3$), 2.90–2.97 (*m*, 4H $2CH_2$), 7.92 (d, 4H, aromatic). IR spectrum (cm^{-1}): 3300–3400 (OH + N^+-H), 2150–2200 (N^+-H), 1550–1600 (COO^- + C-O-H), 1550 (N^+H), 1400 (N^+H), 900–1150 (CH_2), 750–800 (CH_2), 500–600 (C-H aromatic). Determined, *m/z*: 370.1290 $[M+H]^+$. Calculated, m/z: 370.2580 $[M+H]^+$.

2.2. Assessment of the corrosion inhibition properties

To evaluate the corrosion inhibition properties of the synthesised compounds, a set of electrochemical methods was used. Quantum-chemical calculations were also performed.

Samples of low-carbon 35GS steel with rectangular section were used as the working electrode. All the surfaces, except for the working surface, were mounted in epoxy resin. Saturated silver chloride reference electrode (SCE, +201 mV relative to the standard hydrogen electrode) was placed in a separate container linked to the electrolytic cell by an agar-agar based salt bridge filled with a KNO_3 saturated solution. The potentials in the study are presented relative to the standard hydrogen electrode. A platinum grid was used as an auxiliary electrode.

The working solution was a water extract from cement powder (mass ratio of distilled water and cement powder 1:10, extraction for 24 hours followed by filtration, pH 12.5–13.0). Electrochemical measurements were conducted in a glass three-electrode cell with undivided electrode spaces at a temperature of 23±3 °C under natural aeration conditions, in the presence of the inhibitor NaCl with the concentration of 1.00 mol·dm^{-3} (reference experiment) and the studied substances.

The working electrode was preliminarily cleaned with K2000 sandpaper, washed with distilled water, and degreased with chemically pure isopropyl alcohol. The current density *i* was calculated by dividing the actual current *I* by the geometric area of the working electrode (2.25 cm^2).

The corrosion current density (i_{cor}) was determined by the polarization resistance (PR) technique as summarized by Mansfeld [30]. After the free corrosion potential (E_{cor}) became stable, the polarization curve was registered for 30 minutes using an IPC-Pro potentiostat in the potentiodynamic polarization mode (potential scan rate of 0.2 mV·s^{-1}) in the range from E_{cor} −30 mV to E_{cor}+30 mV.

The ability of the studied substances to inhibit corrosion was assessed based on the degree of protection calculated using the formula:

$$Z_i = \frac{i_{cor,\,0} - i_{cor,\,inh}}{i_{cor,\,0}} \cdot 100\,\%,$$

where $i_{cor,0}$ and $i_{cor,inh}$ are the corrosion current density during the reference experiment and in the presence of the inhibitor respectively.

The electrochemical impedance spectroscopy (EIS) was performed using the IPC-Pro potentiostat with a frequency response analyser FRA-2. After E_{corr} was stable for 30 minutes, the frequency dependent impedance was registered within the range from 0.01 to 50 Hz with no current. The analysis of frequency dependences, the selection of the equivalent circuit, and determining its component values was carried out using DCS software. The results are presented as a Nyquist diagram. The inhibition efficiency (η_{inh}) was calculated using the formula:

$$\eta_{inh} = \left(1 - \frac{R_{p,0}}{R_{p,inh}}\right) \cdot 100,$$

where $R_{p,0}$ and $R_{p,inh}$ are polarization resistance in the reference experiment and in the presence of the inhibitor respectively.

The optimisation of the geometry of the studied inhibitor molecules was carried out within the framework of the density functional theory (DFT) using the B3LYP functional

with basis 6-311+ G(d,p) in the Gaussian 09 package. The optimized geometry of molecules is characterized by a lack of negative oscillation frequencies and therefore corresponds to the minimum value on the potential energy surface. In addition, TDDFT (time-dependent density functional theory) calculations for optimized geometry were performed to find the five lowest electronic excitations. Energies of HOMO and LUMO molecular orbitals were used to forecast the inhibition effectiveness. Within the limitation of the Koopmans' theorem, the energies of frontier orbitals are determined by the formulas:

$-E_{HOMO} = IP$ and $-E_{LUMO} = EA$.

Here *IP* is ionisation potential, and *EA* is electron affinity. The inhibition effectiveness was assessed based on the chemical hardness:

$$\eta = \frac{IP - EA}{2}$$

and softness:

$$\sigma = \frac{1}{\eta}.$$

3. Results and discussion

3.1.Potentiodynamic measurements

Substance ***a*** does not have any significant effect on the free corrosion potential of low-carbon steel in the presence of chlorides in the whole range of concentrations studied (taking into account the accuracy of measurements) (Table 2).

When substances ***b-d*** were introduced, E_{cor} shifted towards positive values by 35–80 mV, which indicates the effect primarily on the partial anodic oxidation of metal [31]. This is also confirmed by the comparison of the initial sections of the polarization curves. Thus, for ***a, b*** cathodic sections of the polarization curves for all concentrations of the inhibitor C_{inh} practically coincide with the reference. Anodic sections, when $C_{inh} \geqslant 1.0$ g·dm^{-3}, demonstrated monotonous reduction of the current density at a given value of the electrode potential (Fig. 1*a*). For ***b,*** monotonous reduction in *i* on the anodic sections of the polarization curve was registered at $C_{inh} \geqslant 0.5$ g·dm^{-3} (Fig. 1*b*).

The introduction of ***c*** reduced the current density on both cathodic and anodic section of the polarization curve as compared to the reference experiment (Fig. 1*c*). When the concentration of chlorides was C_{inh} = 0.5 and 1.0 g·dm^{-3} cathodic sections were not registered, while the current density on the anodic sections was lower at C_{inh} = 0.5 g·dm^{-3}. The lowest values of *i* were obtained when C_{inh} = 2.0 g·dm^{-3}.

For ***d*** at higher C_{inh} the anodic current density decreased monotonously, while the cathodic section of the polarization curve decreased only when C_{inh} = 1.0 g·dm^{-3}.

The calculations of the electrochemical parameters by means of polarization resistance technique are given in Table 2. They are compatible with the results of the analysis of the polarization curves. The protection degree generally increases at higher concentrations of the substance (except for ***c***). For ***a-c*** Z_i reaches 41–

Table 2. Kinetic parameters of mild steel electrode in water extract from cement + 1.00 mol·dm^{-3} NaCl in the presence of derivatives of dimethylaminopropylamine

Inhibitor	C_{inh}, g·dm^{-3}	E_{cor}, mV	R_p, kΩ·cm^2	b_a, mV	b_c, mV	*B*, mV	i_{cor}, μA·cm^{-2}	Z_i, %
blank	–	–451	9.21	64.3	63.0	31.8	3.44±0.36	–
a	0.5	–439	8.49	59.9	59.9	30.0	3.52±0.28	–2
	1.0	–453	10.56	53.4	40.4	23.0	2.20±0.30	36
	2.0	–458	10.97	50.4	35.2	20.7	1.92±0.25	44
b	0.5	–414	9.60	65.6	38.2	24.2	2.54±0.28	26
	1.0	–410	11.80	64.7	33.9	22.3	1.87±0.13	46
c	0.5	–374	13.27	65.6	46.5	27.2	2.05±0.19	41
	1.0	–370	12.03	78.2	55.1	32.4	2.71±0.22	21
	2.0	–401	14.08	86.4	49.5	31.5	2.22±0.10	36
d	0.5	–398	12.13	51.2	35.2	20.9	1.73±0.21	50
	1.0	–405	17.44	46.0	27.4	17.2	0.99±0.09	71

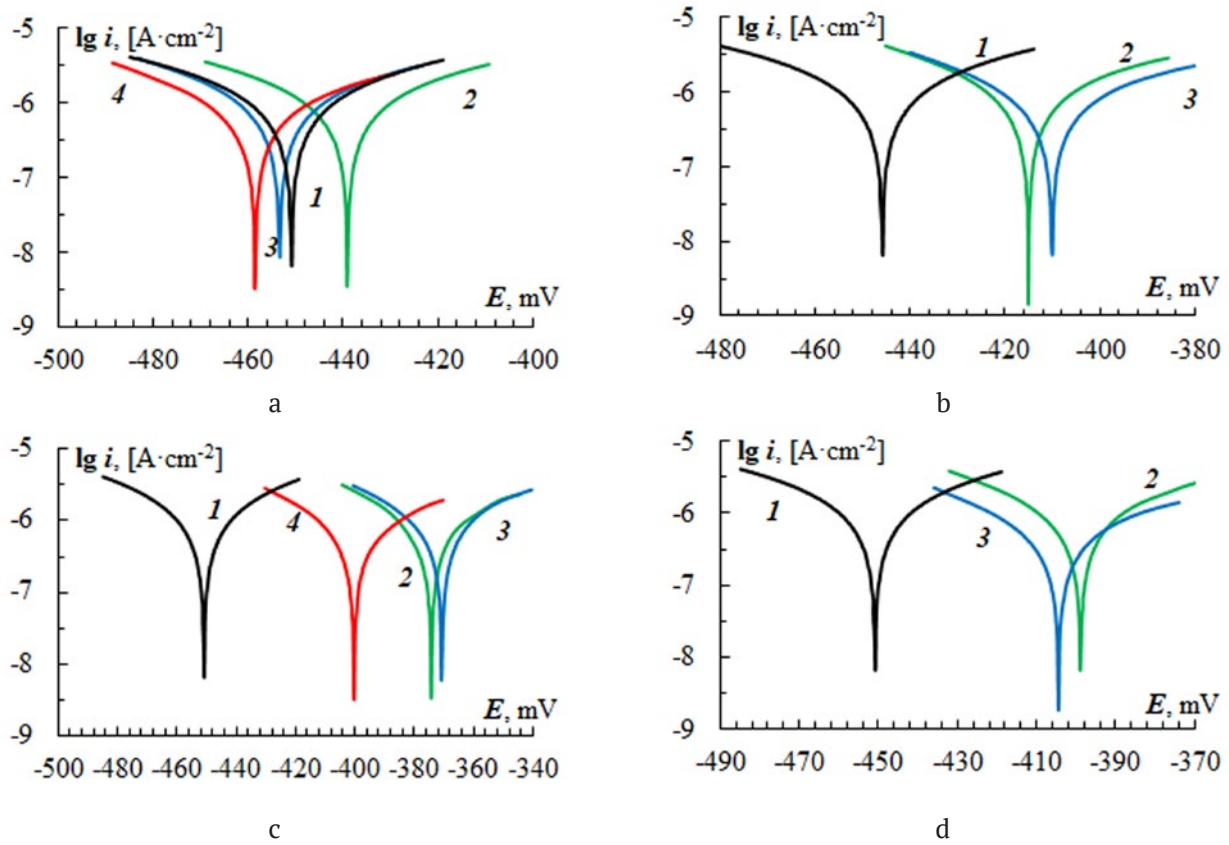

Fig. 1. Anodic and cathodic polarization curves of mild steel in water extract from cement + 1.00 mol·dm^{-3} NaCl without an inhibitor (*1*) and in presence of 3-(dimethylamino)propyl-1-ammonium acetate (***a***), 3-(dimethylamino)propyl-1-ammonium hexanoate (***b***), 3-(dimethylamino)propyl-1-ammonium octanoate (***c***) and 3-(dimethylamino)propyl-1-ammonium terephthalate (***d***) a at concentrations of 0.5 (*2*), 1.0 (*3*) and 2.0 g·dm^{-3} (*4*)

46%. Substance ***d*** is the most effective inhibitor based on the corrosion current density estimated by the method of linear polarization resistance (71% at C_{inh} = 2.0 g·dm^{-3}).

3.2. Electrochemical impedance spectroscopy

Nyquist diagrams obtained in reference experiments and in the presence of the studied substances have the same shape of a distorted semicircle with changing diameter and a linear section in the low-frequency region (Fig. 2).

An equivalent circuit presented in Fig.3 provides a satisfactory description of the diagrams. The results of the calculations are shown in Table 3.

For substances ***a***-***b*** when the length of the alkyl radical increased form C1 to C5 the degree of protection grew from 9.4 to 19.9% at C_{inh} = 1.0 g·dm^{-3}. When the length of the alkyl radical was further increased to C7 with C_{inh} ranging from 0.5 to 1.0 g·dm^{-3}, the inhibitory effect was not registered. However, when C_{inh} = 2.0 g·dm^{-3} the degree of protection was over 35%. For substance ***d*** the concentration did not affect the degree of protection. Z_i approaches 20%.

3.3. Quantum-chemical calculations

Minimum difference between HOMO and LUMO energies and absolute hardness was observed for compound ***d*** (Table 4). Compounds ***a-c*** are characterised by higher values of these parameters. Obviously, for ***d,*** softness is maximum. Therefore, it can be expected to have high adsorption ability and inhibitory properties. ***a-c*** are most likely to have a mild inhibitory effect.

Fig. 4 demonstrates a comparison of the dependencies of inhibitory activity criteria for the studied substances at maximum concentrations. The degree of protection assessed using the polarization resistance method and softness assessed using quantum chemical calculations change symbatically. The inhibition effectiveness assessed using EIS is generally lower than that

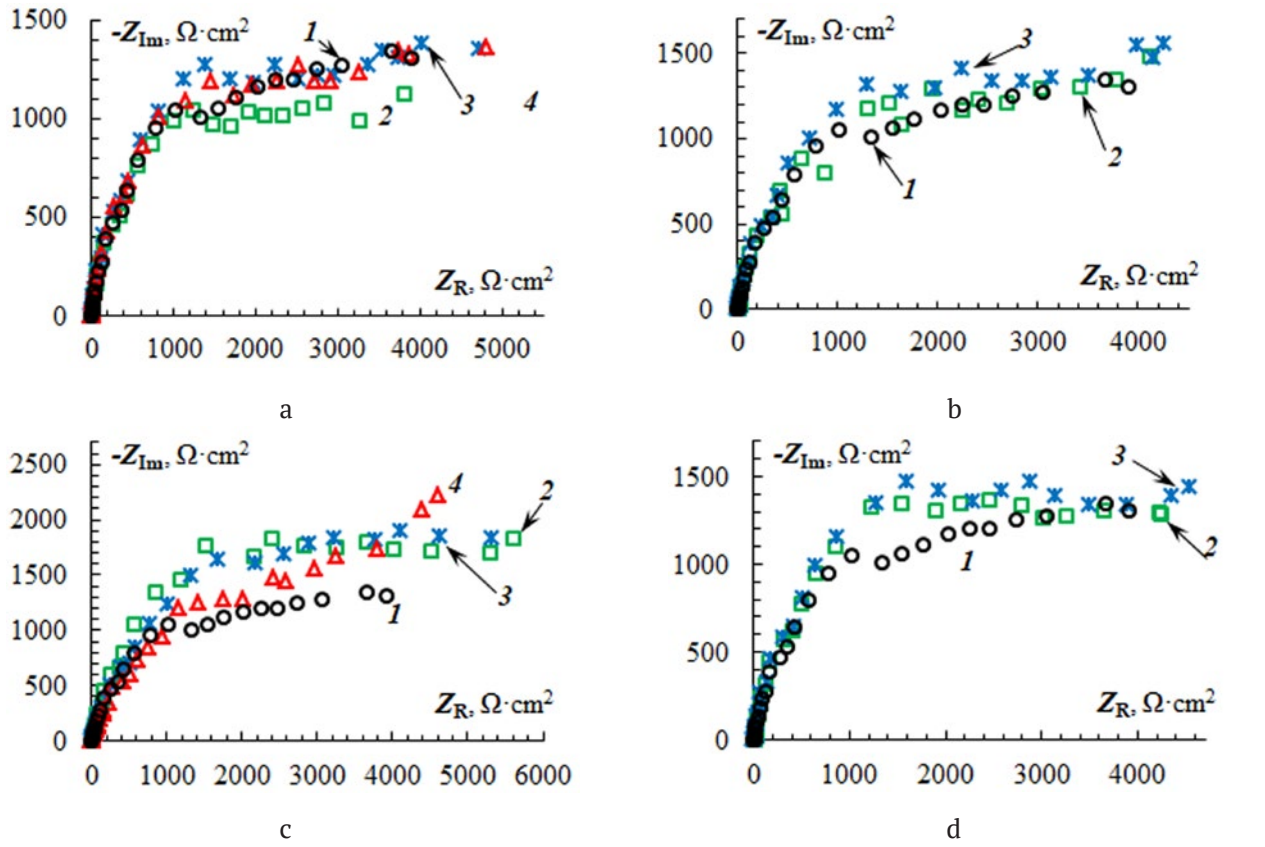

Fig. 2. Nyquist diagrams of mild steel in water extract from cement + 1.00 mol·dm^{-3} NaCl without an inhibitor (*1*) and in presence of 3-(dimethylamino)propyl-1-ammonium acetate (***a***), 3-(dimethylamino)propyl-1-ammonium hexanoate (***b***), 3-(dimethylamino)propyl-1-ammonium octanoate (***c***) and 3-(dimethylamino)propyl-1-ammonium terephthalate (***d***) a at concentrations of 0.5 (*2*), 1.0 (*3*) and 2.0 g·dm^{-3} (*4*)

Table 3. Calculated equivalent circuit elements of mild steel electrode in water extract from cement + 1.00 mol·dm^{-3} NaCl in presence of derivatives of dimethylaminopropylamine

Inhibitor	C_{inh}, g·dm^{-3}	Equivalent circuit element					η_{inh}, %
		R_{Ω}, Ω·cm²	*R*p, Ω·cm²	CPE_{T}, μF·cm^{-2}	CPE_{Φ}	*BW*, Ω·cm²·s$^{-0.5}$	
blank	–	5.0±0.7	2.9±0.3	9.3±1.2	0.79±0.04	523±55	–
a	0.5	7.8±2.5	3.1±0.3	9.0±0.9	0.77±0.01	510±58	5.3
	1.0	5.4±0.5	3.22±0.11	8.2±0.3	0.80±0.02	601±77	9.4
	2.0	5.6±0.5	3.3±1.2	8.6±0.6	0.77±0.02	442±45	13.7
b	0.5	5.6±0.9	3.2±0.3	9.1±1.3	0.77±0.03	496±57	7.5
	1.0	5.8±0.8	3.6±0.3	9.0±0.7	0.79±0.02	514±47	19.9
c	0.5	6.7±0.6	2.5±0.2	13.6±1.9	0.74±0.01	498±52	–14.6
	1.0	14.7±2.2	2.63±0.6	9.8±0.5	0.76±0.02	789±66	–10.7
	2.0	8.7±1.2	4.5±0.7	10.9±1.1	0.65±0.05	752±74	35.6
d	0.5	6.6±1.5	3.6±0.3	8.3±0.5	0.79±0.03	493±34	19.8
	1.0	5.0±0.1	3.6±0.4	7.9±0.9	0.79±0.03	507±42	19.6

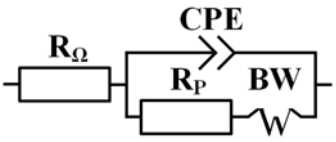

Fig. 3. Equivalent circuit for analysis of electrochemical impedance spectra

Table 4. Calculated energies of HOMO, LUMO, HOMO LUMO gap (HLG), Ionization Potential (IP), Electron Affinity (EA), Absolute Hardness (η) and Softness (σ) in eV at B3LYP/6-311+ G (d, p) level

Inhibitor	E_{HOMO}, eV	E_{LUMO}, eV	*HLG*, eV	*IP*, eV	*EA*, eV	η, eV	σ, eV^{-1}
a	−6.1264	−0,1137	6.0126	6.1264	0.1137	3.0063	0.3326
b	−6.1233	−0.4133	5.7100	6.1233	0.4133	2.8550	0.3502
c	−6.1209	−0.1037	6.0173	6.1209	0.1037	3.0086	0.3324
d	−6.1290	−1.8460	4.2830	6.1290	1.8460	2.1415	0.4669

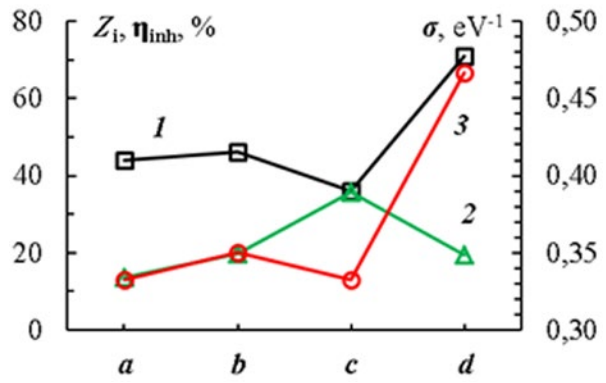

Fig. 4. Degree of protection Z_i (*1*), effectiveness of inhibition η_{inh} (*2*) at the maximum of the studied concentrations and softness σ (*3*) for 3-(dimethylamino) propyl-1-ammonium acetate (***a***), 3-(dimethylamino) propyl-1-ammonium hexanoate (***b***), 3-(dimethylamino)propyl-1-ammonium octanoate (***c***) and 3-(dimethylamino)propyl-1-ammonium terephthalate (***d***)

assessed using PR, but the overall tendency for ***a-c*** remains the same.

The studied substances, when used at maximum concentrations (1.0–2.0 g·dm^{-3}), can be generally characterised as inhibitors with a mild degree of protection. However, we should note that all the experiments were conducted in model liquid environments with a high concentration of chlorides C_{Cl} = 1.00 mol·dm^{-3}. We assume that the studied substances, when used during the production of concrete, can have additional effect on the rheological properties of solutions and physical and mechanical characteristics of set concrete. Lower permeability slows down the penetration of aggressive substances through the concrete shell of reinforcement bars, which can enhance the protective properties. The next stage of this study will include experiments with actual samples of fine-grained concrete.

4. Conclusions

In our study, we synthesised and confirmed the structure of derivatives of salts of carboxylic acids and dimethylaminopropylamine: 3-(dimethylamino)propyl-1-ammonium acetate, 3-(dimethylamino)propyl-1-ammonium hexanoate, 3-(dimethylamino)propyl-1-ammonium octanoate, and 3-(dimethylamino) propyl-1-ammonium terephthalate.

Electrochemical and quantum chemical methods were used to assess the ability of the synthesised compounds to inhibit corrosion of reinforcement steel in a solution simulating concrete pore solution in the presence of chlorides. The results of the polarization measurements, impedance spectroscopy, and quantum chemical calculations are in good agreement. 3-(dimethylamino)propyl-1-ammonium terephthalate is expected to have the highest degree of protection (up to 71%) at the concentration of 2.0 g·dm^{-3}. The highest degree of protection for the derivatives with alkyl radicals is 41–46% in the range of concentrations from 0.5 to 2.0 g·dm^{-3}.

Contribution of the authors

The authors contributed equally to this article.

Conflict of interests

The authors state that they have no known financial conflicts of interest or personal relationships that could affect the work presented in this article.

References

1. Karapetov E. S., Shestovitskiy D. A. Forecast of reinforced concrete bridges' service life on the basis of protective cover carbonization process model. *Proceedings of Petersburg Transport University*. 2016;1: 14–24. (in Russ., abstract in Eng.). Available at: https://www.elibrary.ru/item.asp?id=25776212

2. Samples L. M., Ramirez J. A. *Methods of corrosion protection and durability of concrete bridge decks reinforced with epoxy-coated bars – Phase I*. FHWA/IN/JTPR-98/15 Final Report – West Lafayette. Indiana: Purdue University; 1999. 258 p. https://doi.org/10.5703/1288284313268

3. Morgan D. R. Compatibility of concrete repair materials and systems. *Construction and Building Materials*. 1996;10(1): 57–67. https://doi.org/10.1016/0950-0618(95)00060-7

4. Kulinkovich E. D., Nasir M. O. Improving the efficiency of repair-technical service of production by using the concept of total productive maintenance. In: *Research and development in the field of mechanical engineering, energy and management: materials of the XVIII International Scientific and Technical conf. of students, postgraduates and young scientists*. Gomel: 2018. p. 406–409. (in Belarus).

5. Osterminski K. *Zur voll-probabilistischen Modellierung der Korrosion von Stahl in Beton: Ein Beitrag zur Dauerhaftigkeitsbemessung von Stahlbetonbauteilen*: Diss. ... Dr.-Ing., München, 2013. 211 p. Available at: https://mediatum.ub.tum.de/doc/1164926/1164926.pdf

6. Falikman V. R., Rozentahl N. K., Stepanova V. F. New Russian norms and codes on protection of building structures against corrosion. In: *High Tech Concrete: Where Technology and Engineering Meet: Proceedings of the 2017 fib Symposium, held in Maastricht*. Netherlands: 2017. pp. 2135–2143. https://doi.org/10.1007/978-3-319-59471-2_244

7. Drochytka R., Ledl M., Bydzovsky J., Zizkova N., Bester J. Use of secondary crystallization and fly ash in waterproofing materials to increase concrete resistance to aggressive gases and liquids. *Advances in Civil Engineering*. 2019; 1–12. https://doi.org/10.1155/2019/7530325

8. Møller V. B., Dam-Johansen K., Frankær S. M., Kiil S. Acid-resistant organic coatings for the chemical industry: a review. *Journal of Coatings Technology and Research*. 2017;14(2): 279-306. https://doi.org/10.1007/s11998-016-9905-2

9. Sharma R., Jang J. G., Bansal P. P. A comprehensive review on effects of mineral admixtures and fibers on engineering properties of ultra-high-performance concrete. *Journal of Building Engineering*. 2022;45: 103314. https://doi.org/10.1016/j.jobe.2021.103314

10. Ban C. C., Khalaf M. A., Ramli M., ... Ameri F. Modern heavyweight concrete shielding: Principles, industrial applications and future challenges; review. *Journal of Building Engineering*. 2021;39: 102290. https://doi.org/10.1016/j.jobe.2021.102290

11. Fedrizzi L., Azzolini F., Bonora P. L. The use of migrating corrosion inhibitors to repair motorways' concrete structures contaminated by chlorides. *Cement and Concrete Research*. 2005;35(3): 551–561. https://doi.org/10.1016/j.cemconres.2004.05.018

12. Shevtsov D. S., Zartsyn I. D., ... Kozaderov O. A. Evaluation of the efficiency of the Master Life CI 222 organic corrosion inhibitor additive for the protection of steel reinforcement bars in concrete. *International Journal of Corrosion and Scale Inhibition*. 2022;11(4): 1583–1592. https://dx.doi.org/10.17675/2305-6894-2022-11-4-10

13. Gonzalez J. A., Otero E., Feliu S., López W. Initial steps of corrosion in the steel/$Ca(OH)_2$ + Cl^- system: the role of heterogeneities on the steel surface and oxygen supply. *Cement and Concrete Research*. 1993;23(1): 33–40. https://doi.org/10.1016/0008-8846(93)90132-S

14. Xu Y., He L., Yang L., Wang X., Huang Y. Electrochemical study of steel corrosion in saturated calcium hydroxide solution with chloride ions and sulfate ions. *Corrosion*. 2018;74(10): 1063–1082. https://doi.org/10.5006/2634

15. Vedalakshmi R., Manoharan S. P., Song H. W. Application of harmonic analysis in measuring the corrosion rate of rebar in concrete. *Corrosion Science*. 2009;51(11): 2777–2789. http://dx.doi.org/10.1016/j.corsci.2009.07.014

16. Bertolini L., Bolzoni F., Gastaldi M. Effects of cathodic prevention on the chloride threshold for steel corrosion in concrete. *Electrochimica Acta*. 2009;54(5): 1452–1463. https://doi.org/10.1016/j.electacta.2008.09.033

17. Schießß P., Mayer T. F., Osterminski K. Influence of the chromate content in cement on the corrosion behaviour of steel in concrete. *Materials and Corrosion*. 2008;59(2): 115–121. https://doi.org/10.1002/maco.200804160

18. Yohai L., Vázquez M., Valcarce M. B. Phosphate ions as corrosion inhibitors for reinforcement steel in chloride-rich environments. *Electrochimica Acta*. 2013;102: 88–96. https://doi.org/10.1016/j.electacta.2013.03.180

19. Ormellese M., Lazzari L., Goidanich S., Fumagalli G., Brenna A. A study of organic substances as inhibitors for chloride-induced corrosion in concrete. *Corrosion Science*. 2009;51(12): 2959–2968. https://doi.org/10.1016/j.corsci.2009.08.018

20. Sagoe-Crentsil K. K., Yilmaz V. T., Glasser F. P. Corrosion inhibition of steel in concrete by carboxylic acids. *Cement and Concrete Research*. 1993;23(6): 1380–1388. https://doi.org/10.1016/0008-8846(93)90075-K

21. Genescaa J., Mendozab J., Duranb R. Conventional DC electrochemical techniques in corrosion testing. In: *XV International Corrosion Congress Manuscript submitted for publication, Metallurgical Engineering*. Mexico: 2002. 17 p.

22. Andreev N. N., Starovoitova E. V., Lebedeva N. A. Inhibition of steel corrosion by benzoic acid salts in calcium hydroxide solutions*. *Korrozia: materialy, zashchita*. 2007;5: 29–31. (in Russ.). Available at: https://www.elibrary.ru/item.asp?edn=hexspe

23. Gedvillo I. A., Zhmakina A. S., Andreev N. N., Vesely S. S. Effect of hydroquinone and pyrocatechin on the corrosion and electrochemical behavior of steel

in a model concrete pore liquid. *International Journal of Corrosion and Scale Inhibition.* 2019;8(3): 560–572. https://doi.org/10.17675/2305-6894-2019-8-3-7

24. Holmes N., O'Brien R., Basheer P. A. M. Engineering performance of a new siloxane-based corrosion inhibitor. *Materials and Structures*. 2014;47(9): 1531–1543. https://doi.org/10.1617/s11527-013-0133-2

25. Zomorodian A., Behnood A. Review of corrosion inhibitors in reinforced concrete: conventional and green materials. *Buildings*. 2023;13(5); 1170. https://doi.org/10.3390/buildings13051170

26. Raja P. B., Ghoreishiamiri S., Ismail M. Natural corrosion inhibitors for steel reinforcement in concrete – a review. *Surface Review and Letters*. 2015;22(3): 1550040. https://doi.org/10.1142/S0218625X15500407

27. Andreev N. N., Gedvillo I. A., Bulgakov D. S., Zhmakina A. S., Vesely S. S. On penetration of IFKhAN-80 migrating corrosion inhibitor into cement stone. *International Journal of Corrosion and Scale Inhibition*. 2014;3(4): 238–245. http://dx.doi.org/10.17675/2305-6894-2014-3-4-238-245

28. Gedvillo I. A., Zhmakina A. S., Andreev N. N., Vesely S. S. Protection of rusted reinforcing steel in concrete by IFKhAN-85 inhibitor. *International Journal of Corrosion and Scale Inhibition*. 2020;9(2): 562–570. https://doi.org/10.17675/2305-6894-2020-9-2-11

29. Bolzoni F., Brenna A., Ormellese M. Recent advances in the use of inhibitors to prevent chloride-induced corrosion in reinforced concrete. *Cement and Concrete Research*. 2022;154: 106719. https://doi.org/10.1016/j.cemconres.2022.106719

30. Mansfeld F. Tafel slopes and corrosion rates obtained in the pre-Tafel region of polarization curves. *Corrosion Science*. 2005;47(12): 3178–3186. https://doi.org/10.1016/j.corsci.2005.04.012

31. Nam N. D., Van Hien P., Hoai N. T., Thu V. T. H. A study on the mixed corrosion inhibitor with a dominant cathodic inhibitor for mild steel in aqueous chloride solution. *Journal of the Taiwan Institute of Chemical Engineers*. 2018;91: 556–569. https://doi.org/10.1016/j.jtice.2018.06.007

Information about the authors

Oleg A. Kozaderov, Dr. Sci. (Chem.), Docent, Head of the Department of Physical Chemistry, Voronezh State University (Voronezh, Russian Federation).
https://orcid.org/0000-0002-0249-9517
ok@chem.vsu.ru

Dmitry S. Shevtsov, Researcher of the Department of Physical Chemistry, Voronezh State University (Voronezh, Russian Federation).
https://orcid.org/0000-0003-4480-787X
shevtsov@chem.vsu.ru

Mikhail A. Potapov, Researcher of the Department of Physical Chemistry, Voronezh State University (Voronezh, Russian Federation).
https://orcid.org/0000-0002-1795-7605
amidines@mail.ru

Iliya D., Zartsyn, Dr. Sci. (Chem.), Professor of the Department of Physical Chemistry, Voronezh State University (Voronezh, Russian Federation).
https://orcid.org/0000-0002-7161-9754
zar-vrn@mail.ru

Svetlana N. Grushevskaya, Cand. Sci. (Chem.), Docent of the Department of Physical Chemistry, Voronezh State University (Voronezh, Russian Federation).
https://orcid.org/0000-0002-7083-1438
sg@chem.vsu.ru

Alexey A. Kruzhilin, Cand. Sci. (Chem.), Researcher of the Laboratory of Organic Additives for the Processes of Chemical and Electrochemical Deposition of Metals and Alloys Used in the Electronics Industry, Voronezh State University (Voronezh, Russian Federation).
https://orcid.org/0000-0003-2262-0131
kruzhilin.alexey@gmail.com

Evgeniia A. Ilina, Graduate Student of the Department of Physical Chemistry, Voronezh State University (Voronezh, Russian Federation).
https://orcid.org/0009-0004-4825-5894
zhenya.ali@yandex.ru

Kirill A. Tkachenko, Student of the Department of Physical Chemistry, Voronezh State University (Voronezh, Russian Federation).
https://orcid.org/0009-0002-4971-8921
bioshinf1912@mail.ru

Khidmet S. Shikhaliev, Dr. Sci. (Chem.), Professor, Head of the Department of Organic Chemistry, Voronezh State University (Voronezh, Russian Federation).
https://orcid.org/0000-0002-6576-0305
shikh1961@yandex.ru

Received 01.03.2023; approved after reviewing 12.04.2023; accepted for publication 15.05.2023; published online 25.09.2023.

Translated by Yulia Dymant

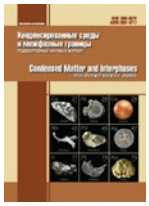

ISSN 1606-867X (Print)
ISSN 2687-0711 (Online)
Condensed Matter and Interphases
Kondensirovannye Sredy i Mezhfaznye Granitsy
https://journals.vsu.ru/kcmf/

Original articles

Research article
https://doi.org/10.17308/kcmf.2023.25/11396

Evaluation of the inhibitory effect of some derivatives of salts of long-chain carboxylic acids in relation to pitting corrosion of reinforcing steel in concrete

O. A. Kozaderov✉, D. S. Shevtsov, M. A. Potapov, I. D. Zartsyn, S. N. Grushevskaya, A. A. Kruzhilin, E. A. Ilina, K. A. Tkachenko, Kh. S. Shikhaliev

Voronezh State University,
1 Universitetskaya pl., Voronezh 394018, Russian Federation

Abstract

Derivatives of salts of long chain carboxylic acids and dimethylaminopropylamine, including those similar in composition to vegetable oils were synthesized. The structure of the molecules of new substances was reliably confirmed using physical methods of IR-Fourier spectroscopy, NMR spectroscopy, and HPLC.

The inhibitory effect of the synthesized substances on 35GS grade reinforcing steel was assessed using voltammetry. Experiments were carried out in an aqueous extract from a mortar, simulating the concrete pore solution, in the presence of chlorides as activators of pitting corrosion, as well as in samples of fine-grained concrete with periodic immersion in a chloride solution. It was found that 3-(dimethylamino)propyl-1-ammonium stearate did not exhibit an inhibitory effect. The introduction of salts of fatty acids of coconut and sunflower oils increased the anti-corrosion properties. The degree of protection was 40-44% in aqueous solutions and 30-32% for concrete samples.

The time before the onset of corrosion in concrete samples was found to increase by 1.75 times compared to the control composition without additives.

Keywords: Reinforcing steel, Reinforced concrete, Corrosion inhibitors, Chlorides, Long-chain salts carboxylic acids

Funding: The study was supported by the Russian Science Foundation (RSF), project no. 22-23-01144, https://rscf.ru/en/project/22-23-01144/

For citation: Kozaderov O. A., Shevtsov D. S., Potapov M. A., Zartsyn, I. D., Grushevskaya S. N., Kruzhilin A. A., Ilina E. A., Tkachenko K. A., Shikhaliev Kh. S. Evaluation of the inhibitory effect of some derivatives of salts of long-chain carboxylic acids in relation to pitting corrosion of reinforcing steel in concrete. *Condensed Matter and Interphases*. 2023;25(3): 445–453. https://doi.org/10.17308/kcmf.2023.25/11393

Для цитирования: Козадеров О. А., Шевцов Д. С., Потапов М. А., Зарцын И. Д., Грушевская С. Н., Кружилин А. А., Ильина Е. А., Ткаченко К. А., Шихалиев Х. С. Оценка ингибирующего действия некоторых производных солей длинноцепочечных карбоновых кислот по отношению к питтинговой коррозии арматурной стали в бетоне. *Конденсированные среды и межфазные границы*. 2023;25(3): 445–453. https://doi.org/10.17308/kcmf.2023.25/11396

✉ Oleg A. Kozaderov, e-mail: ok@chem.vsu.ru

1. Introduction

Reinforced concrete is widely used in the construction of industrial and civil facilities (transport structures, nuclear power plant cooling towers, dams, piers, etc.). The corrosion of reinforcing steel is the main cause of failure of reinforced concrete structures [1]. The most common and dangerous form of corrosion from an operational point of view is caused by the action of chlorides [2], which are contained in large quantities in sea water and de-icing salts. The danger is due to the local nature of steel degradation (pitting, ulcers), which in a relatively short period of time can lead to the destruction of the structure, since it is very difficult to identify local damage using traditional monitoring methods (for example, during visual inspection).

Measures for the primary protection of reinforced concrete against corrosion at the manufacturing stage include the selection of its optimal composition [3], and inhibitor additives are often used to increase the corrosion resistance of reinforcing steel [4]. At the same time, the issue of environmental load during their use remains relevant. The negative impact of nitrites, chromates, and benzotriazole on the environment was repeatedly mentioned [5, 6], despite their rather high protective properties [7–10]. To solve this problem, so-called "green" corrosion inhibitors are proposed for use [11]. Mainly these inhibitors are extracts of products of plant origin: leaves and stems [12–14], fruits [15], and waste products [16, 17]. It is understood that the components contained in the extract are of natural origin and decompose when released into the environment without causing harm. The results presented in published studies convincingly prove the promise of using some extracts as inhibitors in acidic, neutral, and alkaline environments, which provide a degree of protection of more than 80–90%.

A development of this approach in the search for new corrosion inhibitors is the modification of large-scale production products (vegetable oils: sunflower, coconut; food and industrial waste, etc.) using one-stage organic synthesis [18]. At the same time, the issue of rational waste disposal is solved (or cost reduction from the use of inexpensive components) and an increase in protective properties, solubility, or other characteristics is achieved through the introduction of appropriate functional groups. There are examples of modification of soybean, palm, and castor oils with imidazolines [19] with protection levels of low-carbon steel in 1 M HCl of more than 80%. At the same time, a more significant protective effect was noted relative to derivatives based on individual carboxylic acids with the C12, C18 length of the alkyl radical (degree of protection from 60%). In [20], derivatives of maize, soybean, sunflower oils, and beef fat with di- and triethanolamine were studied for steel in an acidic medium simulating the conditions of drilling fluid during oil production. In most combinations studied, protective effects of up to 40–50% were obtained (for several combinations up to 80%). Examples of results with different inhibitory effects allow researchers to take into account existing experience and accordingly select methods for modifying natural compounds and corrosion test conditions to obtain the greatest degree of protection.

There are known examples of the effective action of short-chain carboxylic acids and their salts for the protection of reinforcing steel from corrosion caused by chlorides. In [21], the degree of protection for sodium succinate was established at the level of 55–77% in a model aqueous solution at a chloride concentration of 0.6 M. The authors of [22] showed a decrease in the effectiveness of the protective action in the series of salts malonate > formate > acetate > propionate in samples of fine-grained concrete. In [23] an increase in the protective properties of concrete with the addition of long-chain carboxylic acids during freeze/thaw cycles in the presence of chlorides was revealed. However, there is no mention of the use of modified long-chain carboxylic acids or vegetable oils in solving similar problems.

The purpose of the study was the synthesis and evaluation of the inhibitory effect of new derivatives of salts of long-chain carboxylic acids and dimethylaminopropylamine, including those similar in composition to vegetable oils, in relation to low-carbon reinforcing steel in an aqueous chloride solution simulating the concrete environment, as well as for fine-grained concrete samples during periodic immersion in a chloride solution.

2. Experimental

2.1. Synthesis and analysis of dimethylaminopropylamine derivatives

Ammonium salts of dimethylaminopropylamine with stearic acid and mixtures of fatty acids simulating the composition of vegetable oils (coconut and sunflower) were obtained as inhibitors of chloride corrosion of reinforced concrete (Table 1). The choice of mixtures was determined by the need to assess the possibility of using plant raw materials to obtain inhibitors of this class. All reagents used were purchased from Acros Organics.

High-performance liquid chromatography with high-resolution mass spectrometry (electrospray ionization, HPLC-HRMS-ESI) in combination with UV detection was used to analyse the resulting substances. The analyser unit included an Agilent 1269 Infinity chromatograph and an Agilent 6230 TOF LC/MS detector. Quantitative analysis was performed using an external standard method. ^{1}H NMR spectra were recorded using a Bruker AV600 (600, 13 MHz) spectrometer in a DMSO-d6. TMS was used as the internal standard. The IR spectrum was recorded on Vertex 70 FT-IR spectrometer using a Platinum ATR (Bruker) ATR attachment equipped with a diamond prism in the frequency range from 4000 to 400 cm^{-1} with a resolution of 2 cm^{-1}. The result was obtained by averaging 16 scans.

The study demonstrated that in the absence of a catalyst, when equimolar amounts of dimethylaminopropylamine and carboxylic acids (or mixtures) are boiled in ethanol, a neutralization reaction takes place with almost quantitative yields of the corresponding ammonium salts, this was confirmed by the data of LC/MS spectrometry, ^{1}H NMR-, IR spectroscopy.

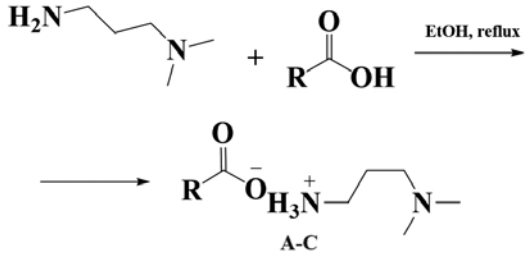

R: (A) $C_{17}H_{35}$,
(B) C_7H_{15} (10%) : C_9H_{19} (10%) : $C_{11}H_{23}$ (50%) : $C_{13}H_{27}$ (20%) : $C_{17}H_{35}$ (10%),
(C) $C_{17}H_{35}$ (10%) : $C_{17}H_{33}$ (40%) : $C_{17}H_{31}$ (50%)

*2.2. Method for the synthesis of ammonium salts of carboxylic acids **A-C***

A mixture of 1 mol of acid (in the case of mixtures, the total amount of substance of all acids should be 1 mol) and 1 mol of amine in 50 ml of ethyl alcohol was boiled until the components were completely dissolved. The completeness of the reaction was monitored using a universal indicator and TLC. After completion of the neutralization process, the resulting homogeneous solution was evaporated from the solvent using a rotary evaporator.

*3-(dimethylamino)propyl-1-ammonium stearate **A**.* The yield was 96%, viscous amber paste. ^{1}H NMR (δ): 0.89–0.93 (*t*, 3H CH_3), 1.17–1.91 (*m*, 34H 15CH_2+βCH_2+CH_2), 2.23–2.30 (s, 6H 2CH_3), 2.61–2.67 (m, 2H CH_2), 2.91–2.95 (*m*, 2H CH_2). IR spectrum (cm^{-1}): 3300–3400 (OH+N$^+$-H),

Table 1. Studied inhibitors

Symbol	Name	Formula
A	3-(dimethylamino)propyl-1-ammonium stearate	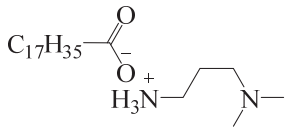
B	3-(dimethylamino)propyl-1-ammonium salts of coconut fatty acids	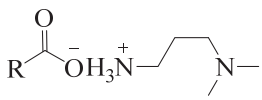 R: C_7H_{15} (10%) : C_9H_{19} (10%) : $C_{11}H_{23}$ (50%) : $C_{13}H_{27}$ (20%) : $C_{17}H_{35}$ (10%),
C	3-(dimethylamino)propyl-1-ammonium salts of sunflower fatty acids	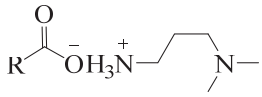 R: $C_{17}H_{35}$ (10%) : $C_{17}H_{33}$ (40%) : $C_{17}H_{31}$ (50%)

2150–2200 (N^+-H), 1700–1750 (C=O), 1550–1600 (COO^- + COH), 1550 (N^+H), 1400 (N^+H), 900–1150 (CH_2), 750–800 (CH_2), 500–580 (CH_3), m/z (M+H): found 386.2841, calculated 386.3872.

1-ammonium salts of coconut oil fatty acids ***B.*** The yield was 94%, viscous amber liquid. ^{1}H NMR (δ): 0.89–0.93(*t*, 3H CH_3), 1.17–1.91 (*m*, 34H 15CH_2+δCH_2+CH_2), 2.23–2.30 (s, 6H 2CH_3), 2.61–2.67 (m, 2H CH_2), 2.91–2.95 (*m*, 2H CH_2).

1-ammonium salts of fatty acids of sunflower oil ***C.*** The yield was 85%, viscous amber liquid. ^{1}H NMR (δ): 0.89–0.93(*t*, 3H CH_3), 1.17–1.91 (*m*, 34H 15CH_2+βCH_2+CH_2), 2.23–2.30 (s, 6H 2CH_3), 2.61–2.67 (m, 2H CH_2), 2.91–2.95 (*m*, 2H CH_2).

2.3. Assessment of the corrosion inhibition properties

To evaluate the corrosion inhibition properties of the synthesised compounds, a set of electrochemical methods was used. Samples of low-carbon steel 35GS with a rectangular cross-section were used as a working electrode. All surfaces, with the exception of the working surface, were reinforced with epoxy resin. A saturated silver chloride reference electrode (SCE, potential +201 mV relative to a standard hydrogen electrode) was placed in a separate container connected to the electrolytic cell by an agar agar based salt bridge filled with a KNO_3 saturated solution. The potentials in the work are presented relative to the SCE. The auxiliary electrode was a platinum mesh.

The working solution was a water extract from cement powder (mass ratio of distilled water and cement powder 1:10, extraction for 24 hours followed by filtration, pH 12.5–13.0). Electrochemical measurements were conducted in a glass three-electrode cell with undivided electrode spaces at a temperature of 23±3 C under natural aeration conditions, in the presence of the activating additive of NaCl with the concentration of 1.00 mol·dm^{-3} (reference experiment), and the studied substances. Due to their long-chain alkyl components, they are characterised by their low solubility in aqueous solutions. In this regard, their effect was studied at the highest concentration, which for all substances was 0.1 g·dm^{-3}.

The working electrode was preliminarily cleaned with K2000 sandpaper, washed with distilled water, and degreased with chemically pure isopropyl alcohol. The current density *i* was calculated by dividing the actual current *I* by the geometric area of the working electrode (2.25 cm^2).

For experiments in concrete, pieces of low-carbon steel 35GS of a periodic profile with a length of ≈100 mm and a diameter of 6 mm were used. A copper-insulated current conductor was soldered to one end of the rod. The place of soldering was covered with epoxy resin. The surface of the electrodes was cleaned with P1000 sandpaper (abrasive Al_2O_3 with a particle size of 14–20 microns) to degree St3 according to ISO 8501-1:2014 and degreased with ethyl alcohol (96%).

A mortar based on a cement-sand mixture was prepared from cement grade M500 according to GOST 10178-85. The water-cement ratio (w/c) was 0.50; the mass ratio of cement and sand was 1:3. Prism samples measuring 160×40×40 mm were formed with the electrode located along the axis. Extraction from the formwork was carried out after 7 days. The samples were cured for 28 days at 100% humidity. Additives of the synthesized substances were introduced together with the mixing water in an amount (relative to the weights of water) similar to the experiments in aqueous solutions.

During the experiment, solution samples were immersed in a 3% NaCl aqueous solution for one day. They were then transferred to a laboratory atmosphere with a natural relative humidity of 35±5% and a temperature of 22±2°C, where they were dried for six days. Afterwards, the cycle was repeated.

The corrosion current density (i_{cor}) was determined by the polarization resistance (PR) method according to F. Mansfeld [24]. After the free corrosion potential (E_{cor}) became stable for 30 minutes, the polarization curve was registered using an IPC-Pro potentiostat in the potentiodynamic polarization mode (potential scan rate of 0.2 mV·s^{-1}) in the range from E_{cor} −30 mV to E_{cor}+30 mV.

The ability of the studied substances to inhibit corrosion was assessed based on the degree of protection calculated using the formula:

$$Z_i = \frac{i_{cor,0} - i_{cor,inh}}{i_{cor,0}} \cdot 100\,\%,$$

where $i_{cor,0}$ and $i_{cor,inh}$ are the corrosion current densities in the control experiment and in the presence of an inhibitor, respectively.

For concrete samples, as efficiency criteria, an increase in the number of cycles until the loss of the passive state relative to control samples without additives and the degree of protection (Z_Q) based on an estimate of the electric charge Q were considered. The value of Q was determined as the area of a curvilinear trapezoid for a function of the corrosion current density at the time of the experiment. The value of Z_Q was determined using the formula:

$$Z_Q = \left(1 - \frac{Q_0}{Q_{inh}}\right) \cdot 100\,\%,$$

where Q_0 and Q_{inch} are the electric charges in the control experiment and in the presence of the inhibitor, respectively.

3. Results and discussion

3.1. Potentiodynamic measurements in water extract from concrete

The introduction of all studied substances, by 11–35 mV, slightly shifted E_{cor} towards positive values (Table 2), which indicates the predominant effect on the anodic partial reaction of metal oxidation [25]. This was also confirmed by comparing the initial segments of the polarization curves (PC). The cathodic sections of PC for all compounds coincide with the control experiment without an additive (Fig. 1). For compound ***A*** the anodic sections of the PC were close (Fig. 1a), with the same polarization, the reduction in current density was not higher than 5%. The addition of

Table 2. Kinetic parameters of mild steel electrode in water extract from cement + 1.00 mol dm^{-3} NaCl in the presence of derivatives

Inhibitor	C_{inh}, g·dm^{-3}	E_{cor}, mV	R_p, kΩ·cm²	b_a, mV	b_c, mV	B, mV	i_{cor}, μA·cm^{-2}	Z_i, %
blank	–	–451	9.21	64.3	63.0	31.8	3.44±0.36	-
A	0.1	–442	7.80	55.8	43.5	24.0	3.02±0.16	12
B	0.1	–416	10.75	58.6	35.2	22.0	2.06±0.13	40
C	0.1	–436	11.13	58.2	33.9	21.0	1.93±0.23	44

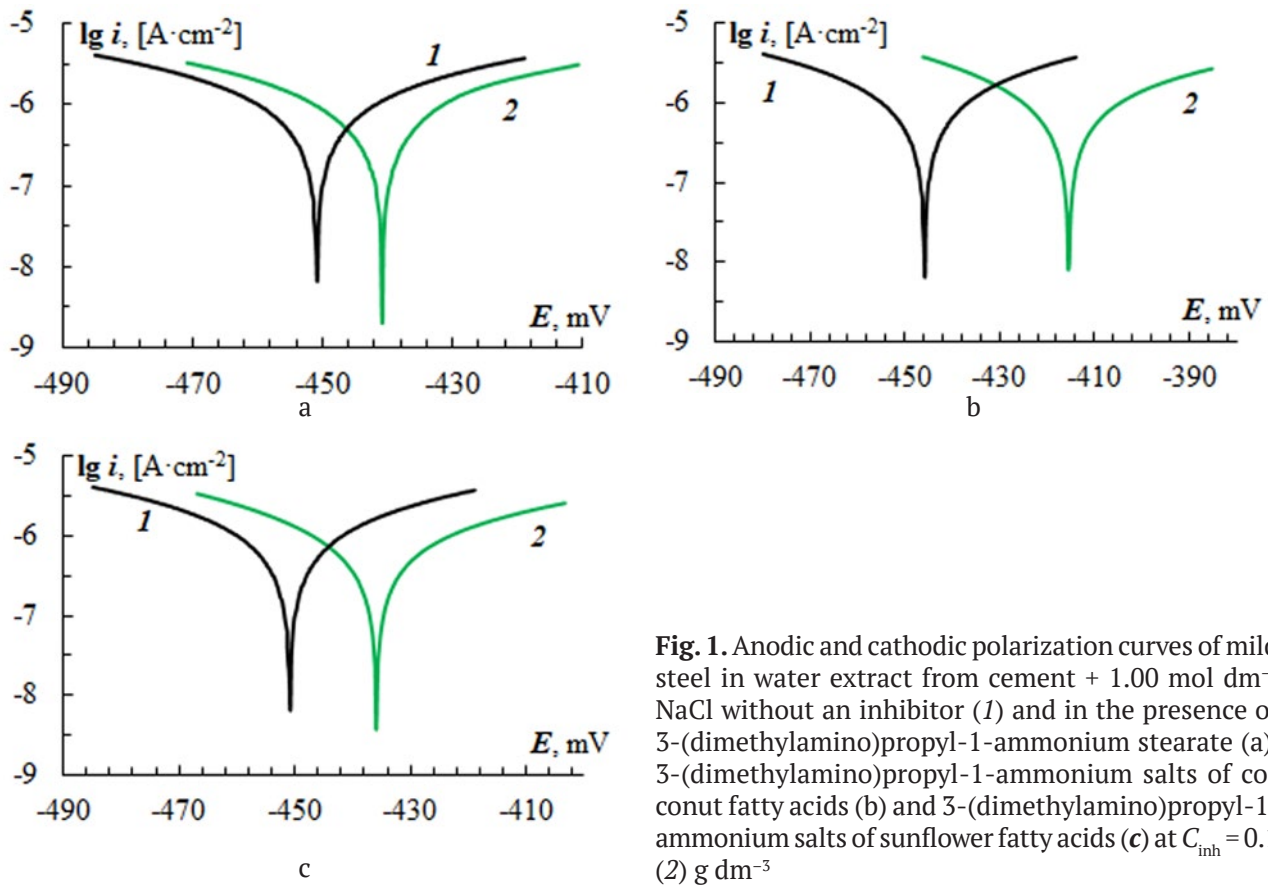

Fig. 1. Anodic and cathodic polarization curves of mild steel in water extract from cement + 1.00 mol dm^{-3} NaCl without an inhibitor (*1*) and in the presence of 3-(dimethylamino)propyl-1-ammonium stearate (a), 3-(dimethylamino)propyl-1-ammonium salts of coconut fatty acids (b) and 3-(dimethylamino)propyl-1-ammonium salts of sunflower fatty acids (***c***) at C_{inh} = 0.1 (*2*) g dm^{-3}

compounds ***B*** and ***C*** caused a decrease in current density in the anodic sections of the PC by 25% and 38%, respectively (Fig. 1b, c).

The results of calculations of electrochemical parameters using the polarization resistance method are presented in Table 2 and are consistent with the data from the analysis of polarization curves. The value of Z_i at 12% was obtained for the compound ***A***. For mixed additives ***B*** and ***C*** the degree of protection was higher and amounted to 40 and 44%, respectively.

Taking into account the obtained preliminary results in model solutions, samples of fine-grained concrete (hereinafter referred to as concrete) were made for the most effective compounds ***B*** and ***C***.

3.2. Potentiodynamic measurements in fine-grained concrete samples

For concrete samples without additives, a violation of the passive state was obtained in a moisture-saturated and dry state after four immersion cycles during the fifth cycle (Figs. 2a, b, curves *1*). This was accompanied by reaching or exceeding a threshold value i_{cor} = 0.1 μA·cm^{-2} [26]. The introduction of the studied additives in an amount of 0.1 g dm^{-3} relative to the amount of mixing water increased the number of cycles of immersion in the chloride solution. For compounds ***B*** and ***C*** activation was revealed between the seventh and eighth immersion for the saturated state and the eighth and ninth for the air-dry state (Figs. 2a, b, curves *2*). Thus, the introduction of the studied additives increased the period before the onset of corrosion by 1.75 times.

Further modification of the calculated values of i_{cor} also indicated the manifestation of an inhibitory effect. In general, i_{cor} for concrete with additives did not exceed the values for control samples.

The calculations of the electric charge are presented in Table 3. After 100 days of experiment after 15 cycles of immersion in chloride solution, the degree of protection for additives ***B*** and ***C*** were close and amounted to 31 and 32%, respectively.

Table 3. Estimation of the electric charge value according to the corrosion rate data

Inhibitor	Q, C·cm^{-2}	Z_Q, %
blank	2.16±0.16	–
B	1.50±0.12	30.6
C	1.47±0.13	31.9

Conclusions

In our study, we synthesised and confirmed the structure of derivatives of salts of long-chain carboxylic acids and dimethylaminopropylamine, including those similar in composition to vegetable oils.

Electrochemical methods were used to assess the ability of the synthesised compounds to inhibit corrosion of reinforcement steel in a

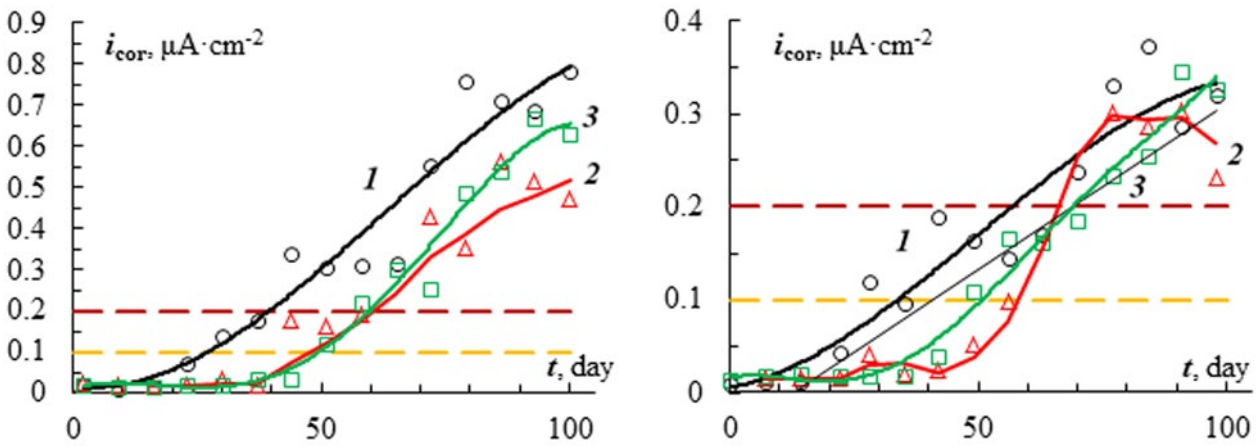

a b

Fig. 2. Changing the i_{cor} of reinforcing steel in mortar in a moisture-saturated state (a) and air-dry (b) without additives (*1*) with additives in the presence of 3-(dimethylamino)propyl-1-ammonium salts of coconut fatty acids (*2*) and 3-(dimethylamino)propyl-1-ammonium salts of sunflower fatty acids (*3*)

solution simulating concrete pore solution in the presence of chlorides. It has been shown that 3-(dimethylamino)propyl-1-ammonium stearate exhibits virtually no inhibitory effect.

For fatty acid salts of coconut and sunflower oils, the degrees of protection were close and comprised 40 and 44% in aqueous solution and 30 and 31% in concrete, respectively, which characterises the resulting substances as moderately effective inhibitors. At the same time, for concrete samples, an increase in the time before the onset of corrosion by 1.75 times was obtained relative to the control composition without additives.

Author contributions

All authors made an equivalent contribution to the publication.

Conflict of interests

The authors declare that they have no known competing financial interests or personal relationships that could have influenced the work reported in this paper.

References

1. Lazorenko G., Kasprzhitskii A., Nazdracheva T. Anti-corrosion coatings for protection of steel railway structures exposed to atmospheric environments: A review. *Construction and Building Materials*. 2021;288: 123115. https://doi.org/10.1016/j.conbuildmat.2021.123115

2. Montemor M. F., Simoes A. M. P., Ferreira M. G. S. Chloride-induced corrosion on reinforcing steel: from the fundamentals to the monitoring techniques. *Cement and concrete composites*. 2003;25(4-5): 491–502. https://doi.org/10.1016/S0958-9465(02)00089-6

3. Mazgaleva A., Bobylskaya V., Reshetnikov M. Concrete polymer material for the protection of concrete and reinforced concrete structures of hydraulic structures from biological damage. *International Scientific Siberian Transport Forum TransSiberia – 2021*. 2021: 1148–1158. https://doi.org/10.1007/978-3-030-96380-4_126

4. Shevtsov, D. S., Zartsyn, I. D., Komarova, E. S., Zhikhareva, D. A., Avetisyan, I. V., Shikhaliev, K. S., Potapov M. A., Kozaderov, O. A. Evaluation of the efficiency of the Master Life CI 222 organic corrosion inhibitor additive for the protection of steel reinforcement bars in concrete. *International Journal of Corrosion and Scale Inhibition*. 2022;11(4): 1583–1592. https://doi.org/10.17675/2305-6894-2022-11-4-10

5. Sastri V. S. *Green corrosion inhibitors: theory and practice*. John Wiley & Sons; 2012. https://doi.org/10.1002/9781118015438

6. Alvarez L. X., Troconis de Rincón O., Escribano J., Rincon Troconis B. C. Organic compounds as corrosion inhibitors for reinforced concrete: a review. *Corrosion Reviews*. 2023. https://doi.org/10.1515/corrrev- 2023-0017

7. Kasatkin, V. E., Dorofeeva, V. N., Kasatkina, I. V., Korosteleva, I. G., Kornienko, L. P. Monitoring the effectiveness of corrosion inhibitors by electrochemical methods. Sodium nitrite as an inhibitor for the protection of steel in a model solution of the concrete pore fluid. *International Journal of Corrosion and Scale Inhibition*, 2023;11(1); 198–220. https://doi.org/10.17675/2305-6894-2022-11-1-11

8. Das J. K., Pradhan B. Study on influence of nitrite and phosphate based inhibiting admixtures on chloride interaction, rebar corrosion, and microstructure of concrete subjected to different chloride exposures. *Journal of Building Engineering*. 2022;50: 104192. https://doi.org/10.1016/j.jobe.2022.104192

9. Abd El Haleem S. M., Abd El Wanees S., Bahgat A. Environmental factors affecting the corrosion behaviour of reinforcing steel. VI. Benzotriazole and its derivatives as corrosion inhibitors of steel. *Corrosion Science*. 2014;87: 321–333. http://dx.doi.org/10.1016/j.corsci.2014.06.043

10. Okeniyi J. O., Omotosho O. A., Ajayi O. O., Loto C. A. Effect of potassium-chromate and sodium-nitrite on concrete steel-rebar degradation in sulphate and saline media. *Construction and Building Materials*, 2014;50: 448–456. http://dx.doi.org/10.1016/j.conbuildmat.2013.09.063

11. Zomorodian A., Behnood A. Review of Corrosion Inhibitors in Reinforced Concrete: Conventional and Green Materials. *Buildings*. 2023;13(5): 1170. https://doi.org/10.3390/buildings13051170

12. Naderi R., Bautista A., Velasco F., Soleimani M., Pourfath, M. Green corrosion inhibition for carbon steel reinforcement in chloride-polluted simulated concrete pore solution using Urtica Dioica extract. *Journal of Building Engineering*. 2022;58: 105055. https://doi.org/10.1016/j.jobe.2022.105055

13. Wang Q., Wu X., Zheng H., Liu L., Zhang Q., Zhang A. Evaluation for Fatsia japonica leaves extract (FJLE) as green corrosion inhibitor for carbon steel in simulated concrete pore solutions. *Journal of Building Engineering*. 2023;63: 105568. https://doi.org/10.1016/j.jobe.2022.105568

14. Harb M. B., Abubshait S., Etteyeb N., Kamoun M., Dhouib A. Olive leaf extract as a green corrosion inhibitor of reinforced concrete contaminated with

seawater. *Arabian Journal of Chemistry*. 2020;13(3): 4846-4856. https://doi.org/10.1016/j.arabjc.2020.01.016

15. Subbiah K., Lee H. S., Mandal S., Park, T. Conifer cone (Pinus resinosa) as a green corrosion inhibitor for steel rebar in chloride-contaminated synthetic concrete pore solutions. *ACS Applied Materials & Interfaces*. 2021;13(36): 43676–43695. https://doi.org/10.1021/acsami.1c11994

16. Ramesh T., Chauhan D. S., Quraishi M. A. Coconut Coir Dust Extract (CCDE) as green corrosion inhibitor for rebar'steel in concrete environment. *International Journal of Corrosion and Scale Inhibition*. 2021;10(2): 618–633. https://doi.org/10.17675/2305-6894-2021-10-2-9

17. Gromboni M. F., Sales A., de AM Rezende, M., Moretti, J. P., Corradini, P. G., Mascaro, L. H. Impact of agro-industrial waste on steel corrosion susceptibility in media simulating concrete pore solutions. *Journal of Cleaner Production*. 2021;284: 124697. https://doi.org/10.1016/j.jclepro.2020.124697

18. Vaidya N. R., Aklujkar P., Rao A. R. Modification of natural gums for application as corrosion inhibitor: a review. *Journal of Coatings Technology and Research*. 2022;19(1): 223–239. https://doi.org/10.1007/s11998-021-00510-z

19. Yoo S. H., Kim Y. W., Chung K., Baik S. Y., Kim J. S. Synthesis and corrosion inhibition behavior of imidazoline derivatives based on vegetable oil. *Corrosion Science*. 2012;59: 42–54. https://doi.org/10.1016/j.corsci.2012.02.011

20. Topilnytskyy P., Romanchuk V., Yarmola T. Production of corrosion inhibitors for oil refining equipment using natural components. *Chemistry & Chemical Technology*. 2018;12(3): 400–404. https://doi.org/10.23939/chcht12.03.400

21. Mohamed A., Visco D. P., Bastidas D. M. Sodium succinate as a corrosion inhibitor for carbon steel rebars in simulated concrete pore solution. *Molecules*. 2022;27(24): 8776. https://doi.org/10.3390/molecules27248776

22. Sagoe-Crentsil K. K., Yilmaz V. T., Glasser F. P. Corrosion inhibition of steel in concrete by carboxylic acids. *Cement and Concrete Research*. 1993:23(6): 1380–1388. https://doi.org/10.1016/0008-8846(93)90075-k

23. Tian Y., Guo W., Wang W., Wang B., Zhang P., Zhao T. Influence of organic corrosion inhibitors on steel corrosion in concrete under the coupled action of freeze–thaw cycles and chloride attack. *Construction and Building Materials*. 2023;368: 130385. https://doi.org/10.1016/j.conbuildmat.2023.130385

24. Mansfeld F. Tafel slopes and corrosion rates obtained in the pre-Tafel region of polarization curves. *Corrosion Science*. 2005;47(12): 3178–3186. https://doi.org/10.1016/j.corsci.2005.04.012

25. Nam N. D., Van Hien P., Hoai N. T., Thu V. T. H. A study on the mixed corrosion inhibitor with a dominant cathodic inhibitor for mild steel in aqueous chloride solution. *Journal of the Taiwan Institute of Chemical Engineers*. 2018;91: 556–569. https://doi.org/10.1016/j.jtice.2018.06.007

26. Andrade C., Alonso C. Test methods for on-site corrosion rate measurement of steel reinforcement in concrete by means of the polarization resistance method. *Materials and Structures*. 2004;37(9): 623–643. https://doi.org/10.1007/bf02483292

Information about the authors

Oleg A. Kozaderov, Dr. Sci. (Chem.), Docent, Head of the Department of Physical Chemistry, Voronezh State University (Voronezh, Russian Federation).
https://orcid.org/0000-0002-0249-9517
ok@chem.vsu.ru

Dmitry S. Shevtsov, Researcher of the Department of Physical Chemistry, Voronezh State University (Voronezh, Russian Federation).
https://orcid.org/0000-0003-4480-787X
shevtsov@chem.vsu.ru

Mikhail A. Potapov, Researcher of the Department of Physical Chemistry, Voronezh State University (Voronezh, Russian Federation).
https://orcid.org/0000-0002-1795-7605
amidines@mail.ru

Iliya D., Zartsyn, Dr. Sci. (Chem.), Professor of the Department of Physical Chemistry, Voronezh State University (Voronezh, Russian Federation).
https://orcid.org/0000-0002-7161-9754
zar-vrn@mail.ru

Svetlana N. Grushevskaya, Cand. Sci. (Chem.), Docent of the Department of Physical Chemistry, Voronezh State University (Voronezh, Russian Federation).
https://orcid.org/0000-0002-7083-1438
sg@chem.vsu.ru

Alexey A. Kruzhilin, Cand. Sci. (Chem.), Researcher of the Laboratory of Organic Additives for the Processes of Chemical and Electrochemical Deposition of Metals and Alloys Used in the Electronics Industry, Voronezh State University (Voronezh, Russian Federation).
https://orcid.org/0000-0003-2262-0131
kruzhilin.alexey@gmail.com

Evgeniia A. Ilina, Graduate Student of the Department of Physical Chemistry, Voronezh State University (Voronezh, Russian Federation).
https://orcid.org/0009-0004-4825-5894
zhenya.ali@yandex.ru

Kirill A. Tkachenko, Student of the Department of Physical Chemistry, Voronezh State University (Voronezh, Russian Federation).
https://orcid.org/0009-0002-4971-8921
bioshinf1912@mail.ru

Khidmet S. Shikhaliev, Dr. Sci. (Chem.), Professor, Head of the Department of Organic Chemistry, Voronezh State University (Voronezh, Russian Federation).
https://orcid.org/0000-0002-6576-0305
shikh1961@yandex.ru

Received 27.03.2023; approved after reviewing 18.04.2023; accepted for publication 15.05.2023; published online 25.09.2023.

Translated by Valentina Mittova

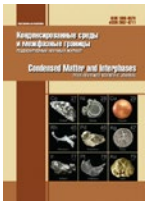

ISSN 1606-867X (Print)
ISSN 2687-0711 (Online)
Condensed Matter and Interphases
Kondensirovannye Sredy i Mezhfaznye Granitsy
https://journals.vsu.ru/kcmf/

Original articles

Research article
https://doi.org/10.17308/kcmf.2023.25/11398

Localization of the *E. coli* Dps protein molecules in a silicon wires under removal of residual salt

E. V. Parinova[1]✉, S. S. Antipov[1,2], V. Sivakov[3], E. A. Belikov[1], O. A. Chuvenkova[1], I. S. Kakuliia[1], S. Yu. Trebunskikh[1], K. A. Fateev[1], M. S. Skorobogatov[1], R. G. Chumakov[1], A. M. Lebedev[4], O. V. Putintseva[1], V. G. Artyukhov[1], S. Yu. Turishchev[1]

[1]*Voronezh State University,*
1 Universitetskaya pl., Voronezh 394018, Russian Federation

[2]*Institute of Cell Biophysics of the Russian Academy of Sciences,*
3 Institutskaya ul., Pushchino 142290, Russian Federation

[3]*Leibniz Institute of Photonic Technology, Department Functional Interfaces,*
Albert Einstein Str. 9, 07745 Jena, Germany

[4]*National Research Center "Kurchatov Institute",*
1 Akademika Kurchatova pl., Moscow 123182, Russian Federation

Abstract

The work is related to the removal of residual salts in hybrid structures formed as a result of silicon wires arrays combining with a nanomaterial of natural origin – bacterial ferritin-like protein Dps. The study of the morphology and composition of the surface and the bulk part of the hybrid structure as a result of combination and subsequent washing in water was carried out.

The method of metal-assisted wet chemical etching was used to obtain silicon wires arrays. To obtain recombinant protein, *Escherichia coli* BL21*(DE3) cells with chromatographic purification were used as producers. The combination of silicon wires with protein molecules was carried out by layering them in laboratory conditions, followed by drying. The residual salt found earlier in the hybrid material was removed by washing in water. The resulting hybrid material was studied by scanning electron microscopy and X-ray photoelectron spectroscopy. A well-proven complementary combination of scanning electron microscopy and X-ray photoelectron spectroscopy together with ion etching was used to study the morphology of the hybrid material "silicon wires – bacterial protein Dps" and the composition with physico-chemical state respectively.

In arrays of silicon wires with a wire diameter of about 100 nm and a distance between them from submicron to nanometer sizes, protein was found as a result of layering and after treatment in water. At the same time, the amount of residual NaCl salt is minimized on the surface of the hybrid structure and in its volume.

The obtained data can be used in the development of coating technology for the silicon wires developed surface available for functionalization with controlled delivery of biohybrid material.

Keywords: Nanostructures, Biomolecules, Hybrid materials, Developed surface, Recombinant ferritin-like protein Dps, Silicon wires, Scanning Electron Microscopy, X-ray Photoelectron Spectroscopy

Funding: The study was supported by Russian Science Foundation (Project 19-72-20180). The work is supported under scholarship of the President of Russian Federation SP-189.2021.1 for young scientists in part of the silicon wires arrays formation, the methodology of work with protein molecules from *E.coli* cell material. V.S. gratefully acknowledges financial support by the German Research Foundation (DFG) under Grant SI 1893/18-1.

For citation: Parinova E. V., Antipov S. S., Sivakov V., Belikov E. A., Chuvenkova O. A., Kakuliia I. S., Trebunskikh S. Yu., Fateev K. A., Skorobogatov M. S., Chumakov R. G., Lebedev A. M., Putintseva O. V., Artyukhov V. G., Turishchev S. Yu.

✉ Elena V. Parinova, e-mail: parinova@phys.vsu.ru

Localization of the *E.coli* Dps protein molecules in a silicon wires under removal of residual salt. *Condensed Matter and Interphases*. 2023; 25(3): 454–461. https://doi.org/10.17308/kcmf.2023.25/11398

Для цитирования: Паринова Е. В., Антипов С. С., Sivakov V., Беликов Е. А., Чувенкова О. А., Какулия Ю. С., Требунских С. Ю., Фатеев К. А., Скоробогатов М. С., Чумаков Р. Г., Лебедев А. М., Путинцева О. В., Артюхов В. Г., Турищев С. Ю. Локализация молекул белка Dps *E.coli* в нитевидном кремнии при удалении остаточной соли. *Конденсированные среды и межфазные границы*. 2023;25(3): 454–461. https://doi.org/10.17308/kcmf.2023.25/11398

1. Introduction

In modern technologies, new functional biohybrid materials are beginning to occupy more and more leading positions, primarily due to the simplicity and efficiency of their formation, properties often dictated by nature itself, and application prospects. Simple methods of formation and convenient, tunable characteristics significantly contribute to the creation of effective devices based on such materials. One of the most relevant and promising directions is the formation, study and further application of hybrid nature-like nanoobjects obtained from various biocultures [1].

A striking representative of the natural functional hybrid nanomaterial is the Dps protein. The Dps protein (DNA-binding protein of starving cells) belongs to the family of bacterial ferritins, whose function is to accumulate iron reserves in the organism. The Dps protein is found in almost all known types of living organisms [2, 3–5]. The Dps protein molecule can be a hybrid nano-biological object consisting of an outer organic shell, the size of which is about 9 nm, and an inorganic core contained in the inner cavity of a molecule up to 5 nm in size [6, 7]. The protein part includes 12 identical subunits with a homododecamer structure [6, 7]. The inorganic core deposited in the inner cavity of the molecule is a nanoparticle of the iron-oxygen system [6]. A hybrid nanomaterial based on Dps protein molecules obtained from *Escherichia coli* cell culture may be of interest as a potential container of natural origin with the wide range of use: from the accumulation and storage of nanomaterials to their targeted delivery.

Earlier, we demonstrated the possibility of forming two-dimensional structures by ferritin Dps molecules [8], and also obtained the understanding of the nuclei morphological features of a biohybrid nanomaterial using the transmission electron microscopy and their composition by X-ray photoelectron spectroscopy (XPS) [9]. An effective combination of the XPS method (with ion profiling) and the scanning electron microscopy (SEM) method has been studied the possibility of filling with Dps protein (free of inorganic nanoparticles) pores of a functional semiconductor material with a developed surface – silicon wires (Si-NW) [10, 11]. However, a significant residual NaCl salt content of buffer solution was found in the formed structures of silicon wires – protein Dps [11]. In this work, the same combination of SEM and XPS was used, providing information on the composition, morphology and physico-chemical state of the object under study, for the silicon wires – protein Dps structures after removal of the NaCl salt residual amount as a result of water washing.

2. Experimental

The metal-assisted wet chemical etching [12, 13] was used to form Si-NW. Wafers of crystalline silicon of *p*- and *n*-types conductivity (~ 1-5 Ω/cm and < 0.02 Ω/cm, respectively) were used after washing in a solution of hydrofluoric acid HF (2%) for 10 seconds. Next, silver nanoparticles were deposited on the surface of the prepared wafers when immersed in a solution of $AgNO_3$ (0.01 M) and HF (5 M). Immersion times were 15 s for *p*-type substrates and 45 s for *n*-type substrates, followed by three-minute etching in a 30% solution of H_2O_2 and HF (5 M). Finally, silver nanoparticles were removed for 10 minutes by washing in 65% aqueous HNO_3 solution, followed by air drying of the structures. Further, the silicon wires structures were used identical to those studied in [11], as simultaneously processed parts of the same wafers.

Cells of *Escherichia coli* BL21*(DE3) bacteria, hereinafter *E.coli*, transformed by pGEM_dps, were used as producers to obtain the recombinant Dps protein. Detailed information on the recombinant protein preparation is given in [6]. The protein solution had a concentration of 2 mg/ml in a

buffer containing 10 mM NaCl, 50 mM tris-HCl (pH 7.0) and 0.1 mM EDTA. After controlling the size of protein molecules by dynamic light scattering, a single layering of 10 µl of protein molecules solution was performed on the surface of Si-NW arrays. Further, in order to remove the residual NaCl salt [11], a single layering of 10 µl of water was carried out, followed by its removal after 30 seconds using filter paper without contact with the surface of the structure and drying the sample at 37 °C until completely dry.

The morphology of the Si-NW surfaces source array and the hybrid structure based on it with a layered protein after washing was studied by scanning electron microscopy. The Carl Zeiss ULTRA 55 microscope was used in the mode of secondary electrons registration with an accelerating voltage value of 2 kV, which is necessary for working with structures of biological origin. To estimate the areas occupied by the wires array and pores, as well as the degree of the arrays filling with molecular culture after washing, the Image J software package was used.

The XPS research was carried out using the ESCA module electron energy analyzer SPECS Phoibos 150 of the Kurchatov synchrotron (National Research Center Kurchatov Institute, Moscow) NANOFES ultrahigh vacuum experimental station [14]. Monochromatized Al Kα radiation of an X-ray tube (1486.61 eV) was used, the depth of the informative layer was ~ 2–3 nm [15]. Survey spectra were recorded in the range of binding energies 0–850 eV. To normalize and calibrate the data, a standard approach was used based on the independent recording of the pure gold foil (Au 4*f*) signal. To identify the features of the survey spectra, well-known databases were used, from which the most relevant and accurate (monochromatic) spectra were selected [15–17]. A focused source of surface etching with argon ions was used at an accelerating voltage of 3 kV with an etching duration of 20 minutes. The area of the etching area was selected with an excess of the surface area from which the XPS data were recorded.

3. Results and discussion

Fig. 1 shows the data of SEM studies for the initial Si-NW arrays and biohybrid structures. Note that in our previous work [11] we used morphologically identical Si-NW. Simultaneously formed parts of the same plate were used in protein layering [11] and in this work, where washing of the obtained biohybrid structures in water was added to the sequence of formation procedures. For this reason, Fig. 1a, c contains data on the work of [11] Si-NW substrates of *p*- and *n*-type. At the same scale, the SEM images of Fig. 1b, d were obtained for surfaces of biohybrid structures after layering of a molecular protein culture obtained from *E.coli* bacteria and washing. For *p*-type substrates, the formation of more pronounced wires with a uniform distribution of submicron size pores ~ 200-500 nm between the wires has been established. For *n*-type substrates, large pores of similar size are observed together with much smaller ones, about 10–100 nm in size. The formed characteristic upper parts of the wires are indicated by arrow 1, and the pores are indicated by arrow 2 in Fig. 1a, b. It is shown that all the observed Si-NW pores are available for filling as a result of Dps protein molecules layering with a size up to 10 nm [11].

According to the results obtained earlier, the surface of Si-NW, which is different in its morphology for *p*-type and *n*-type substrates, was almost completely covered with layered protein, and only the uppermost parts of the wires were fragmentally observed. The large pores dimensions provided a relatively greater penetration of the biomaterial into the silicon wires arrays of the *n*-type substrate. Significantly different morphology of biohybrid structures was observed as a result of washing aiming to remove residual NaCl salt. According to Fig. 1b no observations of micron- and submicron-sized salt microcrystals on the surface of a biohybrid material for a Si-NW *p*-type substrate have been recorded. Moreover, the total amount of protein decreased as a result of washing, since the upper sections of the silicon wires are reproducibly observed, indicated by arrows 1 in Fig. 1b. At the same time, large island formations (Fig. 1b, arrow 2) of micrometer sizes are observed on the surface of the silicon wires arrays, significantly exceeding the dimensions of the pores between wires (pore sizes) and without the faceted shape characteristic of NaCl salt. On the surface of these island formations, in turn, voids with sizes close

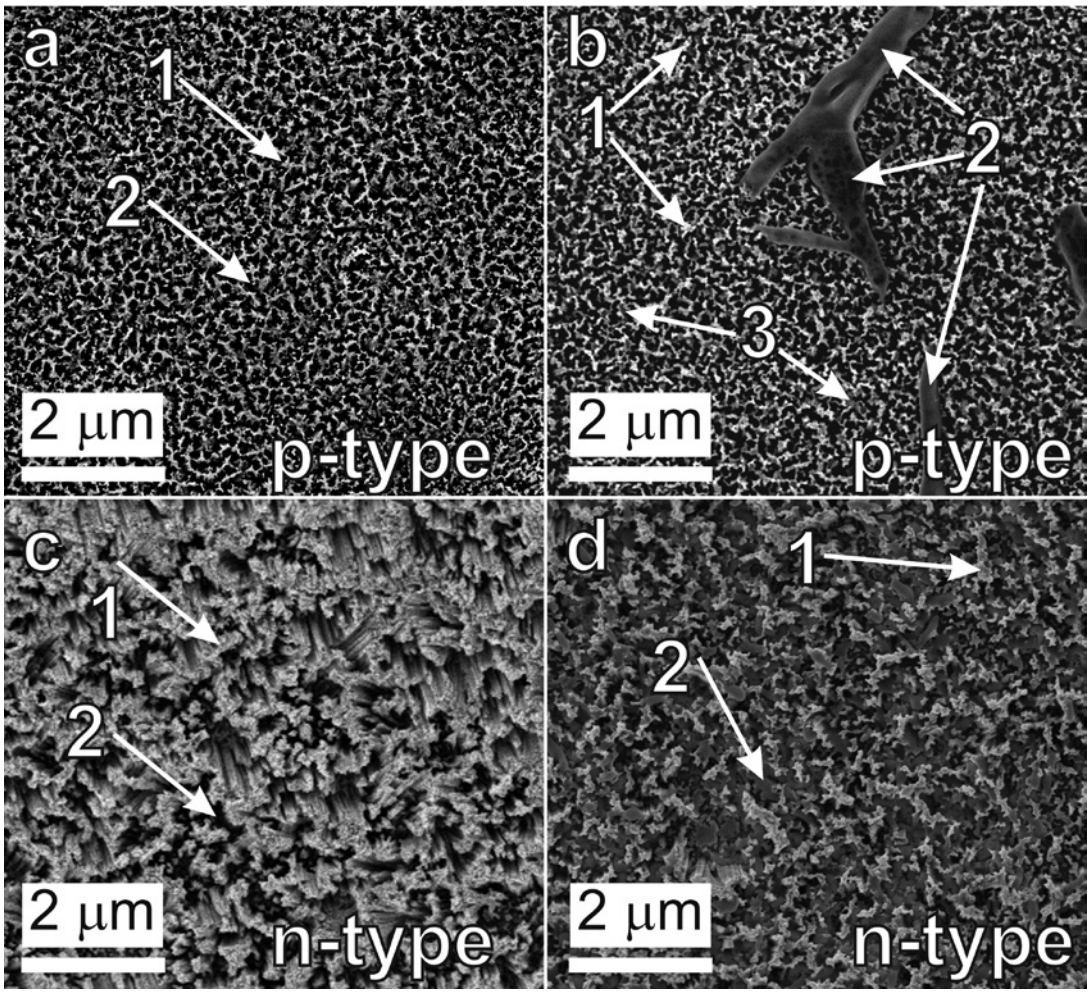

Fig. 1. Scanning electron microscopy of the initial samples of silicon wires arrays surfaces formed from *p*-type (a) and *n*-type (c) substrates [11], as well as after layering of the Dps protein molecular culture and washing in water (b) and (d), respectively. 1 – the tops of the wires (walls of pores), 2 (a and c) – pores between the wires, 2 and 3 (b and d) elements of protein culture

to 100 nm are noted. This indicates the presence of a residual amount of protein that has not entered the pores, but is a source of biomaterial localized in the Si-NW array. Localization of biocomponents in the pores of the studied structures is marked in Fig. 1b by arrows 3. It seems possible to state that the washing of the forming biohybrid structure led to the removal of residual salt crystals from structures surface and the observation of a Si-NW array with a localized molecular culture with incomplete filling of the pores. Protein localization in the spaces between silicon wires is much more noticeable for the Si-NW of the n-type substrate in Fig. 1d. Arrow 1 shows the characteristic upper part of the uncoated silicon wires, and arrow 2 shows a significant amount of protein in the pores of the Si-NW array. The degree of pore filling also decreases as a result of washing, compared with the data [11].

The survey XPS spectra are shown in Fig. 2 for arrays of *p*- and *n*-type silicon wires after layering of the molecular culture of Dps cells of *E. coli* and subsequent washing. All lines corresponding to the biological component of the studied biohybrid structures are marked. For both types of substrates used, the 1*s* oxygen line is the main one. The significant intensity of the 1*s* oxygen line excludes the contribution only from the natural SiO_2 oxide covering the silicon wires. The reason for such a high intensity of the oxygen line, along with the observation of the 1*s* carbon and nitrogen lines (in order of decreasing relative signal intensity), is the Dps molecular culture

localized in the Si-NW array. Also, insignificant in intensity 2*s* and 2*p* silicon lines from wires uncovered by molecular culture are observed. Finally, it should be noted that the set of chlorine (2*s* and 2*p*) and sodium lines (2*p* line and Auger KLL line) is weak in relative intensity. It should be noted that in [11] for biohybrid structures not subjected to removal of the residual NaCl salt, in some cases the signal from the sodium KLL Auger line was the main one in intensity, as was the signal from chlorine atoms. Thus, it can be stated that the applied approach to the dissolution and removal of residual salt leads to the almost complete removal of NaCl from the surface of the studied biohybrid structures Si-NW – molecular culture of Dps cells of *E.coli*. Finally, it should be noted the general similarity in the observed XPS lines in their energy position and relative intensity (Fig. 2, two lower spectra). This indicates an almost identical physico-chemical state of the surface of the studied biohybrid structures after layering of the molecular culture of Dps cells of *E.coli* and subsequent washing, regardless of the type of substrate and its processing mode. That is, the localization of the biomaterial is observed in the pores of Si-NW arrays for both types of surface morphology of the initial array of silicon wires. And the washing process allows removal the residual NaCl salt from the surface of biohybrid structures. Due to the observed identity of the physico-chemical state of the studied structures surface, we removed a significant part of the surface in 20 minutes of etching at a relatively high voltage accelerating argon ions (3 kV) only for a sample of a biohybrid structure formed on an *n*-type substrate. The etching rate estimation using the NANOFES station module along with calibration measurements show the removal rate for silicon atoms ~ 2.5 nm/min. For the residual part of the molecular culture, this rate may differ several times [18]. The removal of more than 50 nm of the surface by an ion beam in this way leads to significant changes. The relative intensity of the O 1*s* line is significantly reduced, which indicates the removal of a considerable part of the Dps molecular culture localized in the pores. At the same time, silicon lines reached almost the same intensity, as a result of a significant

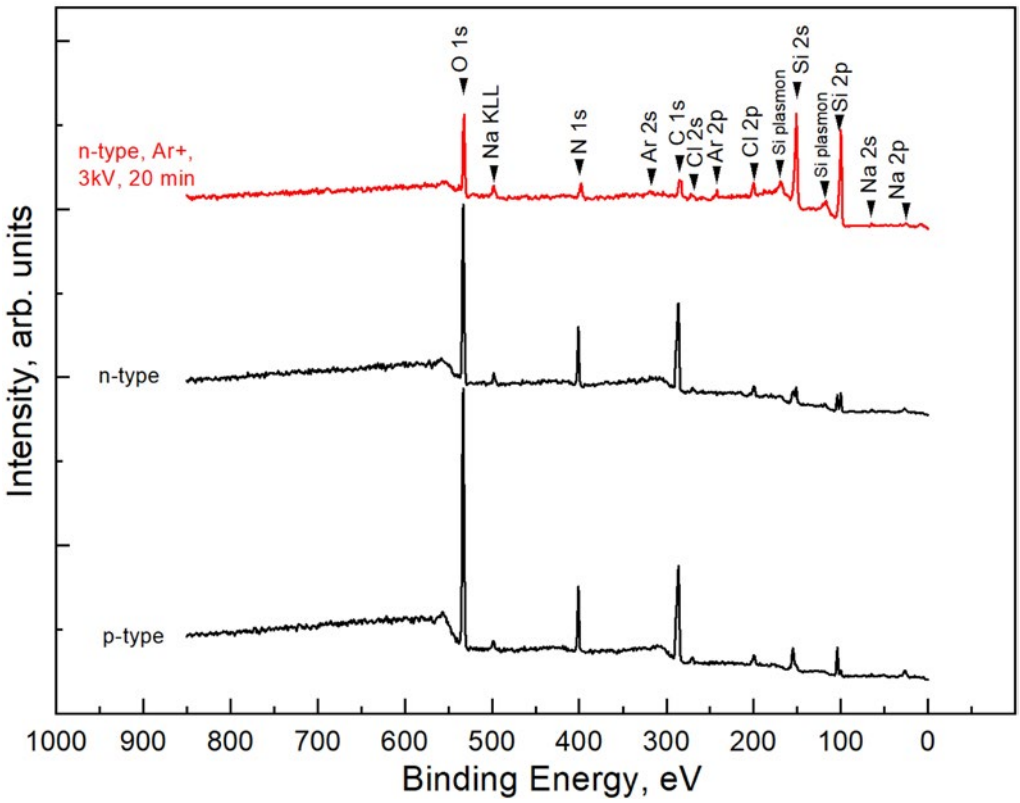

Fig. 2. XPS survey spectra of a silicon wires arrays samples formed on an *n*- and *p*-type substrate before (black) and after (red) ion beam etching (Ar+ 3 kV 20 min). The characteristic elements that make up the studied surface are noted

difference in the rates of ion profiling of the biomaterial and the inorganic silicon "frame". Nevertheless, the nitrogen and carbon lines are still observed, confirming the presence of a Dps molecular culture in the depth of the pores. At the same time, the residual salt lines do not change relative and low intensity. The reason for this observation is the incomplete removal of the NaCl salt, which, nevertheless, is evenly distributed in the volume of the biohybrid structure, probably due to re-precipitation as a result of dissolution during washing with water. Observation of argon lines is associated with ion etching (profiling) of the surface.

4. Conclusions

A combination of X-ray photoelectron spectroscopy and scanning electron microscopy methods demonstrated the possibility of localization of the molecular culture of bacterial ferritin Dps of *E.coli* cells as a result of effective filling of silicon wires arrays pore after washing of the formed biohybrid structures in order to remove the residual NaCl salt.

It is shown that the morphology of the initial silicon wires array does not significantly affect the characteristics of filling pores with a molecular culture of the Dps protein as a result of washing, which leads to the almost complete removal of the residual salt.

Thus, the possibility of silicon wires developed surface functionalization by driven coating with controlled delivery of biohybrid material is confirmed.

Authors comment

During the preparation of this paper, which is a continuation of the research started in [11], it was found that a technical inaccuracy was made. The scale of the image of the initial Si-NW surface formed on a p-type substrate is indicated incorrectly in Fig. 1a of [11], where it is necessary to consider the specified scale equal to 1 μm. However, this scale makes it relatively difficult to compare the morphology with the rest of the SEM images in [11]. For this reason, in this paper we provide an image of the same surface area of the original Si-NW sample from *p*-type substrates with a correctly selected scale of 2 μm. Mistake made does not affect the understanding of the discussed results in the paper [11]. The authors apologize for this technical inaccuracy.

Author contributions

All authors made an equivalent contribution to the preparation of the publication.

Conflict of interests

The authors declare that they have no known competing financial interests or personal relationships that could have appeared to influence the work reported in this paper.

References

1. Behrens S. Synthesis of inorganic nanomaterials mediated by protein assemblies. *Journal of Materials Chemistry*. 2008;18: 3788–3798. https://doi.org/10.1039/B806551A

2. Andrews S. C. Iron storage in bacteria. *Advances in Microbial Physiology*. 1998;40: 281–351. https://doi.org/10.1016/S0065-2911(08)60134-4

3. Harrison P. M., Arosio P. The ferritins: molecular properties, iron storage function and cellular regulation. *Biochimica et Biophysica Acta (BBA) - Bioenergetics*. 1996;1275(3): 161–203. https://doi.org/10.1016/0005-2728(96)00022-9

4. Massover W. H. Ultrastructure of ferritin and apoferritin: A review. *Micron*. 1993;24(3): 389–437. https://doi.org/10.1016/0968-4328(93)90005-L

5. Theil E. C. The ferritin family of iron storage proteins. *Advances in enzymology and related areas of molecular biology*. 1990;63: 421–449. https://doi.org/10.1002/9780470123096.ch7

6. Antipov S., Turishchev S., Purtov Yu., ... Ozoline O. The oligomeric form of the Escherichia coli Dps 3 protein depends on the availability of iron ions. *Molecules*. 2017;22(11): 1904. https://doi.org/10.3390/molecules22111904

7. Zhang Y., Fu J., Chee S. Y., Ang E. X., Orner B. P. Rational disruption of the oligomerization of the mini-ferritin E. coli DPS through protein–protein interface mutation. *Protein Science*. 2011;20(11): 1907–1917. https://doi.org/10.1002/pro.731

8. Antipov S. S., Pichkur E. B., Praslova N. V., ... Turishchev S. Yu. High resolution cryogenic transmission electron microscopy study of Escherichia coli Dps protein: first direct observation in quasinative state. *Results in Physics*. 2018;11: 926–928. https://doi.org/10.1016/j.rinp.2018.10.059

9. Parinova E. V., Antipov S. S., Belikov E. A., ... Turishchev S. Yu. TEM and XPS studies of bio-nanohybrid material based on bacterial ferritin-like protein Dps. *Condensed Matter and Interphases*. 2022;24(2): 265–272. https://doi.org/10.17308/kcmf.2022.24/9267

10. Parinova E. V., Antipov S. S., Belikov E. A., Kakuliia I. S., Trebunskikh S. Y., Turishchev S. Y., Sivakov V. Localization of DPS protein in porous silicon nanowires matrix. *Results in Physics*. 2022;35, 105348. https://doi.org/10.1016/j.rinp.2022.105348

11. Parinova E. V., Antipov S. S., Sivakov V., ... Turishchev S. Yu. Localization of the E. coli Dps protein molecules in a silicon wires matrix according to scanning electron microscopy and X-ray photoelectron spectroscopy. *Condensed Matter and Interphases*. 2023;25(2): 207–217. https://doi.org/10.17308/kcmf.2023.25/1110

12. Sivakov V. A., Brönstrup G., Pecz B., Berger A., Radnoczi G. Z., Krause M., Christiansen S. H. Realization of vertical and zigzag single crystalline silicon nanowire architectures. *The Journal of Physical Chemistry C*. 2010;114: 3798–3803. https://doi.org/10.1021/jp909946x

13. Lo Faro M. J., Leonardi A. A., D'Andrea C., ... Irrera A. Low cost synthesis of silicon nanowires for photonic applications. *Journal of Materials Science: Materials in Electronics*. 2020;31: 34–40. https://doi.org/10.1007/s10854-019-00672-y

14. Lebedev A. M., Menshikov K. A., Nazin V. G., Stankevich V. G., Tsetlin M. B., Chumakov R. G. NanoPES photoelectron beamline of the Kurchatov Synchrotron Radiation Source. *Journal of Surface Investigation: X-ray, Synchrotron and Neutron Techniques*. 2021;15(5): 1039–1044. https://doi.org/10.1134/S1027451021050335

15. John F. *Moulder handbook of X-ray photoelectron spectroscopy*. Minnesota: Published by Perkin-Elmer Corporation Physical Electronics Division United States of America; 1992. 261 p.

16. *Handbook of the elements and native oxide*. XPS International, Inc.; 1999. 658 p.

17. srdata.nist.gov/xps

18. Hüfner S. (ed.). Very high resolution photoelectron spectroscopy. In: *Lecture Notes in Physics*. Berlin: Springer; 2007. https://doi.org/10.1007/3-540-68133-7

Information about the authors

Elena V. Parinova, Cand. Sci. (Phys.-Math.), Assistant Professor, General Physics Department, Voronezh State University (Voronezh, Russian Federation).
https://orcid.org/0000-0003-2817-3547
parinova@phys.vsu.ru

Sergey S. Antipov, Dr. Sci. (Biology), Associate Professor, Biophysics and Biotechnology Department, Voronezh State University (Voronezh, Russian Federation).
https://orcid.org/0000-0003-3244-1428
ss.antipov@gmail.com

Sivakov Vladimir, PhD, Deputy Head, Leibniz Institute of Photonic Technology (Jena, Germany).
https://orcid.org/0000-0002-3272-501X
vladimir.sivakov@leibniz-ipht.de

Evgeny A. Belikov, Engineer of Joint Laboratory "Atomic and Electronic Structure of Functional Materials", Voronezh State University (Voronezh, Russian Federation).
https://orcid.org/0000-0001-8336-2231
belikov@phys.vsu.ru

Olga A. Chuvenkova, Cand. Sci. (Phys.-Math.), Senior Researcher of the Joint Laboratory "Atomic and Electronic Structure of Functional Materials", Voronezh State University (Voronezh, Russian Federation).
https://orcid.org/0000-0001-5701-6909
chuvenkova@phys.vsu.ru

Iuliia S. Kakuliia, Leading engineer, General Physics Department, Voronezh State University (Voronezh, Russian Federation).
https://orcid.org/0000-0002-0953-9024
kakuliia@phys.vsu.ru

Sergey Yu. Trebunskikh, Cand. Sci. (Phys.-Math.), Researcher of the Joint Laboratory "Atomic and Electronic Structure of Functional Materials", Voronezh State University (Voronezh, Russian Federation).
https://orcid.org/0000-0002-2481-2797
trebunskikh@phys.vsu.ru

Kirill A. Fateev, Laboratory Physicist, General Physics Department, Voronezh State University (Voronezh, Russian Federation).
fateev@phys.vsu.ru

Matvey S. Skorobogatov, Bachelor student, Biophysics and Biotechnology Department, Voronezh State University (Voronezh, Russian Federation).
https://orcid.org/0000-0003-3244-1428
mataska7111@gmail.com

Ratibor G. Chumakov, Cand. Sci. (Phys.-Math.), Senior Researcher of the National Research Center "Kurchatov Institute" (Moscow, Russian Federation).
https://orcid.org/0000-0002-3737-5012
ratibor.chumakov@gmail.com

Alexei M. Lebedev, Cand. Sci. (Phys.-Math.), Senior Researcher of the National Research Center "Kurchatov Institute" (Moscow, Russian Federation).
https://orcid.org/0000-0001-9998-8941
lebedev.alex.m@gmail.com

Olga V Putintseva, Dr. Sci. (Biology), Professor of the Biophysics and Biotechnology Department, Voronezh State University (Voronezh, Russian Federation).
o.v.putintseva@gmail.com

Valerii G Artyukhov, Dr. Sci. (Biology), Professor, Head of the Biophysics and Biotechnology Department, Voronezh State University (Voronezh, Russian Federation).
https://orcid.org/0000-0002-5872-8382
artyukhov@bio.vsu.ru

Sergey Yu. Turishchev, Dr. Sci. (Phys.-Math.), Associate Professor, Head of the General Physics Department, Voronezh State University (Voronezh, Russian Federation).
https://orcid.org/0000-0003-3320-1979
tsu@phys.vsu.ru

Received 02.12.2022; approved after reviewing 10.12.2022; accepted for publication 15.12.2022; published online 25.09.2023.
Translated by Sergey Turishchev

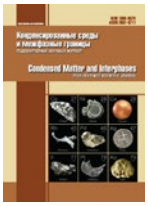

ISSN 1606-867X (Print)
ISSN 2687-0711 (Online)
Condensed Matter and Interphases
Kondensirovannye Sredy i Mezhfaznye Granitsy
https://journals.vsu.ru/kcmf/

Short communications

Research article
https://doi.org/10.17308/kcmf.2023.25/11268

Mass spectrometry of complex compound of bis-thiourea-lead (II) chloride

M. Yu. Krysin[1], V. N. Semenov[1], T. V. Samofalova[1]✉, N. M. Ovechkina[2]

[1]*Voronezh State University,*
1 Universitetskaya pl., Voronezh 394018, Russian Federation

[2]*Voronezh State Medical University named after N. N. Burdenko,*
10 Studencheskaya st., Voronezh 394036, Russian Federation

Abstract

Complex compounds of lead salts and thiourea are of interest due to the possibility of their practical application as precursors in the deposition of metal sulphide films. It is relevant to establish the relationship between the composition and structure of the initial complex compounds and the structure of the sulphides formed as a result of their thermal destruction. This paper presents the results of studying the complex compounds formed in an aqueous solution of lead chloride and thiourea.

The structure of the complex compounds was determined by matrix-assisted laser desorption/ionisation mass spectrometry. The mass spectrometry data confirmed the formation of the $[Pb((NH_2)_2CS)_2Cl_2]$ complex in the solution, which is a precursor in the deposition of PbS films. It was demonstrated that mass spectrometry fragmentation of the molecular ion of the $[Pb((NH_2)_2CS)_2Cl_2]$ compound leads to the formation of a lead sulphide ion.

The obtained data confirm the formation of the lead-sulphur bonds in the inner sphere of the complex compound, which are fragments of the crystal structure of the prospective sulphide formed during the thermolysis of the complex.

Keywords: thiourea complex compounds, complexation, lead sulphide, mass spectrometry

For citation: Krysin M. Yu., Semenov V. N., Samofalova T. V., Ovechkina N. M. Mass spectrometry of complex compound of dichlorodithiocarbamide lead (II). *Condensed Matter and Interphases*. 2023;25(3): 462–466. https://doi.org/10.17308/kcmf.2023.25/11268

Для цитирования: Крысин М. Ю., Семенов В. Н., Самофалова Т. В., Овечкина Н. М. Масс-спектрометрия координационного соединения дихлородитиокарбамид свинца (II). *Конденсированные среды и межфазные границы*. 2023;25(3): 462–466. https://doi.org/10.17308/kcmf.2023.25/11268

✉ Tatyana V. Samofalova, e-mail: TSamofalova@bk.ru

1. Introduction

A topical issue of modern materials science is the search, design, and improvement of cost-effective and accessible methods of deposition of semiconductor films of metal sulphides. The solid phase of a sulphide can be formed during the decomposition of thiourea complex compounds (TCCs) in aqueous solutions [1, 2], during the thermal degradation of TCCs during the pyrolysis of their solution aerosol [3–6], or the combustion of solid samples of complexes containing an oxidising anion NO_3^- [7, 8].

Pyrolysis of aerosol solutions of thiourea complex compounds on a heated substrate meets all the requirements for the deposition of metal sulphide films with variable properties [3, 4, 9]. This method is based on the thermal destruction of thiourea complexes formed by the interaction of the metal cation with the sulphur atom of $(NH_2)_2CS$ (thiourea). Thus, sulphide fragments (-metal-S-) begin to form already in the solution. The resulting complex compound is a precursor in the process of metal sulphide formation. Therefore, it is important to determine the relationship between the composition and structure of thiourea complexes formed in the initial solution and the structure of sulphides formed by this process.

Previously, complexation in aqueous solutions of various lead salts and thiourea was studied, and the domination regions of lead TCCs used for the deposition of PbS films were determined [10–13]. In studies [14, 15], it was found that, depending on the ratio of components, the interaction of lead nitrate, sodium thiosulphate, and thiourea in aqueous solutions forms $[Pb(\textit{bi}\text{-}S_2O_3)(SC(NH_2)_2)(H_2O)]$ and $[Pb(\textit{mono}\text{-}S_2O_3)(SC(NH_2)_2)_2(H_2O)]$ complexes. Upon the thermolysis of these complexes, lead sulphide is formed. In the paper [16], the geometry of the $[Pb((NH_2)_2CS)_2(\textit{mono}\text{-}CH_3COO)_2]$ complex compound was determined using quantum-chemical modelling. This work presents a mass spectrometric study of the thermolysis of the precursor of bis-thiourea-lead(II) chloride formed in aqueous solution by the interaction of lead chloride and thiourea.

2. Experimental

Lead TCCs were synthesised in aqueous solutions of lead chloride and thiourea $(NH_2)_2CS$. The solid phase complexes were obtained by slow evaporation of the solvent from aqueous solutions of 0.02 mol/L lead salt and thiourea at molar ratios of $C_{Pb^{2+}}:C_{SC(NH_2)_2}$ from 1:1 to 1:4. To obtain the TCCs, pure-grade $PbCl_2$ and $(NH_2)_2CS$ were used.

The structure of the synthesised TCCs was identified by mass spectrometry. The spectra were recorded on a VISION 2000 mass spectrometer (MKS Instruments, Inc.) with matrix-assisted laser desorption ionisation using a pulsed nitrogen laser (λ = 337 nm). In this method, the desorption rate exceeds the degradation rate [17]. Thus, it is possible to capture the primary fragment ions formed during the fragmentation of the molecular ion of the complex. Initially, the samples were prepared in powder form.

3. Results and discussion

Matrix-assisted laser desorption/ionisation mass spectrometry was used to study the directions of fragmentation of the molecular ion of the TCCs of lead. The use of this method to determine the structure of $(NH_2)_2CS$ complexes proved to be more representative than electron ionisation mass spectrometry due to rather soft ionisation conditions [17]. Nevertheless, the intensity of the peaks of the molecular ion of the complex and of several fragment ions was low (Table).

It should be noted that the content of aqua complexes in the solution is insignificant, and these compounds mainly have coordination numbers of 1 or 2. Under electron ionisation conditions, these ions were not observed [18].

The most probable direction of the fragmentation of the molecular ion of the $[Pb((NH_2)_2CS)_2Cl_2]$ complex is the initial removal of one or two chlorine atoms to form $Pb((NH_2)_2CS)_2Cl^+$ and $Pb((NH_2)_2CS)_2^+$ ions. Further decomposition of these ions involves the release of $(NH_2)_2CS$ molecules (Figure).

Another fragmentation direction of the $Pb((NH_2)_2CS)_2Cl^+$ fragmentation ion is the rearrangement with the removal of the HCl molecule, resulting in the $[Pb((NH_2)_2CS)_2\text{-}H]^+$ ion. The latter is stabilised as a result of diiminomethane release, which leads to $PbSH^+$ ion and, further, to PbS^+. Probably, their formation causes the formation of PbS films. The layers

Table. Peak intensity and mass of ions under the conditions of mass spectrometry of matrix-assisted laser desorption/ionization of the complex $[Pb((NH_2)_2CS)_2Cl_2]$

Ion	Molecular formula	Molecular mass (m/z), c.u.		Peak Intensity, %
		Calculated	Found	
$Pb((NH_2)_2CS)_2Cl_2^+$ (molecular ion)	$Pb(CH_4N_2S)_2Cl_2$	429.933	*	5
$Pb((NH_2)_2CS)_2Cl^+$	$Pb(CH_4N_2S)_2Cl$	394.946	395.085	20
$[Pb((NH_2)_2CS)_2\text{-}H]^+$	$Pb(CH_4N_2S)\cdot(CH_3N_2S)$	358.987	358.954	90
$[Pb((NH_2)_2CS)Cl\text{-}H]^+$	$Pb(CH_3N_2S)Cl$	317.946	317.841	25
$Pb((NH_2)_2CS)^+$	$Pb(CH_4N_2S)$	283.955	283.900	10
$[Pb((NH_2)_2CS)\text{-}H]^+$	$Pb(CH_3N_2S)$	282.977	282.957	100
$Pb(H_2O)_2^+$	$Pb(H_2O)$	243.997	*	*
$PbCl^+$	PbCl	242.944	*	*
$PbSH^+$	PbSH	240.956	240.594	8
PbS^+	PbS	239.948	*	*
$Pb(H_2O)^+$	$Pb(H_2O)$	225.986	*	*
Pb^+	Pb	207.976	*	*

* Low intensity

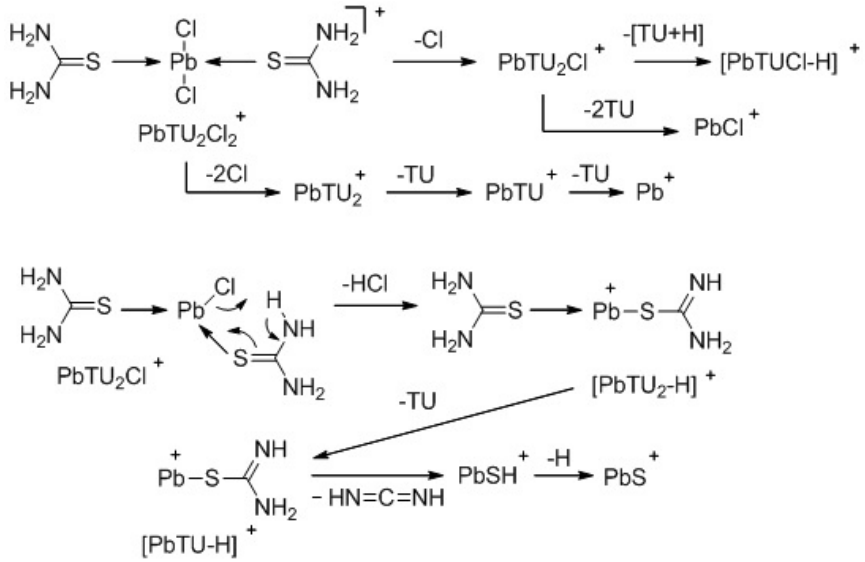

Figure. Scheme of mass spectrometric fragmentation under conditions of matrix-assisted laser desorption/ionisation of the molecular ion of the $[Pb((NH_2)_2CS)_2Cl_2]$ complex

are deposited as a result of the layering of these fragments on the surface of the substrate due to the valence electrons in these ions.

Thus, according to the mass spectrometry data, in an aqueous solution of $PbCl_2$ and $(NH_2)_2CS$ a complex compound is formed, with $(NH_2)_2CS$ included in its inner sphere. The fragmentation of this compound occurs with the preservation, at least partially, of the Pb-S covalent bond. So, it can be assumed that during the deposition of sulphide films by aerosol pyrolysis, thiourea acts as a sulphur donor, coordinating to the metal ion already in the initial solution. The formation of the sulphide structure fragments occurs in the inner sphere of the complex compound. During thermal decomposition of this compound, a PbS layer is formed on the heated substrate.

Contribution of the authors

The authors contributed equally to this article.

Conflict of interests

The authors declare that they have no known competing financial interests or personal relationships that could have influenced the work reported in this paper.

References

1. Markov V. F., Maskaeva L. N., Ivanov P. N. *Hydrochemical deposition of metal sulfide films: modeling and experiment**. Ekaterinburg: UrO RAN; 2006, 217 p. (in Russ.)

2. Soonmin H. Deposition of metal sulphide thin films by chemical bath deposition technique: review. *International Journal of Thin Film Science and Technology*. 2021;10(1): 45–47. https://doi.org/10.18576/ijtfst/100108

3. Semenov V. N., Naumov A.V. Processes of directed synthesis of metal sulfide films from the thiocarbamide coordination compounds. *Proceedings of Voronezh State University. Series: Chemistry. Biology. Pharmacy*. 2000;2: 50–55. (in Russ.). Available at: https://elibrary.ru/item.asp?id=21847224

4. Semenov V. N., Naumov A.V. Thermal decomposition of cadmium thiourea compounds. *Russian Journal of General Chemistry*. 2001;71(4): 533–537. https://doi.org/10.1023/a:1012306512566

5. Mohammad G. F., Pakhuruddin M. Z. Deposited lead sulfide thin films on different substrates with chemical spray pyrolysis technique. *International Journal of Thin Film Science and Technology*. 2015;4(3): 215–217. Available at: https://digitalcommons.aaru.edu.jo/ijtfst/vol4/iss3/10

6. Abdulnabi R. K. Using spray pyrolysis technique to prepare PbS lead sulfide thin films and study their structural and electrical properties as function of thickness. *International Journal of Soft Computing and Engineering*. 2016;6(4): 60–63. Available at: https://www.ijsce.org/wp-content/uploads/papers/v6i4/D2902096416.pdf

7. Tukhtaev R. K., Boldyrev V. V., Gavrilov A. I., Larionov S. V., Myzchina L. I., Savel'eva Z. A. Metal sulfide synthesis by self-propagating combustion of sulfur-containing complexes. *Inorganic Materials*. 2002;38(10): 985–991. https://doi.org/10.1023/a:1020508817410

8. Tukhtaev R. K., Gavrilov A. I., Boldyrev V. V., Larionov S. V. Production of powder electroluminofors based on zinc sulfide under combustion conditions. *Doklady Physical Chemistry*. 2004;395(4–6): 101–103. https://doi.org/10.1023/b:dopc.0000025221.32110.13

9. Krunks M., Mellikov E. Metal sulfide thin films by chemical spray pyrolysis. *Proceedings of SPIE*. 2001;4415: 60–65. https://doi.org/10.1117/12.425472

10. Semenov V. N., Averbah E. M., Ugai Ya. A. About the interaction of lead salts with thiourea in the preparation of PbS films by the spraying method*. *Russian Journal of Applied Chemistry*. 1980;53(1): 30–34. (in Russ.). Available at: https://www.elibrary.ru/item.asp?id=28890880

11. Semenov V. N., Ovechkina N. M., Volkov V. V. Formation of coordination compounds in water solutions of $PbCl_2$–N_2H_4CS. *Proceedings of Voronezh State University. Series: Chemistry. Biology. Pharmacy*. 2010;2: 36–40. (in Russ.). Available at: https://elibrary.ru/item.asp?id=15608640

12. Semenov V. N., Karnushina V. A., Ovechkina N. M. Synthesis of lead thiourea acetate coordination compounds. *Proceedings of Voronezh State University. Series: Chemistry. Biology. Pharmacy*. 2016;(1): 25–29. (in Russ.). Available at: https://elibrary.ru/item.asp?id=25910296&ysclid=ljnjk6njw6427245614

13. Semenov V. N., Volkov V. V., Pereslyckih N. V. Complexation processes in "$PbCl_2$–N_2H_4CS" aqueous solutions during deposition of lead sulphide films. *Condensed Matter and Interphases*. 2021;23(4): 543–547. https://doi.org/10.17308/kcmf.2021.23/3673

14. Egorov N. B., Usov V. F., Fiterer I. P., Eremin L. P., Larionov A. M. Thiosulfatothiourea lead complexes. *Russian Journal of Inorganic Chemistry*. 2008;53(1): 117-122. https://doi.org/10.1134/S0036023608010166

15. Egorov N. B., Eremin L. P., Larionov A. M., Usov V. F. Transformations of thiosulfate-thiourea complexes of lead during heating*. *Bulletin of the Tomsk Polytechnic University*. 2010;317(3): 99–102. (in Russ.). Available at: https://www.elibrary.ru/item.asp?id=15282243

16. Semenov V. N., Naumov A. V., Nechaeva L. S., Malygina E. N. Lead thiocarbamide diacetate as a precursor for the precipitation of lead sulfide films. *Glass Physics and Chemistry*. 2020;46(1): 78–83. https://doi.org/10.1134/S1087659620010150

17. Lebedev A. T. *Mass spectrometry in organic chemistry**. Moscow: TEHNOSFERA Publ.; 2015. 704 p. (in Russ.)

18. Zaikin V. G. Varlamov A. V., Mikaja A. I., Prostakov N. S. *Fundamentals of mass spectrometry of organic compounds**. Moscow: MAIK «Nauka/Interperiodika» Publ.; 2001. 286 p. (in Russ.)

* *Translated by author of the article.*

Information about the authors

Mikhail Y. Krysin, Dr. Sci. (Chem.), Associate Professor, Professor of Department of Organic Chemistry, Voronezh State University (Voronezh, Russian Federation).
https://orcid.org/0000-0002-4336-8935
kaf261@rambler.ru

Victor N. Semenov, Dr. Sci. (Chem.), Professor, Chair of Department of General and Inorganic Chemistry, Voronezh State University (Voronezh, Russian Federation).
https://orcid.org/0000-0002-4247-5667
office@chem.vsu.ru

Tatyana V. Samofalova, Cand. Sci. (Chem.), Associate Professor of the Department of General and Inorganic Chemistry, Voronezh State University (Voronezh, Russian Federation).
https://orcid.org/0000-0002-4277-4536
TSamofalova@bk.ru

Nadezhda M. Ovechkina, Assistant of the Department of Chemistry, Voronezh State Medical University named after N. N. Burdenko (Voronezh, Russian Federation).
https://orcid.org/0000-0002-5841-0403
nadezhda.ovechkina@rambler.ru

Received 05.07.2023 approved after reviewing 15.07.2023; accepted for publication 15.08.2023; published online 25.09.2023.

Translated by Anastasiia Ananeva

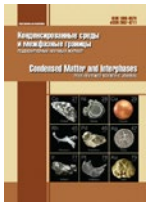

ISSN 1606-867X (Print)
ISSN 2687-0711 (Online)
Condensed Matter and Interphases
Kondensirovannye Sredy i Mezhfaznye Granitsy
https://journals.vsu.ru/kcmf/

Anniversaries

Anniversary of Professor Victor Semenov

Yu. M. Bondarev

Voronezh State University,
1 Universitetskaya pl., Voronezh 394018, Russian Federation

On September 1, 2023 Victor Semenov, Dr. Sci. (Chem.), Dean of the Faculty of Chemistry, Professor at the Department of General and Inorganic Chemistry of Voronezh State University, celebrated his anniversary. He turned 75 years old!

His research interests are related to the development of a physico-chemical model for the formation and destruction of complex compounds, enabling the directed synthesis of semiconductor films, complex compositions, and heterostructures based on them. During his career he has published more than 600 research and educational works.

Victor Semenov is a highly competent professional, with a unique methodological approach and creative autonomy. For us, his colleagues, he is not only an example of a classical teacher, but also a model of decency and honesty. He has supervised and paved the way for many graduates! They are very grateful to him and consider him to be an outstanding, energetic teacher with exceptional and striking pedagogical abilities; as a lecturer who presents complex issues of chemical science in an accessible and clear way, who is able to focus attention on the key aspects; and as a person who can find the key to each student and motivate them to solve difficult problems.

His life is marked by numerous awards and titles. He was awarded the title of Honorary Worker of Higher Professional Education of the Russian Federation and the badge of honor for serving Voronezh State University. In 2021, he won the national award of the Russian Professorial Assembly "Dean of the Year". These are only some of his achievements and merits.

Professor Semenov is highly respected among his colleagues. He has long been the Chair of the Academic Council of the Faculty of Chemistry, member of the Academic Council of Voronezh State University, Chair of the Dissertation Board for Analytical Chemistry, Organic Chemistry and Solid State Chemistry and Deputy Chair of the Dissertation Board for Inorganic Chemistry, Physical Chemistry and Electrochemistry at VSU. Currently, he is the Editor-in-Chief of the journal Condensed Matter and Interphases and a member of the editorial board of the journal Proceedings of VSU. Series: Chemistry, Biology, Pharmacy.

✉ Yury M. Bondarev, Cand. Sci. (Chem.), Associate Professor, Department of General and Inorganic Chemistry, Voronezh State University (Voronezh, Russian Federation).
bondarev@chem.vsu.ru

Victor Semenov is a sociable and cheerful person. He infuses everyone with his positive energy and optimism. He has many interests: books, sports, fishing, cars, and meeting interesting people, which he successfully pursues.

There is a category of people on earth who do not want and do not know how to work badly. Whatever business they undertake, they always strive for perfection. Victor Semenov is this kind of person.

We heartily congratulate Victor Semenov on his anniversary. The age of 75 is a blissful combination of energy, characteristic of enthusiastic people, and experience, both professional and personal. So, combining his work as Dean of the Faculty of Chemistry and Head of the Department of General and Inorganic Chemistry of VSU, he will be able to fulfill his most ambitious creative plans.

The team of the Faculty of Chemistry,
the Department of General and Inorganic Chemistry
and the editorial board
of the journal Condensed Matter and Interphases

Translated by Anastasiia Ananeva